Magnetotelluric characterisation and monitoring of the Hontomín CO_2 storage site, Spain

Xènia Ogaya García

Xènia Ogaya García, 2014

Magnetotelluric characterisation and monitoring of the Hontomín CO_2 storage site, Spain

Magnetotelluric characterisation and monitoring of the Hontomín CO_2 storage site, Spain

Xènia Ogaya García

Ph.D. Thesis

Supervisors:
Dr. Pilar Queralt, Dr. Juanjo Ledo and Dr. Alan G. Jones

UNIVERSITAT DE BARCELONA

Geomodels Research Institute
Departament de Geodinàmica i Geofísica
Facultat de Geologia
Universitat de Barcelona

geomodels
Institut de Recerca

Geomodels Research Institute
Departament de Geodinàmica i Geofísica
Facultat de Geologia
Universitat de Barcelona

Magnetotelluric characterisation and monitoring of the Hontomín CO_2 storage site, Spain

Memoria presentada por **Xènia Ogaya García** para optar al título de Doctora dentro del programa de doctorado de Ciencias de la Tierra de la Universitat de Barcelona. Esta memoria ha sido realizada bajo la dirección de la **Dra. Pilar Queralt** (*Universitat de Barcelona*), del **Dr. Juanjo Ledo** (*Universitat de Barcelona*) y del **Dr. Alan G. Jones** (*Dublin Institute for Advanced Studies*).

Xènia Ogaya García
Barcelona, Julio 2014

Dra. Pilar Queralt	Dr. Juanjo Ledo	Dr. Alan G. Jones
Directora y tutora de la tesis	Director de la tesis	Director de la tesis

Esta tesis se ha realizado gracias al apoyo de la Fundación Ciudad de la Energía, a través de la ayuda para la realización de tesis doctorales en almacenamiento geológico de CO_2 (Resolución de 30 de septiembre de 2009) y de la ayuda de la Universitat de Barcelona 'Ajuts de personal investigador predoctoral en formació (APIF)' (Convocatoria 2012-2013).

Los siguientes proyectos y grupos de investigación han financiado esta tesis:

Acuerdo Fundación Bosch i Gimpera y CIUDEN ALM-09-009, para el desarrollo y adaptación de técnicas electromagnéticas: caracterización de almacenes geológicos, con cargo al presupuesto de gastos del Ministerio de Industria, Energía y Turismo. Proyecto cofinanciado por el Programa Energético Europeo para la Recuperación (PEER), en el marco del proyecto OXYCFB300 Compostilla.

PIERCO2 (CGL2009-07604)

Grup de Recerca de Geodinàmica i Anàlisi de Conques (2009SGR1198)

Geomodels Research Institute

A mi familia,

Acknowledgments

Poso punt i final a aquesta tesis i en fer-ho, em vénen a la ment las 'camas elásticas' d'Hontomín. Han estat uns anys intensos en els que he après més del que mai m'hagués imaginat (i tot s'ha de dir, no només en el camp de la MT i del CO_2). Gràcies a tots els que heu fet possible aquesta tesis i aquesta etapa.

Primer de tot, gràcies als meus directors de tesis. Gràcies Pilar y gracias Juanjo per ensenyar-me, guiar-me, aconsellar-me i donar-me un cop de mà sempre que ho he necessitat. Gràcies pel temps que m'heu dedicat. Thank you Alan for your advice and all facilities and opportunities you have given to me.

Quiero agradecer a la Fundación Ciudad de la Energía la financiación que ha permitido la realización de esta tesis. Del mismo modo, quiero agradecer a la Universidad de Barcelona la ayuda predoctoral recibida en estos últimos meses.

Thank you Gary Egbert and Anna Kelbert for providing the ModEM code; Weerachai Siripunvaraporn for providing WSINV3DMT code and the Irish Centre for High-End Computing (ICHEC) for availing the Stokes cluster to carry out the numerical computations. I want to thank Dublin Institute for Advanced Studies (DIAS) for availing their clusters for my research and for the two months I was there learning MT in 3D. Thank you Jan Vozar for your guidance and help on the 3D inversion process.

Moltes gràcies a l'EXES (Pilar, Juanjo, Alex, Anna, Fabián, Perla, Joan, Oriol, Lena, David i Eloi) per l'ambient de treball, per crear aquesta família on les trapelleries i les bromes han estat sempre permeses; sempre serà com tornar a casa. Gràcies a tots els que heu participat a les campanyes d'MT d'Hontomín: Perla, Lena, Joan, Eloi, Yonas, Mikel, David, Rafa (Alex), Marc i Fabián. Van ser uns campaments memorables. Gràcies a l'Hostal Sotopalacios per acollir-nos de la millor de les maneres i pel 4433E.

Gràcies a tot el personal del departament de Geodinàmica i Geofísica per aquests anys. Vull donar les gràcies de forma especial a l'equip dels dinars, sempre puntuals a les 13:00:00 h (Anna E., Eva, Marta, Mar, Avalanchis, Lena D., Sara, Manu...), i als companys de despatx (Eloi C., Lena, Eloi V., Anna Q., David, Perla, Anna C., Fabián i Oriol), heu estat una companyia immillorable.

A Andrés Pérez-Estaún muchas gracias por todo, gracias por transmitirnos ese entusiasmo por la ciencia, por el proyecto y por el vino. Hablar contigo siempre ha supuesto una verdadera inyección de energía y optimismo. Mucho ánimo. A Modesto Montoto, gracias por la confianza que siempre has tenido en mí. A Dani, gracias por echarnos una mano siempre que lo hemos necesitado y por ese paseo en traje por las calles de Christiania.

Gracias a todos mis compañeros bercianos y en especial a Amanda, Javi, Jacobo y Juan por formar esa pequeña familia en el Bierzo. A los nueve doctorandos de Ciuden, un brindis con vino de Mencía por los avatares vividos y porque al final, pese a todo, podríamos decir que lo hemos conseguido! Gràcies Eloi, no només per explicar-me i corregir-me la geologia una vegada rera l'altra, sinó també per acompanyar-me aquests anys i per mantenir-me sempre informada de la lletra petita.

Para acabar, quiero dar las gracias a todos aquellos que, fuera de lo profesional, me han acompañado en esta y otras etapas. Gracias por vuestro ánimo y apoyo incondicional, sin vosotros nada sería lo mismo.

Gracias a mis suecas, Amaia, Sara y Helena, por las comidas de tupper, los ánimos y los Caminos de Santiago.

Als fisics i en especial a les meves fisiquines, gràcies pels ànims de la darrera etapa.

Gràcies als del Goya, grupo donde os incluyo también a vosotros Alex y Perla, pels ànims i els mimos. És un veritable plaer saber que tinc a gent com vosaltres acomiadant-me sempre que marxo, rebent-me sempre que torno i disposats a creuar-se la península en una discoteca mòbil per ajudar-me en el que necessiti. Gràcies de tot cor, és un plaer tenir-vos a la vora.

Gracias Perla por todas las sesiones de cerveza y magnetotelúrica, por las rutas en hippie camper y por todos los 'arriba mi kurni' que me has regalado. Ha sido un verdadero placer maquinar contigo. Gracias por la ayuda en el sprint final.

Gracias Juan por haber sido el mejor compañero de viaje. Sin ti las aventuras de estos últimos años y las anécdotas de este doctorado no hubiesen sido lo mismo. Gracias por la paciencia, las discusiones, el apoyo y en definitiva, el día a día. Somos un gran equipo.

Finalmente, quiero dedicar esta tesis a mi familia. Podría agradeceros tantas cosas que no vale la pena ni intentar escribirlas. Gracias por sentiros siempre orgullosos de mí y por apoyarme sea cual sea la aventura que decida emprender.

A mis padres, a mi hermana y a mis abuelos,
esta tesis es vuestra.

Contents

List of figures

Introduction and overview

Geological and geophysical setting

Magnetotelluric characterisation

Magnetotelluric monitoring

Supplementary figures

List of tables

Magnetotelluric characterisation

Magnetotelluric monitoring

Preface

Carbon Capture and Storage (CCS) technology is presented as a major solution to the problem caused by the increase of anthropogenic emissions of carbon dioxide (CO_2) to the atmosphere. Geological storage of CO_2 constitutes the last part of the CCS chain and implies the disposal of CO_2 in deep geological formations. The Hontomín site is a Technological Development Plant (TDP) for CO_2 geological storage in a deep saline aquifer. The facility is established in the framework of the OXYCFB300 Compostilla Project of the European Energy Programme for Recovery.

This thesis focuses on the magnetotelluric characterisation and monitoring of the Hontomín site. The major aim of the research reported in this thesis is to obtain the three-dimensional (3D) geoelectrical baseline model of the TDP to be used for future time-lapse electromagnetic monitoring experiments of the site. The thesis also pursues evaluation of the monitoring capabilities of the MT method. An innovative methodology is developed to enhance the resolution of MT responses to resistivity variations produced in the reservoir due to the CO_2 injection.

The work is organised into five chapters, with Chapter 3 (Magnetotelluric characterisation) and Chapter 4 (Magnetotelluric monitoring) being the core of the thesis.

Chapter 1 provides an introduction and overview. The chapter begins with the problem caused by the increase of concentrations of greenhouse gases in the atmosphere, and presents CCS technology as a bridging solution towards a sustainable green energy system. Focusing on the geological storage of CO_2, the chapter reports how physical properties of the reservoir rock change after the gas injection and how is possible to monitor the evolution of the injected gas, studying the evolution of these properties through time. The chapter highlights the importance of electromagnetic methods in these kinds of projects, underlying the abilities of the magnetotelluric method to characterise a storage site. Finally, the Hontomín underground research laboratory is introduced and the aims and objectives of the thesis are enumerated.

Chapter 2 summarises both the geological and geophysical setting of the study area. In this chapter, one-dimensional (1D) resistivity models are derived from the resistivity log data of the existing wells. These 1D models constitute the point of departure of the magnetotelluric characterisation presented in the following chapter.

Chapter 3 describes in detail the two magnetotelluric surveys carried out at the Hontomín site: the 2D survey undertaken in Spring 2010 and the 3D survey undertaken in Autumn 2010. Each description of them is basically structured into logical time sequence: data processing and dimensionality analysis, inversion and modelling process, interpretation and discussion of the preferred models and final conclusions of the survey. To complete the chapter, the resistivity log data of the injection and monitoring wells, drilled at the end of 2013, are compared to the electrical resistivity structure provided by the 3D model. Likewise, the geoelectrical baseline model of the Hontomín site is correlated with other geophysical data acquired in the study area (3D reflection seismics and microgravimetry).

Chapter 4 explores the monitoring capabilities of the magnetotelluric method. In this chapter, an approach is developed to enhance the resolution of surface magnetotelluric responses to small resistivity changes: a layer stripping approach. This innovative methodology is validated through synthetic studies, and theoretically tested using the geoelectrical baseline model of the Hontomín site.

Chapter 5 presents conclusions and future work. Although the conclusions drawn in the thesis are presented at the end of the different sections, this final chapter summarises all major results of the work from a more general point of view. Moreover, this chapter enumerates some perspectives of advance.

The latest sections that complete the thesis are References and Supplementary Figures. Supplementary figures plot the MT data and the 3D model responses at all sites, as well as the misfits of all profiles.

The research presented here has resulted in the following publications:

- **Ogaya, X.**, Ledo, J., Queralt, P., Marcuello, A., Quintà, A., 2013. First geoelectrical image of the subsurface of the Hontomín site (Spain) for CO_2

geological storage: A magnetotelluric 2D characterization. International Journal of Greenhouse Gas Control 13, 168-179, doi: 10.1016/j.ijggc.2012.12.023.

- **Ogaya, X.**, Queralt, P., Ledo, J., Marcuello, A., Jones, A.G., 2012. Preliminary results of the 3-D magnetotelluric characterization of the subsurface of the Technology Demonstration Plant of Hontomín (Burgos, Spain) for geological storage of CO_2, In: Zurutuza, J. (Ed.) 7AHPGG: Proceedings. Portuguese-Spanish Assembly of Geodesy and Geophysics, pp. 703-708, ISBN: 978-84-941323-1-5.

- **Ogaya, X.**, Queralt, P., Ledo, J., Marcuello, A., Jones, A.G., 2014. Geoelectrical baseline model of the subsurface of the Hontomín site (Spain) for CO_2 geological storage in a deep saline aquifer: a 3D magnetotelluric characterisation. International Journal of Greenhouse Gas Control 27,120-138, doi: 10.1016/j.ijggc.2014.04.030.

At the end of the thesis, a copy of the PEER reviewed papers (Ogaya et al., 2013 and Ogaya et al., 2014) is included.

Since the thesis is presented in the Universitat de Barcelona, a summary in Spanish (Resumen) is attached.

Resumen

La captura y almacenamiento geológico de dióxido de carbono (CO_2) constituye una de las soluciones tecnológicas propuestas en la actualidad para reducir las emisiones de este gas a la atmosfera. El objetivo de esta tecnología es capturar y transportar el gas desde los grandes focos emisores hasta los lugares seleccionados como almacenes geológicos, donde es inyectado. Esta tesis se centra en la Planta de Desarrollo Tecnológico (PDT) de Hontomín (España), donde el almacenamiento geológico se llevará a cabo en un acuífero salino profundo. La PDT se enmarca en el proyecto Compostilla OXYCFB300, dentro del Programa Energético Europeo para la Recuperación (European Energy Programme for Recovery).

La mayoría de las propiedades físicas de la roca almacén, en especial la resistividad eléctrica, variarán tras la inyección de CO_2. El fluido salino conductor contenido en el poro será sustituido por el gas, de carácter más resistivo, reduciendo el volumen de agua disponible para la conducción iónica. Por ello, los métodos electromagnéticos, sensibles a la resistividad eléctrica, son especialmente interesantes para este tipo de proyectos ya que permiten estudiar la evolución del gas inyectado y estimar la saturación de CO_2 en el poro.

Esta tesis tiene por objetivo la caracterización, control y seguimiento de la PDT de Hontomín mediante el método magnetotelúrico. El objetivo principal es la obtención de un modelo geoeléctrico tridimensional (3D) de referencia, que permita caracterizar la zona en la situación de preinyección y sirva de modelo base para los posteriores estudios de seguimiento con métodos electromagnéticos de fuente controlada. Asimismo, esta tesis persigue evaluar la capacidad de control y seguimiento del método magnetotelúrico. Con este propósito, se ha desarrollado una nueva metodología para mejorar la resolución de las respuestas magnetotelúricas superficiales a cambios de resistividad producidos en el reservorio (metodología denominada *layer stripping*).

La caracterización de la PDT de Hontomín se ha llevado a cabo en dos etapas. En la primera etapa se adquirió un perfil magnetotelúrico de orientación NS. Este primer

estudio demostró la idoneidad del método para caracterizar la zona de estudio y proporcionó un modelo geoeléctrico bidimensional (2D) de la misma. En la segunda etapa se completó la adquisición de los datos, lo que permitió la obtención del modelo geoeléctrico 3D de la PDT. Esta tesis presenta ambos estudios de caracterización. Cada uno de ellos es justificado por un análisis previo de dimensionalidad de los datos y detalla la metodología de inversión empleada para alcanzar resultados válidos y apropiados.

El modelo 2D obtenido previamente ha sido validado por el modelo 3D, el cual se correlaciona satisfactoriamente con datos hidrogeoquímicos, sísmicos, gravimétricos y datos de pozos, entre otros. Este modelo 3D constituye el modelo geoeléctrico de referencia de la PDT, siendo la principal contribución de esta tesis. El modelo muestra la estructura de domo de Hontomín y los principales conjuntos de fallas. Permite así identificar las posibles zonas de fuga y definir las necesidades de control y seguimiento de la PDT.

De este modo, esta tesis supone una importante contribución a los proyectos de caracterización de almacenes de CO_2 en acuíferos salinos profundos. El método magnetotelúrico ha demostrado ser una técnica electromagnética apropiada para caracterizar el área de estudio. Los resultados obtenidos son significativos y ponen de manifiesto la importancia de establecer un modelo geoeléctrico de la situación de preinyección a fin de caracterizar la estructura, concretar las necesidades de control de la planta y definir el modelo de referencia para los posteriores estudios de seguimiento. Los estudios electromagnéticos son complementarios a estudios de caracterización sísmicos y dada su sensibilidad a la conductividad eléctrica, se establecen como métodos de resolución superior para determinados aspectos de interés en el almacenamiento de CO_2 y su seguimiento a largo plazo.

1 Introduction and overview

Carbon Capture and Storage (CCS) technology aims to prevent the release of large quantities of carbon dioxide (CO_2) to the atmosphere. Geological storage of CO_2 involves the injection and permanent disposal of CO_2 in deep geological formations. The injection of the CO_2 gas into the porous reservoir formation will result in the variation of the physical properties of the host rock. Thus, by studying the evolution of these properties through time it is possible to monitor the injected CO_2. Since electrical resistivity is more sensitive to CO_2 saturation than other physical properties, electromagnetic methods are presented as suitable monitoring techniques. In this context, the natural source electromagnetic technique called magnetotellurics could be especially useful for characterisation and monitoring purposes. This chapter contextualise the thesis and presents a brief introduction to all the above mentioned basic concepts. Finally, the Hontomín site (case study of this thesis) is introduced and the aims and objectives of the research work are presented.

1.1. CO_2 problem and CCS technology as a short term solution

Since the industrial revolution of the early part of the 19th century, concentrations of greenhouse gases (GHG) in the atmosphere have increased hugely and exponentially, perturbing the equilibrium of the natural greenhouse effect of the Earth and leading to a climate warming (Bryant, 1997). One of the major contributors to the greenhouse effect is the carbon dioxide (CO_2) (Bryant, 1997; Bachu, 2000). Svante Arrhenius was the first to show how changes in the atmospheric CO_2 levels could significantly alter the temperature at the Earth's surface (Arrhenius, 1896). More recent studies have also documented the effects

of anthropogenic emissions on the Earth's climate and the increase in Earth's surface temperature (IPCC, 2005) (Fig. 1.1).

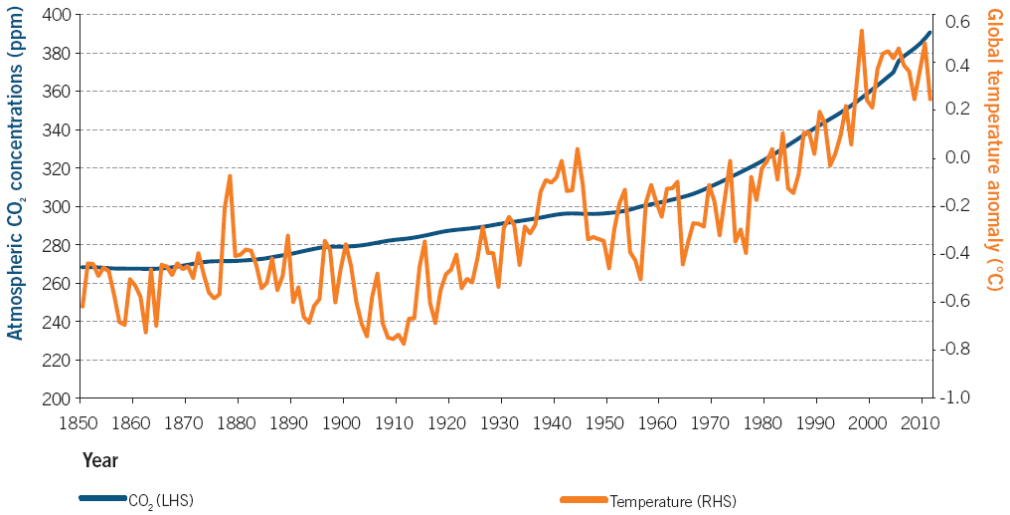

Fig. 1.1. Global CO_2 atmospheric concentrations and temperature (from Global CCS Institute, 2011).

On a sectorial basis, the major contribution to GHG comes from the energy sector (around 45%) (Bachu, 2000). Fossil fuels account for over 80 % of world's energy supply, being by far the major contributor to the GHG emissions (IEA, 2012). Thus, there is a large dependence on fossil fuels and an energy system solely based on renewable energies is not currently feasibly. Therefore, Carbon Capture and Storage (CCS) is presented as an essential bridge towards a truly sustainable green energy system. Wide implementation of CCS is estimated to be able to reduce CO_2 emissions by 54 % in European Union (EU) and 33 % globally in 2050 compared to emissions levels in 2007 (Stangeland, 2007).

According to Bachu (2003), the meaning of CCS is 'the removal of CO_2 directly from anthropogenic sources (capture) and its disposal in geological media, either permanently (sequestration), or for significant time periods (storage)'. CCS technology is based on the fact that naturally, the Earth's subsurface is the largest carbon reservoir. The greatest part of the Earth's carbon is found in coals, oils, gas organic-rich shales and carbonate rocks (IPCC, 2005). Thereby, CO_2 sinks are part of the Earth's carbon cycle (e.g., soils, vegetation and oceans) and the geological storage of CO_2 is a natural process within this cycle (IPCC, 2005) (Fig. 1.2). However, as natural terrestrial sinks are not sufficient to absorb current emissions of CO_2 to the atmosphere (NETL, 2009), CCS is one of the approaches suggested

to both reduce GHG emissions and enhance GHG sinks (Turkenburg, 1997). The method is considered safe and environmentally friendly, as CO_2 is only problematic at very high concentrations and any leakage from the CO_2 storage is estimated to be in much lower concentration. Possible leaks are not expected to raise local concentrations much above normal atmospheric levels because geological formations will diffuse the gas making the massive leakage extremely unlikely.

The Kyoto Protocol (an international agreement linked to the United Nations Framework Convention on Climate Change, adopted in December 1997 and entered into force in February 2005) sets internationally binding GHG emission reduction targets[1]. In Europe, since around 11% of the GHG emitted globally each year come from the EU, the EU established a political agenda to reduce its own emissions under the Kyoto Protocol for 2020[2]. The EU's energy and environment policy '*20/20/20*' (adopted by the European Parliament in December 2008) laid down the following targets: i) reduce by 20 % the GHG emissions comparing with 1990 level; ii) increase to 20 % the share of renewables in the final energy consumption and up to 10 % the share of biofuels in transport fuels; and iii) achieve an improvement of 20 % in energy efficiency, which means a 20 % reduction in energy consumption (Streimikiene, 2012).

To address these issues, in 2009 the European Commission set up the European Energy Programme for Recovery (EEPR). It aimed to co-finance different projects designed to make energy supplies more reliable, help reduce greenhouse emissions and stimulate Europe's economic recovery[3]. The projects include: 44 gas and electricity infrastructures projects, 9 offshore wind projects and 6 CCS projects. In this way, the EU is encouraging its member countries to implement CCS technology as one of the vehicles used to reach these targets (Directive 2009/31/EC).

The Spanish OXYCFB300 Compostilla Project[4] is one of these 6 CCS projects. The main target of the project is to validate a flexible and competitive CCS technology at industrial

[1] http://unfccc.int/kyoto_protocol/items/2830.php (visited April 2014).
[2] http://ec.europa.eu/clima/policies/g-gas/index_en.htm (visited April 2014).
[3] http://ec.europa.eu/energy/eepr/ (visited April 2014).
[4] http://www.compostillaproject.es/ent (visited April 2014).

level. The project is led by Endesa, and Fundación Ciudad de la Energía[5] (CIUDEN) is one of the partners. The first phase of the OXYCFB300 Compostilla Project is called 'Technological Development' and aims to construct and operate three Technological Development Plants (TDPs) for CO_2 capture, transport and storage at pilot scale. The CO_2 capture plant is located in Compostilla (León, Spain) (Lupion et al., 2011a; Lupion et al., 2011b) and the TDP for CO_2 geological storage is located in Hontomín (Burgos, Spain). This work will be focus on the TDP at Hontomín for CO_2 geological storage in a deep saline aquifer.

The EU and the Spanish Government have set the legal framework for the geological storage of CO_2 in Europe and Spain (Directive 2009/31/EC and Law 40/2010, respectively). Within this framework, research-aimed projects (such as the Hontomín project) are allowed to store a maximum of 100 kilotons of CO_2.

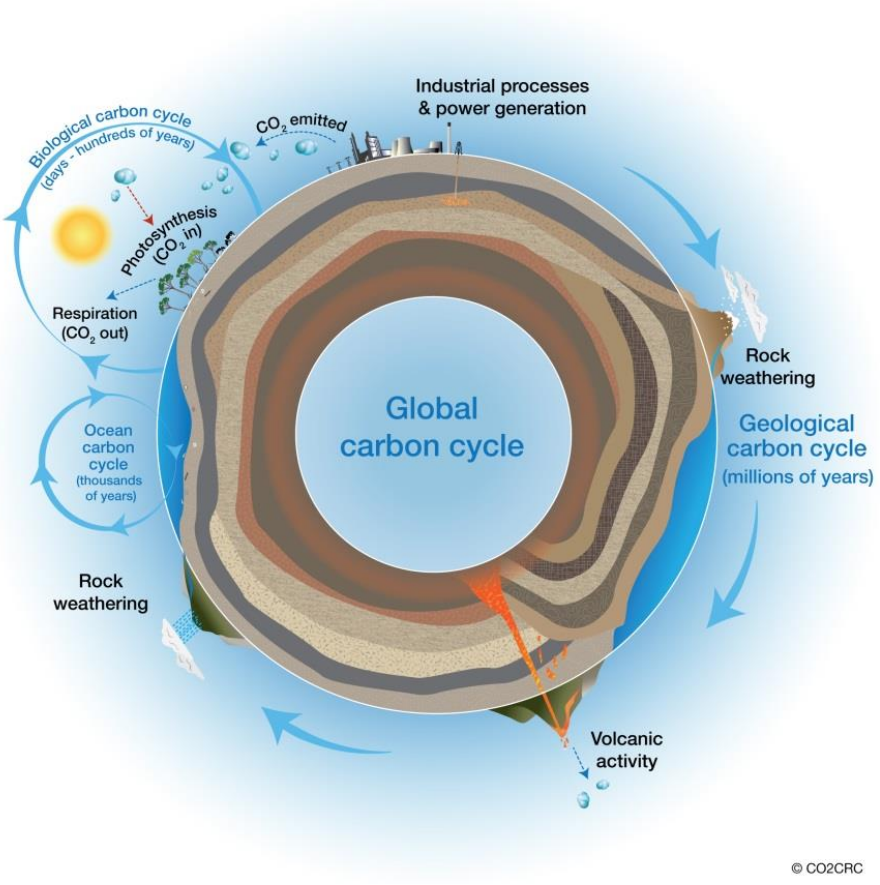

Fig. 1.2. Global carbon cycle (source: CO2CRC[6])

[5] www.ciuden.es (visited April 2014).
[6] www.co2crc.com.au/imagelibrary (visited April 2014).

1.2. Geological storage of CO_2

CCS technology aims to capture the CO_2 after combustion in large stationary emission sources and transport it to suitable storage sites enabling power plants and a wide range of other industries to reduce their emissions to the atmosphere. In the storage site, the CO_2 is stored into the pores of a permeable formation (reservoir) which is capped by another impermeable formation (seal) that prevents it from migration to the surface (IPCC, 2005). It is based on the natural trapping mechanism that has kept huge volumes of oil and gas underground for millions of years. Several rock formations are considered suitable for CO_2 storage (IPCC, 2005) (Fig. 1.3): depleted oil and gas reservoirs, deep saline aquifers and unminable (uneconomic) coal beds. Moreover, other scenarios, such as sedimentary formations, caverns, basalt and organic-rich shales, are being contemplated. The injection of CO_2 has been undertaken for years for enhanced oil recovery (EOR), enhanced gas recovery (EGR) and enhanced coal bed methane recovery (ECBMR) (Bachu, 2003). According to the IPCC (2005), there is a large global capacity: depleted oil and gas reservoirs are estimated to have 675-900 Gigatons of CO_2 of storage capacity; deep saline formations, at least 1000 Gigatons (some studies suggest an order of magnitude greater than this), and unminable coal formations, between 3 and 200 Gigatons. Thus, saline aquifers are thought to be the most promising type of geological storage in terms of total potential volume. To put these storage capacities into context, it is interesting to bear in mind that the global emissions of CO_2 coming from the use of fossil-fuel was about 23.5 Gigatons in the year 2000, and close to 60% was attributed to large stationary emission sources (IPCC, 2005).

To date, geological storage of CO_2 is being carried out offshore and onshore and both at pilot and industrial-scale (Global CCS Institute, 2011). The CO_2 gas is injected at depths below 800 m, where reaches supercritical conditions (T_c= 31.1 °C and P_c= 7.38 MPa). At these conditions, CO_2 behaves still like a gas filling all the available volume, but with a liquid-like density. With the same volume, at supercritical state it is able to store a greater quantity of CO_2 because the density is higher (Fig. 1.4); e.g., 100 m^3 of CO_2 at the surface is estimated to occupy 0.28 m^3 at 1500 m depth. Thereby, by increasing the density, the storage of CO_2 in the pore space is more efficient and becomes safer since buoyancy forces decrease (Bachu, 2003).

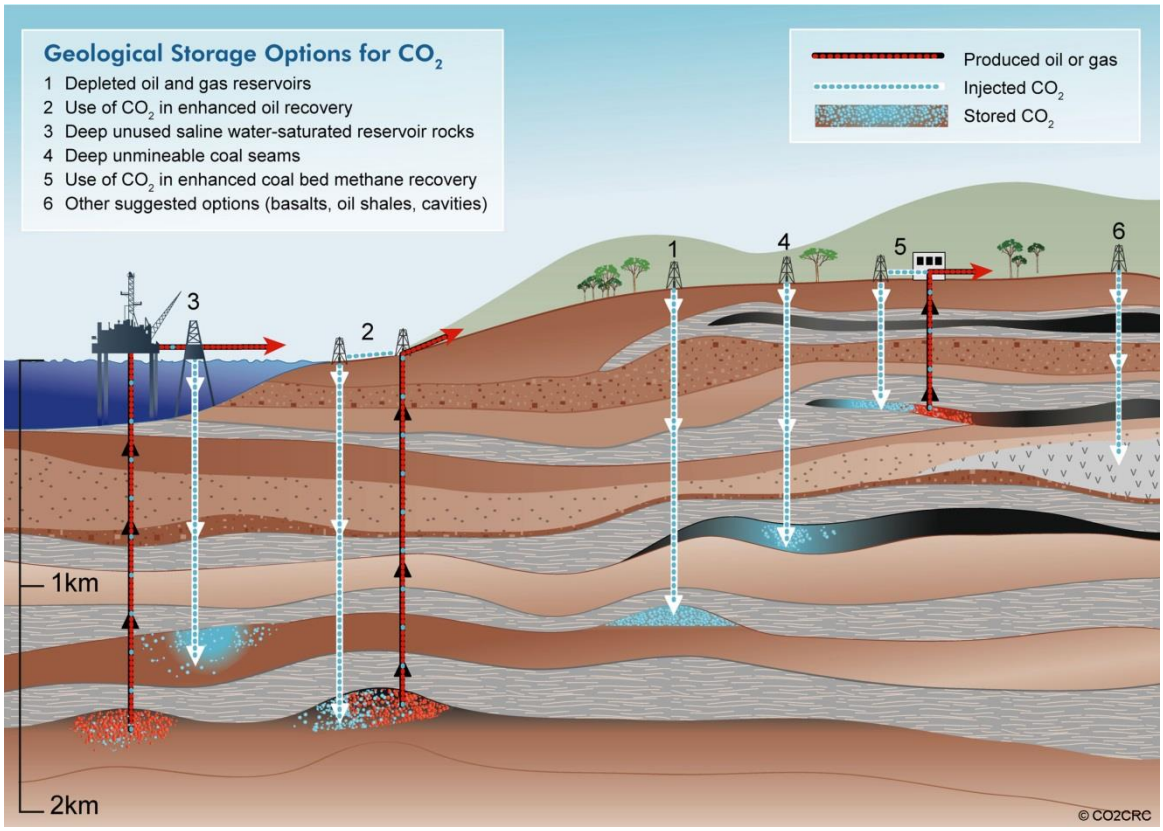

Fig. 1.3. Geological options for CO_2 storage (from CO2CRC, 2008).

Once the CO_2 is pumped into the pores of the geological formation, the geological storage itself is essentially a combination of four physical and chemical trapping mechanisms (IPCC, 2005): structural and stratigraphic (Fig. 1.5a), residual (Fig. 1.5b), solubility (Fig. 1.5c) and mineral. Physical trapping mechanisms are immediate; since the injected CO_2 is less dense than water, it rises up through the reservoir rock until it reaches the seal (structural and stratigraphic trapping) (Fig. 1.5a). During the migration of the injected CO_2, some of the gas can be retained by capillarity action in the porous space (residual trapping) (Fig. 1.5b). Chemical trapping mechanisms require longer time, but entail an increase of the storage security (Fig. 1.6). The injected CO_2 interacts with the rock and the water contained in the porous media, and as a consequence, geochemical reactions take place in the reservoir. The CO_2 is dissolved into the salty water (solubility trapping) (Fig. 1.5c) and, as water with CO_2 is denser than water without CO_2, the solution sinks. This generates a convective flow that favours the mixing of the rest of the CO_2 with water. The CO_2 dissolved in the salty water

becomes slightly acidic and starts to chemically react with minerals. The interaction between the different ionic species might result in stable carbonate minerals (mineral trapping).

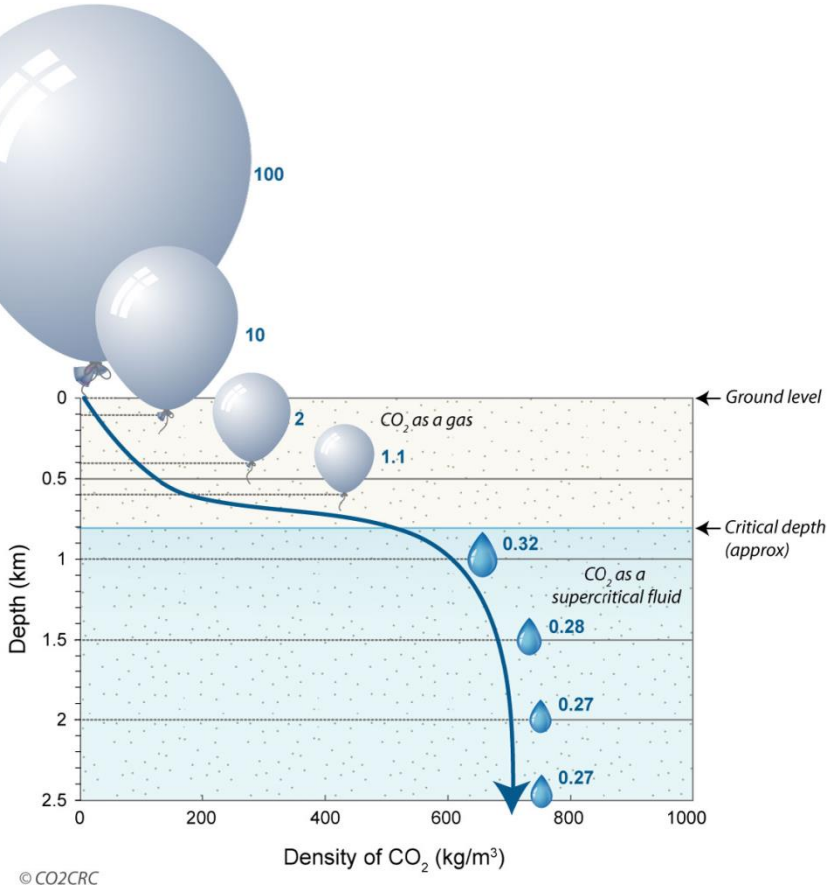

Fig. 1.4. Variation of CO_2 density with depth for hydrostatic pressure and a geothermal gradient of 25°C/km from 15°C at the surface. The volumetric relationship is indicated by blue numbers. Above the critical depth (above 800 m depth), the CO_2 is in gas state (displayed by balloons) and below the critical depth (below 800 m), the CO_2 is in liquid-like state (displayed by drops). At depth below 1500 m, the volume is nearly constant (from CO2CRC, 2008).

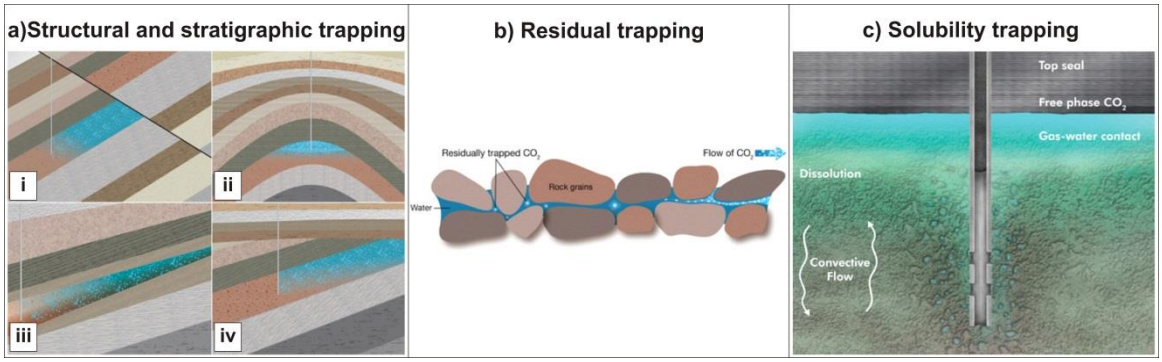

Fig. 1.5. Different trapping mechanisms. a) Structural and stratigraphic trapping at four different scenarios: (i) fault trapping, (ii) anticline or stratigraphic trapping, (iii) facies change trapping and (iv) unconformity trapping. b) Residual trapping. c) Solubility trapping and residual trapping around the injection well. When the CO_2 is dissolved in water, the water becomes denser and begins to sink downwards, this generates a convective flow that favours the mixing of water and injected CO_2 (modified from CO2CRC[7]).

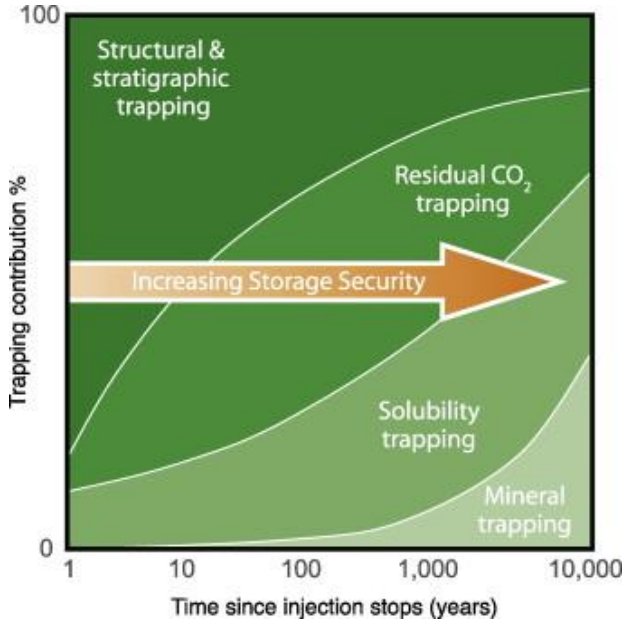

Fig. 1.6. Trapping contribution versus time since injection stops. In the first moment, the major trapping contribution comes from the physical processes (structural, stratigraphic and residual trapping) and over time, the contribution of chemical process (solubility and mineral trapping) increases, enhancing the storage security (from IPCC, 2005).

[7] www.co2crc.com.au/imagelibrary (visited April 2014).

1.3. From CO_2 saturation to electrical resistivity

The electrical resistivity of Earth materials (also commonly defined in terms of its inverse, electrical conductivity) is essentially a transport property of the medium, compared to the propagation velocity of elastic waves which is a property that is associated to the transmission of mechanical (vibrational) energy. The electrical resistivity of Earth materials ranges over more than 10 orders of magnitude (Palacky, 1987) (Fig. 1.7) whereas seismic velocity varies at most by a factor of 10, and rock density by at very most factor of 3 (Bedrosian, 2007).

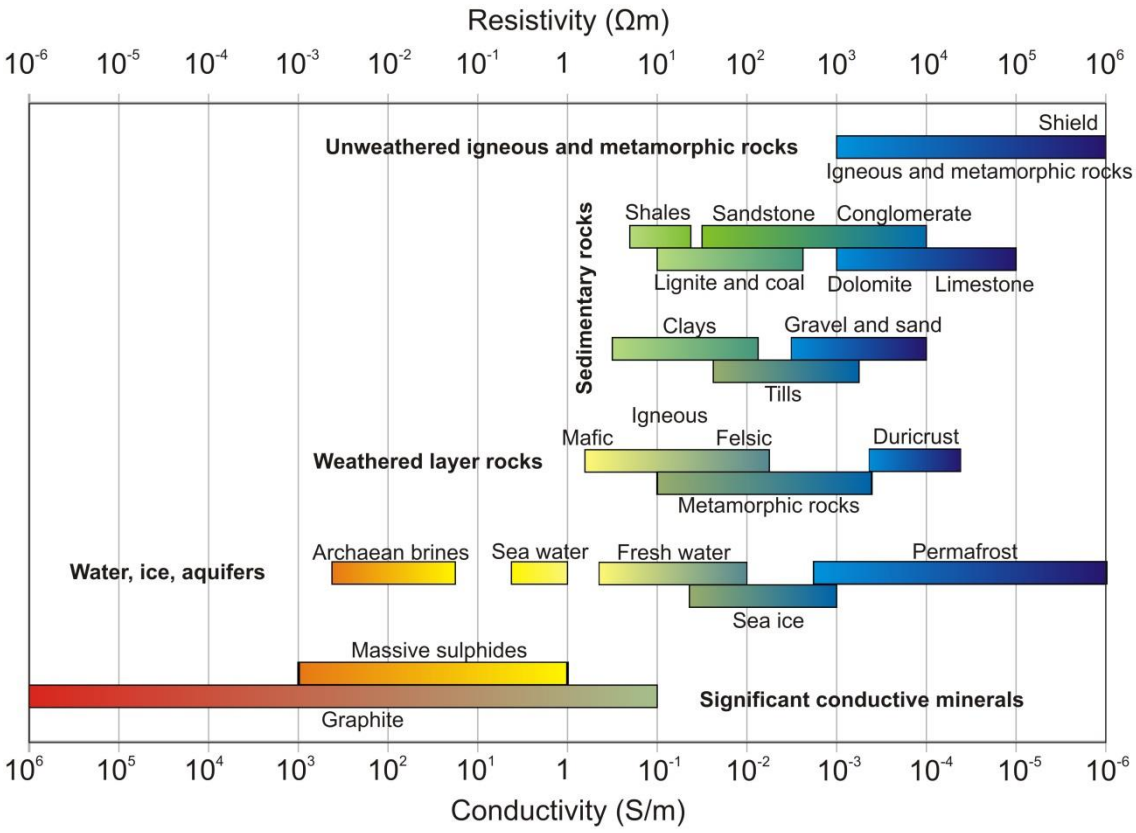

Fig. 1.7. Electrical resistivity and conductivity range of variation of some common Earth materials (modified from Miensopust, 2010).

Electrical resistivity is a physical property sensitive to the nature of the rock constituents (mineralogy composition of the rock) but also to the characteristics of the pore space. The electrical resistivity depends on fluid salinity, temperature, porosity, pore connectivity,

saturation and pressure (Bedrosian, 2007). Archie's law (Archie, 1942), defined initially for sandstones but more generally applicable, describes reasonably well the bulk electrical resistivity of the rock as a function of these parameters:

$$\rho = a \cdot \frac{\rho_w}{\phi^m . S_w^n} \qquad (1.1),$$

where ρ_w is the water resistivity; S_w the water saturation; ϕ the rock porosity; m the cementation factor; n the saturation exponent and a a proportionality constant.

Accordingly, Archie's law is useful to estimate the resistivity changes produced due to the CO_2 injection when the conductivity is dominated by the electrolytic conduction of brine ions (Bourgeois and Girard, 2010; Kiessling et al., 2010; Nakatsuka et al., 2010; Wirianto et al., 2010; Hagrey, 2011; Carrigan et al., 2013). The law is not valid in the presence of clays because they tend to enhance the path for electric currents and results in a lower resistivity (Samouëlian et al., 2005; Nakatsuka et al., 2010). In the specific case of CO_2 storage in saline aquifers, Archie's law is very suitable because the injected CO_2 replaces the saline fluid contain within the porous of the reservoir rock. This fact reduces the volume of saline brine contained in the pore space, obstructing the ionic transport and increasing the resistivity significantly.

Although there are more advanced formulations of the Archie's law (e.g., Glover et al., 2000), to adopt just two fluid phases within the reservoir formation is reasonable: the initial brine and the injected CO_2 ($S_w + S_{co_2} = 100$ %) (Bourgeois and Girard, 2010; Nakatsuka et al., 2010; Hagrey, 2011). Assuming that the CO_2 does not interact with the rock and that porosity remains constant (neither dissolution nor precipitation occurs), pre-injection resistivity (ρ_0) and post-injection resistivity (ρ) of the bulk rock can be related in a simple manner:

$$\frac{\rho}{\rho_0} = \left(1 - S_{CO_2}\right)^{-n} \qquad (1.2).$$

For a saturation exponent n equal to 2 (clean sand), a significant increase of the resistivity is observed when the CO_2 saturation increases (Fig. 1.8). The approach shown in Eq. (1.2) is a first estimation to assess the resistivity variation in the reservoir when the physical trapping

dominates (Fig. 1.6). An increasing amount of literature is reporting on laboratory-scale experiments that investigate the electrical characteristics of the injection process and the impact of the injected CO_2 on the pore water conductivity (Myer, 2001; Nakatsuka et al., 2010; Breen et al., 2012; Liu and Moysey, 2012; Börner et al., 2013; Vialle et al., 2014). Some laboratory-scale studies also explore how to detect fresh water salinization produced by the displacement of formation native saline water due to the injected CO_2 (Wagner et al., 2013).

As well as electrical resistivity, most physical properties of the rock change when the fluid within the pores changes from water to CO_2 (Magee, 1991; Batzle and Wang, 1992; Wang et al., 1998; Myer, 2001; Blanchard, 2011; Rutqvist, 2012; Vialle et al., 2014). Thus, through studying the evolution of these properties through time it is possible to monitor the geological storage process (IPCC, 2005). Geophysical techniques are presented as the most suitable tool to characterise and monitor the reservoir complex and the seal and reservoir integrities. Integration of different techniques make it possible to locate the gas plume and understand the CO_2 migration (Hoversten and Gasperikova, 2005; IPCC, 2005; Giese et al., 2009; NETL, 2009; JafarGandomi and Curtis, 2011; Sato et al., 2011; Bergmann et al., 2014). Traditionally, the petroleum industry has used seismic methods far more often than electromagnetic (EM) methods. This is because of the resolution of conventional EM data is lower than seismic resolution due to the fact that EM energy propagates diffusively (Wright et al., 2002). However, laboratory-scale studies and field experiments show that electrical resistivity is generally far more sensitive to CO_2 saturation than seismic velocity (Lumley, 2010; Nakatsuka et al., 2010; Alemu et al., 2011; Hagrey, 2011; MacGregor, 2012) (Fig. 1.9).

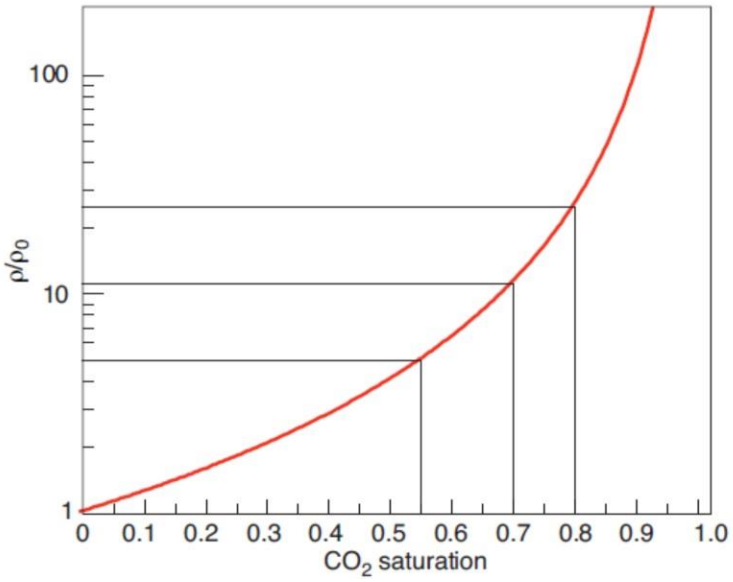

Fig. 1.8. Ratio between the resistivity of a rock flooded with CO_2 and the resistivity of the same rock saturated with water, as a function of the CO_2 saturation. The relation was obtained using Eq. 1.2 for a saturation exponent n equal to 2 (clean sand). Three different saturations, and their corresponding resistivity variation, are indicated: a CO_2 saturation of 55 % corresponds to a resistivity variation of 5; a CO_2 saturation of 70 % corresponds to a resistivity variation of 11 and a CO_2 saturation of 80 % corresponds to a resistivity variation of 25. Thereby, the CO_2 saturation can be estimated from the ratio between the monitored resistivity and the pre-injection resistivity (from Bourgeois and Girard, 2010).

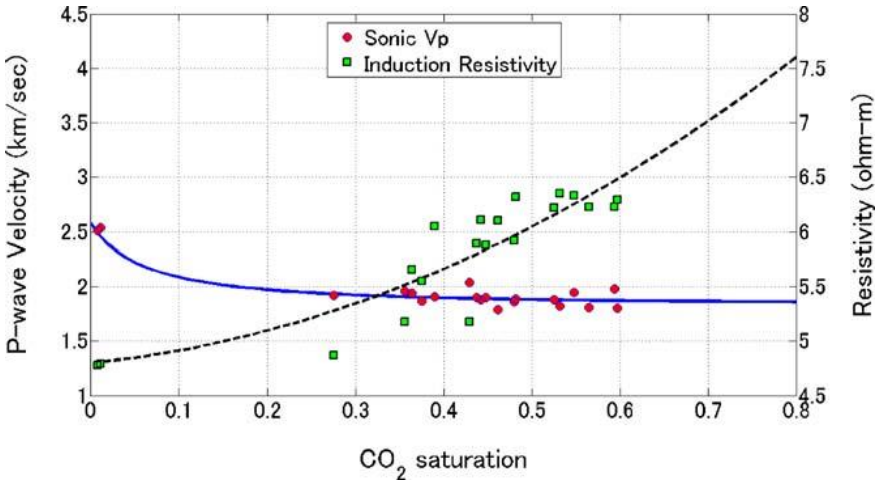

Fig. 1.9. Seismic compressional velocity (v_p) and resistivity as a function of CO_2 saturation at Nagaoka pilot site (Japan) for CO_2 injection in a saline aquifer. It is observed that v_p experiences a small variation for CO_2 saturations above 20 % whereas the resistivity increases over the whole range (from Nakatsuka et al., 2010).

1.4. Monitoring with electromagnetic methods

Monitoring of CO_2 storage sites permits control of gas injection and storage operations, detection of possible leakage, and support of the required safety conditions (IPCC, 2005; NETL, 2009). Different geophysical techniques are presented as suitable for monitoring purposes, and a number of multidisciplinary monitoring schemes have been designed to study and control the evolution of the injected CO_2 plume (Hoversten and Gasperikova, 2005; IPCC, 2005; Giese et al., 2009; NETL, 2009; JafarGandomi and Curtis, 2011; Sato et al., 2011). Hydrocarbon exploration activity has provided significant experience in this field (Hoversten et al., 2003; Harris and MacGregor, 2006; Harris et al., 2009). Electromagnetic methods are presented as valuable since they constrain the electrical conductivity of the storage complex and are sensitive to the contrast of physical properties (saline aquifer reservoir/conductor and injected CO_2/resistive). Moreover, they offer a high degree of complementarity between their different techniques for studying the different scales and depths of interest in a storage site (Kiessling et al., 2010; Streich et al., 2010; Girard et al., 2011; Bergmann et al., 2012; Vilamajó et al., 2013) (Fig. 1.10).

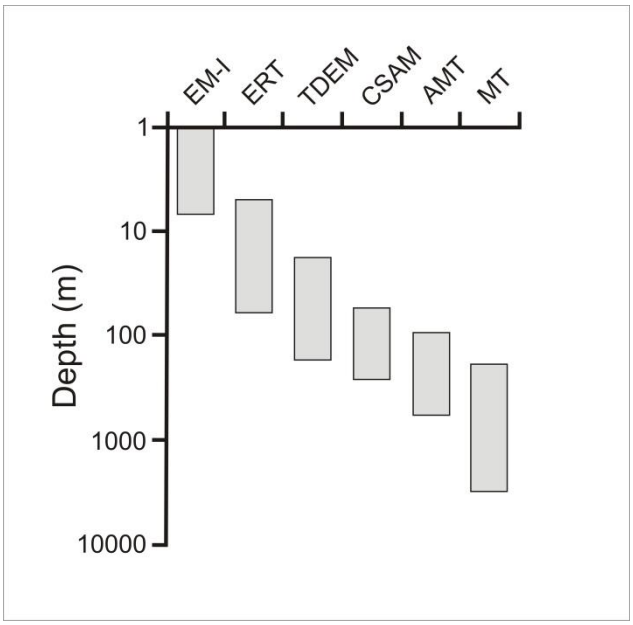

Fig. 1.10. Different electromagnetic techniques and their penetration depth: electromagnetic induction (EM-I); electrical resistivity tomography (ERT); time domain electromagnetics (TDEM); controlled-source audiomagnetotellurics (CSAMT); audiomagnetotellurics (AMT) and magnetotellurics (MT).

In the last few years, many EM studies for monitoring CO_2 storage sites are being carried out using: electrical resistivity tomography (ERT) or its extensions, cross-hole and surface-downhole ERT; controlled-source electromagnetics (CSEM), magnetotellurics (MT) and controlled-source magnetotellurics (CSMT).

The applicability of cross-hole ERT and surface-downhole ERT has been evaluated through synthetic studies (e.g. Ramirez et al., 2003; Christensen et al., 2006; Carrigan et al., 2009; Hagrey, 2011) and the method has provided interesting results in the field (Bergmann et al., 2010; Kiessling et al., 2010; Bergmann et al., 2012; Carrigan et al., 2013; Hagrey et al., 2013).

CSEM is presented as an important technique for monitoring purposes because the presence of a controlled-source makes it possible to control and minimise the effects of the man-made EM noise. Interesting reviews on the method are Constable (1990), Boerner (1992), Edwards (2005), Constable and Srnka (2007), Constable (2010), Key (2012) and Ziolkowski and Wright (2012). During the last decades, the method has been used in the marine context to monitor hydrocarbon extraction and injection (Lien and Mannseth, 2008; Black and Zhdanov, 2009; Orange et al., 2009; Andréis and MacGregor, 2011; Berre et al., 2011; JafarGandomi and Curtis, 2011; Kang et al., 2012; Bhuyian et al., 2012), but more recently, the method has been introduced to terrestrial contexts (Bourgeois and Girard, 2010; Wirianto et al., 2010; Schamper et al., 2011; Zhdanov et al., 2013). Some of the CSEM experiments undertaken at the Ketzin site (Germany) are reported in Becken et al. (2010), Kiessling et al. (2010) and Girard et al. (2011).

In reference to CSMT, some synthetic works exploring and evaluating the possibilities of the method for monitoring have also been presented (Streich et al., 2010). The MT method is typically used to characterise structures at regional and crustal scale (further explanation of the method in section 1.5); however, in the recent years, some attempts have been done to use the method as a monitoring technique (Aizawa et al., 2010; Aizawa et al., 2011; Peacock et al., 2012a). A more extended explanation about MT monitoring is presented in Chapter 4.

For most techniques, monitoring is based on repeated time-lapse studies: the changes produced by the injection of CO_2 are identified and quantified carrying out a comparative analysis with the reference pre-injection state. For that reason, a thorough characterisation must be taken first (before the injection) to define a high-resolution baseline model of the storage site subsurface. Site characterisation aims to establish the geological conditions and the range of geological parameters that are relevant for the project (depth, geometry, internal architecture, lithology, porosity, permeability, degree of fracturing and overall integrity among others). Site characterisation using EM methods will provide a full description (image) of the subsurface in terms of electrical resistivity. Likewise, the characterisation of the site will help to design the proper monitoring setup and the appropriate injection strategy.

1.5. Magnetotelluric method

The MT method is well-established as an EM characterisation technique. The method has been used in both regional (e.g., Rosell et al., 2011) and local (e.g., Ogaya et al., 2013) characterisation work since it is the only EM technique with a penetration depth ranging from tens of metres to hundreds of kilometres (Fig. 1.10). Moreover, its tensorial character (explained below) enables determination of the dominant directionality of geological structures and thereby aid inferring subsurface processes, and their variation with depth.

The MT method infers the electrical conductivity structure of the subsurface using the naturally occurring time variation of the EM field. The method is based on the simultaneous measurement of the natural EM field fluctuations at the Earth's surface. The origins of the MT for geophysical exploration are attributed to Tikhonov (1950), Rikitake (1951) and Cagniard (1953) who established the theoretical bases. Some fundamentals aspects of the method are going to be introduced in this work; for an extended explanation, see e.g., Simpson and Bahr (2005), Berdichevsky and Dmitriev (2008), and Chave and Jones (2012) or the review papers presented at the EM Induction workshops (available on MTNet[8]).

[8] www.mtnet.info (visited April 2014).

The propagation of the EM field is governed by Maxwell's equation. In MT, the incident EM field is treated as a plane wave propagating downwards. The EM waves propagate diffusively through the conducting Earth, and their penetration depends on its oscillation frequency ω and the electrical conductivity of the penetrated medium σ (inverse of the electrical resistivity, ρ). The skin depth δ is a reasonable estimate of the inductive scale length:

$$\delta = \sqrt{2/\mu\sigma\omega} \qquad (1.3),$$

where μ is the magnetic permeability, typically assumed equal to its free space value μ_0. Using SI units, Eq. (1.3) may be simplified to

$$\delta = 503\sqrt{\rho T} \qquad (1.4)$$

where δ has units of metres, T is the period in seconds and ρ is the electrical resistivity in Ωm. The skin depth is the distance over which EM fields are attenuated to 1/e of their amplitudes at the Earth's surface in a uniform medium. Thereby, the longer the period, the deeper is the penetration depth.

The orthogonal electric and magnetic field variations recorded at the Earth's surface are related to each other through the impedance tensor $Z_{ij}(\omega)$, a complex second-rank tensor function of frequency. The impedance tensor contains the amplitude and phase relations between the measured horizontal components of the electric ($\vec{E}$) and magnetic ($\vec{H} = \vec{B}/\mu_0$) fields,

$$\begin{bmatrix} E_x \\ E_y \end{bmatrix} = \begin{bmatrix} Z_{xx}(\omega) & Z_{xy}(\omega) \\ Z_{yx}(\omega) & Z_{yy}(\omega) \end{bmatrix} \begin{bmatrix} H_x \\ H_y \end{bmatrix} \quad (1.5).$$

From each element of the impedance tensor are derived the MT response functions: apparent resistivity ($\rho_{a_{ij}}$),

$$\rho_{a_{ij}}(\omega) = \frac{1}{\mu\omega}\left|Z_{ij}(\omega)\right|^2 \qquad (1.6),$$

and phase (φ_{ij}),

$$\varphi_{ij}(\omega) = \tan^{-1}\left[\frac{Im\, Z_{ij}(\omega)}{Re\, Z_{ij}(\omega)}\right] \quad (1.7).$$

Different methods are used for the impedance tensor estimation (Egbert and Booker, 1986; Jones et al., 1989; Vozoff, 1991; Simpson and Bahr, 2005; Chave, 2012). The remote reference (RR) technique is normally applied to improve the quality of the acquired data in areas with a non-contemptible level of EM noise. The RR method was introduced into magnetotellurics by Gamble et al. (1979) and consists in the simultaneous recording of local and remote magnetic fields. The method aims to eliminate uncorrelated noise in the recorded fields assuming that the uncontaminated (natural) part of the induced field is expected to be coherent over large distances whereas noise is generally random and incoherent.

The form of the impedance tensor is related to the dimensionality of geoelectrical structures. For that reason, a thorough dimensionality analysis of the MT data is necessary to determine which approach is more adequate: one-dimensional (1D), two-dimensional (2D) or three-dimensional (3D). In a 1D Earth, the electrical conductivity only varies with depth and the form of the impedance tensor is

$$\boldsymbol{Z}_{1D} = \begin{pmatrix} 0 & Z \\ -Z & 0 \end{pmatrix} \quad (1.8).$$

In a 2D Earth, electrical conductivity varies along one lateral direction and with depth. Thereby, a strike direction is defined along which electrical conductivity remains constant. In the 2D case, electric and magnetic fields are mutually orthogonal and the equivalent impedance tensor can be decoupled into two independent modes,

$$\boldsymbol{Z}_{2D} = \begin{pmatrix} Z_{xx} & Z_{xy} \\ Z_{yx} & Z_{yy} \end{pmatrix} \xrightarrow{\boldsymbol{R}_{\theta_{strike}}} \begin{pmatrix} 0 & Z_{TE} \\ Z_{TM} & 0 \end{pmatrix} (1.9),$$

as Maxwell's Equations decouple into two independent modes in the 2D case. One of these modes is referred to as the transverse electric, TE mode, and describes the response of the electric currents flowing along the strike of the 2D structure (Eq. 1.9). The other mode is known as the transverse magnetic, TM mode, and describes the responses for the currents flowing perpendicular to the strike of the structure. In this way, the TM and TE modes satisfy the principle of complementary information and reliable and comprehensive information on the Earth's conductivity can be obtained by means of joint TM and TE mode modelling, inversion and interpretation.

Finally, in a 3D Earth, the electrical conductivity varies along the two lateral directions and with depth and the form of the impedance tensor is

$$\boldsymbol{Z}_{3D} = \begin{pmatrix} Z_{xx} & Z_{xy} \\ Z_{yx} & Z_{yy} \end{pmatrix} \quad (1.10).$$

In practise, the EM response of the studied structures can be masked by distortions produced by local or regional effects that are out of the scope of the study. Distortion effects constitute a major issue in magnetotellurics as they can lead to erroneous data interpretations. Consequently, the effects of distortions have been extensively studied (Berdichevsky et al., 1973; Berdichevsky and Dimitriev, 1976a; Jones, 1983b; Bahr, 1988; Jiracek, 1990; Chave and Jones, 1997; Jones, 2012). Berdichevsky et al. (1973) divided distortion effects into galvanic effects and inductive effects. The first ones are due to distributions of charges that generate electric fields, and the second ones are because of distributions of currents that generate magnetic fields. In regional MT surveys, galvanic distortion is the most problematic (Berdichevsky and Dmitriev, 1976b). This type of distortion may be produced by small-scale geological inhomogeneities near the surface. In a 1D or 2D Earth with axis oriented along and across the strike direction, galvanic distortion results in a vertical displacement of the apparent resistivity curves (static shift). Nevertheless, in a 3D Earth, or 2D Earth with axis not oriented along and across the strike direction, the distortion depends on the frequency which is more difficult to correct as is discussed in Jones (2011).

Dimensionality analysis yields information about the geoelectric strike direction and makes it possible to correct the MT data by detecting, identifying and removing most of the possible galvanic distortion effects. A description and comparison of the different existing methodologies is given in Jones (2012). In this work, three different approaches were applied on the MT data: (i) Groom-Bailey (GB) distortion decomposition method for a regionally 2D geoelectrical subsurface (Groom and Bailey, 1989); (ii) analysis of the set of rotational invariants of the impedance tensor presented by Weaver et al. (2000), and (iii) the study of the phase tensor which relates the real and imaginary parts of the impedance tensor (Caldwell et al., 2004). A brief description of each of them is given below.

(i) The impedance tensor of a 2D Earth affected by galvanic distortion ($\boldsymbol{Z}_{obs}$) can be described by the equation

$$\boldsymbol{Z}_{obs} = \boldsymbol{R}(\theta)\boldsymbol{C}\boldsymbol{Z}_{2D}\boldsymbol{R}^{T}(\theta) \quad (1.11),$$

where $\boldsymbol{R}(\theta)$ is the rotation matrix, $\boldsymbol{C}$ is the distortion matrix (real frequency independent matrix) and $\boldsymbol{Z}_{2D}$ is the 2D impedance tensor, not affected by galvanic distortion, in the regional 2D strike coordinates. The GB distortion decomposition method consists of decomposing the $\boldsymbol{C}$ matrix by

$$\boldsymbol{C} = g\boldsymbol{T}\boldsymbol{S}\boldsymbol{A} \quad (1.12),$$

where g is the gain parameter (which accounts for the static shift), $\boldsymbol{T}$ is the twist tensor, $\boldsymbol{S}$ is the shear tensor and $\boldsymbol{A}$ is the anisotropy tensor (Groom and Bailey, 1989). Neither g nor $\boldsymbol{A}$ can be resolved separately (although $\boldsymbol{A}$ can be inferred from the short periods asymptotes of the TE and TM mode apparent resistivity curves after correction for twist and shear); consequently, GB decomposition cannot remove the static shift. The accuracy of the GB distortion model is given by the misfit between the observed data and the modelled data. The method is implemented in the multi-site, multi-frequency STRIKE code of McNeice and Jones (2001).

(ii) Weaver et al. (2000) presented a dimensionality study based on a set of eight rotational invariants of the impedance tensor: seven independent ($I_1, I_2, I_3, I_4, I_5, I_6, I_7$) and one dependent ($Q$). Each of them has a physical interpretation related to the geoelectrical dimensionality. In particular, there is a criterion to determine the dimensionality and identify galvanic distortion according to the vanishing of invariants I_3- I_7 and Q (Weaver et al., 2000; Martí et al., 2009). However, the invariant values for real data are in general never zero due to the presence of noise. Consequently, a threshold value is introduced for each of them, below which the invariants are taken to be zero. This methodology is implemented in the WALDIM code of Martí et al. (2009).

(iii) Finally, the phase tensor is a real magnitude defined by

$$\boldsymbol{\Phi} = \boldsymbol{X}^{-1}\boldsymbol{Y} \quad (1.13),$$

where $\boldsymbol{X}$ is the real part and $\boldsymbol{Y}$, the imaginary part of the impedance tensor (Caldwell et al., 2004). The phase tensor is independent of galvanic distortion and can be characterised by three invariants: Φ_{max}, Φ_{min} and β (skew angle). It is commonly represent by an ellipse where Φ_{max} and Φ_{min} are the principal axis (semi-major and semi-minor axes, respectively). The orientation of the major axes depends on the skew angle and on the dimensionality. The azimuth of the semi-major axes (dependent on the coordinate system) corresponds to the strike direction and the difference between the length of the semi-major and semi-minor axis gives an estimate of the dimensionality complexity of the geoelectrical structure.

The MT inverse problem (Rodi and Mackie, 2012) has been addressed in 1D (detailed review in Whittall and Oldenburg, 1992), 2D (e.g. de Groot-Hedlin and Constable, 1990; Siripunvaraporn and Egbert, 2000; Rodi and Mackie, 2001 -code used for the 2D modelling of Hontomín) and 3D. In 3D, different MT inversion algorithms have been developed in the last years. However, 3D inversion requires further development and understanding of the advantages and limitations. Recently, Miensopust et al. (2013) presented a test and comparison of the current available 3D codes. In this Hontomín work, three different 3D inversion codes were used: the code described by Mackie and Madden (1993) subsequently developed and implemented by Geosystem (called Geosystem code hereafter); WSINV3DMT (Siripunvaraporn et al., 2005) and ModEM (Egbert and Kelbert, 2012). The first one is a commercial code and uses a truncated non-linear conjugate gradient approach. The second, WSINV3DMT, is based on a data-space variant of the Occam's approach. Finally, ModEM, is a modular system of computer codes for different EM problems and the inversion algorithm is also based on a non-linear conjugate gradient scheme. For a comprehensive explanation about 3D inversion and modelling, see the following reviews: Avdeev (2005), Börner (2010) and Siripunvaraporn (2012).

In the past years, thanks to the progress made in 3D MT inversion algorithms (Avdeev, 2005; Siripunvaraporn, 2012), a number of MT studies have been undertaken in 3D in order to overcome the limitations of 2D interpretation (Ledo et al., 2002; Ledo, 2006; Becken et al., 2008). Some of the MT investigations were focussed on near surface structures demonstrating the suitability of the method in a variety of contexts: mineral

exploration (Tuncer et al., 2006; Farquharson and Craven, 2009; Xiao et al., 2010); waste site characterisation (Newman et al., 2003); volcano and geothermal studies (Heise et al., 2008; Newman et al., 2008; Ingham et al., 2009; Ghaedrahmati et al., 2013; Piña-Varas et al., 2014) and hydrocarbon exploration (He et al., 2010; Zhdanov et al., 2011).

1.6. Case study: the Hontomín CO_2 storage site

In Spain, the Centro de Investigaciones Energéticas, Medioambientales y Tecnológicas (CIEMAT) and the Instituto Geológico y Minero de España (IGME) in 2004 launched a study to select the most suitable geological formations for geological storage of CO_2 in the country (Ruiz et al., 2007; Prado et al. 2008; Pérez-Estaún et al., 2009; García Lobón et al., 2011) (Fig. 1.11). Saline aquifers were concluded to be the most suitable storage scenario in Spain (Pérez-Estaún et al., 2009). Accordingly, CIUDEN, on behalf of the Spanish Government, established a TDP for CO_2 storage in a deep saline aquifer in Hontomín (Spain) (Fig. 1.11), in the framework of the EEPR-funded OXYCFB300 Compostilla project.

The Hontomín site is an underground research laboratory (URL) that aims to generate the knowledge and experience needed for geological storage of CO_2. One of the main objectives of the Hontomín project is to promote the development of new technologies, techniques and methodologies to better understand the behaviour of the injected CO_2 in the subsurface, identifying the most suitable and efficient ones for monitoring at industrial scale. With this aim, large number of multidisciplinary experiments are being undertaken to characterise the subsurface and monitor the evolution of the expected CO_2 plume (e.g., Rubio et al., 2011; Benjumea et al., 2012; Buil et al., 2012; Ogaya et al., 2012; Alcalde et al., 2013a; Alcalde et al., 2013b; Canal et al., 2013; Elío, 2013; Elío et al., 2013; García-Ríos et al., 2013; Metcalf et al., 2013; Nisi et al., 2013; Ogaya et al., 2013; Quintà, 2013; Ugalde et al., 2013; Vilamajó et al., 2013; Alcalde et al., 2014; Ogaya et al., 2014). This thesis presents a component of this on-going project: the magnetotelluric characterisation and monitoring of the Hontomín CO_2 storage site, Spain.

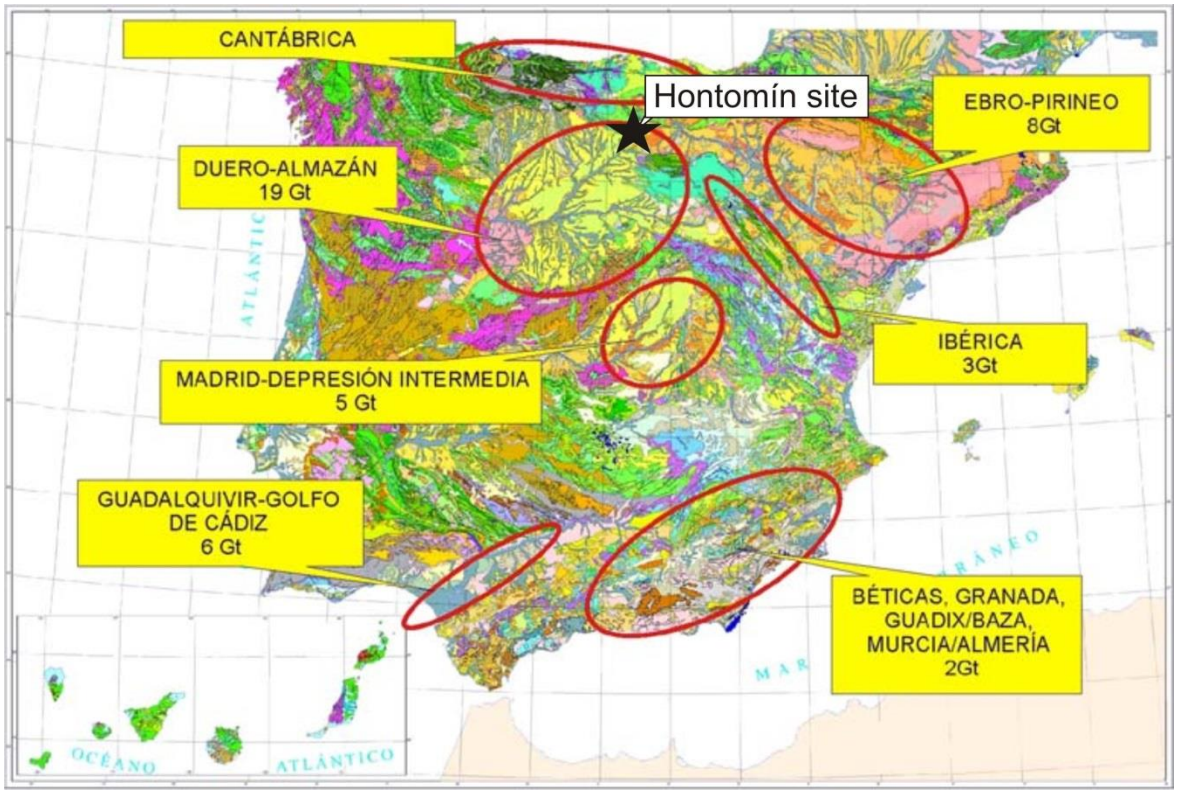

Fig. 1.11. Geological map of the Iberian Peninsula indicating the location of the main Mesozoic and Cenozoic sedimentary basins. The theoretical storage capacity of the basins is also indicated. Black star marks the location of the Hontomín site for CO_2 geological storage in a deep saline aquifer (modified from Pérez-Estaún et al., 2009).

1.7. Aims and objectives

The aim of this thesis is to describe efforts to characterise and monitor the subsurface of Hontomín URL for CO_2 geological storage in a deep saline aquifer using the magnetotelluric method. Thus, this work will explore to what extent the magnetotelluric method can contribute to the geoelectrical characterisation and monitoring of onshore CO_2 geological storage sites.

This thesis constitutes the first 3D MT characterisation survey of a CO_2 geological storage site. To obtain a high-resolution 3D resistivity model of the pre-injection state was the major challenge of the research undertaken. Despite the recent advances in 3D MT inversion codes, a better understanding of the 3D inverse problem is still required. Man-

made EM noise, depth of study (between 800 and 2000 m) and resolution of the data are other challenges of this work.

The aim of the thesis is pursued through the following objectives:

A) Related to the geoelectrical characterisation of the Hontomín site,

1. Investigate the viability of the MT method in the study area, minimising the effect of the existing man-made EM noise on the data.
2. Obtain the 3D resistivity model of the Hontomín URL in order to:
   2.1. Characterise the study area.
   2.2. Define the geoelectrical monitoring requirements of the site.
   2.3. Provide the 3D geoelectrical baseline model of the site, to be used in the future time-lapse EM monitoring experiments.

B) In reference to the geoelectrical monitoring of the Hontomín site,

3. Investigate the monitoring possibilities of the MT method at the Hontomín URL by carrying out different synthetic studies and sensitivity tests.
4. Develop new methodologies to enhance the resolution of surface MT responses.

2 Geological and geophysical setting

Exploration activities have provided geological and geophysical information of the study area since the nineteen-sixties. This chapter presents both the geological and geophysical setting of the Hontomín site, reporting the main characteristics of the primary reservoir. A first idea of the geoelectrical structure of the site is derived from the available resistivity log data.

2.1. Introduction

The Hontomín site is located in the south-western sector of the Basque-Cantabrian Basin (Western Pyrenees, north Spain) and belongs to the North-Castilian Platform (Serrano and Martínez del Olmo, 1990; Tavani, 2012) (Fig. 2.1a). The boundaries of the Hontomín structure are the Ubierna Fault and the Duero Foreland Basin to the south and west, the Poza de la Sal diapir to the north-east and the Rojas-Buezo Anticlines and Ebro Foreland Basin to the east (Tavani et al. 2011; Quintà et al., 2012) (Fig. 2.1b).

The south-western sector of the Basque-Cantabrian Basin has attracted the attention of oil companies since 1920 (Quesada et al., 1993; Alvarez, 1994; Merten, 2006; Beroiz and Permanyer, 2011; Permanyer et al., 2013). In Ayoluengo (Fig. 2.1a), there is an onshore productive oilfield discovered in 1964 (Álvarez de Buergo and García, 1996; Merten, 2006) and in Hontomín, there has also existed hydrocarbon exploration activity since the nineteen-sixties. This prior exploration activity provided vintage 2D seismic profiles and well-log data of the study area that helped to construct a first impression of the Hontomín structure. These geological and geophysical data have been complemented with recent studies including 3D reflection seismics (Alcalde et al., 2013a; Alcalde et al., 2013b; Alcalde et al., 2014), gravimetry (Rubio et al., 2011), microgravimetry (Implemental

Systems, 2011) and magnetotellurics (Ogaya et al., 2012; Ogaya et al., 2013; Ogaya et al., 2014).

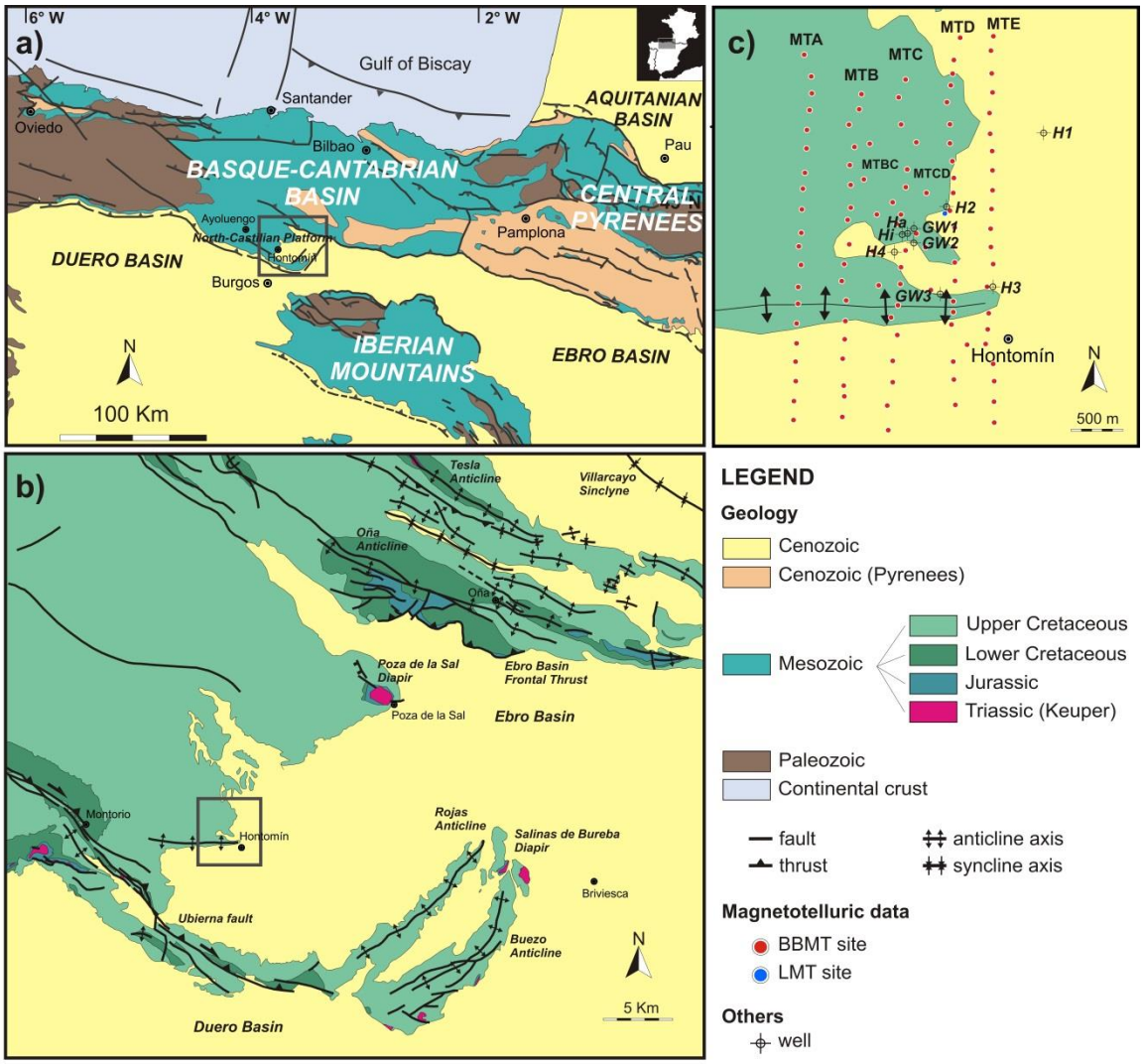

Fig. 2.1. Geological maps of the study area: (a) Geological map of the Basque-Cantabrian Basin indicating the North-Castilian Platform and the location of the study area (modified from Muñoz, 2002); (b) Geological map of the Hontomín surrounding area indicating the location of the Hontomín structure; (c) Red and blue dots show the locations of the broadband MT (BBMT) and long period MT (LMT) sites, respectively. Also indicated are the acronym of the various profiles (MTA-MTE) (Chapter 3) and the locations of the wells H1-H4, GW1-GW3 and Hi-Ha (section 2.3) (from Ogaya et al., 2014).

2.2. Geological setting

2.2.1. Regional geological setting

The regional evolution of the study area during Mesozoic and Cenozoic times was defined by three major regional events (Fig. 2.2) (Beroiz and Permanyer, 2011): a Permian-Triassic extensional stage, a Late Jurassic-Early Cretaceous extensional stage and a Cenozoic contractional stage.

Firstly, the Permian-Triassic extensional stage took place as a consequence of an early continental rifting, previous to the spreading of the sea-floor in the Central Atlantic. This stage resulted in the development of WNW-ESE and E-W faults (Ziegler, 1988; García-Mondéjar, 1996).

Secondly, a Late Jurassic-Early Cretaceous major extensional stage occurred related with the opening of North and Central Atlantic and Gulf of Biscay (Le Pichon and Sibuet, 1971; Montadert et al., 1979; Ziegler, 1988; Ziegler, 1989; Vera, 2004; Roca et al., 2011). The Basque-Cantabrian Basin developed during this extensional stage. The basin covers an extensive offshore and onshore area of the northern part of Iberia (Fig. 2.1a). The extensional event reactivated Permian-Triassic WNW-ESE faults and generated NNE-SSW transverse extensional faults (Tavani and Muñoz, 2012; Tavani et al., 2013). The event originated a synformal domain filled with a thick sequence of sediments (Pujalte et al., 2004; Robles et al., 2004; Quesada et al., 2005; Quintà and Tavani, 2012). The Upper Triassic (Keuper) evaporitic sediments acted as a regional ductile level decoupling the deformation of the cover sequence from the basement (Tavani et al., 2011; Carola et al., 2013; Tavani et al., 2013). The forced folding of the cover above a basement fault triggered the migration of the salt (Tavani et al., 2013).

Finally, during the Cenozoic a contractional stage, related with the collision between Eurasian and Iberian tectonic plates, resulted in the subduction of the latter and led to the development of the doubly-vergent Pyrenean orogen (Boillot and Capdevila, 1977; Boillot and Malod, 1988; Roest and Srivastava, 1991; Muñoz, 1992). During this period, previous Mesozoic basins were inverted and incorporated into the Pyrenean orogen (Tavani et al.,

2011; Quintà and Tavani, 2012; Tavani et al., 2013). This stage reactivated the development of evaporitic structures as the one of Hontomín.

2.2.2. Structure and stratigraphy of the site

Geological and geophysical data indicate that the Hontomín site is a smooth Jurassic domed anticline structure with an overall lateral extent of 3x5 km^2 (Quintà, 2013; Tavani et al., 2013).

In reference to the stratigraphy of the study area (Fig. 2.2), Upper Triassic evaporitic sediments (Keuper facies) overlie Palaeozoic to Lower Triassic metamorphic and siliciclastic basement rocks and constitute the core of the Jurassic dome. The Upper Triassic sediments act as a decoupling layer that separates the deformation of the sedimentary cover from the deformation of the basement. Overlying the Keuper facies and an Anhydrite unit (Fig. 2.2), the Jurassic succession is grouped in two main depositional systems: a shallow marine carbonate ramp (Puerto Palombera Fm., Sopeña Fm. and Río Polla Fm.) (Quintà, 2013) (Fig. 2.2) and a hemipelagic ramp (Puerto Pozazal Fm., Camino Fm., Castillo Pedroso Fm. and the carbonatic Dogger) (Quintà, 2013) (Fig. 2.2). The shallow marine carbonate ramp system is constituted of evaporites, dolostones, limestones and siliciclastic sediments. The hemipelagic ramp system is formed by alternations of marls and marly limestones, limestones and shales. The Jurassic succession is divided in four units that, from bottom to top, are: carbonatic Lias, marly Lias, Pelletic Lias and carbonatic Dogger (Pujalte et al., 1988; Robles et al., 1989; Quesada et al., 1991; Quesada et al., 1993; Pujalte et al., 2004; Robles et al., 2004; Quesada et al., 2005; Rosales et al., 2006; Quintà, 2013) (Fig. 2.2). Purbeck facies lay over the Jurassic marine sediments; they have a marine-continental transitional origin and are composed of clays, sandstones and carbonatic rocks, depending on the structural position inside the basin (Fig. 2.2). The continental succession of the Lower Cretaceous sediments is completed (from bottom to top) by Weald facies, Escucha Fm. and Utrillas Fm. (Pujalte et al., 2004; Quintà, 2013) (Fig. 2.2). They are formed by siliciclastic sediments that contained fluvial facies alternating sandstones from channel filling and clays from flood plains. The stratigraphic sequence in Hontomín is completed by Upper

Cretaceous limestones and marls, and Cenozoic lacustrine and detritic sediments (Quintà, 2013) (Fig. 2.2).

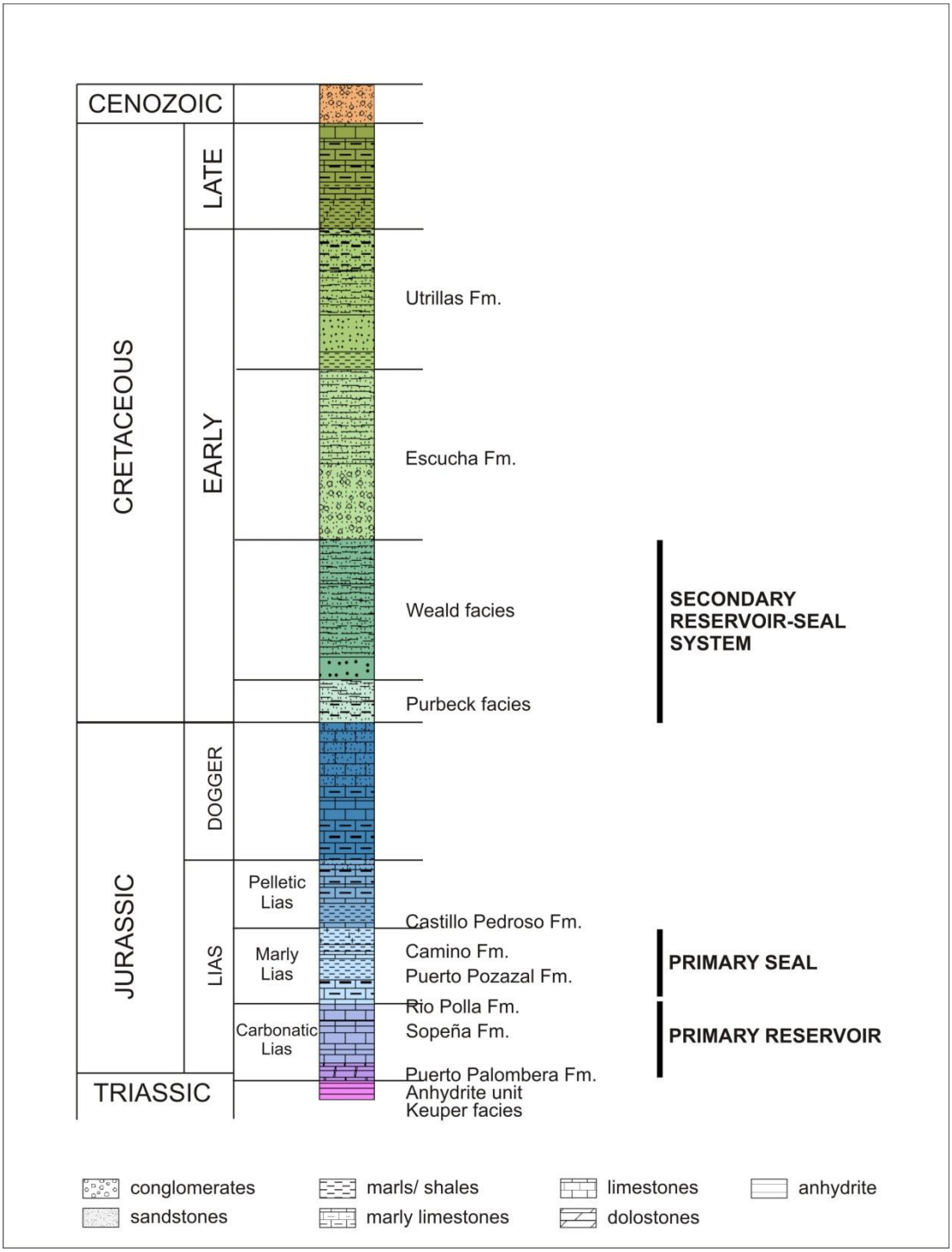

Fig. 2.2. Stratigraphic column of the study area. In general, colours indicated different units and formations (source: ICTJA-CSIC).

2.2.3. Reservoir and seal units

The stratigraphic sequence shows several reservoir and seal units of different ages (Beroiz and Permanyer, 2011; Quintà, 2013). On one hand, exploration activity in Hontomín revealed the existence of a hydrocarbon reservoir in Jurassic limestones sealed by Jurassic marls (Beroiz and Permanyer, 2011; Permanyer et al., 2013). On the other hand, in Ayoluengo oilfield, the hydrocarbon extraction is from Lower Cretaceous sandstones comprising the Purbeck paleochannels. The reservoir is sealed by Purbeck and Weald facies clays (Beroiz and Permanyer, 2011; Permanyer et al., 2013). There also exist more reservoir levels, such as Utrillas Fm. and other Upper Cretaceous limestone levels (Quintà, 2013). However, in Hontomín they are located at shallow depths and are not suitable for CO_2 geological storage purposes.

According to the depths required for CO_2 geological storage (section 1.2), the injection in the Hontomín site is projected to occur in the basal part of the Lower Jurassic carbonates at about 1500 m TVD (True Vertical Depth). The primary reservoir is constituted by a dolostone unit (upper part of Puerto Palombera Fm.) and an oolitic limestone unit (Sopeña Fm.) (Fig. 2.2). The reservoir has a thickness of more than 100 m and hosts a saline aquifer. The primary seal comprises four black-shale levels interbedded in Lower Jurassic marls (Camino Fm.) (Fig. 2.2). Upwards, the intercalations of sandstones, shales and conglomerates from the Purbeck and Weald facies (Upper Jurassic-Lower Cretaceous) (Fig. 2.2) represent a suitable secondary reservoir-seal system. They may act as appropriate stratigraphic trap ensuring against the CO_2 upwards migration.

2.2.4. Primary reservoir - saline aquifer

The primary reservoir rock is mainly constituted of calcite (around 97 %) and dolomite (around 1 %) and the porosity estimate, according to vintage well logs, ranges from 0 % to 18 % (Márquez and Jurado, 2011). A porosity value between 9 % and 17 % was derived from the 2D resistivity model of the study area (Ogaya et al., 2013) and a porosity of 8.5 % was reported in the 3D seismic studies (Alcalde et al., 2014). In reference to the saline aquifer, the salinity of the brine is over 20 g/l and the pH has a median value of 7.3 (Buil et

al., 2012). The average electrical conductivity is 47 mS/cm which equates to a resistivity of 0.22 Ωm (Buil et al., 2012). For characteristics of the oil in Hontomín, see Permanyer et al. (2013).

2.3. Geophysical setting

In the study area, there exist vintage 2D reflection seismics and well-log data since nineteen-sixties because of the previous hydrocarbon exploration activity. New geophysical data have been collected lately in the framework of the URL; five more wells have been drilled and a variety of characterisation surveys have been carried out. These recent studies include, among others, regional gravimetry (Rubio et al., 2011), microgravimetry (Implemental Systems, 2011), 3D reflection seismics (Alcalde et al., 2013a) and magnetotellurics (Ogaya et al., 2012; Ogaya et al., 2013; Ogaya et al., 2014).

Focusing on the EM studies undertaken at the Hontomín site, diverse EM techniques are being assessed for different purposes according to their resolution and penetration depth (Fig. 1.10). The area was characterise by means of the MT method (work presented in this thesis) (Ogaya et al., 2012; Ogaya et al., 2013; Ogaya et al., 2014) and CSEM were used to evaluate monitoring strategies (Vilamajó et al., 2013), as well as to analyse and characterise the EM noise in the region (Escalas et al., 2013).

In the Hontomín site, there are currently nine drilled wells (Fig. 2.3). The H1, H2, H3 and H4 wells (displayed in yellow in Fig. 2.3) were drilled for oil exploration purposes (H1 and H2 in the late nineteen-sixties; H3 in 1991 and H4 in 2007) and their depths range up to 1769 m TVD. GW1, GW2 and GW3 are hydrogeological boreholes (displayed in blue in Fig. 2.3), and were drilled in 2012 to carry out groundwater studies. Their depths range between 150 m and 405 m TVD (Benjumea et al., 2012). Finally, in 2013, two wells were drilled in the framework of the CO_2 storage facility (displayed in red in Fig. 2.3): the injection well (Hi) and the monitoring well (Ha). Their depths are up to 1580 m TVD. The Hi and Ha wells are located on the crest of the Jurassic dome; their positions were established according to the geological interpretation derived from the available well-log data and the seismic studies (Quintà, 2013; Alcalde et al., 2014).

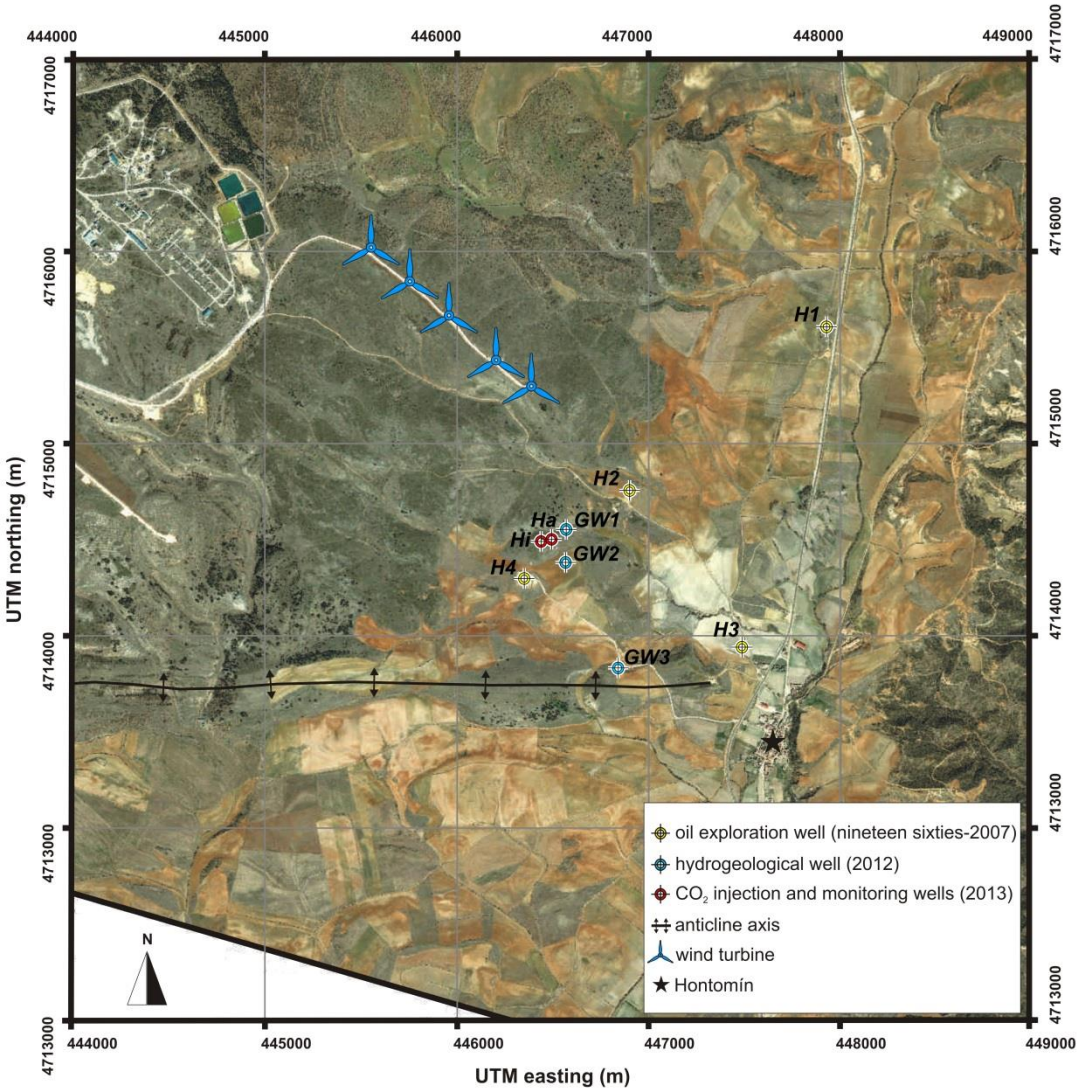

Fig. 2.3. Map of the URL of Hontomín indicating the position of all existing wells: H1-H4, GW1-GW3 and Hi-Ha.

2.3.1. 1D geoelectrical models

One-dimensional resistivity models were derived for each well with the aim of: (i) composing a general idea of the geoelectrical structure of the Hontomín site subsurface (which would help in the design of the fieldwork); (ii) correlating different lithologies to electrical properties, and (iii) describing the electrical behaviour of the primary reservoir, the primary seal and the secondary reservoir-seal system.

The resistivity log data of each well were smoothed into the minimum number of layers required to describe the subsurface and an equivalent 1D resistivity model was sought for each of the existing wells. These 1D models produce the same MT responses at the surface as those ones obtained from forward modelling using the logged resistivities (to within experimental error of the highest possible quality MT data). For the H-wells, the Deep Induction Standard Processed Resistivity (ILD) measure was used, deriving the average medium with the Deep induction Standard Processed Conductivity (CILD) measure when it was possible. Since the H4 well with a depth of 1610 m (TVD) lacked resistivity log data, its 1D resistivity model was inferred using the H2-well data to correlate the different lithologies to electrical properties. That constituted a good approximation, as the two wells are located in the centre of the dome and, consequently, they are expected to show a similar pattern. The distance between the two wells is 707 m. For the GW wells, the long DUIN measure was used. Figures 2.4-2.10 show the resistivity log data and the derived 1D models of all wells: H1, H2, H3, H4, GW1, GW2 and GW3, respectively. The drilling of Hi and Ha wells was finished in the end of 2013, after obtaining the 3D geoelectrical baseline model of the site. Consequently, the resistivity log data of both wells were correlated directly with the final 3D model without deriving equivalent 1D models (section 3.5.1).

In the earliest stage of the project, H2 was the only well with resistivity log data available that crossed the crest of the target dome. For that reason, the H2 well was used to estimate the skin depth of the study area, defining the range of periods that should be recorded in the fieldwork. From the correlation of both its resistivity log data and its lithological information (Fig. 2.11), it was determined that the main reservoir-seal system is mainly imaged in the period range of 0.5 to 0.8 s by a relative minimum in the apparent resistivity curve (Fig. 2.5). The primary reservoir-seal system can be detected at shorter periods in the

phases, as is displayed by a maximum in the range of 0.1 to 0.6 s. The end of the well is reached at approximately 0.9 s which corresponds to 1500 m TVD according to the skin depth equation (Eq. 1.4) and assuming a homogenous Earth of 10 Ωm (resistivity of the most conductive layer of the well). Thus, it was advisable to record periods up to 10 s in the fieldwork.

Figure 2.11 shows the correlation between the 1D resistivity models and the stratigraphic column for all wells. The correlation made it possible to link the stratigraphy of the study area to the electrical properties of the different lithologies and formations. Thus, the primary reservoir, which hosts the saline aquifer, corresponds to the most conductive unit of the models (10 Ωm in H2 well). The primary seal also has a conductive behaviour, whereas the secondary reservoir-seal system is resistive.

The expected increase in reservoir resistivity due to the CO_2 injection was estimated using Archie's law (Eq. 1.1). The approach is valid for the Hontomín case study because the resistivity of the brine and the clay content are both low. Thus, according to Eq. 1.2, for an n value equal to 2 (clean sand) and assuming a homogenous saturation of 50 %, the expected post-injection resistivity is four times the pre-injection reservoir resistivity. Accordingly, the primary reservoir resistivity is estimated to change from 10 Ωm (value in H2 well) to 40 Ωm, for a CO_2 saturation of 50 %.

The volume occupied by the injected CO_2 at the reservoir depth was also evaluated. The volume was estimated according to the variation of CO_2 density with depth, for hydrostatic pressure and a geothermal gradient of 25°C/km from 15° at the surface (Fig. 1.4). The Hontomín site is a non-commercial project and the injection is limited to 100 kilotons by regulation (see section 1.1). However, a maximum of 20 kilotons is planned to be injected which is expected to correspond to an approximate volume of 135x135x25 m^3 at 1500 m TVD.

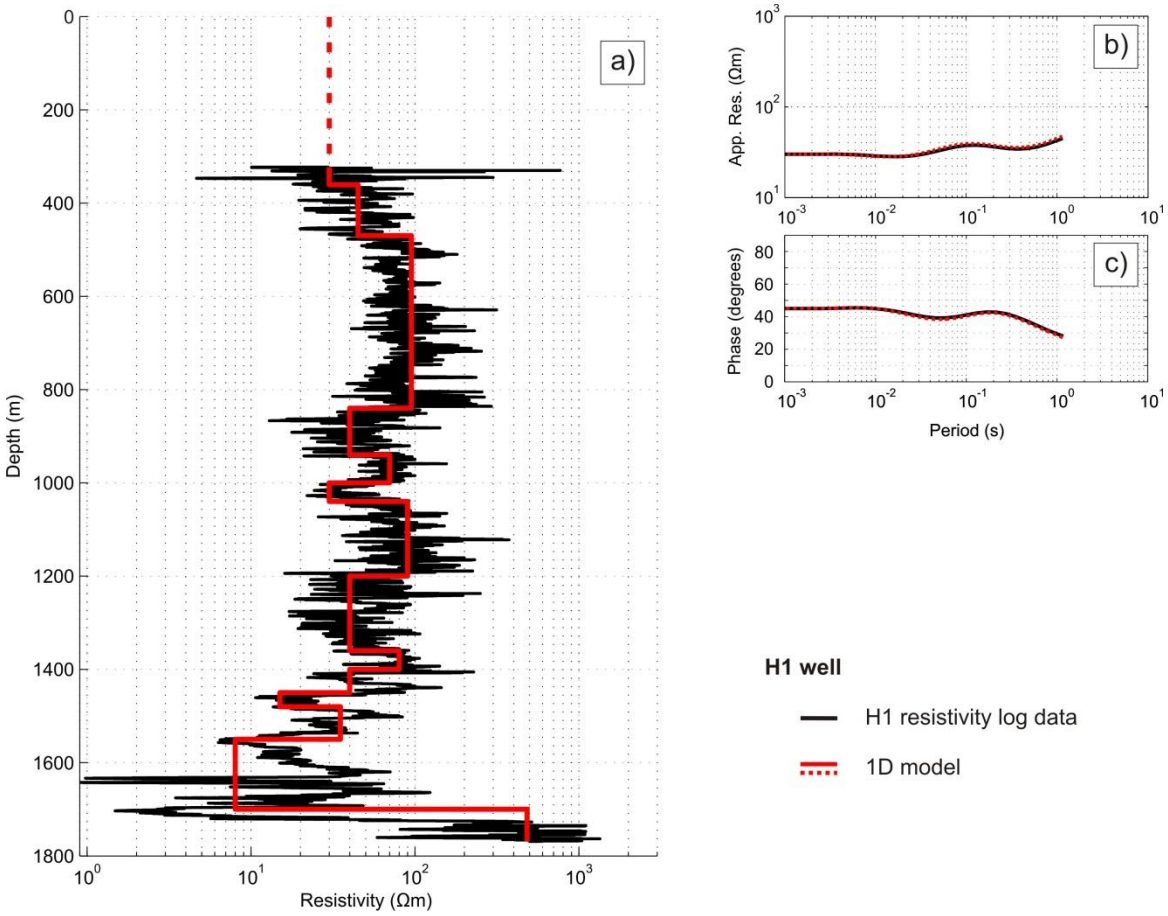

Fig. 2.4. H1 well: resistivity log data and corresponding 1D model. The end of the well is reached at approximately 1.2 s which corresponds to 1769 m TVD according to the skin depth equation (Eq. 1.4) and a homogenous Earth of 10 Ωm (resistivity of the most conductive layer of the H2 well). Depths are given in terms of True Vertical Depth (TVD).

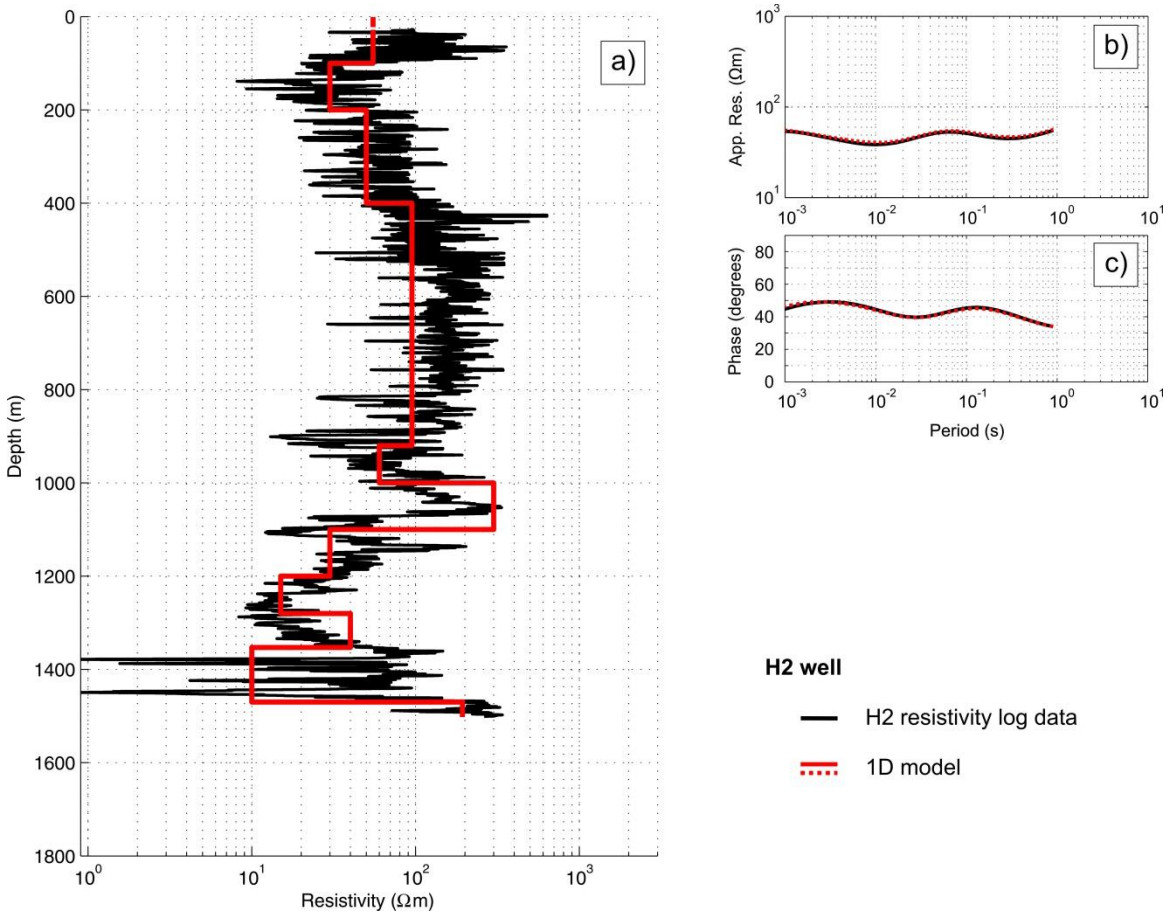

Fig. 2.5. H2 well: resistivity log data and corresponding 1D model. The end of the well is reached at approximately 0.9 s which corresponds to 1500 m TVD according to the skin depth equation (Eq. 1.4) and a homogenous Earth of 10 Ωm (resistivity of the most conductive layer of the H2 well). Depths are given in terms of TVD.

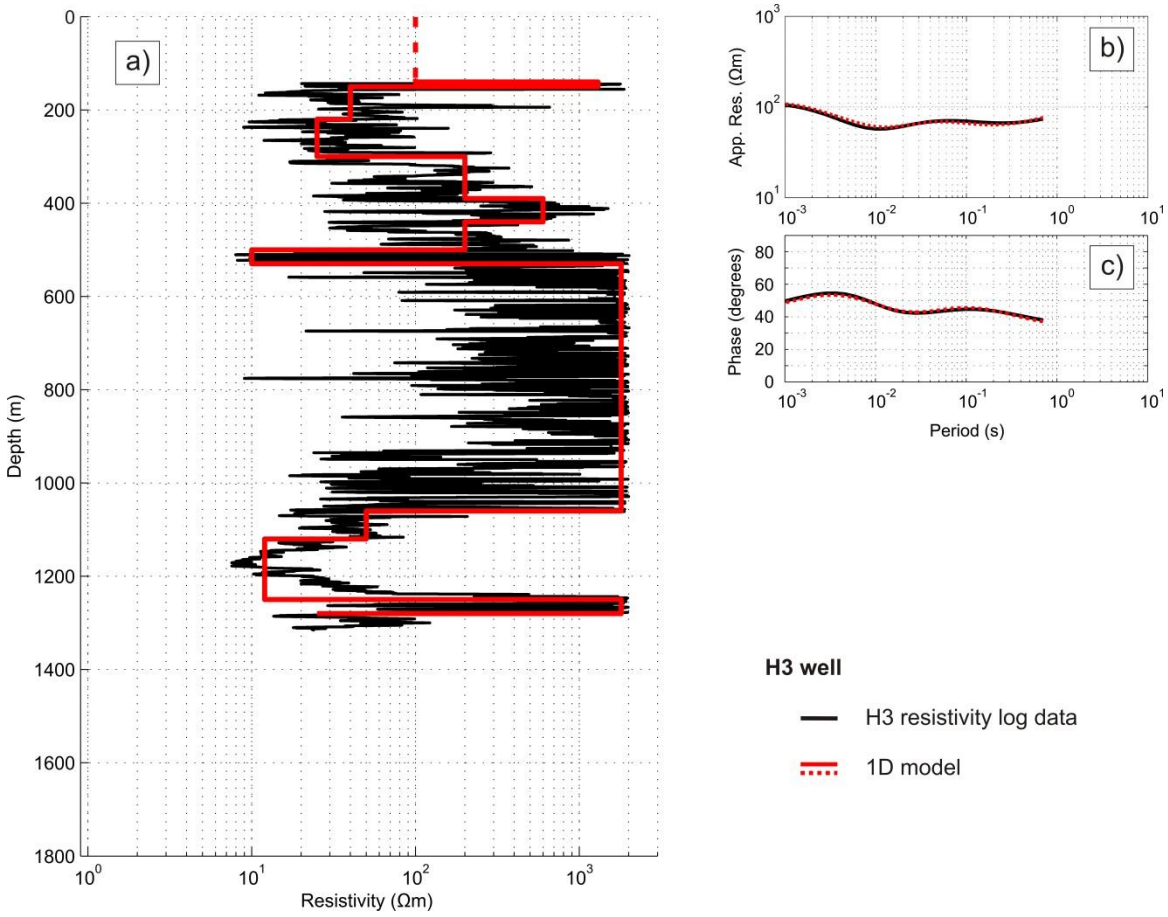

Fig. 2.6. H3 well: resistivity log data and corresponding 1D model. The end of the well is reached at approximately 0.7 s which corresponds to 1315 m TVD according to the skin depth equation (Eq. 1.4) and a homogenous Earth of 10 Ωm (resistivity of the most conductive layer of the H2 well). Depths are given in terms of TVD.

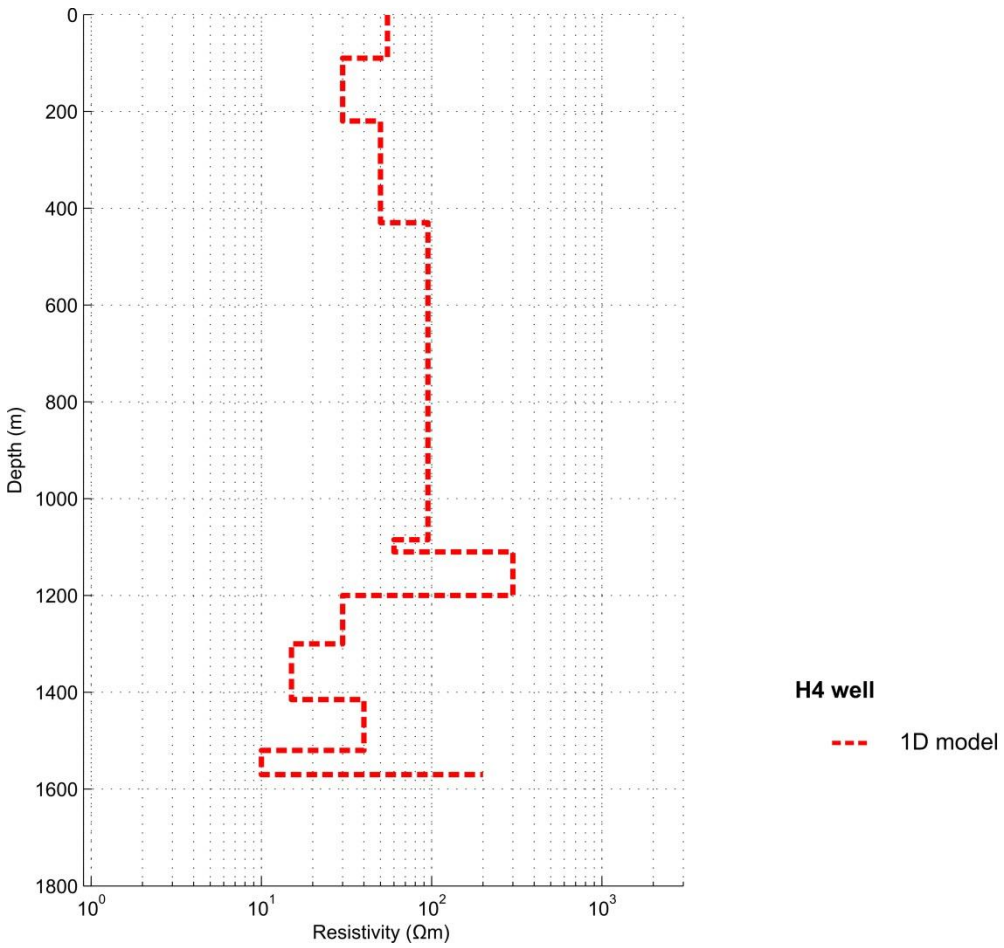

Fig. 2.7. H4 well: 1D model inferred using the H2-well data to correlate the different lithologies to electrical properties. Depths are given in terms of TVD.

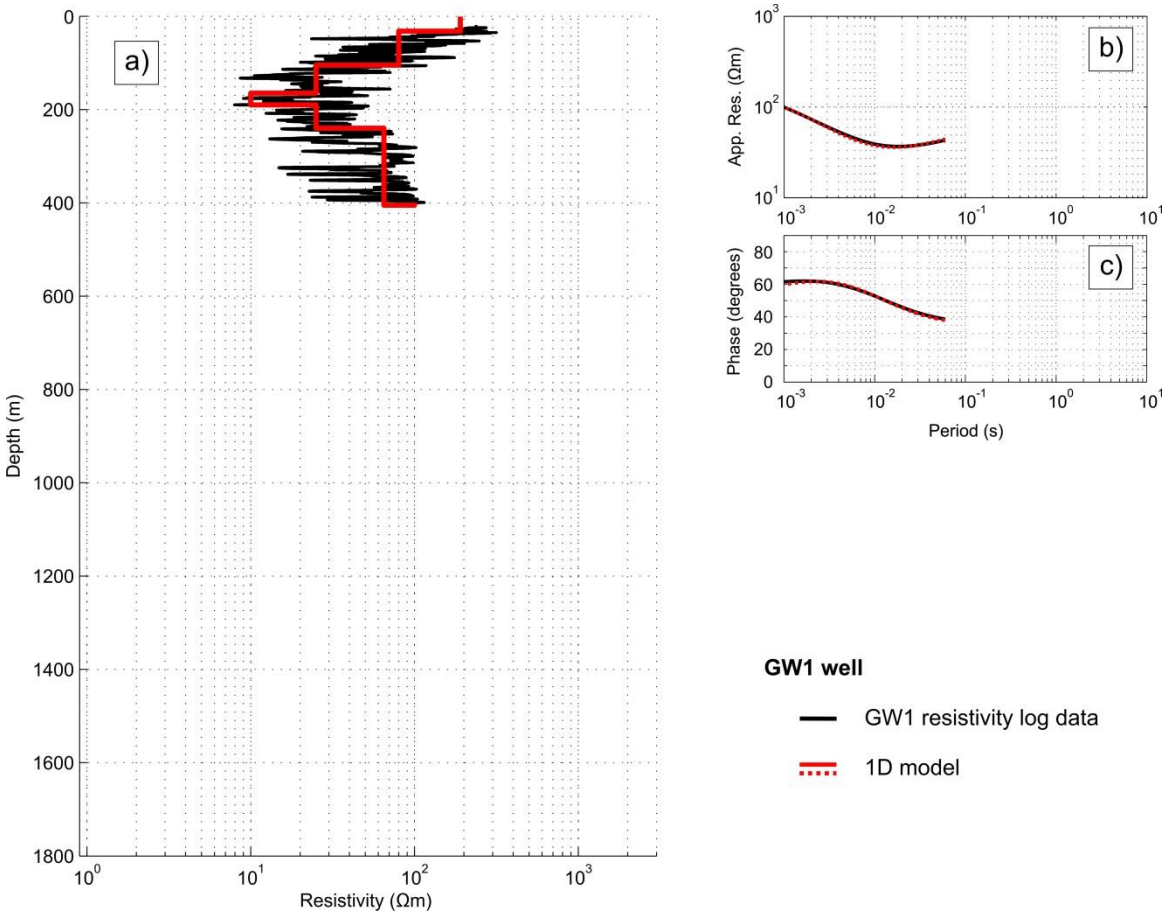

Fig. 2.8. GW1 well: resistivity log data and corresponding 1D model. The end of the well is reached at approximately 0.06 s which corresponds to 400 m TVD according to the skin depth equation (Eq. 1.4) and a homogenous Earth of 10 Ωm (resistivity of the most conductive layer of the H2 well). Depths are given in terms of TVD.

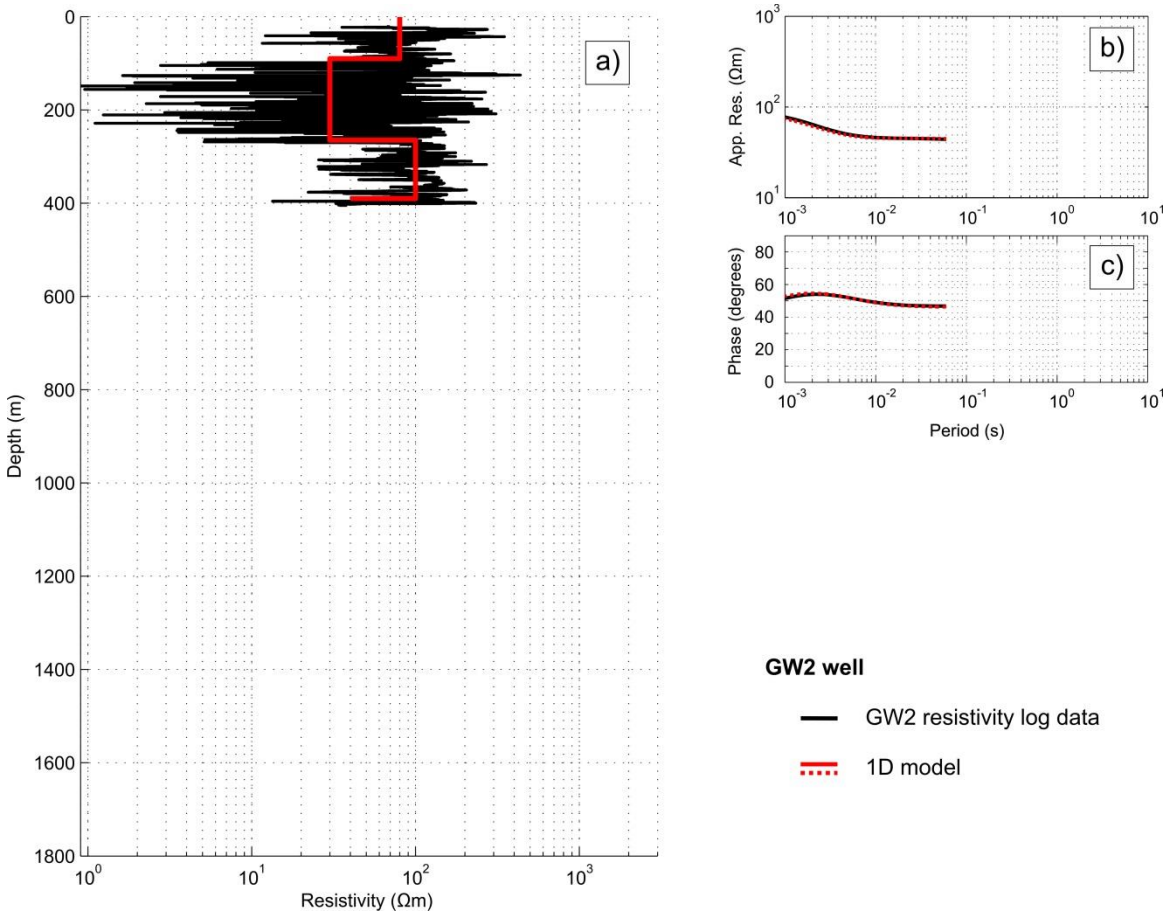

Fig. 2.9. GW2 well: resistivity log data and corresponding 1D model. The end of the well is reached at approximately 0.06 s which corresponds to 405 m TVD according to the skin depth equation (Eq. 1.4) and a homogenous Earth of 10 Ωm (resistivity of the most conductive layer of the H2 well). Depths are given in terms of TVD.

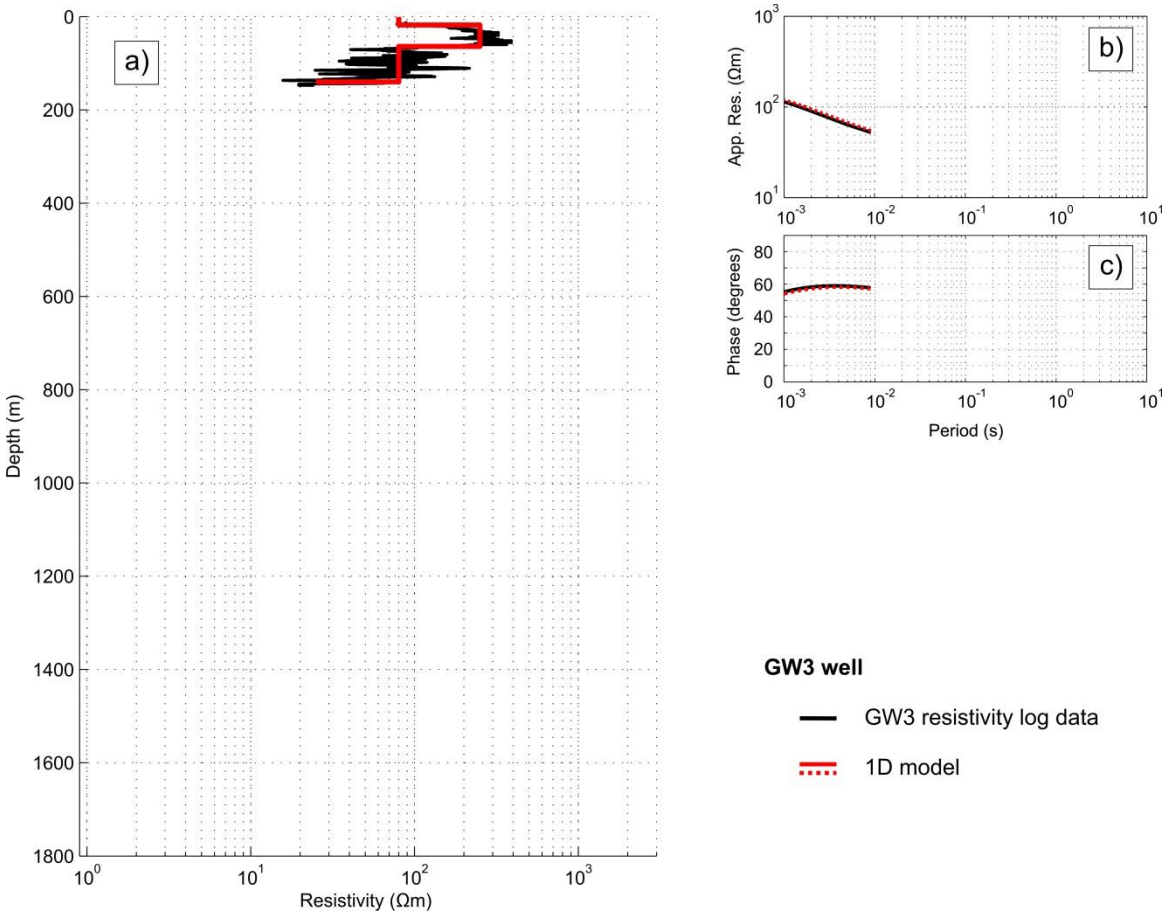

Fig. 2.10. GW3 well: resistivity log data and corresponding 1D model. The end of the well is reached at approximately 0.009 s which corresponds to 150 m TVD according to the skin depth equation (Eq. 1.4) and a homogenous Earth of 10 Ωm (resistivity of the most conductive layer of the H2 well). Depths are given in terms of TVD.

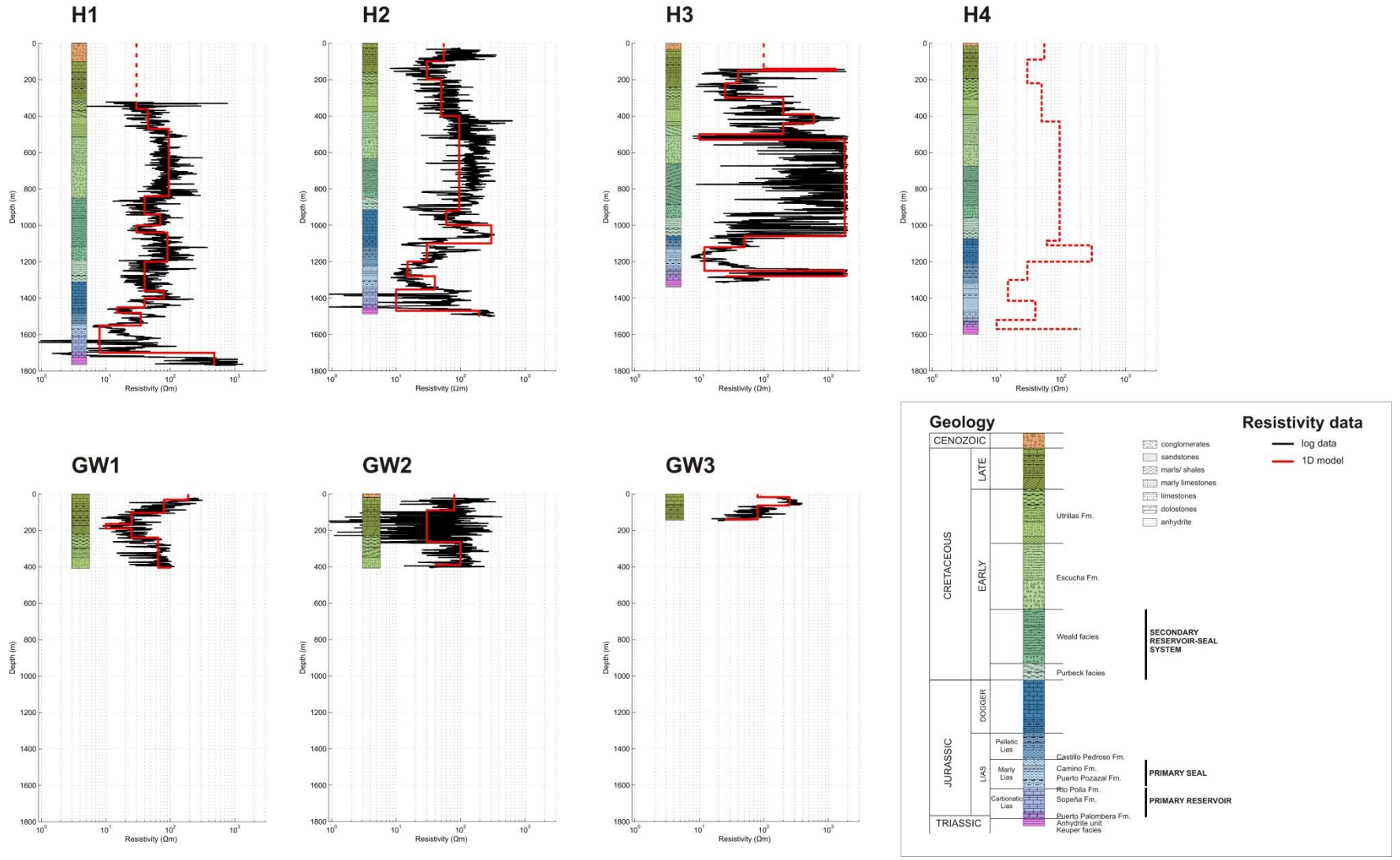

Fig. 2.11. Resistivity log data of all H and GW wells and their corresponding 1D models and stratigraphic columns. Depths are given in terms of TVD (source: ICTJA-CSIC).

Magnetotelluric characterisation

3

The MT characterisation of the Hontomín site comprised a 2D survey and a 3D survey. The initial 2D survey provided the first 2D geoelectrical model of the site's subsurface proving the validity of the method to supply a high resolution 3D resistivity model. Accordingly, a 3D survey was subsequently carried out that resulted in the 3D geoelectrical baseline model of the Hontomín URL. This chapter presents both MT characterisation surveys and the correlation of the final 3D model with results provided by other geophysical techniques. The 2D survey is published in Ogaya et al. (2013), the 3D survey in Ogaya et al. (2014), and the dimensionality analysis of the MT data in Ogaya et al. (2012). These previously published PEER reviewed papers are attached to the thesis.

3.1. Introduction

The EM characterisation of the Hontomín site took place in two stages: a 2D MT data acquisition carried out in Spring 2010 and a 3D MT data acquisition undertaken in Autumn 2010. The objectives pursued in each survey are detailed below.

[1] The first 2D survey aimed to study the viability of the method in the study area as well as to obtain the first geoelectrical image of the URL subsurface.

[2] The 3D survey addressed the extension of the MT characterisation carried out in the previous 2D survey. It aimed to compute the 3D geoelectrical baseline model of the site to be used for the planned future time-lapse EM monitoring experiments at the Hontomín URL. In agreement with results of the dimensionality analysis of the MT data, the goal was to undertake a 3D inversion of the data in order to overcome the limitations of 2D interpretation. Different 3D inversion codes were employed to invert the data.

3.2. MT data

In the study area, a total grid of 109 closely-spaced BBMT sites was collected covering an areal extent of 3x5 km^2. In the first fieldwork (2D survey-Spring 2010), 22 BBMT sites (indicated in red in Fig. 3.1) were acquired. These data were named MTx (MT1, MT2…) in the 2D survey but were renamed to MTDx (MTD1, MTD2…) in the following 3D survey to facilitate the compilation. In the second fieldwork (3D survey-Autumn 2010), 87 new BBMT sites (indicated in yellow in Fig. 3.1) were acquired to complement the 22 acquired in the first fieldwork.

The BBMT data were mainly organised along five NS profiles (Fig. 3.1): MTA, MTB, MTC, MTD (profile collected in the 2D survey) and MTE. To refine the grid in the injection area (Hi region), two smaller NS profiles were acquired: MTBC and MTCD (indicated with yellow dotted lines in Fig. 3.1). All profiles were perpendicular to the EW trend of geological structures and crossed the EW anticline shown in Fig. 3.1. The length of each profile was around 4 km and the average distance between them was approx. 500 m. The stations were distributed at 200 m intervals along the profiles.

The instrumentation consisted of Metronix ADU06, Metronix ADU07 and Phoenix V8 recorders with induction coil magnetometers and NaCl-type electrodes with a typical electrode line length of 70 m in an X-configuration. The x-axis was oriented in the magnetic NS direction with the positive direction pointing to the north, and the y-axis in the EW direction pointing to the east. The data were acquired in the period range of 0.001 to 100 s (1000 – 0.01 Hz frequency range). Assuming a homogenous Earth of 50 Ωm, as was derived from H2 resistivity log data (Fig. 2.5), according to the skin depth equation (Eq. 1.4) this period range allowed characterisation of structures at depths between 112 m and 11 km. In the most conservative case of a homogenous Earth of 10 Ωm (average H2 resistivity log data at the reservoir depth), the penetration depth ranged from 5 m to 5 km. Thus, this period range allowed full characterisation of the target depth.

During 2D acquisition the EM noise was dealt with both long time series (to minimise its effects by statistics) and RR acquisition methods (to remove the incoherent part of the

signal). Thereby, the data were recorded during 48 hours and a permanent RR station was placed 20 km away from the H2 well to improve the quality of the longest periods.

During 3D acquisition, the processing and quality control of the new data were the same as that used in the 2D survey. However, the data were recorded during 24 hours because in the previous survey was found that 48 hours of recording did not noticeably improve the quality of the data compared to 24 hours of recording. The permanent RR station was placed in the same location for the 3D survey as for the 2D survey. Moreover, BBMT acquisition was designed in a manner that at least four stations were recording at the same time; this facilitated minimising the effects of the EM noise using also local multiple RR techniques. Moreover, an additional single long period MT (LMT) data set was acquired to obtain information about the deeper structures (green dot in Fig. 3.1). The LMT data were acquired in the period range of 16 to 20000 s using a LEMI-417 system (Lviv Center of Institute of Space Research).

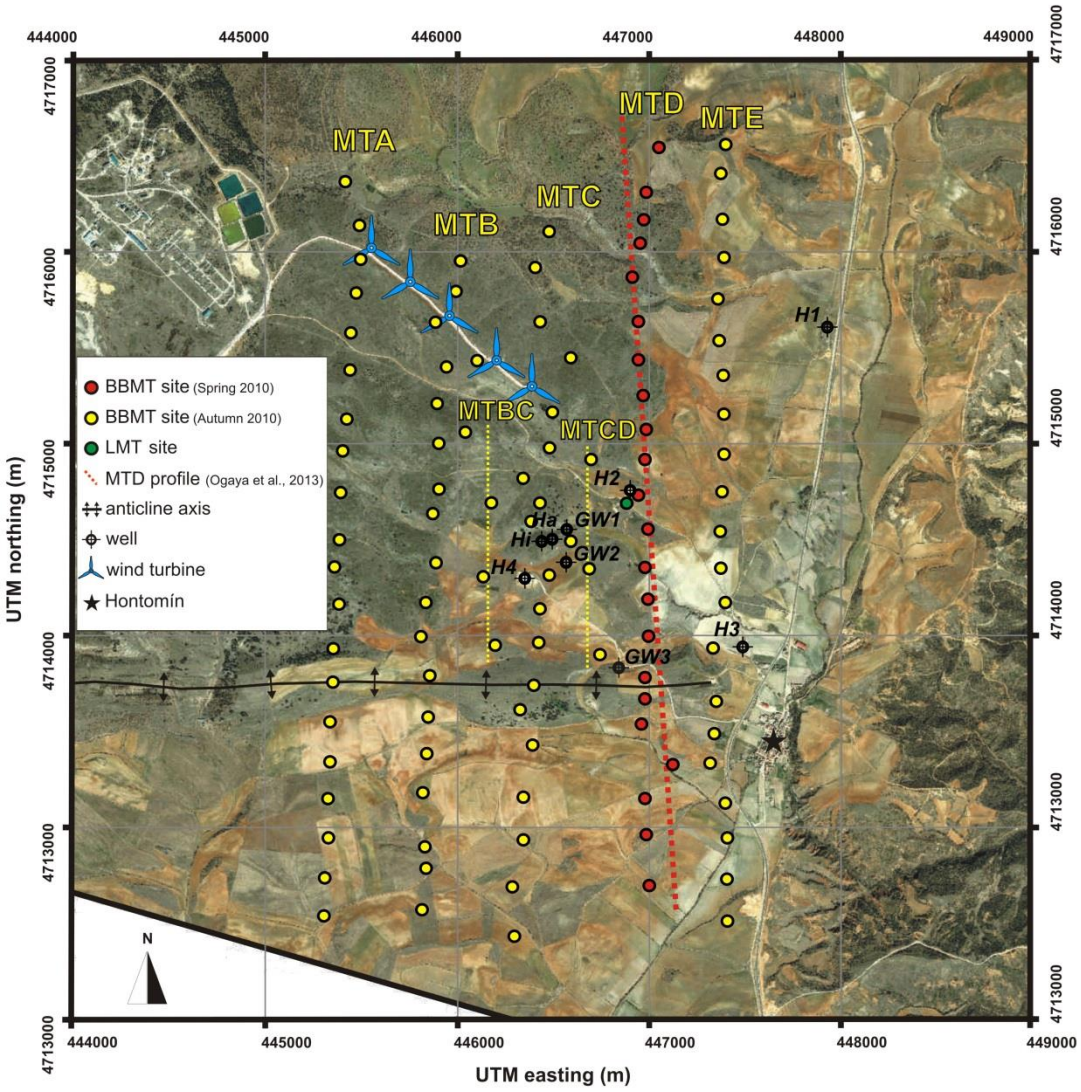

Fig. 3.1. Locations of the BBMT and LMT sites. In red, the BBMT sites collected in Spring 2010; in yellow, the BBMT sites collected in Autumn 2010 and in green, the single LMT site. Indicated are the acronyms of the profiles as well as the orientation of the 2D model. Small yellow dotted lines indicated MTBC and MTCD profiles. Also shown are the positions of the wells and wind turbines (major EM noise source within the study area) (from Ogaya et al., 2014).

3.3. 2D survey

The 2D characterisation presented here was undertaken using the 22 BBMT sites acquired in Spring 2010 (red dots in Fig 3.1). We remind the reader that in this work sites were named MTx (MT1, MT2…) and the term *profile* makes reference to which would be the MTD profile in the 3D survey.

3.3.1. Data processing and dimensionality analysis

Different robust processing codes using remote reference methods (Gamble et al., 1979 and Egbert and Booker, 1986) were tested and used at all stations of the profile to derive optimal MT responses (Fig. 3.2 exemplified the processing of the data at site MT16). Due to the important presence of wind turbines, DC power-supply lines and other electrical-noise sources in the area, the RR technique was essential to improve the quality of the MT data between 0.5 and 10 s (Fig. 3.2a and Fig.3.2b). At periods exceeding 10 s, the analysis of the MT responses highlights the presence of noise with phases decreasing to 0º and apparent resistivities showing slopes of 45º (Fig. 3.2), which is a clear signal of a nearby noise source that dominates the time series. Consequently, all the following studies were undertaken in the period range of 0.001 to 10 s.

The MT data acquired at site MT10 (located close to H2 well) was compared to the H2 well resistivity log data for periods shorter than 0.9 s (Fig. 3.3). The apparent resistivity and phase responses were observed to present similar behaviour.

Prior to any geophysical interpretation of the MT responses, the MT dimensionality of the acquired data was computed using the distortion decomposition method of Groom and Bailey (1989) (GB), which is implemented in the STRIKE code of McNeice and Jones (2001). This method facilitates the estimation of the regional impedance tensor by detecting and removing most of the effects caused by local near-surface heterogeneities. The strike direction ambiguity of 90º was fixed considering the orientation of the main geological units of the zone. The best geoelectrical strike direction obtained for each site is shown in Fig. 3.4. All sites of the profile display misfits to the GB distortion model with an RMS (root

mean square) less than 2.0. Thus, responses along the profile are consistent with the 2D assumption and therefore, suitable for the 2D modelling. The best-fit average multi-site, multi-frequency GB regional strike is N86ºE, which represents a dominant EW strike direction consistent with the pre-existing geological and geophysical information of the area. Consequently, the data were rotated 4ºW (Fig. 3.2c).

In this study, static shift was corrected using the resistivity log data provided by well H2. The resistivity log data fixed the resistivity values at shallow depth, defining the reference level for the apparent resistivity curves. As the first metres of the Earth can be assumed to be mainly 1D, both polarisations asymptote together at short periods. In all the BBMT sites the correction was smaller than a decade (Fig. 3.2c).

Finally, the physical consistency of the data through the D^+ model solutions (Parker, 1980; Parker and Whaler, 1981) was studied. The method consists of analysing the physical validity of the MT responses finding the 1D Earth that best fits both apparent resistivity and phase curves. This technique has demonstrated to be valid for most 2D cases and for some 3D cases (Beamish and Travassos, 1992). Using an estimated error of 10 % in the apparent resistivity and in the phase, the D^+ solution allowed the detection and removal of the outliers and noisy points whose apparent resistivity and phase values show an inconsistent behaviour. In this way, the D^+ solution provided the smoothing of the data. In total, around 25 % of the MT data were discarded (this percentage includes MT data in the period range of 10 to 100 s-noisy region, coloured by lighter colours in Fig. 3.2c).

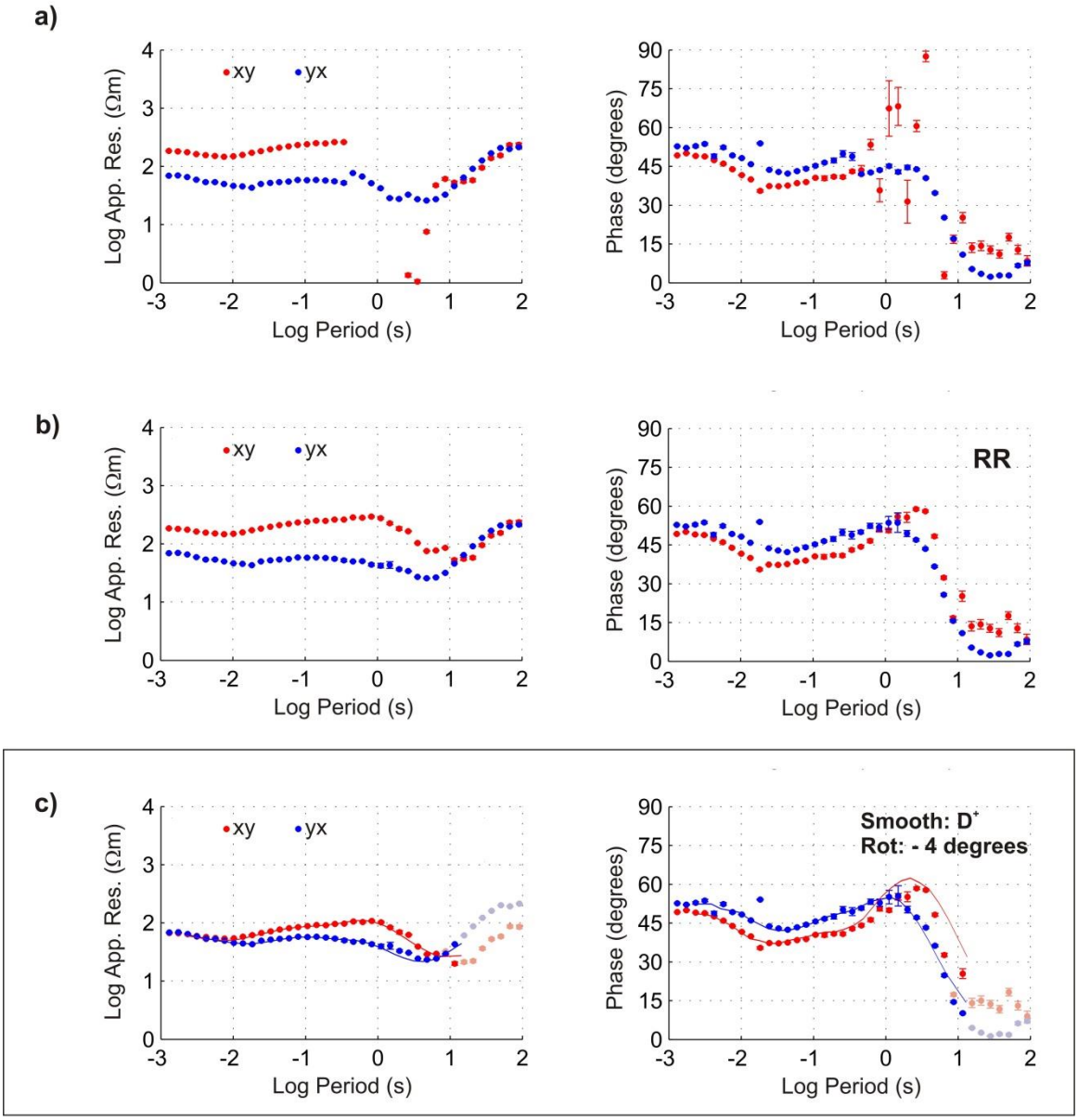

Fig. 3.2. Data processing at site MT16. a) Robust processing not using the remote reference technique. b) Robust processing using the remote reference (RR) technique. c) Final MT responses at site MT16 after using the RR technique, rotating the data (4°W) according to the regional strike and correcting the static shift. The smoothed curves (D^+ solution) are plotted using solid lines. Outliers and noisy points (removed data) are indicated by lighter colours. Since the rotation of the axes is small, there does not exist an appreciable change in the apparent resistivity and phase curves (from Ogaya et al., 2013).

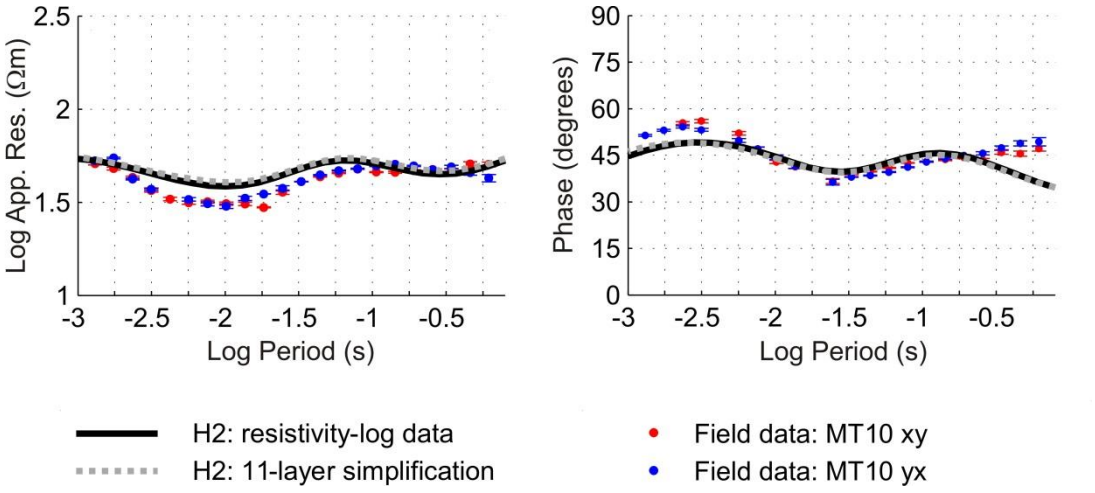

Fig. 3.3. MT responses of the H2 resistivity log data and acquired MT data at site MT10. The black solid line reproduces the MT response of H2 resistivity-log data. The grey dotted line shows the MT response of the 11-layer simplification of H2 (1D model) (Fig. 2.5). Both MT responses at the surface are coincident. Dots displayed the two polarisations of the MT data acquired at site MT10 (located close to H2). The figure shows data from 0.001 to 0.9 s because the end of the well is approximately reached at 0.9 s (from Ogaya et al., 2013).

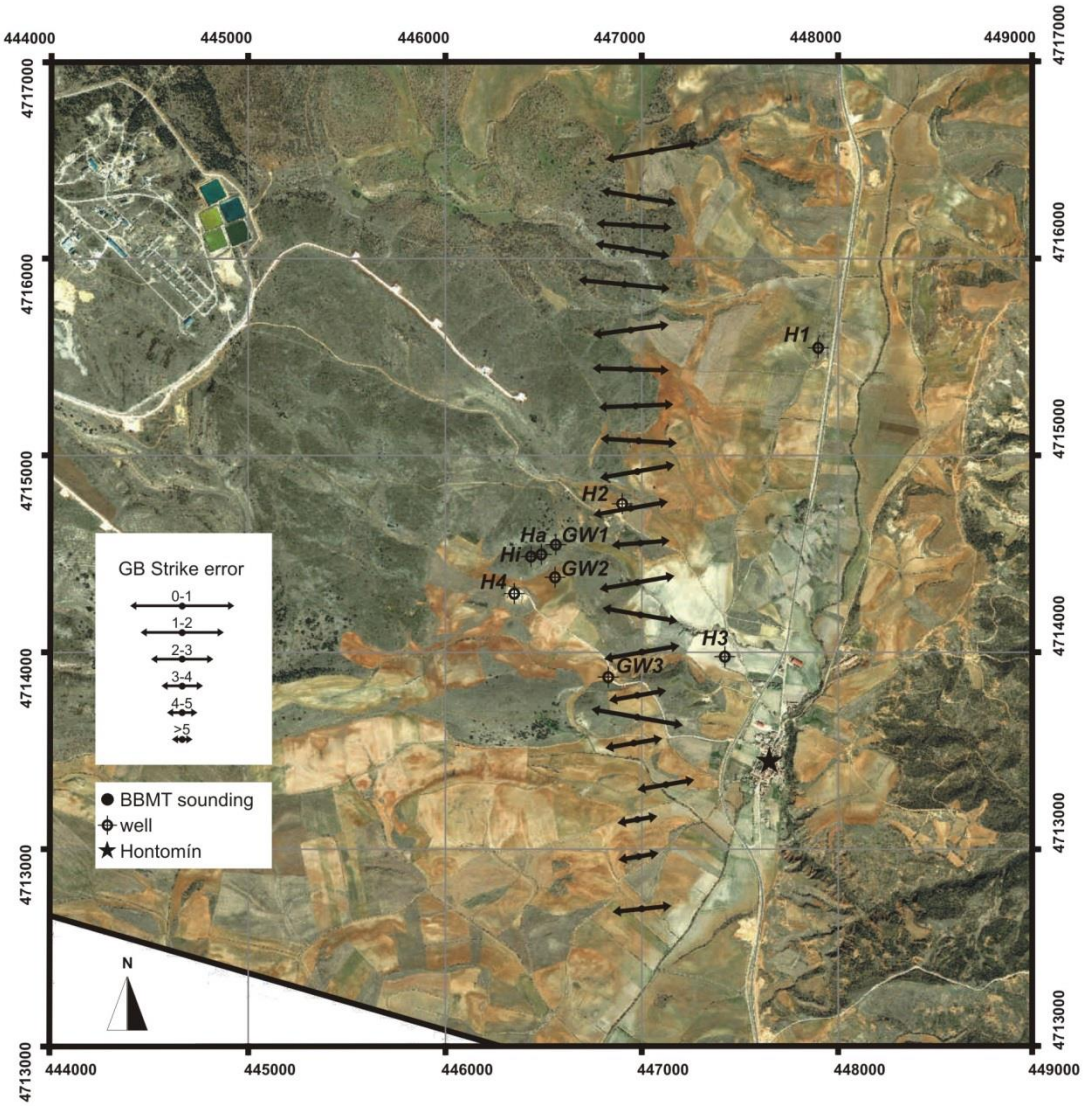

Fig. 3.4. Geoelectrical strike angle for the period range of 0.001 to 10 s with an error floor of 5 % on the impedance tensor components. Black dots indicate the location of the BBMT sites and arrows indicate the GB strike angle. Their length is associated with the compatibility of the data with the 2D assumption. The best-fit average multi-site, multi-frequency GB regional strike is N86ºE. The location of the four wells drilled in the past (H1-H4) is also indicated (from Ogaya et al., 2013).

3.3.2. 2D inversion

According to the results of the dimensionality analysis, which demonstrated that 2D modelling of the data was valid and appropriate, a joint 2D inversion of the smoothed TE and TM apparent resistivity and phase data was undertaken after rotating the impedance tensor to the strike direction. All the 22 BBMT sites of the profile were considered for the inversion. The TE mode was identified with the YX polarisation and TM mode with the XY polarisation. The 2D inversion code used is the one described by Rodi and Mackie (2001). The algorithm searches for the model that trades off the lowest overall RMS misfit with the smallest lateral and vertical conductivity gradients in a regularised manner. The starting model was the 1D model derived from the resistivity log data of well H2 (Fig. 2.5), since the well is placed around 100 m away from the profile (Fig. 3.4). The cells of the model associated to this well were fixed during the inversion and modelling processes. The topography on the profile was also taken into consideration.

On average, the model fits the smoothed data with an acceptable RMS misfit of 1.29. The error floor for the phases was set to 1.45 degrees, and 5 % for the apparent resistivities. The final model, together with the 1D model derived from the H2 well resistivity log (an 11-layer simplification), are shown in Fig. 3.5. Comparisons between the data and model responses for the apparent resistivities and phases of both modes are shown in Fig. 3.6 (TE mode) and Fig. 3.7 (TM mode). As is illustrated, the residuals between the observed data and the model responses are random and small, and no strong feature in the data is unexplained. Thus the fit between the data and model responses is highly satisfactory.

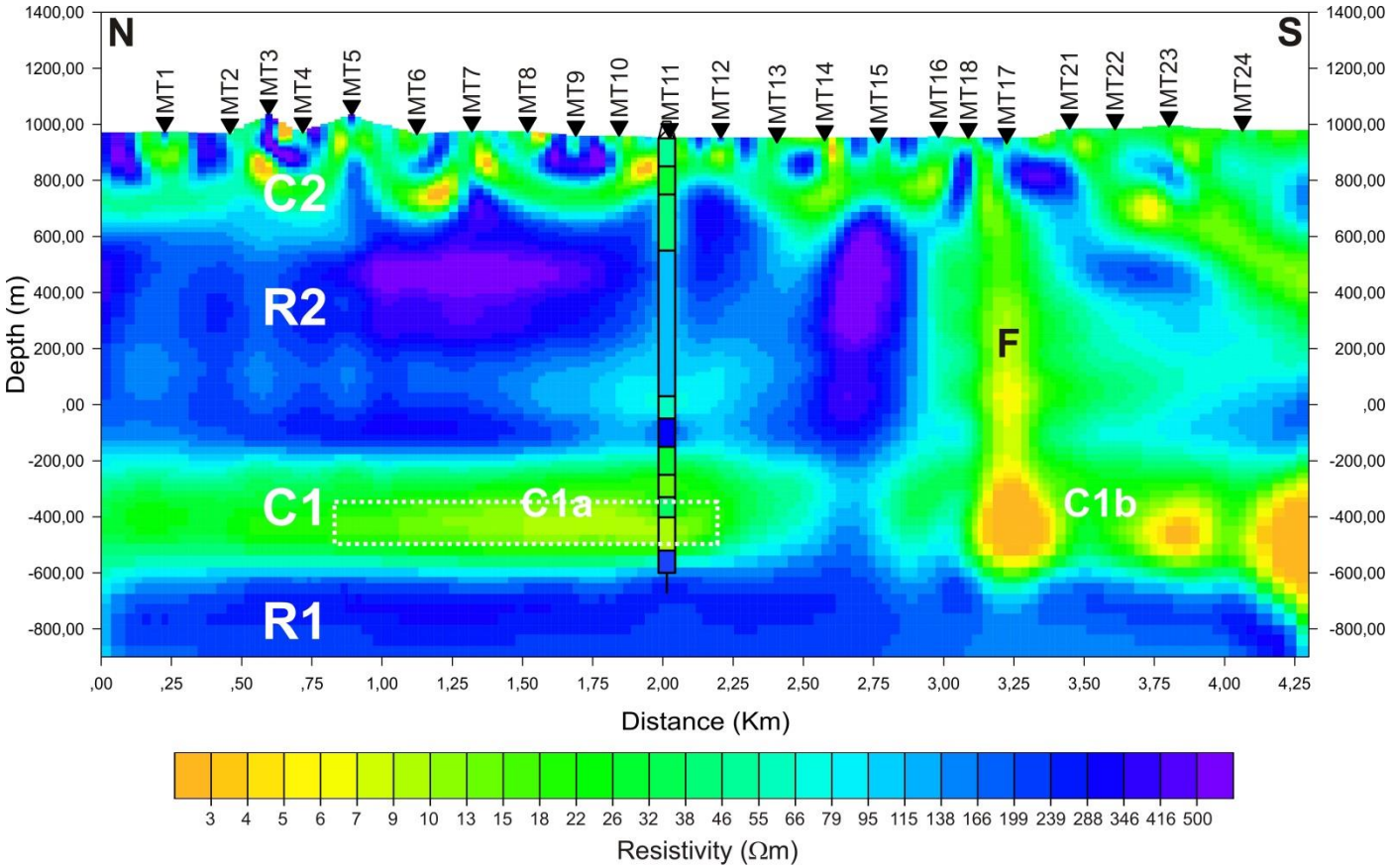

Fig. 3.5. 2D resistivity model. The model fits the data with an RMS misfit of 1.29. The 1D model provided by the resistivity-log data of H2 well is superimposed. The MT sites' positions are marked as black triangles. The four main layers of the resistivity distribution are labelled (from bottom to top): R1, C1, R2 and C2. The deep saline aquifer (main reservoir) and the main seal are within conductive unit C1. A more resistive area beneath sites MT14 and MT15 divided this layer in two regions: C1a (where the injection is planned) and C1b. The secondary reservoir and seal system is contained in region R2. F indicates a vertical low resistivity structure disrupting R2 layer (a fault region). The dotted line indicates the homogenous structure used to compute non-linear sensitivity tests in the main reservoir region. (See text for further information). The depths are given in terms of metres above sea level (m.a.s.l.) (from Ogaya et al., 2013).

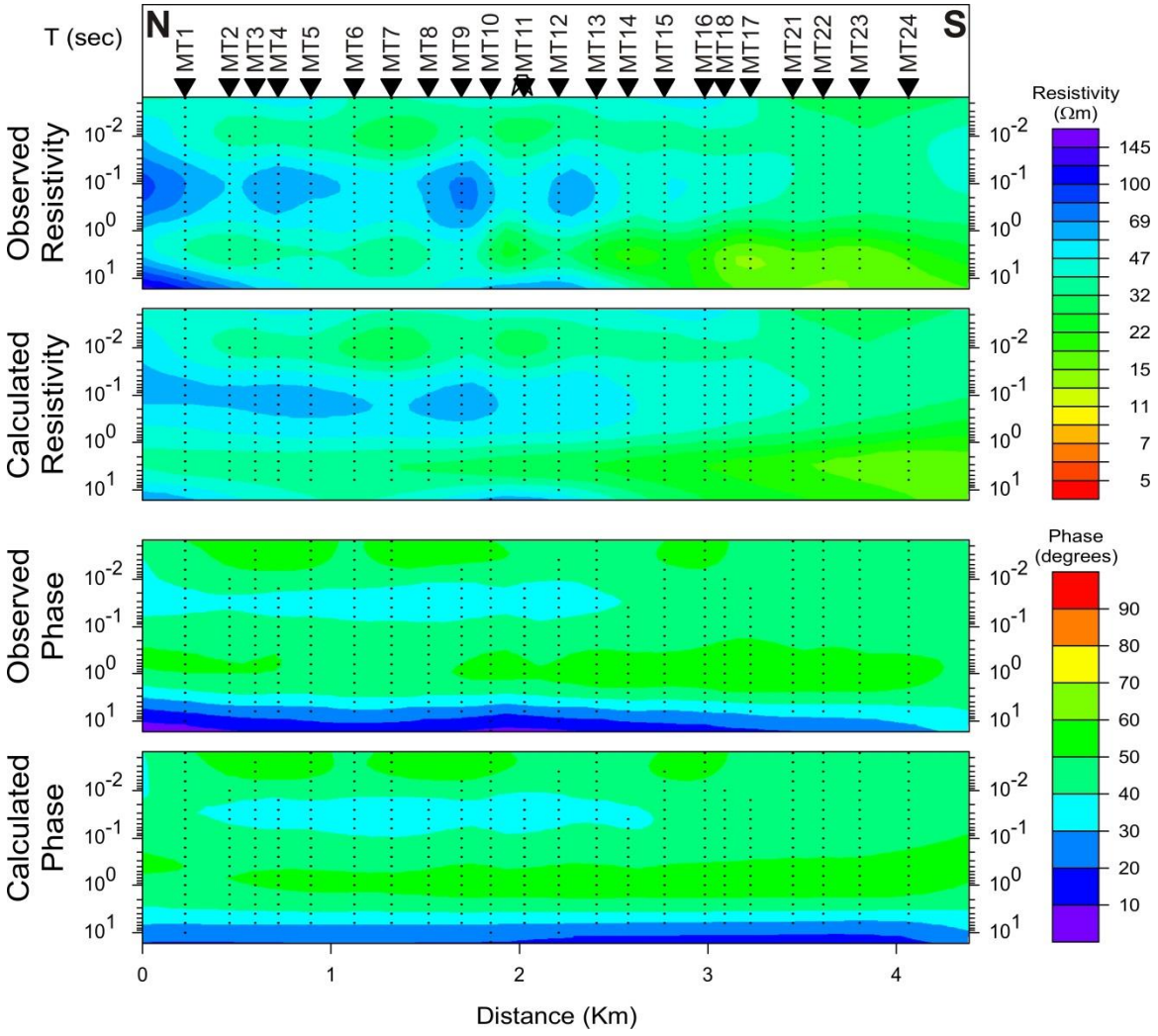

Fig. 3.6. Pseudosections of TE mode (YX polarisation): comparison of apparent resistivity and phase for the observed data and model responses of TE mode. The MT sites' positions are marked as black triangles (from Ogaya et al., 2013).

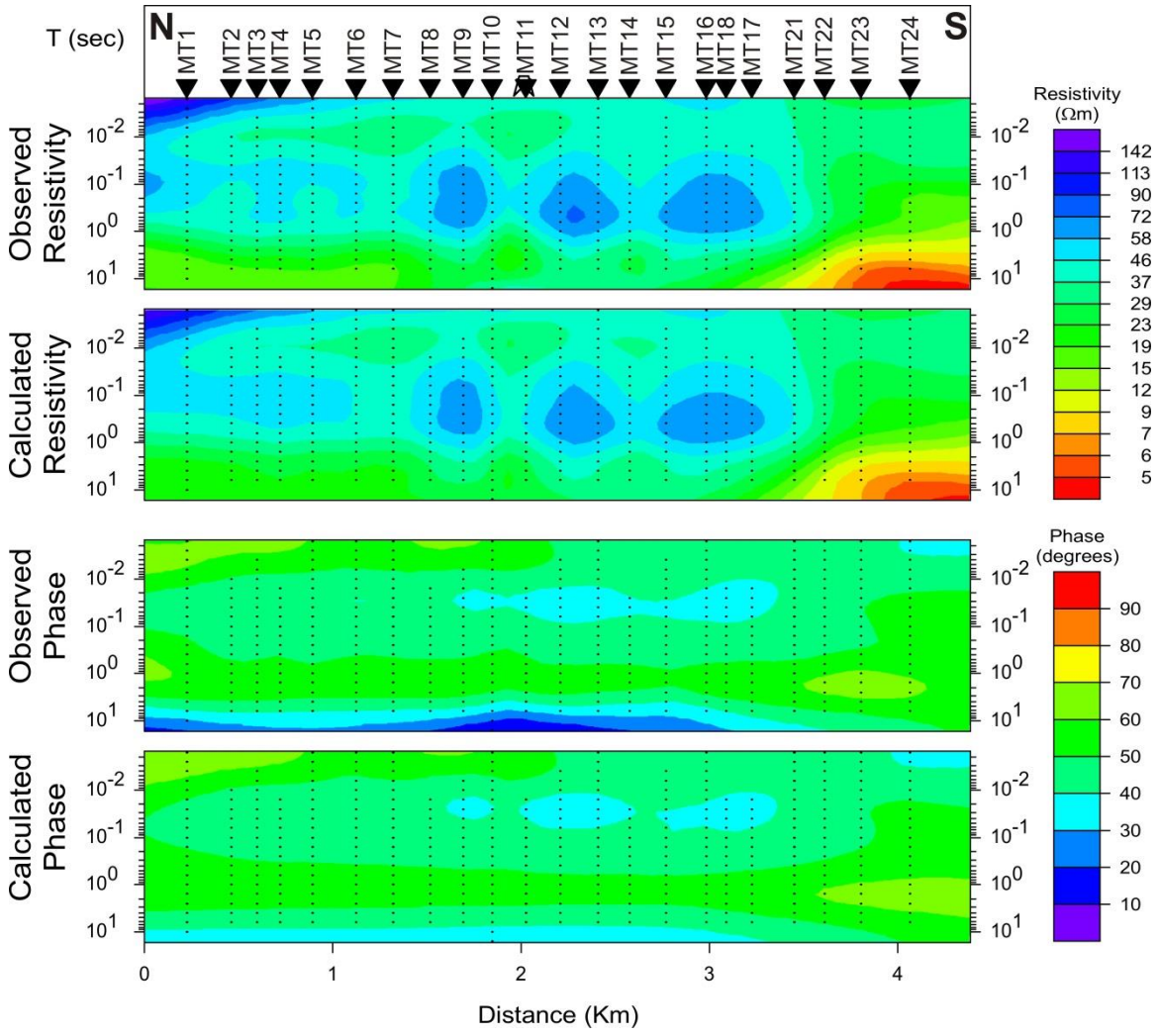

Fig. 3.7. Pseudosections of TM mode (XY polarisation): comparison of apparent resistivity and phase for the observed data and model responses of TM mode. The MT sites' positions are marked as black triangles (from Ogaya et al., 2013).

3.3.3. 2D model: interpretation and discussion

The MT data were inverted in the period range of 0.001 to 10 s and produced a reliable resistivity image from the near-surface to over 1800 m TVD imaging the primary reservoir (saline aquifer) and the primary seal, as well as the secondary reservoir-seal system. All depths are given in terms of sea level since the topography has been taken into account (m.a.s.l.) (Fig. 3.5). The resistivity distribution is composed of four main layers (from bottom to top): 1) a resistive layer (region R1) present below -600 m.a.s.l. (bottom of the model); 2) a very conductive layer (area C1) imaged below -200 m.a.s.l. with a thickness up to 400 m; 3) a resistive middle layer, between +700 m.a.s.l. and -200 m.a.s.l. corresponding to region R2; 4) a conductive top layer (C2) with more resistive and conductive scattered small bodies evident from surface to +700 m.a.s.l.. The H2 well made it possible to link these electrical properties to the different lithologies.

The resistive layer at the bottom of the model (R1) is required by the increase of the apparent resistivity observed at around 1 s and coincides with the resistive Upper Triassic unit (Keuper facies and Anhydrite unit) (Fig. 2.11). This is an impermeable and resistive unit which may constitute an interesting bottom seal (below the main reservoir).

The C1 layer mainly corresponds to the data in the period range of 0.1 to 1 s. The deep saline aquifer (primary reservoir) and the primary seal are located within the conductive unit C1. The resistivity values of these structures are very similar and cannot be separately resolved only from surface MT measurements. The data from the H2 well log facilitated superior association of the small changes of electrical resistivity values within C1 to the different lithological units. The C1 layer is divided in two regions (labelled C1a and C1b to facilitate the comprehension of the following discussion) (Fig. 3.5) by a more resistive area beneath sites MT14 and MT15. At -450 m.a.s.l., inside region C1a, a more conductive area (9-11 Ωm) is imaged. This anomaly is probably associated to the Lower Jurassic (Lias) rocks, corresponding to the target reservoir units. Above the primary reservoir, the primary seal would be imaged as a layer with resistivity values of 18-23 Ωm, due to the presence of thin layers of black shales belonging to the Camino Fm. The top of C1 could represent the lower part of the Dogger, formed of marly limestones.

The region R2 is the thickest of the model and contains the secondary reservoir-seal system (Early Cretaceous). This system is formed by sandstones, conglomerates and shales from Purbeck facies. The boundary between the R2 and C2 regions is located in the upper part of the Lower Cretaceous materials and could mark the top of the Utrillas Fm. (Fig. 2.11). In the southern part of the model, within sites MT16 and MT21, region R2 is disrupted by a near vertical low resistivity structure indicated by an 'F' in Fig. 3.5. This F structure could be related to the Ubierna Fault (Fig. 2.1), as was later imaged in the 3D seismic studies (Alcalde et al., 2013b; Alcalde et al., 2014). The resistivity distribution suggests an important conductive fluid circulation along the fracture region, since the conductive signature is too powerful to be generated by a thin accumulation of clays along the fault. Further studies have attempted to evaluate if the presence of this fault could suggest a possible leakage pathway. Elío et al. (2013), after determining the baseline of CO_2 flux in the soil-atmosphere interface, concluded with affirming that the flow gas in the fault region was as low as in other regions without fractures. However, some of the surface water samples in the eastern part of the fault acquired by Buil et al. (2012) contained a higher content of sulphates and chlorides and higher electrical conductivity, suggesting its mixing with deeper waters. In any case, due to the research character of the project, no more than 20 kilotons are planned to be injected. This represents an approximate injection volume of 135x135x25 m^3 at the reservoir depth, assuming a homogenous saturation of 50 % (section 2.3.1). As the injection is planned in the C1a region, the probability of the injected gas reaching the C1b region, and consequently the fault, is improbable. Moreover, beneath sites MT14 and MT15 the connection between C1a and C1b seems to be sealed, as inferred from the resistive area.

Finally, the C2 region could correspond to Upper Cretaceous limestones and marls that dominate the surface of the study area.

An overall view of the model shows a very smooth dome-shape structure, with the axis of the dome located close to H2 well (MT11 site). As it is also observed in the preliminary 3D seismic images of the Hontomín site (Alcalde et al., 2014) the flanks of the dome structure dip at lower angle than was interpreted from the vintage seismic data.

The primary reservoir is imaged as the most conductive region inside C1a. The saline aquifer is linked to the lowest resistivity values of the model, as reported by the resistivity log data provided by well H2. Thanks to the well log constraint, the position of the units and their resistivity values are well determined. In order to check whether the upper and lower resistivity limits of the saline aquifer are compatible with the measured surface data, non-linear sensitivity tests were computed, following those described by Ledo and Jones (2005). Thus, a homogeneous structure with constant resistivity at the reservoir depth was assumed (Fig. 3.5). The electrical resistivity of this structure was increased and decreased from the original value until the difference between the responses of the final model and the modified model reached a value of 5 % for the apparent resistivities and/or 1.45 degrees in the phases. Thereby, this resolution study concluded that the electrical resistivity of the primary reservoir ranges between 8 and 25 Ωm (Fig. 3.8). This result makes it possible to estimate the reservoir porosity using the Archie's law (Eq. 1.1): assuming 100 % water saturation ($S_w = 1$), $m = 2$ and $a = 1$, the porosity of the main reservoir was derived to be comprised between 9 % and 17 %. This porosity range agrees with the first estimation obtained by Márquez and Jurado (2011) from the vintage well logs of the area (from 0 % to 18 %).

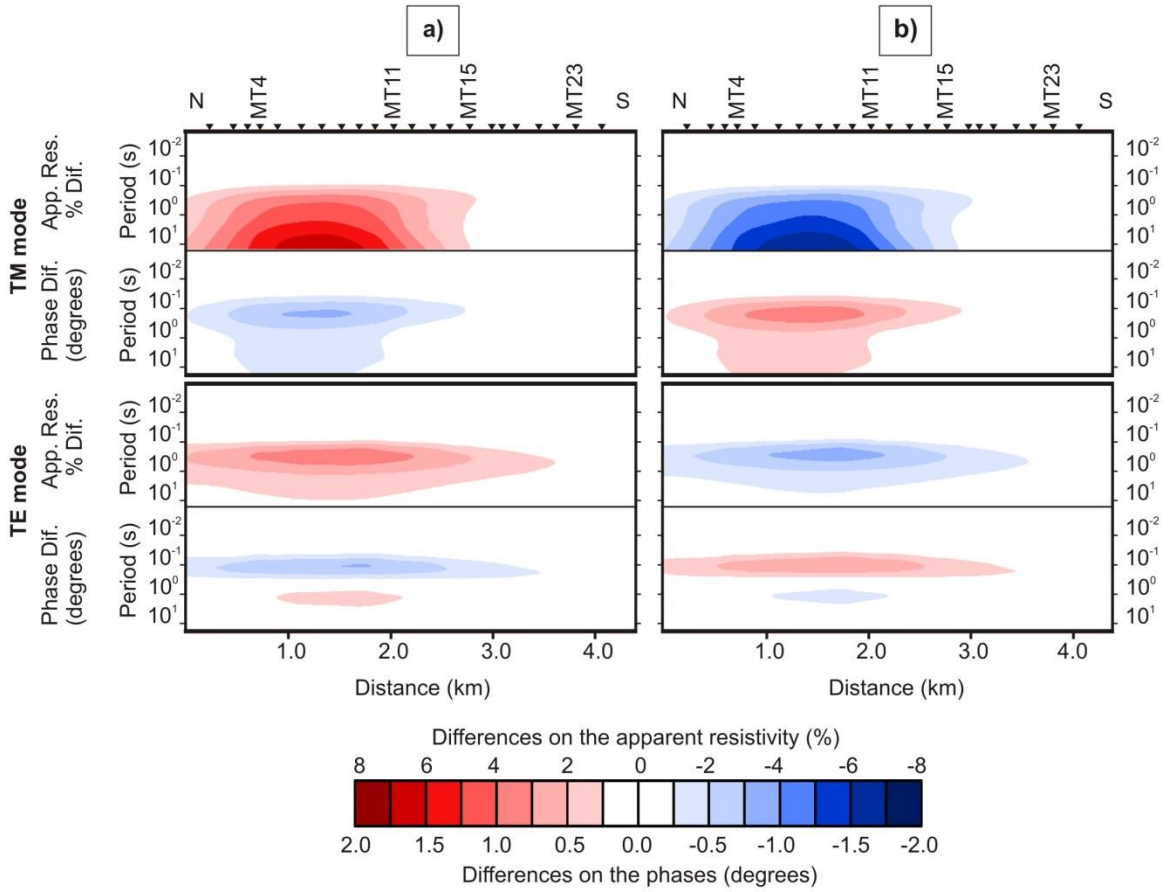

Fig. 3.8. Non-linear sensitivity tests to find the precision in determining the reservoir resistivity. The figure displays the difference between the responses of the final model and the modified assuming a homogenous structure of 8 Ωm (a) and 25 Ωm (b) at the reservoir depth. Apparent resistivity of TM mode reaches in both cases (A and B) a value of 5 % of difference which means that the main reservoir electrical resistivity ranges between 8 and 25 Ωm. Periods are displayed on a logarithmic scale (from Ogaya et al., 2013).

3.3.4. Conclusions of the 2D survey

The MT method was demonstrated to be an appropriate technique for characterising the study area and providing a high resolution geoelectrical baseline model. The 2D resistivity model highlighted the viability of the method in the Hontomín site, and was performed in spite of the EM noise, which was successfully minimised and removed from the acquired MT data. Facing the second stage of the geoelectrical characterisation, this work suggested some strategies for dealing with this EM noise and underlined the importance of using RR techniques as a way to eliminate uncorrelated signal from the acquired data. On the analysis of both the MT data and the H2 resistivity log data, the primary system (primary reservoir and seal) was observed to be approximately imaged in the period decade of 0.1 to 1 s, whereas dominant EM noise in the area appeared at periods longer than 10 s.

The obtained 2D resistivity model constituted the first geoelectrical image of the Hontomín site. Thus, it contributed to understanding the geoelectrical structure of the area and made it possible to correlate the different lithologies and formations to electrical resistivities. The model confirmed a clear contrast between electrical properties of the primary reservoir-seal system, more conductive as it contained the saline aquifer, and the more resistive character of the secondary reservoir-seal system. The electrical resistivity of the primary reservoir ranged between 8 and 25 Ωm which means, according to Archie's law, a porosity of between 9 % and 17 %.

The model imaged an EW fault in the southern part associated to the Ubierna Fault and linked it to a probable important fluid circulation. However, this fault is not expected to constitute an important leakage pathway, since the injection well is located close to the H2 well (centre of the dome), rather far from the fault region. One the other hand, no more than 20 kilotons of CO_2 are planned to be injected at the Hontomín site, which implies a small plume of 135x135x25 m^3 given the pressure and temperature conditions at the reservoir depth (assuming a homogenous saturation of 50 %).

The constrained 2D inversion carried out using the H2 well log data provided a high quality geoelectrical model and motivate the subsequent 3D survey.

3.4. 3D survey

For the 3D characterisation of the Hontomín URL, the total grid of 109 BBMT site and the LMT site (Fig. 3.1) were taken into account. Data acquired in Spring 2010 were renamed to MTD (MTD1, MTD2…), to facilitate ease of assignment, as mentioned above.

3.4.1. Data processing and dimensionality analysis

Robust processing codes employed to derive the BBMT responses were the ones that demonstrated their validity in the previous 2D survey (Egbert and Booker, 1986). The RR technique (Gamble et al., 1979) was used at all stations to improve the quality of the BBMT data between 0.5 and 10 s. The implementation of the local RR technique was crucial for improving the data collected near the wind turbine region (Fig. 3.1) and consisted of undertaking RR with sites located in the southern part of the study region (less noisy area). At periods exceeding 10 s, ambient noise dominated the natural signal and consequently, the studies were undertaken in the period range of 0.001-10 s (1000 to 0.1 Hz). The LMT data were processed using Birrp.5 (Chave and Thomson, 2004).

The dimensionality analysis of the acquired MT data was evaluated using (i) the WALDIM code of Martí et al. (2009) based on the Weaver impedance invariants (Weaver et al., 2000), and (ii) studying the phase tensor (Caldwell et al., 2004). Figure 3.9 shows the results obtained using the WALDIM code at each site for four different period ranges: 0.001-0.01 s, 0.01-0.1 s, 0.1-1 s and 1-10 s. The assigned error level in the impedance components was of 5 % and the threshold set for the invariants were: τ=0.19 for invariants I_3-I_7 and τ_Q=0.10 for invariant Q. For short periods (shallow depths), the results indicate 1D/2D conductivity, being mainly 1D in the F region (in the south). On the contrary, when increasing the period (equivalent to increasing the depth of penetration), geoelectrical structures become more complex and present a 3D behaviour. The strike direction obtained for the MTD profile using the WALDIM code agrees with the strike direction obtained using the multi-frequency STRIKE code (N86ºE) (Ogaya et al., 2013). In this way, the results supported the validity of the previous 2D modelling since the main reservoir and seal

units (sensed within the period band 0.1-1 s) (Ogaya et al., 2013) present a predominantly 2D behaviour.

Figure 3.10 plots the phase tensor at each site for four different periods: 0.003 s, 0.03 s, 0.3 and 3 s. As the phase tensor is independent of the electric effects of galvanic distortion, this analysis aimed to determine if there existed an important galvanic distortion in the WALDIM results and, in this way, to estimate to what extent this distortion was perturbing the data. Results indicate that the geoelectrical structure becomes more complex, i.e., higher dimensionality, with increasing the period, as showed for the WALDIM analysis. Once again, the validity of 2D modelling of the MTD profile was confirmed given the predominant 2D behaviour of those sites. The strike directions agree with the results provided by the previous studies.

Thereby, the dimensionality analysis corroborated that a 3D inversion of all the BBMT data set was necessary to avoid misinterpretation of the geoelectrical structure of the Hontomín URL at periods longer than 0.1 s (Ogaya et al., 2012). Moreover, it was concluded that galvanic distortion in the study area was small, since results of the phase tensor study were consistent with the ones obtained using the WALDIM code.

As in the 2D survey, the internal self-consistency of the XY and YX BBMT data apparent resistivity and phase curves was analysed through D^+ model solutions (Parker, 1980; Parker and Whaler, 1981) in order to detect and remove outliers and noisy points by analysing the physical validity of the MT responses. Thus, using an estimated data error of 10 % for the apparent resistivity and phase, some 30 % of the BBMT data was discarded. This fraction included data from all sites in the range of 10 s to 100 s – the noisy region. Seven BBMT sites were excluded from the inversion because they were considered too noisy with a high and linearly polarised signal (Escalas et al., 2013). Almost all of them were near the wind turbine region. Figure 3.11 summarises the quality of the BBMT data, indicating: complete period bands (white); period bands with gaps (grey); empty period bands (black) and excluded sites (blue). Most of the grey cases correspond to curves with shortest periods longer than 0.001 s and/or longest periods shorter than 10 s. This defines the data set for the 3D inversion.

For the data set for the 3D inversion, the minor static effects of galvanic distortion were dealt with prior to the inversion using the available resistivity log data to fix the resistivity values at shallow depths. In general terms, the static shift corrections were smaller than a logarithmic decade and did not illustrate any spatial consistency (Fig. 3.12 shows raw responses at some sites along the north-border of the F fault region). Static shift correction could imply a loss of information but related to near surface structures that are not the target of this study. In other works as Heise et al. (2008) and Newman et al. (2008), who also report on shallow characterisation surveys (approx. 5 km) with a dense grid of sites, static shift was similarly corrected prior to the inversion, thereby obtaining accurate results.

Giving the predominant 3D behaviour of the geoelectrical structures for periods longer than 0.1 s, the diagonal components of the impedance tensor, Z_{xx} and Z_{yy}, were considered for the inversion. The importance of including the diagonal components in 3D inversion was recently emphasised by Kiyan et al. (2014). For the shortest periods, the amplitude of the apparent resistivity of the diagonal components at most sites is two to three decades smaller than the off-diagonal components. However, for the longest periods, the difference of amplitude between the diagonal and off-diagonal components is less than a decade. In general, the diagonal component data are of reasonable quality and their apparent resistivity and phase curves are not scattered; their amount of error is relatively low (see supplementary figures Fig. S1-S17).

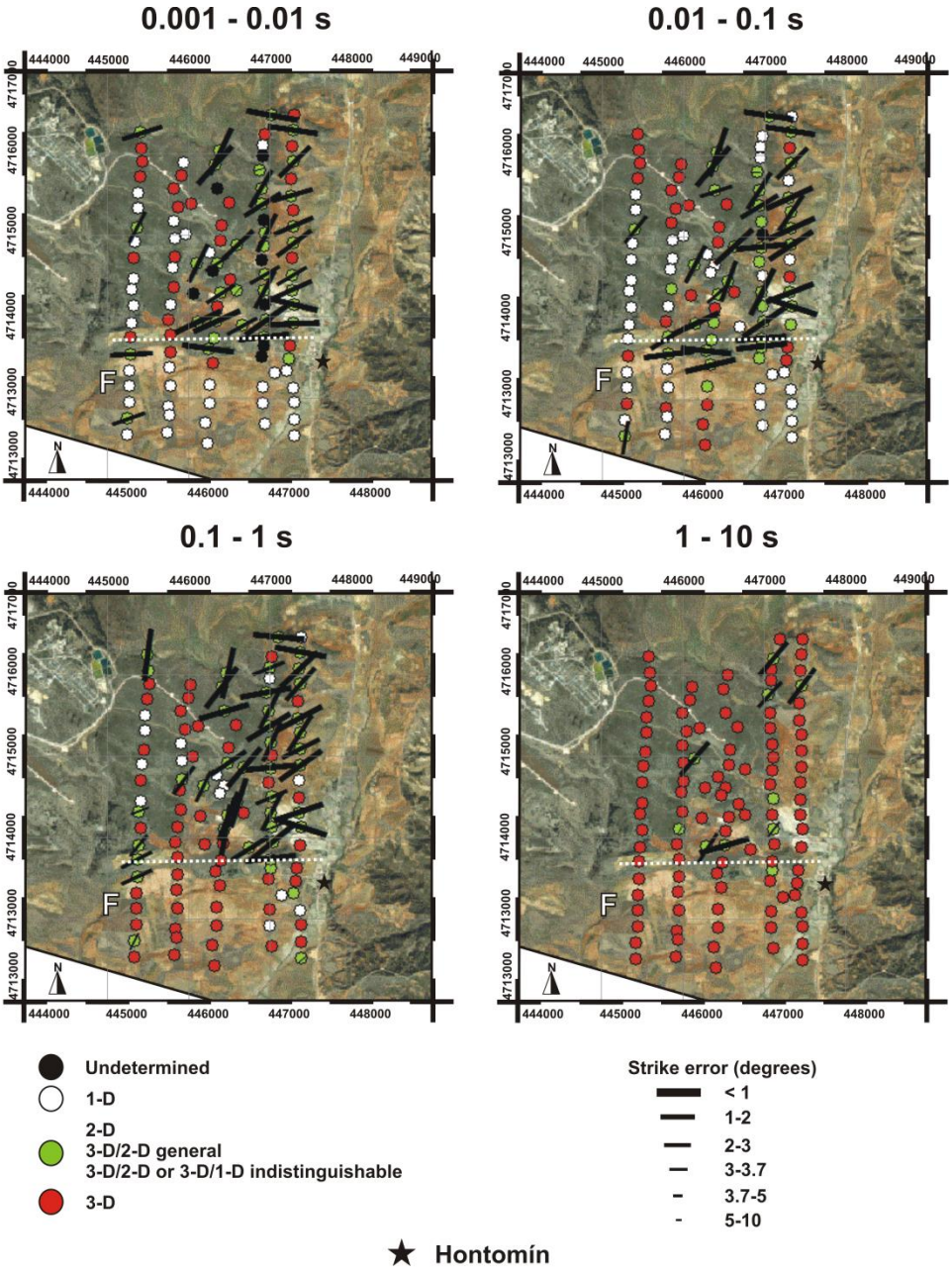

Fig. 3.9. Map of dimensionality analysis using the WALDIM code for four different period ranges: 0.001-0.01 s, 0.01-0.1 s, 0.1-1 s (primary reservoir-seal system) and 1-10 s. White dots infer 1D geoelectrical structures. Green dots group all inferred 2D cases: purely 2D case, 3D/2D general case with 2D structures affected by galvanic distortion and indistinguishable cases 3D/2D and 3D/1D, where the galvanic distortion makes impossible to determine the strike direction. Red dots designate the inferred 3D cases. Geoelectric strike is indicated by black lines of length inversely proportional to its error. The white dotted line shows the approximate north border of the F region. The location of Hontomín village is indicated (from Ogaya et al., 2012).

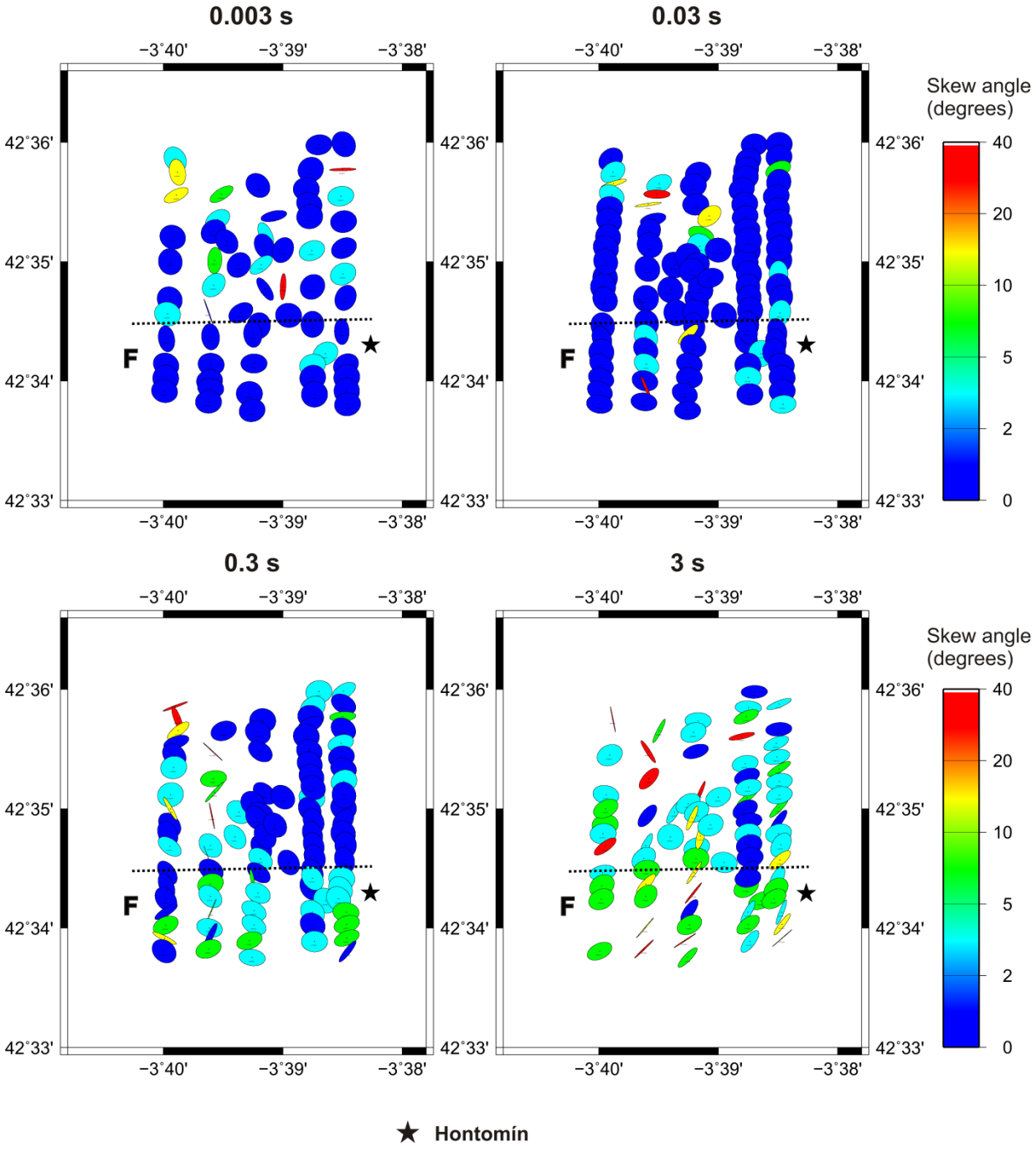

Fig. 3.10. Phase tensor at each site for four different periods: 0.003 s, 0.03 s, 0.3 and 3 s. The azimuth of the semi-major axis corresponds to the strike direction and the difference between the length of the semi-major and semi-minor axis gives an estimate of the dimensional complexity of the geoelectrical structure (i.e., a circle matches with the 1D case). The colour of the ellipse shows the skew angle β which indicates the 3D character of the resistivity distribution ($\beta = 0$ for a 2D case). As the plot corresponds to four single periods, some of the sites do not have data. The black dotted line shows the approximate north border of the F region. The location of Hontomín village is indicated (from Ogaya et al., 2012).

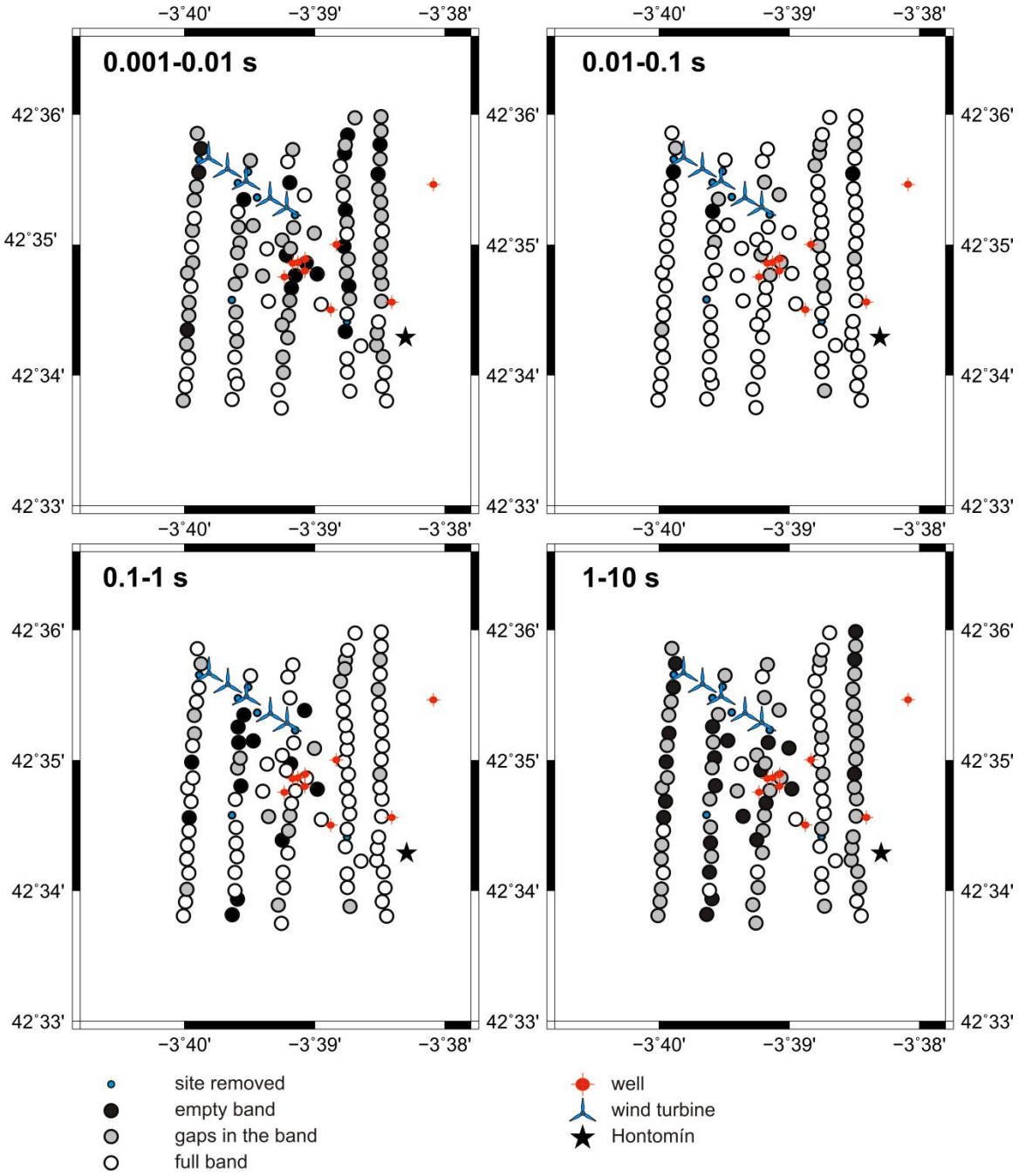

Fig. 3.11. Quality of the BBMT data. White big dots indicate sites with information in the whole range of periods whereas large black dots indicate sites without any data in the range. Intermediate cases with gaps in the period range are indicated by grey dots. Small blue dots represent the excluded noisy sites. The positions of the wells and the wind turbines, main EM noise source of the study area, are indicated (from Ogaya et al., 2014).

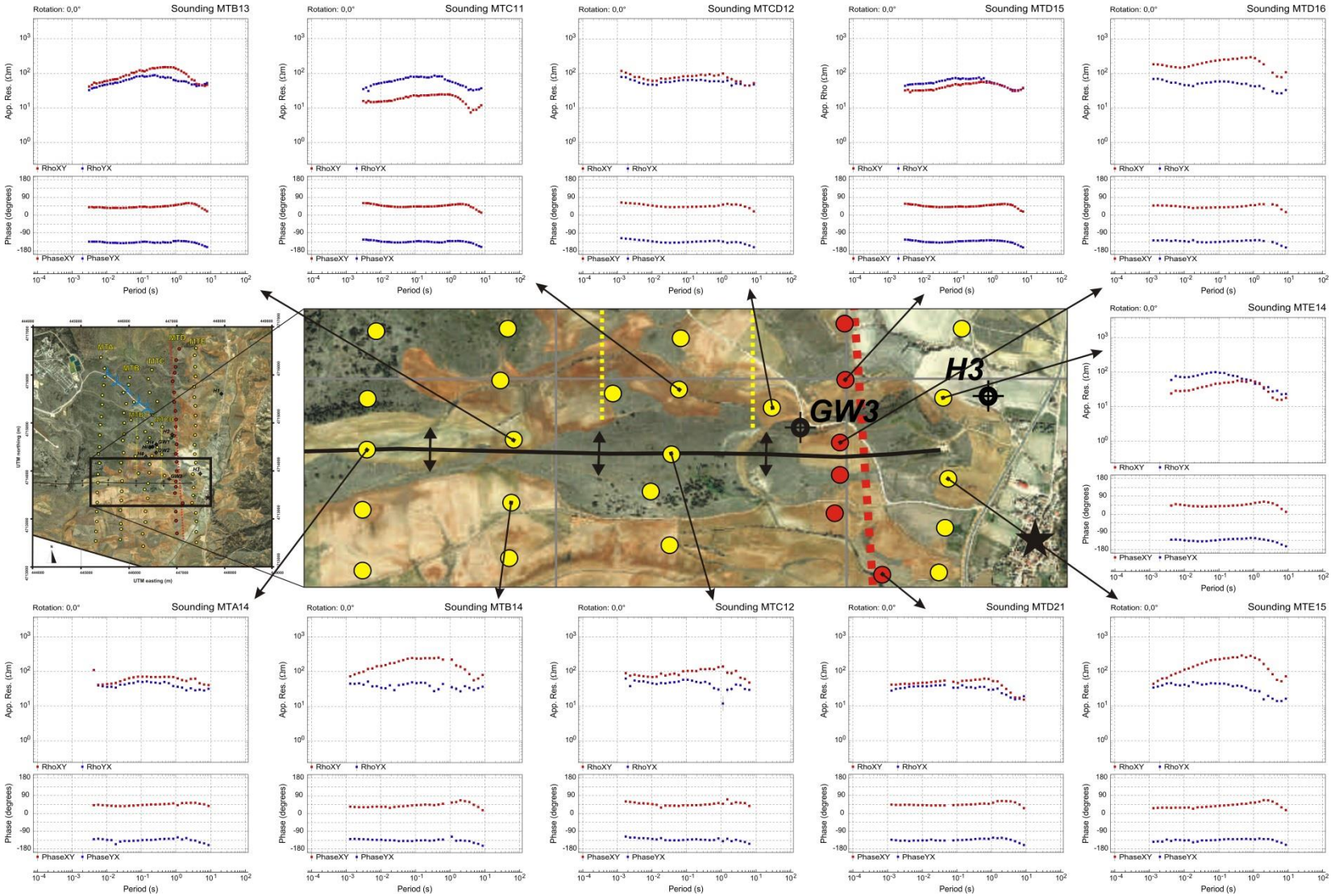

Fig. 3.12. Raw BBMT data at some sites along the north-border of the F fault region. The static shift in the data does not display any spatial consistency.

3.4.2. 3D inversion

3.4.2.1. General aspects (setup)

The work flow for 3D inversion consisted in improving a preliminary model provided by Geosystem (Mackie and Madden, 1993) (model Ø hereafter) (Fig. 3.13) using the ModEM code (Egbert and Kelbert, 2012). The WSINV3DMT of Siripunvaraporn et al. (2005) was also used to undertake some testing and to study the consistency of the models.

The topography of the study area is relatively gentle: elevations of the sites range from 919 to 1040 m.a.s.l. with the highest ones to the NW area (wind turbine region). As the target regions are located at depths below the surface no greater than 1800 m TVD, it was considered important to incorporate topography in the model. To avoid sharp boundaries between the air and earth cells, a smooth topography was implemented. The mesh was a 73x114x113-layer grid including topography for Geosystem and ModEM's cases (approximate model extension of 61x63x54 km^3). For WSINV3DMT's test cases, the mesh was a 52x68x60-layer grid but excluded topography (approximate model extension of 70x72x52 km^3).

Table 3.1. Specifications of the computers used.

Computer used	Specifications
Stokes (ICHEC)	SGI Altix ICE 8200EX, 320 compute nodes. Each compute node has two Intel (Westmere) Xeon E5650 hex-core processors and 24GB of RAM[1].
Mallet (DIAS)	Linux (CentOS), 64-bit, 2x6-core 3.33 GHz Intel (R) Xeon (R) X5680 (HT) processors, 48 GB memory
Lehmann (DIAS)	Linux (CentOS), 64-bit, 2x6-core 2.67 GHz Intel (R) Xeon (R) X5650 (HT) processors, 96 GB memory

[1] http://www.ichec.ie/infrastructure/stokes (visited August 2013).

The final inversions were undertaken using up to 29 periods of the full impedance tensor for the 102 BBMT sites in the range of 0.001 to 10 s. The error floor set was 5 % for the off-diagonal components (2.865 degrees for the phases and 10 % for apparent resistivity) and 10 % for the diagonal components (5.73 degrees and 20 % for the apparent resistivity). Missing data periods were interpolated and included, to avoid issues related to data set inhomogeneity, but had assigned large error bars.

The models were run on the Stokes cluster of the Irish Centre for High-End Computing (ICHEC) and on the Mallet and Lehmann clusters from Dublin Institute for Advanced Studies (DIAS) (see details in Table 3.1). The main aspects of the inversion process are detailed below.

3.4.2.2. Initial 3D inversion

Some initial inversions were run using ModEM and WSINV3DMT codes to validate the initial model Ø used and to assess its geological consistency. The initial model was for both cases a halfspace of 50 Ωm (as for Geosystem's inversion) which agrees with the average resistivity value of the H2 well log data (Fig. 2.5, Fig. 3.3). The inversions were undertaken using the full impedance tensor. However, in order to assure the convergence of these initial models, first iterations were undertaken using only 50 sites uniformly distributed and covering all the area, and the off-diagonal components only. Once the main structures were defined, more sites and components were included in the inversion. The greater was the amount of data incorporated to the inversion, the greater was the definition and resolution of the imaged structures. As was also seen in Ingham et al. (2009), the resistivity structure obtained from the first inversions with only a small number of sites was basically the same as that obtained with the whole data set, i.e., the existence of conductivity structures is a robust first-order feature in the data set. The data fit was superior doing a correction of the static shift prior to the inversion.

Figure 3.13 shows a section of the 3D model coincident with the MTD 2D profile modelled in Ogaya et al. (2013), for each of the three initial inversions from a uniform half space: (a) model Ø, (b) ModEM and (c) WSINV3DMT. The 3D models fit the data with an RMS

misfit of 1.36, 2.25 and 2.05, respectively. Despite the discrepancies related to topography, as it is included in (a) and (b) cases and not included in (c) case, the results from the initial 3D inversions confirmed that the three models are equivalent in the sense that all of them recovered the same main resistivity features. Moreover, the obtained electrical resistivity distribution resembles the one imaged in the previous 2D model (Ogaya et al., 2013) (Fig. 3.5), proving the geological consistence of the models. Thus, it was considered appropriate to define the model Ø as the initial model for the subsequent inversions with the ModEM code.

Nevertheless, comparing the obtained models to both the 2D model (Ogaya et al., 2013) (Fig. 3.5) and the resistivity well logs existing in the area (Fig. 2.11), it was noticed that none of the inversions recovered the resistive structure located at 1600 m TVD (R1 in Fig. 3.5). The models only imaged a slight increase in the resistivity at around 2200 m TVD (at -1200 m.a.s.l. for models with topography). This depth is indicated by a black dashed line in Fig. 3.13. Therefore, the fitting of the deepest part needed to be improved.

To address this issue, several inversions using the ModEM code were carried out for different period bands: the shortest periods were fit first and then the longest periods were inverted fixing the upper part of the model. The fit of the shortest periods was improved but improvement did not occur in the same manner with the longest ones. Through 3D synthetic studies it was corroborated that the primary system (primary reservoir and seal) MT responses were principally in the range of 0.1 to 1 s, as was previously affirmed in the 2D survey (Ogaya et al., 2013). In this way, the data collected at the Hontomín site were imaging the deepest resistive layer R1 but a non-constrained 3D inversion was unable to recover the layer. The inversion needed to be better constrained at depth in order to resolve the bottom of the main reservoir and recover the R1 layer.

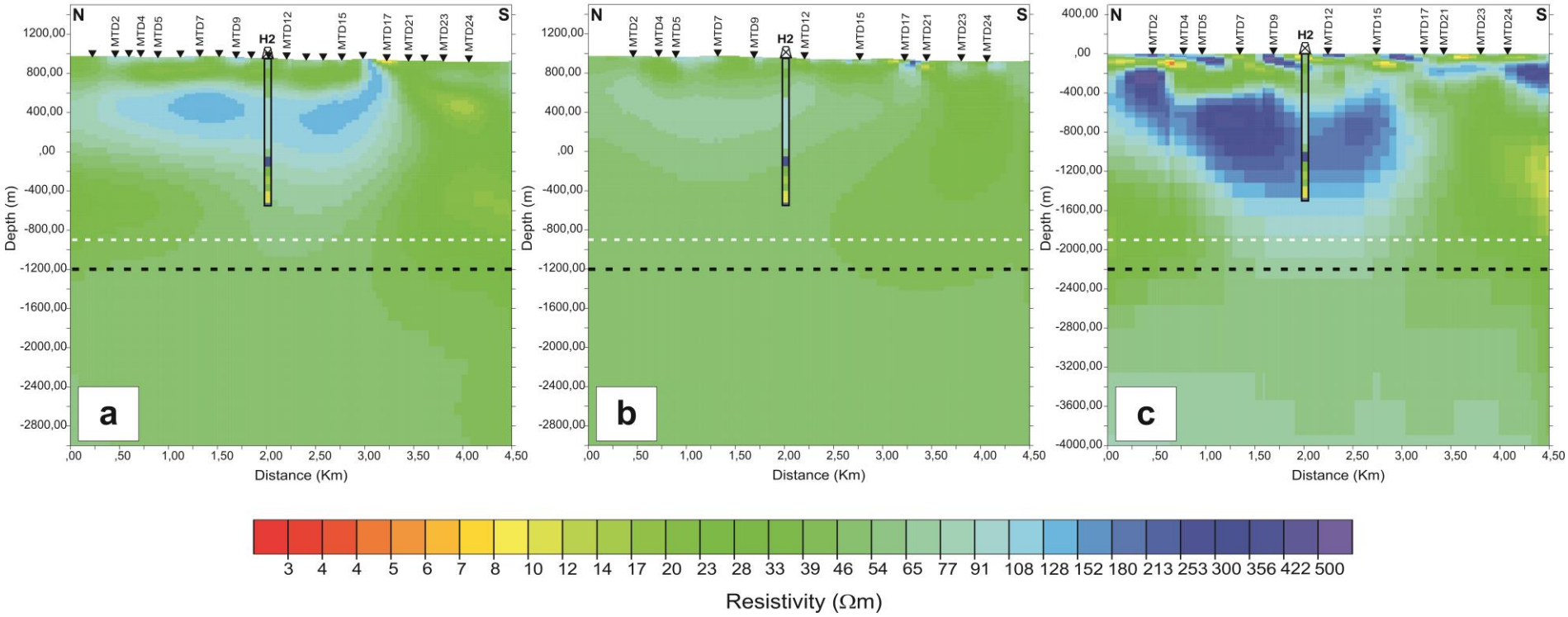

Fig. 3.13. Equivalent section to the MTD profile modelled in Ogaya et al. (2013) for each of the three initial inversions from a uniform 50 Ωm half space: (a) model Ø, (b) ModEM and (c) WSINV3DMT. The black dashed line indicates the approximate depth at which the resistivity increase is observed (depths are given in terms of m.a.s.l. in (a) and (b) cases, and in terms of TVD in (c) case). The white dashed line indicates the bottom of the 2D model shown in Fig. 3.5. Superimposed appears the 1D resistivity model of the H2 well (Fig. 2.5). BBMT sites are marked by black triangles (from Ogaya et al., 2014).

3.4.2.3. Final 3D resistivity model

For the final model, a more constrained inversion was carried out incorporating new information for the initial model. As has been discussed in other publications (e.g., Piña-Varas et al., 2013), an appropriate selection of the initial model is sometimes necessary to produce a meaningful model from a geological point of view. Thus, according to the existing resistivity-log data and the geoelectrical structure imaged in Ogaya et al. (2013) (Fig. 3.5), included in the initial model was a 25 Ωm conductive layer at approximately -220 m.a.s.l. and a resistive layer of 200 Ωm between -600 and -2000 m.a.s.l.. Data from the single LMT site were incorporated to the inversion (period range of 10 to 340 s) (see supplementary figure Fig. S12).

The final 3D model fits the data with an RMS misfit of 1.71 (Fig. 3.14). Figure 3.15 plots the responses of model Ø and the final model at site MTD7 showing the improvement of the fit at the longest periods and also for the diagonal components. The data and model responses at all sites are plotted in supplementary figures Figs. S1-S17. Comparisons between data and final model responses for the off-diagonal components are shown in Fig. 3.16 for the MTB profile and in Fig. 3.17 for the MTD profile (approximate limits of the URL). The misfits of the other profiles are shown in supplementary figures Figs. S18-S22. As is illustrated, the fit is satisfactory and the residuals are random and small; no significant feature in the data is unexplained.

The geoelectrical structure from near surface to -900 m.a.s.l. is an alternation of conductive and resistive layers (from bottom to top) (Fig. 3.14 and Fig. 3.18): R1, C1, R2 and C2. The location of the tops and bottoms of the layers, as well as their thicknesses, vary along each profile and between profiles. The southern part of the model (F region) is mostly conductive, being much more conductive in the eastern part than in the western part (Fig. 3.14 and Fig. 3.18). Through non-linear-sensitivity tests (e.g., Ledo and Jones, 2005) the most conductive eastern part of the F fault region (region 1 in Fig. 3.18b) and the continuity of the R2 layer in the southern part of the model (region 2 in Fig. 3.18b) were both evaluated. The tests consisted of replacing the resistivity values of these regions by their surrounding resistivity value: 30 Ωm for region 1 and 200 Ωm for region 2. In both cases, the difference between the responses of the final model and the modified one was greater

than the error floor imposed in the MT data for the inversion (results for region 1 in Fig. 3.19 and results for region 2 in Fig. 3.20). In this way, that conductive region 1 is required by sites located in the southern part of the model, mainly the ones in the MTD and MTE profiles, was corroborated. This conductive feature was also imaged in the 2D model (Fig. 3.18a). Results from region 2 indicate that there is no continuity of the R1 layer in the southern region of the model.

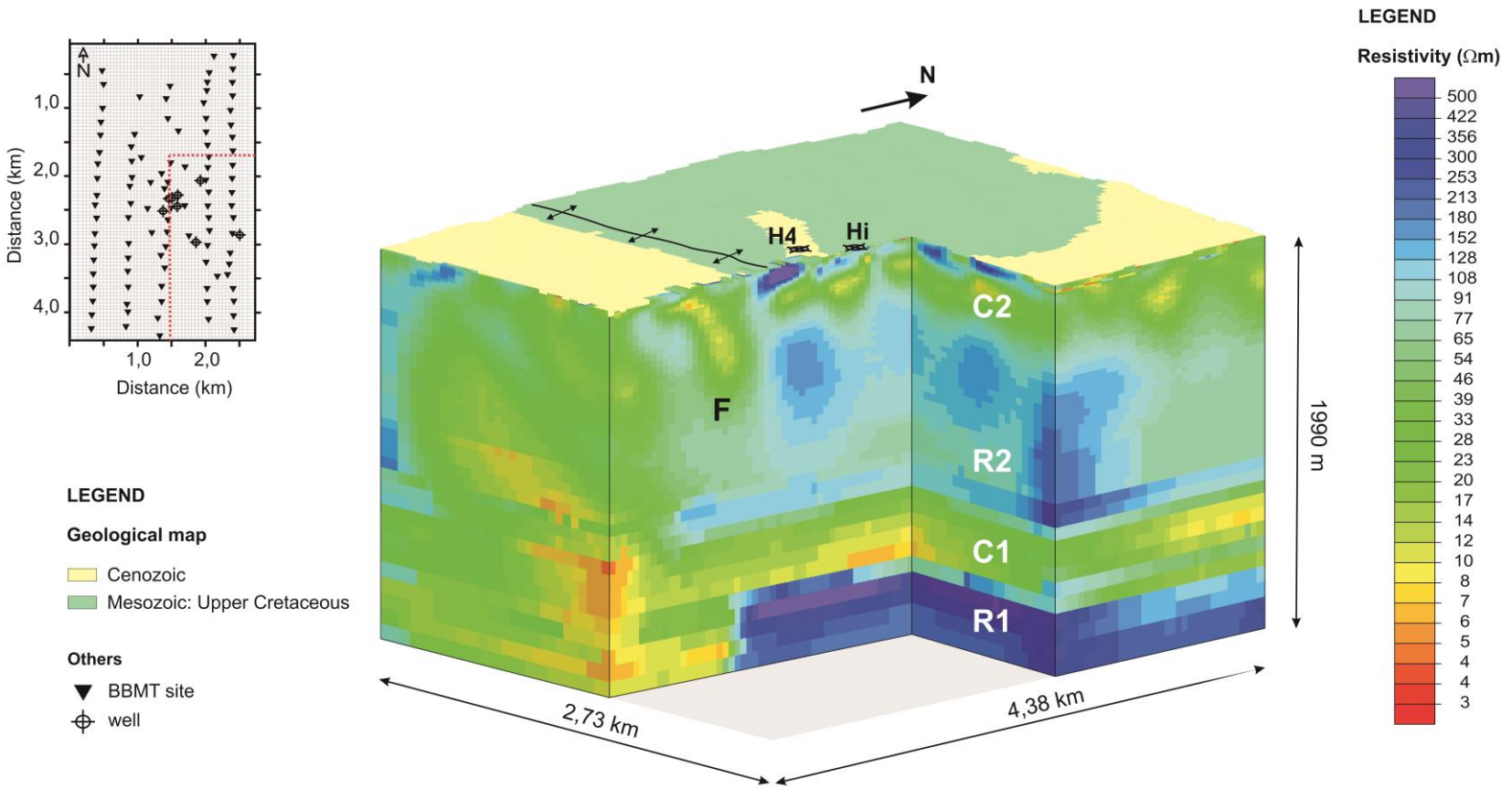

Fig. 3.14. Final 3D resistivity model of the Hontomín URL subsurface with a cutout (red dotted lines indicate the location of the NS and EW cuts). The geological map of the study area is shown and the positions of the wells and BBMT sites are marked. The F region and the main resistivity layers (R1, C1, R2 and C2) are also indicated. Depths are given in terms of m.a.s.l. (from Ogaya et al., 2014).

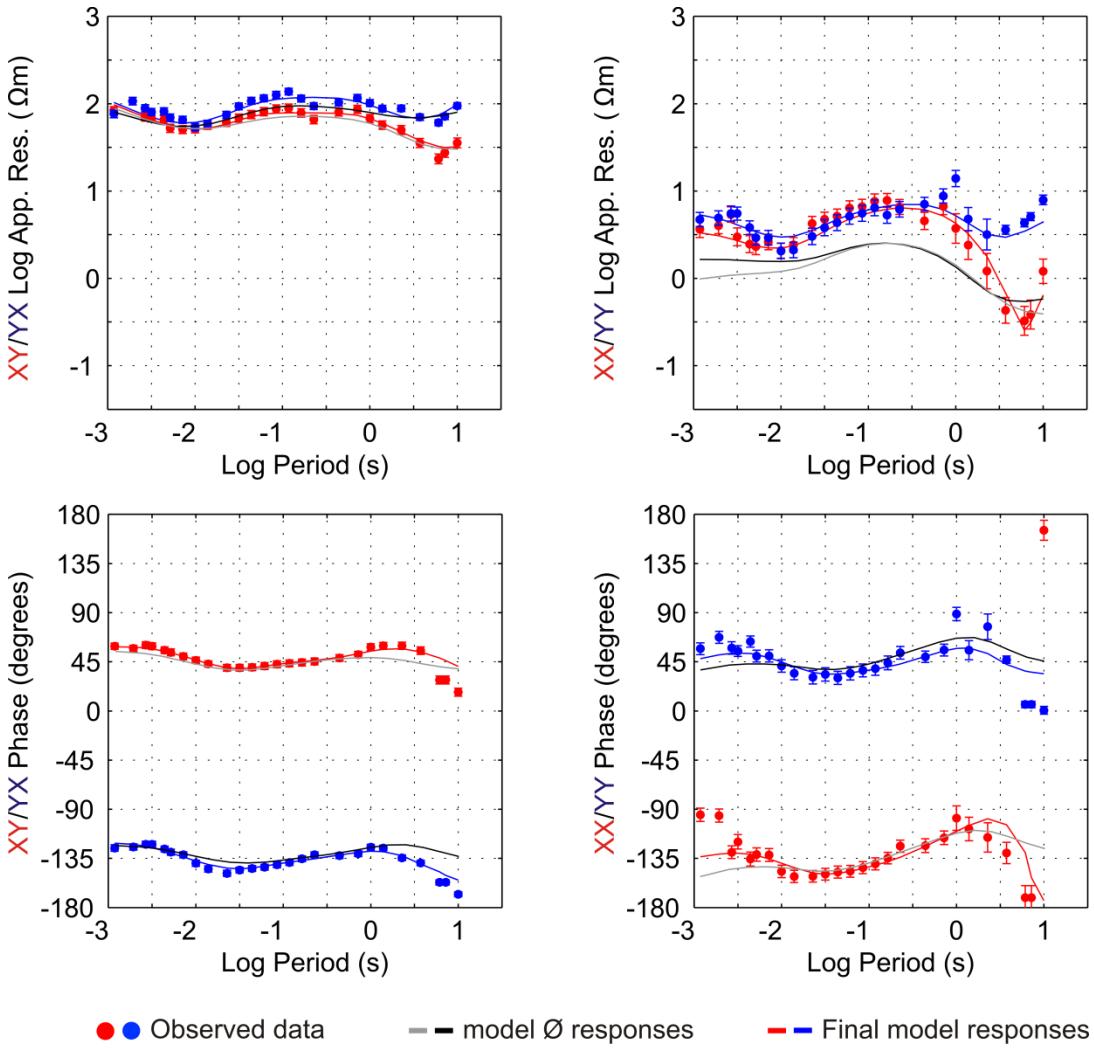

Fig. 3.15. Responses of the model Ø and the final 3D model at site MTD7 (from Ogaya et al., 2014).

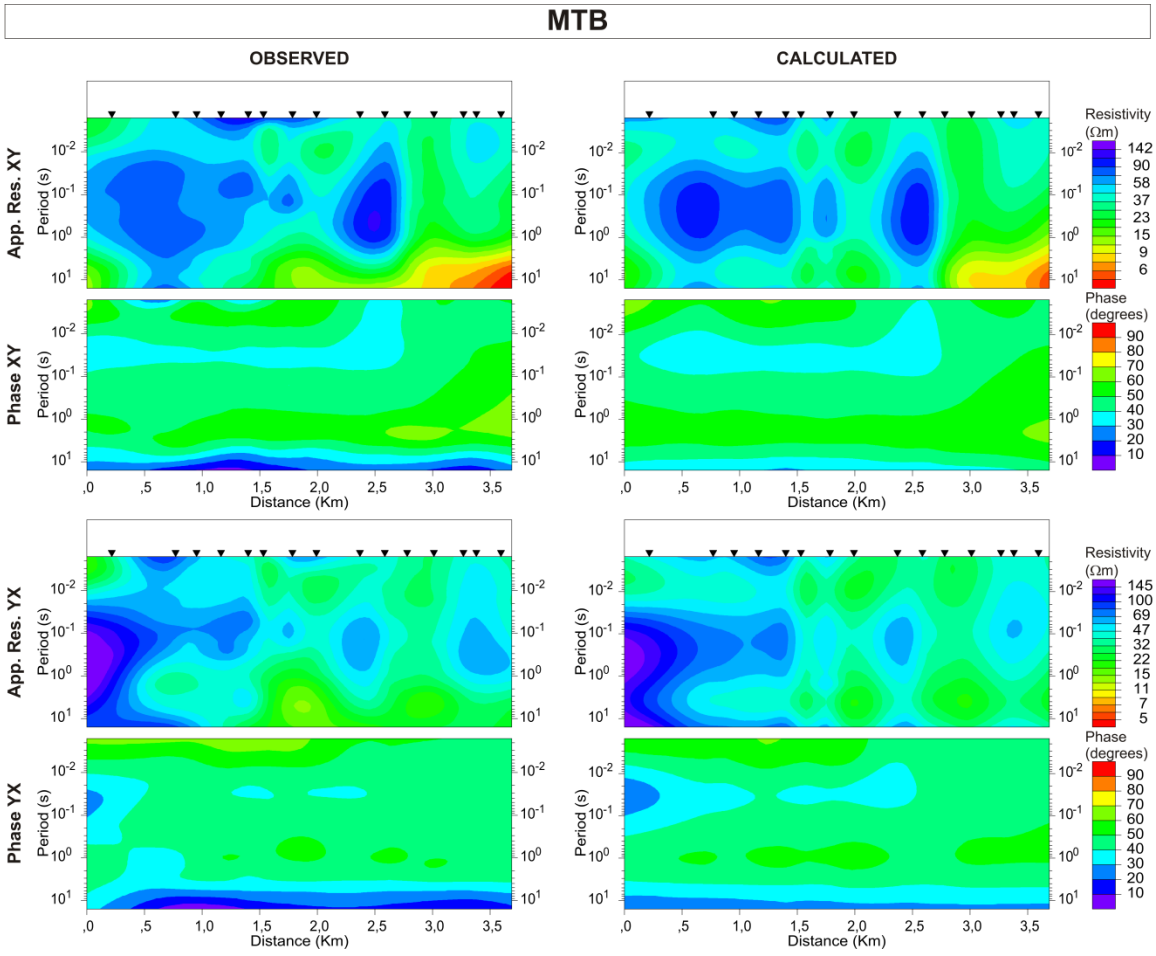

Fig. 3.16. Pseudosections of MTB profile: Apparent resistivity and phase for observed data and model responses. The positions of the BBMT sites are marked by black triangles (from Ogaya et al., 2014).

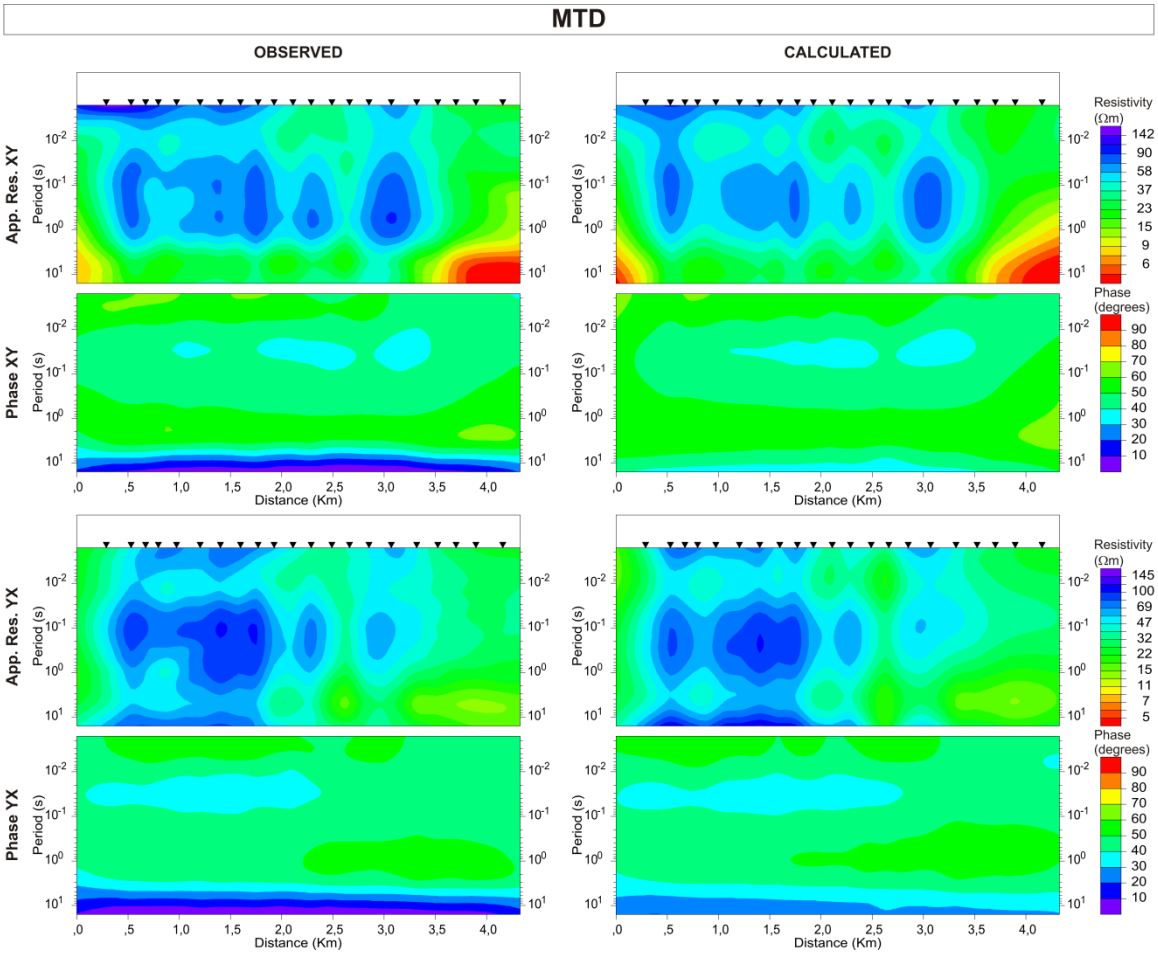

Fig. 3.17. Pseudosections of MTD profile: Apparent resistivity and phase for observed data and model responses. Differences with pseudosections shown in Fig. 3.6 and Fig. 3.7 are because the MT data were not rotated in this work. For the 2D survey (Ogaya et al., 2013) the data were rotated 4°W; the transverse magnetic (TM) mode was identified with XY polarisation and the transverse electric (TE) mode, with YX polarisation. The positions of the BBMT sites are marked by black triangles (from Ogaya et al., 2014).

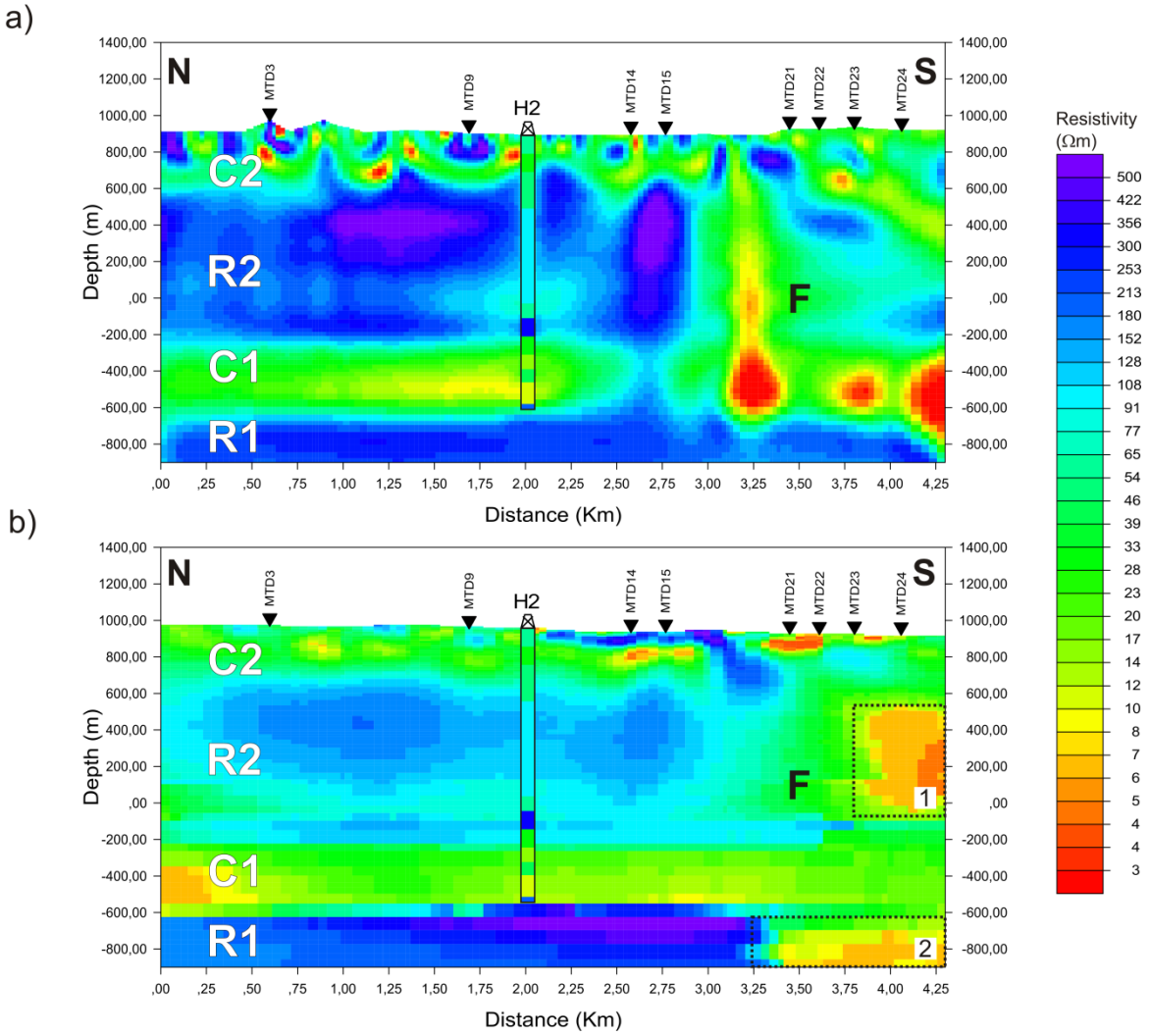

Fig. 3.18. (a) 2D model of the MTD profile (Fig. 3.5) (Ogaya et al., 2013) and (b) its equivalent section of the final 3D model. The same resistivity colour scale is used for both models. The main resistivity layers (R1, C1, R2 and C2) and the F region are indicated. The 1D model provided by the resistivity-log data of the H2 well is superimposed and some BBMT sites are marked by black triangles. The differences in topography are apparent because it was defined on a smoother surface for the 3D model. Black dotted lines indicate the two more conductive regions studied through non-linear-sensitivity tests: region 1 (Fig. 3.19) and region 2 (Fig. 3.20). Depths are given in terms of m.a.s.l. (from Ogaya et al., 2014).

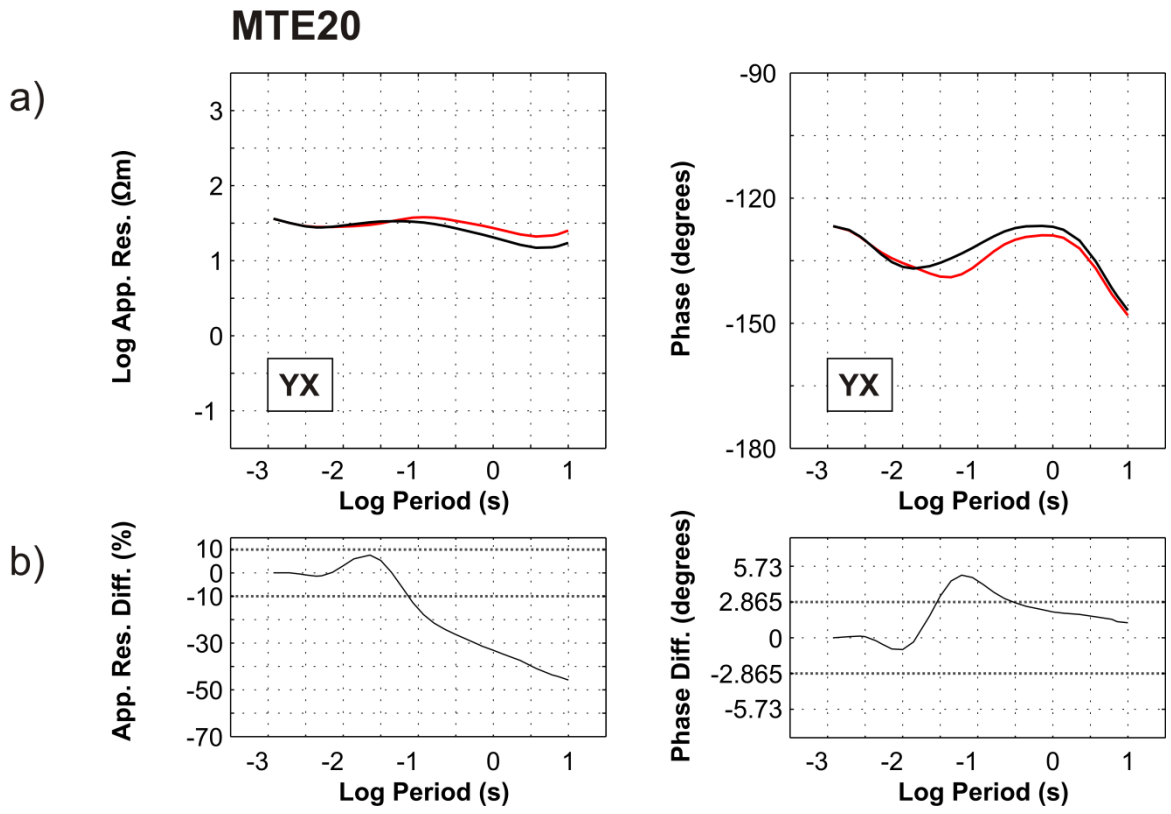

Fig. 3.19. Non-linear sensitivity test to study the conductive region 1 (indicated by black dotted lines in Fig. 3.18). (a) YX responses at site MTE20 of the final model (black) and the modified one (red) derived by replacing the resistivity values of the region 1 by 30 Ωm. (b) Difference between the YX apparent resistivity and phase responses. The differences are greater than the error floor imposed in the MT data for the inversion (10 % for the YX apparent resistivity and 2.865 degrees for the YX phases). Thus the more conductive region 1 is required by sites located in the southern region of the model, mainly the ones in the MTD and MTE profiles (from Ogaya et al., 2014).

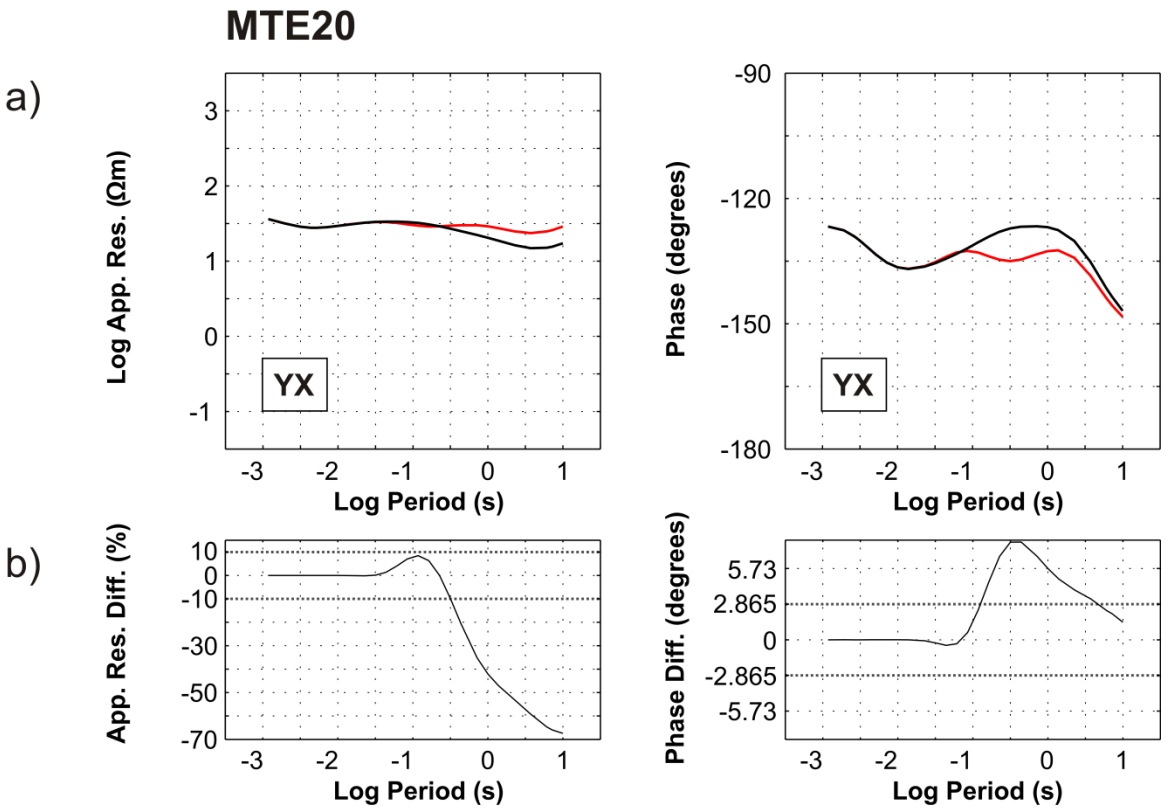

Fig. 3.20. Non-linear sensitivity test to study the conductive region 2 (indicated by black dotted lines in Fig. 3.18). (a) YX responses at site MTE20 of the final model (black) and the modified one (red) derived by replacing the resistivity values of the region 2 by 200 Ωm. (b) Difference between the YX apparent resistivity and phase responses. The differences are greater than the error floor imposed in the MT data for the inversion (10 % for the YX apparent resistivity and 2.865 degrees for the YX phases). Thereby, the results indicate that there is not a continuity of the R1 layer in the southern region of the model (from Ogaya et al., 2014).

3.4.3. Comparison with other EM studies

3.4.3.1. 2D model –MTD profile

Figure 3.18 shows the 2D model (Fig. 3.18a) and its equivalent section from the final 3D model (Fig. 3.18b). The topography of the two models is slightly different because of the smoothing of the 3D topography. The models are consistent and only relatively minor differences are apparent. In the 3D model: (i) R1 layer is more resistive under sites MTD14-MTD15 sites and does not extend under sites MTD21-MTD24; (ii) the most conductive portion of C1 layer is located in the north and there is no clear discontinuity of the layer because of a more resistive area under sites MTD14-MTD15; (iii) in general terms, R2 range of resistivity values is narrower, and (iv) C2 layer contains less scattered bodies. Regarding the F region, its structure is less well defined. In none of the models (neither the 2D nor the 3D) does the F fault seem to outcrop.

The major discrepancies are observed in the deepest structures (R1 and C1 layers). These structures are located in the period range of 0.1 to 10 s (Ogaya et al., 2013), which is the band where the data are not purely 2D and some 3D effects are observed (Ogaya et al., 2012) (Fig. 3.9 and Fig. 3.10). The observed differences are therefore concluded to be mainly because of two reasons: the greater smoothness of the 3D models, primarily due to larger cell sizes, and the possible influence of 3D structures in the previous 2D inversion.

3.4.3.2. Correlation with resistivity log data

Figure 3.21 shows three sections (profiles I, II and III) that cut the resulting 3D model by the existing H1-H4 wells. The simplified resistivity-log data of each well correlate well with the 3D model. The main differences are noticed for the H4 well, which is reasonable since its 1D resistivity model was derived from the H2 well log data and the H2 well is located 707 m away. Likewise, the structure of the upper part of the model agrees with the 1D model derived from the GW wells (section 2.3.1).

Correlation of the final 3D model with the resistivity log data show that discrepancies are not significant, neither for the H wells nor for the GW wells. Thus, for this case study, the correction of the static shift prior to the inversion provided accurate results.

3.4.4. 3D geoelectrical baseline model: interpretation and discussion

Resistive layer R1

R1 is the deepest layer imaged in the 3D model. Synthetic studies showed it was mainly sensed at periods around 1 s. The top of this layer is shallowest (-552 m.a.s.l.) in the centre-eastern part of the model under profiles MTC, MTD and MTE (Fig. 3.22h). The layer is also more resistive in that region (up to 1000 Ωm) (Fig. 3.21). There is not a continuity of this layer in the southern region of the model (Fig. 3.18).

The R1 layer is interpreted as the Upper Triassic unit (Anhydrite unit and Keuper facies) (Fig. 2.2). This unit is comprised of a succession of dolomites, anhydrites, and salt, which could explain its high resistivity. It is an impermeable layer that may constitute a suitable bottom seal for the main reservoir.

Conductive layer C1

The C1 layer is sensed in the period range of 0.1 to 1 s. The top of the layer is approximately at -216 m.a.s.l. (Fig. 3.22f). It has a dome-like structure with its axis situated in the injection area. The slope of the north flank is less steep and the dome seems to be elongated to the NW (Fig. 3.22f-g). The extension of the dome crest in this layer is about 1x1 km^2.

The C1 layer contains Jurassic rocks according to the well log data. The main reservoir and seal units are interpreted to be located within it. The saline aquifer (main reservoir), is linked to the most conductive region inside C1, a 7-14 Ωm region labelled as C1a in Fig. 3.22g. The top of this most conductive layer is located around -400 m.a.s.l.. The overlying primary seal also features a conductive behaviour, probably because of its marly composition (marlstones and black shales).

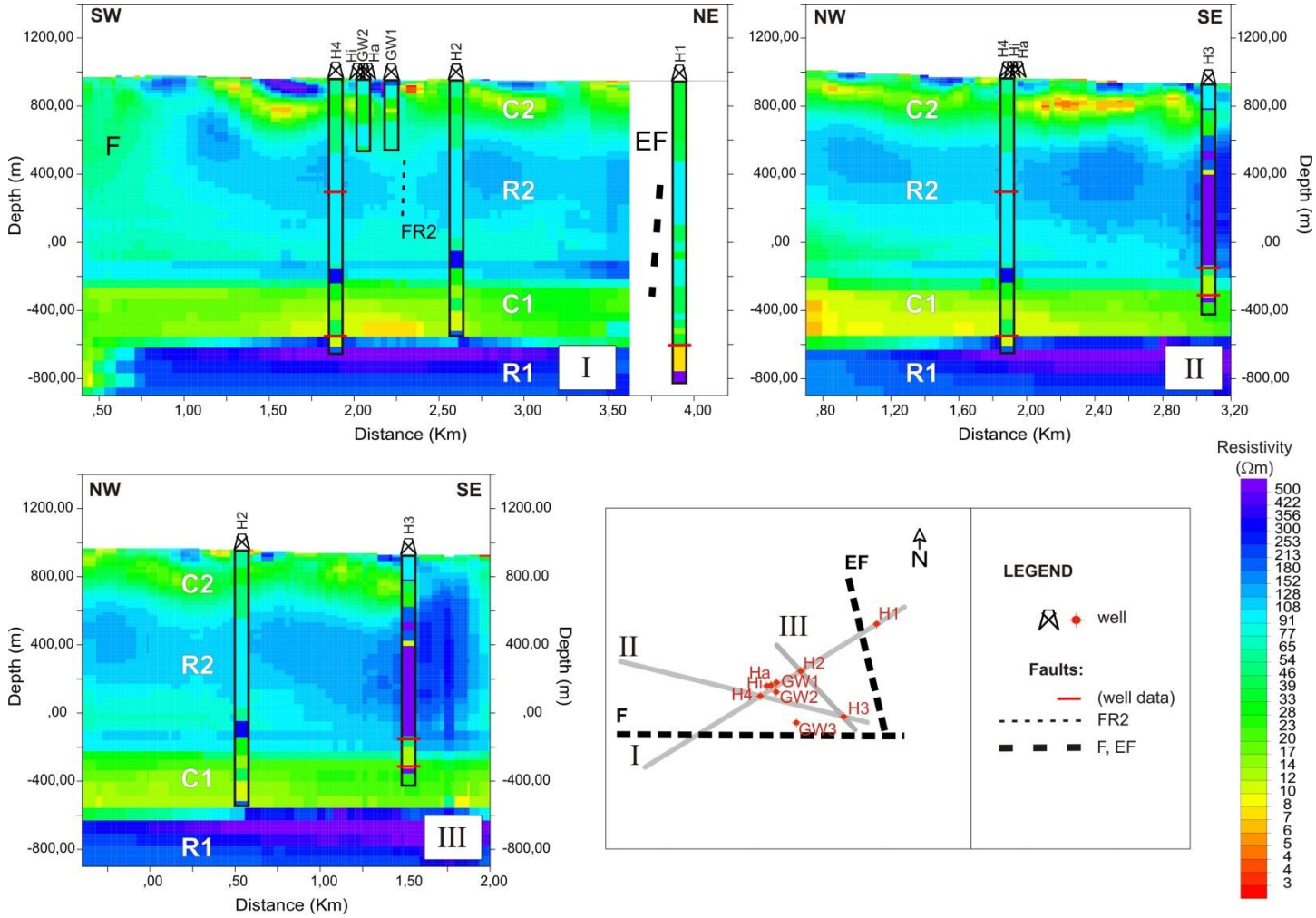

Fig. 3.21. Three sections (I, II and III) cutting the final 3D model by the existing wells. The main resistivity layers (R1, C1, R2 and C2) and the F and EF fault regions are indicated. Possible FR2 fracture regions and faults that cross the H wells according to well data, are also specified. The 1D resistivity models derived for each well (simplified resistivity-log data) are superimposed. Depths are given in terms of m.a.s.l. (from Ogaya et al., 2014).

Resistive layer R2

R2 is the thickest layer within the model. The top of this layer is shallower in the NW part of the model, where is located at approximately 700 m.a.s.l. (Fig. 3.22b). R2 is interpreted as the upper part of the Jurassic succession (upper part of the Dogger) and Upper Cretaceous (Weald and Purbeck facies and Escucha Fm.) units. The secondary reservoir-seal system would be contained within the R2 layer.

Analysing the layer from bottom to top, one can deduce the possible evolution of the dome structure.

(i) The bottom of the R2 layer is defined by a more resistive sub-layer of up to 130 Ωm and approximately 100 m thickness (Fig. 3.21 and Fig. 3.22e). According to the lithological information provided by the different wells, this increase in resistivity may be explained by a slightly increase on limestone content. In Fig. 3.22e is observed a less resistive region (below 100 Ωm) in the centre of R2 around the locations of the wells, which agrees with the dome-shape observed for the C1 layer.

(ii) Upwards, there exists a displacement of the dome crest to the east. At around 177 m.a.s.l. (Fig. 3.22d), the crest of the dome seems to be located in the surroundings of the H2 well.

(iii) In the overlying layers (Fig. 3.22c) the resistive dome (resistivity values up to 220 Ωm) migrates to the NW of the model. Consequently, at around 700 m.a.s.l. (Fig. 3.22b), the crest of the dome appears to be imaged in the NW region.

The R2 layer seems to be more conductive in the NW part of the model, but this aspect may not be due to a geological explanation. As the quality of the data was lower in that region (wind turbine region; see Fig. 3.11), the error bars were larger, thus resolution is poorer and naturally the smoothness constraint drives resistive regions to the lowest possible values they can take.

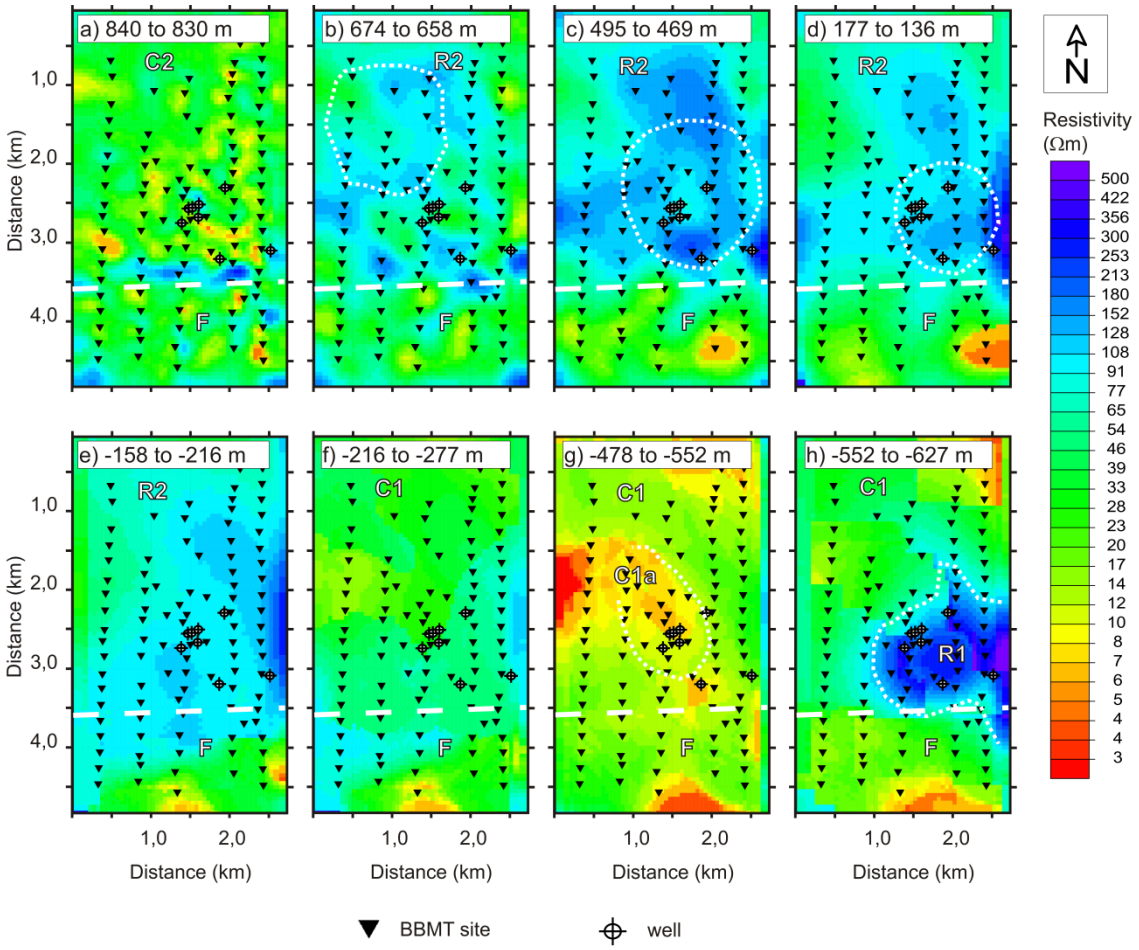

Fig. 3.22. Z-slices of the model from top (a) to bottom (h), with depths indicated in each sub-plot. The main resistivity layers (R1, C1, R2 and C2) and the F region are indicated. EW white dashed line indicates the approximate north-border of the F region. From bottom to top (depths given in terms of m.a.s.l.): h) top of the R1 layer; g) main reservoir C1a (saline aquifer); f) top of the C1 layer; e) bottom of the R2 layer; d), c) and b) evolution of the R2 layer's dome structure and a) C2 layer and bend of the R2 layer due to the presence of the F region. See text for more information about the white dotted lines (from Ogaya et al., 2014).

Conductive layer C2

The C2 layer is the surficial part of the model, i.e., the topmost layer. According to the well log data, it contains the Upper Cretaceous and Cenozoic materials that dominate the surface of the study area. The clear limit between the R2 and C2 layers (Fig. 3.18 and Fig. 3.21) is marked by the top of the Utrillas Fm.. The R2 layer emerges in C2 (EW resistive body in Fig. 3.22a) due to the presence of the F region.

Sets of faults

The 3D model shows the EW prolongation of the main fault F imaged in the previous 2D model (Fig. 3.5). The F fault region is associated to the strike-slip movement of the Ubierna fault (Tavani et al., 2011; Quintà, 2013). The EW white dashed line in Fig. 3.22 indicates the approximate north-border of that region. The F fault affects all layers of the model, although it does not outcrop at surface and its top is observed at C2 layer's depth (Fig. 3.22a). It is characterised by a conductive behaviour, and the resistivity distribution suggests conductive fluid circulation along the fracture region. It is more conductive in the eastern part of the study area (Fig. 3.18), whereas in the western part it is less conductive and seems to be imaged as different faults (Fig. 3.23). These branches of the F fault are also observable in some sections of the seismic volume (Alcalde et al., 2013b). Consequently, the western part seems to be more sealed than the eastern part. As was mentioned in the interpretation of the 2D model, hydrogeochemical studies of surface and spring waters in the surroundings of the Hontomín URL (Buil et al., 2012; Nisi et al., 2013) found that water samples acquired in the eastern part of the F fault region could be indicative of mixing processes between deep and shallow aquifers. However, Elío et al. (2013) investigated the CO_2 flux baseline in the soil-atmosphere interface at the Hontomín site, and those authors did not find any anomaly in the F region, neither in the western nor in the eastern part.

In the eastern part of the model (under sites on the MTE profile) a more resistive behaviour of the R2 layer is observed (resistivity values up to 300 Ωm) (see II and III profiles in Fig. 3.21). It could be due to a set of NS faults located in the east (called EF hereafter and indicated in Fig. 3.21) (Quintà, 2013; Alcalde et al., 2014). The EF faults are located

outside the modelled region, but their presence could explain the increase of the R2 layer thickness and resistivity in the eastern part of the model. The 1D resistivity model of the H3 well may differ from the others, because is affected by F and EF sets of faults.

Small resistivity variations (more conductive areas) observed within the R2 layer could be associated with a set of minor faults in the Dogger and Purbeck units (Quintà, 2013; Alcalde et al., 2014). Some of these faults are indicated by FR2 in Fig. 3.21 and Fig. 3.23. In Fig. 3.21 are also shown the faults that cross the H wells according to well data (Quintà, 2013).

Injection area

Figure 3.23 shows a NS and an EW section that cuts the 3D model by the injection well Hi. The smooth dome-like structure of the C1 and R2 layers with Hi located close to the axis is observed. The expected volume of CO_2 in the Hontomín URL (20 kilotons) is shown by a white square in Fig. 3.23. Since that the amount of CO_2 injection is small, none of the geoelectrical structures would appear to constitute a likely leakage pathway. However, according to the model, special attention should be paid to the possible FR2 faults neighbouring the Hi well and to the F fault (especially in the eastern part) during the monitoring of the URL.

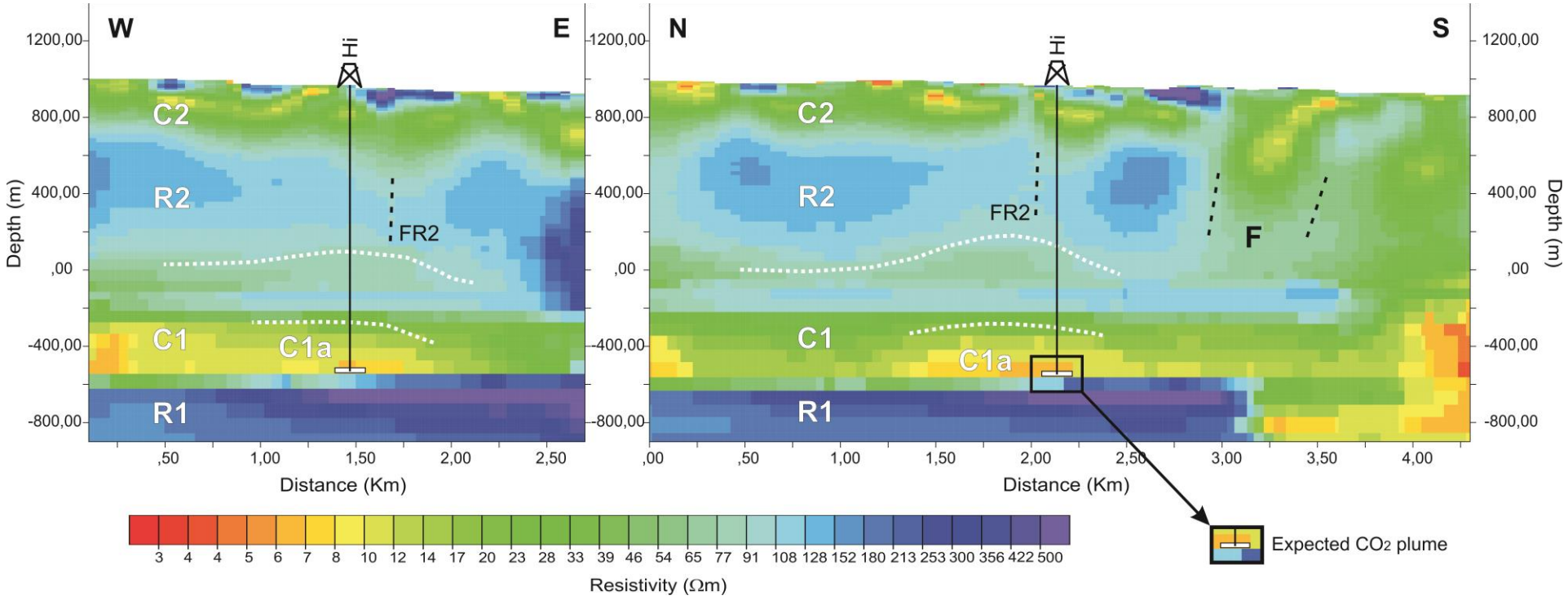

Fig. 3.23. NS and EW sections cutting the model by the injection well (Hi). The image shows the main resistivity layers (R1, C1, R2 and C2) and the F and FR2 fault regions. White dotted line traces the approximate soft dome-like structure of C1 and R2 layers. The expected CO_2 injection plume is indicated by a white square. Depths are given in terms of m.a.s.l. (from Ogaya et al., 2014).

3.4.5. Conclusions of the 3D survey

The obtained 3D resistivity model constitutes the geoelectrical baseline model of the Hontomín URL. It defines the subsurface structure in the pre-injection state and allows the detection of changes due to the CO_2 injection. It will be the reference model for the future EM monitoring experiments.

The thorough dimensionality analysis of the data revealed a predominant 3D behaviour of geoelectrical structures at periods longer than 0.1 s and showed that galvanic distortion in the study area is small (Ogaya et al., 2012). Accordingly, a 3D inversion of all BBMT data set was carried out so as not to misinterpret the geoelectrical structure of the site.

The multiple 3D inversions of the MT data combining different codes greatly enriched the inversion process. The 3D inversion made possible modelling the different 3D effects and improving the previous 2D model (Ogaya et al., 2013). The resistive layer located at approximately 1600 m TVD (under the conductive main reservoir-seal system) was only imaged when it was introduced into the initial model. Otherwise, the smoothness regularisation excluded exploration of that part of model space. The removal of static shifts in the data was effective within the 3D inversion process. Correlation with other geophysical data demonstrated that static shift correction did not imply a significant loss of information.

The final model contributes to a better understanding of the subsurface at the Hontomín site. In general, the electrical responses of each formation coincide with the ones imaged in the previous 2D model. However, the 3D model provides an important 3D spatial characterisation of the different units as well as images the prolongation of the main fault F. In this way, it is possible to determine the possible leakage pathway and design the monitoring setup according to the site requirements. Special attention needs to be paid to the possible FR2 faults neighbouring the Hi well, and to the eastern part of the F fault since the resistivity distribution there suggests conductive fluid circulation along this part of the fault.

3.5. Correlation with other geophysical data

3.5.1. Hi and Ha Wells

The drilling of Hi and Ha wells was completed at the end of 2013. The resistivity log data of both wells were correlated with the 3D geoelectrical model of the Hontomín URL. The log data used combined the following measures: Deep Induction Standard Processed Resistivity (ILD), Long Normal Resistivity (LNR) and Normal Resistivity with electrode spacing of 64 inches (R64).

Figure 3.24 shows the location of Hi and Ha wells in the 3D mesh. The log data of each well were compared to the 1D model provided by the column of the 3D geoelectrical model located at the position of the well. In this way, Hi well resistivity log data were spatially related to the 1D model obtained at position 1 (Fig. 3.25). Since Ha well is located between two cells, its resistivity log data were related to the 1D models obtained at positions 2 and 3 (Fig. 3.26). The three 1D models (Fig. 3.25 and Fig. 3.26) are quite similar because they belonged to adjacent cells of the 3D mesh (Fig. 3.24). For the Ha well (Fig. 3.26), the geoelectrical model at position 3 (red model) shows a superior fit of the upper layers than that at position 2 (blue model). For depths above 500 m TVD, both models are similar and almost overlap each other.

The resistivity log data of the Hi and Ha wells (Fig. 3.25 and Fig. 3.26) show comparable geoelectrical patterns and agree with the 1D models provided by the geoelectrical baseline model of the site. The MT responses at surface are similar, and only small differences are observed. Thus, the resistivity structure of both wells is well recovered by the 3D model. These results constitute a first approximated correlation. The deviation of the wells (no more than 3 degrees in Hi well and around 12 degrees in Ha well) should also be taken into account in order to carry out a more accurate comparison.

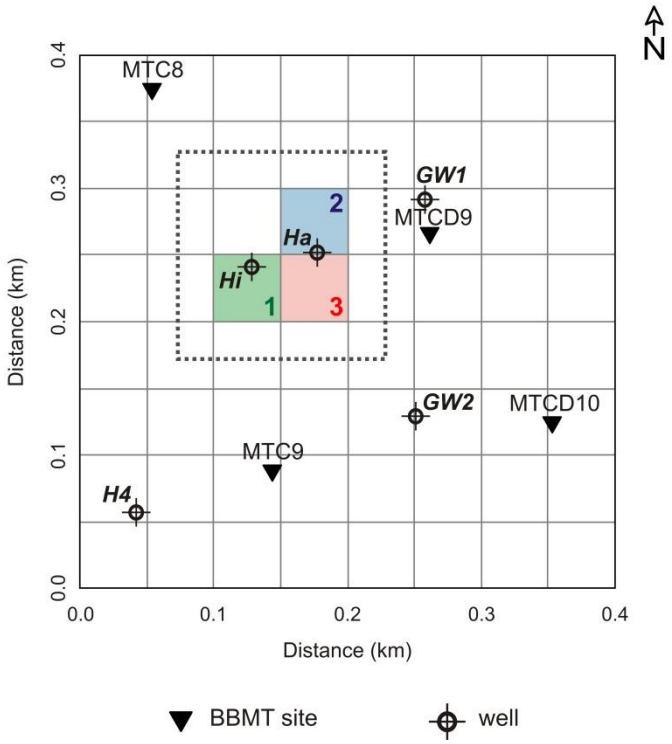

Fig. 3.24. Fragment of the 3D model mesh showing Hi and Ha wells. Position of the nearest wells and BBMT sites are also indicated. Small square with dotted line marked the zoom of the area shown in Fig. 3.25 and in Fig. 3.26.

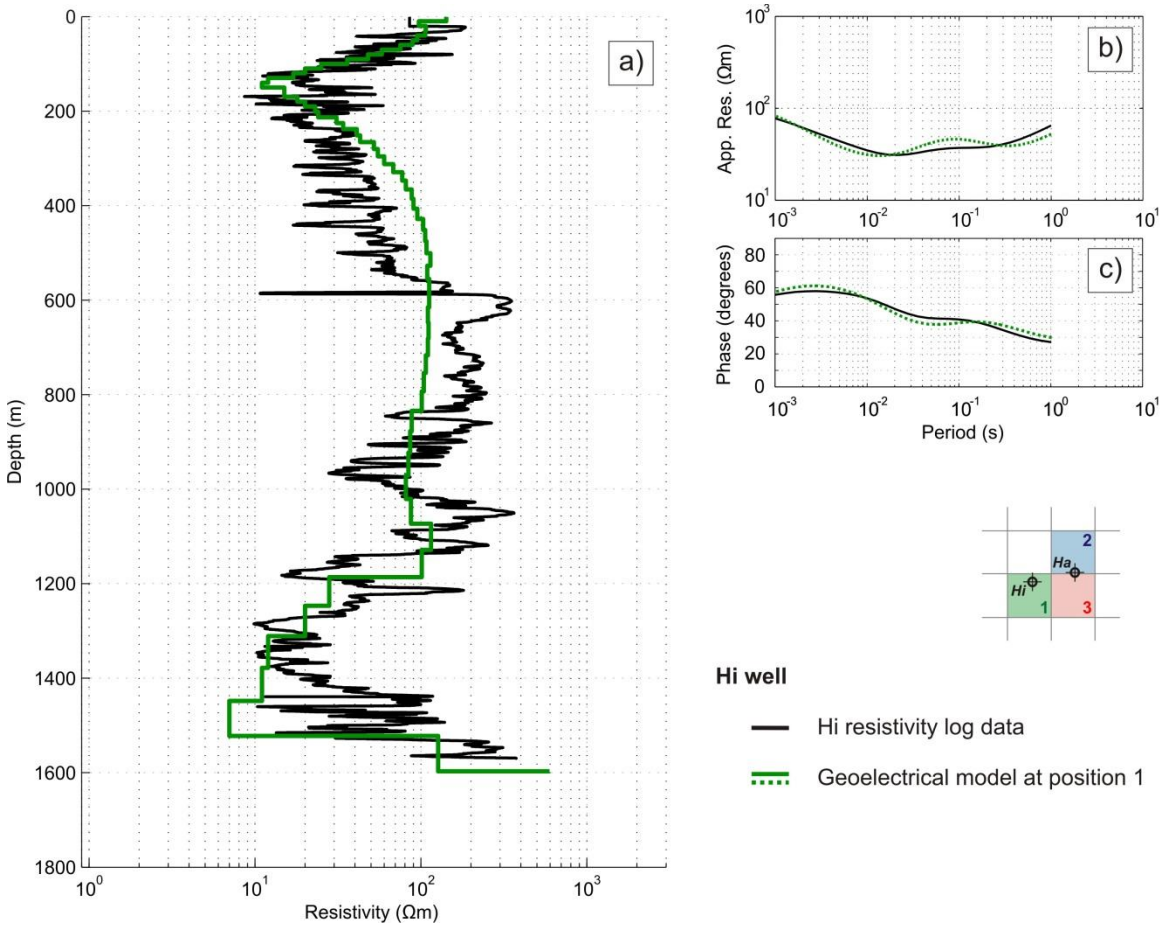

Fig. 3.25. Hi well. (a) In black, Hi resistivity log data and in green, the geoelectrical model at position 1 (1D model provided by the column of the 3D geoelectrical model at position 1). (b) Apparent resistivity and (c) phase responses on the surface for both 1D models: Hi resistivity log data in black and 1D column of the geoelectrical model in green dotted line.

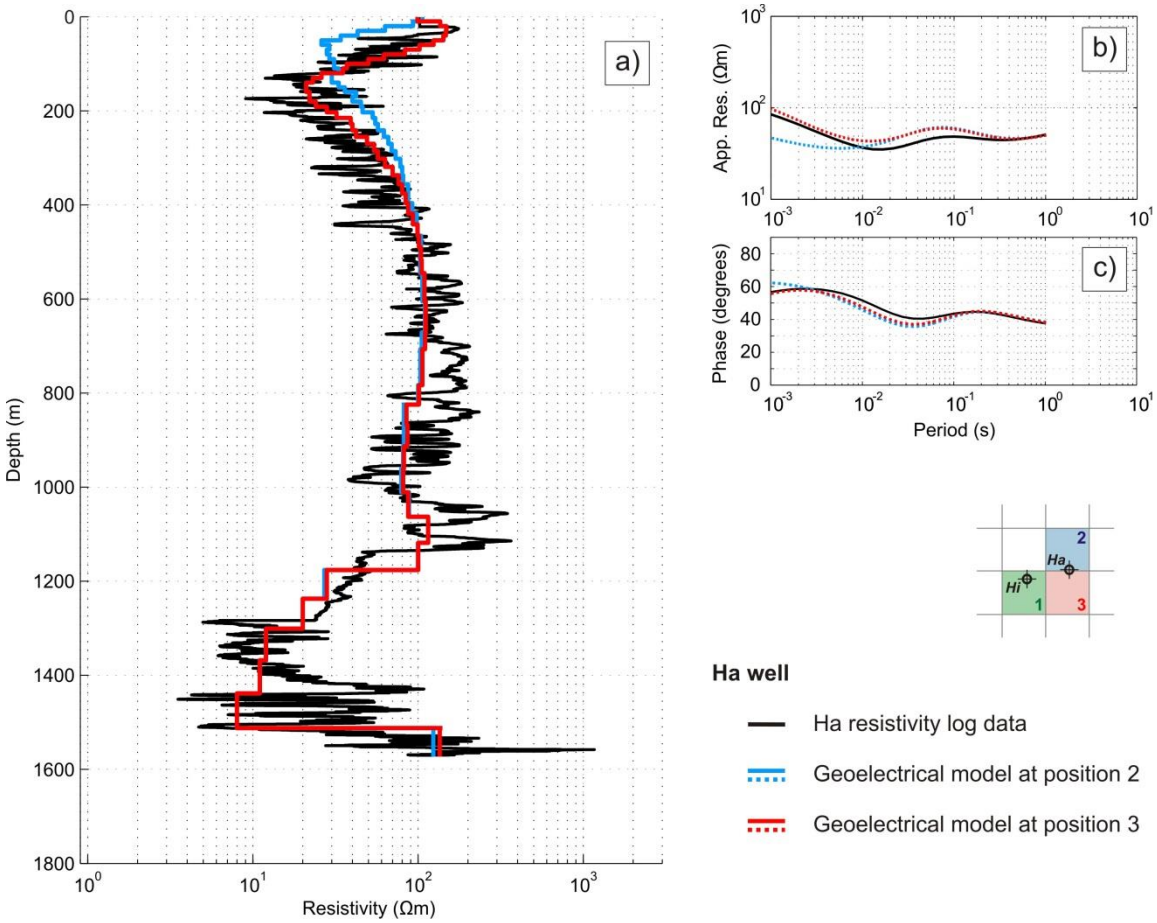

Fig. .3.26. Ha well. (a) In black, Ha resistivity log data; in blue, geoelectrical model at position 2 (1D model provided by the column of the 3D geoelectrical model at position 2), and in red, geoelectrical model at position 3 (1D model provided by the column of the 3D geoelectrical model at position 3). (b) Apparent resistivity and (c) phase responses on the surface for the three models: Hi resistivity log data in black, 1D column of the geoelectrical model at position 2 in blue dotted line and 1D column of the geoelectrical model at position 3 in red dotted line. The geoelectrical model at position 3 (red model) offers a better fit of the upper layers than the geoelectrical model at position 2 (blue model). For depths above 500 m TVD, both models almost overlap each other.

3.5.2. 3D seismics

Three-dimensional reflection seismic data were acquired at the Hontomín URL in Summer 2010 (Alcalde et al., 2013a). The survey characterised 36 km^2 of the study area, including part of the area covered by the MT 3D survey.

The seismic results were correlated with the 3D geoelectrical model of the site in order to compare the observed structures and the different sets of faults. With this aim, two clear surfaces were evaluated: the top of the Anhydrite unit, which represents the bottom of the primary reservoir (Fig. 2.2), and the top of the Weald, which is the top of the secondary reservoir-seal system (Fig. 2.2). Two sections of the structural model interpreted from seismics (α and β profiles in Alcalde et al., 2014) coincident with profiles I and III of the 3D resistivity model (Fig. 3.21) were also compared.

The seismic images included in this section contain an interpretation of the tops of the main units and faults (Alcalde et al., 2014). The eight horizons mapped through-out the seismic volume are: top Utrillas (KU5); top Escucha (KE2); top Weald (KW3); top Purbeck (JKP2); top Dogger (JD4); top Marly Lias (Seal) (LM5); top Carbonatic Lias (Reservoir) (LC4) and top Anhydrite unit (UA). Likewise, the four sets of faults indicated are: (i) set X faults, active during the sedimentation of the Lower Lias; (ii) set N faults, active during the sedimentation of the Dogger and Purbeck units; and the major (iii) set E and (iv) set S faults, reactivated during the Alpine compressional stage and associated with the Ubierna Fault.

In the 3D geoelectrical model, the resistive layer R1 is interpreted as the Upper Triassic Unit (Fig. 2.2), since the succession of dolomites, anhydrites and salt might explain the observed resistivity increase. Accordingly, the z-slice of the geoelectrical model located at -552 to -627 m.a.s.l. (Fig. 3.22h) was likened with a time slice from the migrated seismic volume at 1000 ms (one of the time slices where the Anhydrite unit top surface is mapped) (Fig. 3.27). Similarly, Fig. 3.28 shows the correlation of the z-slice with the depth map of the top of the Anhydrite unit. Both figures displayed superimposed the features of the geoelectrical model highlighted in Fig. 3.22h: the limits of the more resistive layer R1 at -552 to -627 m.a.s.l. and the north-border of the F fault region. The results proved that the top of the resistive layer R1 is coherent with the depth map of the Anhydrite unit top (Fig.

3.28). The 3D inversion of the MT data demonstrated good recover of the bottom resistive layer without constraining the inversion using seismic data. In general, the morphology described by the seismic horizons interpreted in Fig. 3.27 is consistent with the observed resistivity distribution (Fig. 3.22), even taking into account that the seismic image is in time. In reference to the fault sets, the F fault region match with set S faults (Fig. 3.27 and Fig. 3.28).

The dome structure imaged in the 3D geoelectrical model (Fig. 3.22) was also compared with the structural model interpreted from seismics (Quintà, 2013; Alcalde et al., 2014). The correlation with the top of the Weald (top of the secondary reservoir-seal system) is shown in Fig. 3.29. In this figure, the features of the geoelectrical model highlighted in Fig. 3.22d appear superimposed: the limits of the more resistive region of layer R2 at 177 to 136 m.a.s.l. (identified as the dome crest at that depth), and the north-border of the F fault region. The results demonstrated that the resistivity distribution imaged in Fig. 3.22d is consistent with the depth map of the top Weald surface, and that the F fault region is coincident with S-faults.

Finally, profile I and profile III (Fig. 3.21), that cut the 3D geoelectrical model by the existing wells, were compared with their equivalents in the structural model interpreted from the seismic volume. Figure 3.30 and Fig. 3.31 display the two geoelectrical sections with the top of the different units and the main fault sets superimposed. Sets S, E and N faults can be correlated to F, EF and FR2 fault regions in the 3D geoelectrical model, respectively. In the geoelectrical model, the western part of the F fault region is less conductive than the eastern part, and seems to be imaged as different faults (Fig. 3.23). The seismic data image the F fault region as a system of fractures (set S) (Fig. 3.27-3.30).

In general, the top of the layers, as well as the interpreted sets of faults, are explained reasonably well by the obtained geoelectrical structure. The presence of the F fault (with a conductive fluid circulation probably associated) is observed to highly alter the geoelectrical behaviour of the different units.

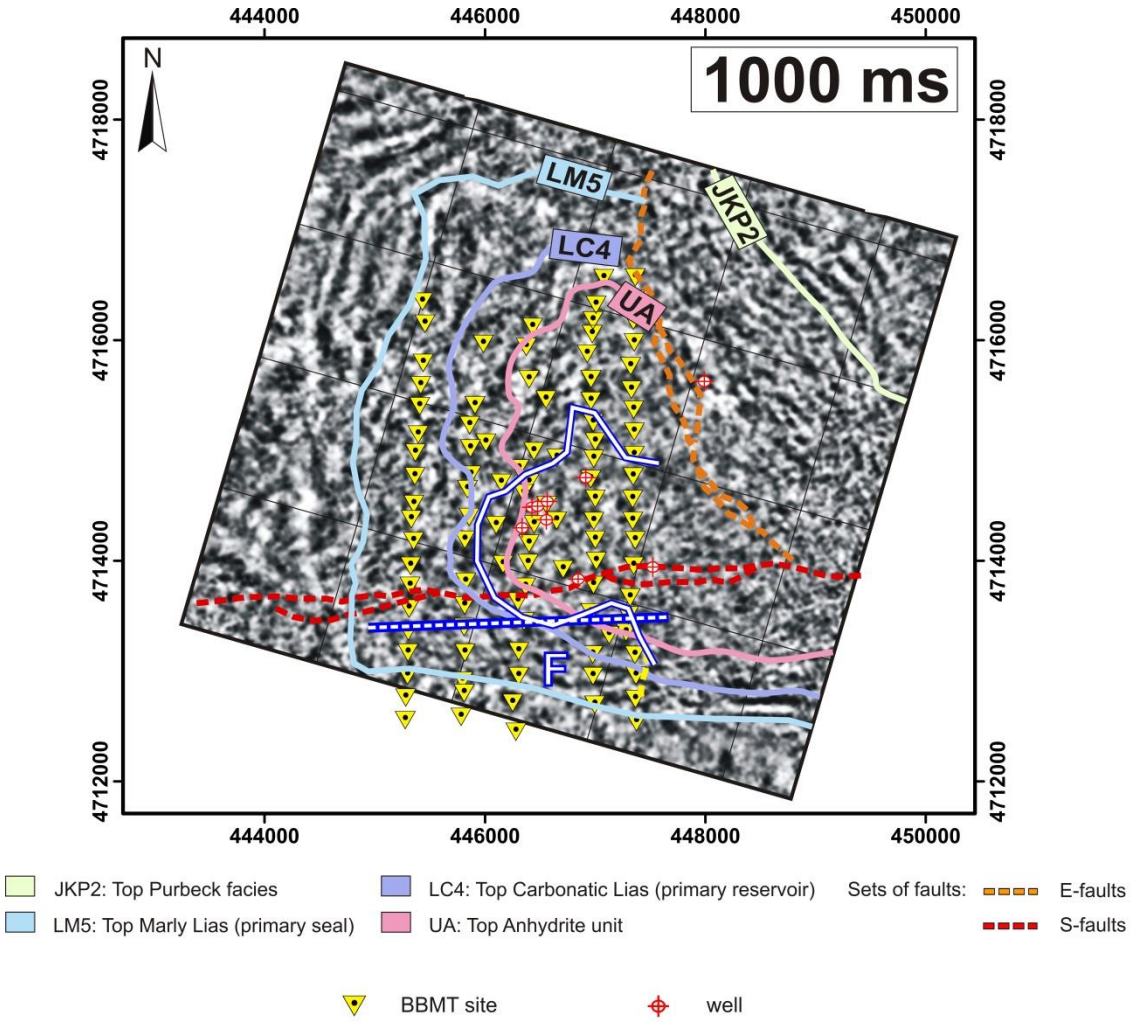

Fig. 3.27. Time slice from the migrated seismic volume at 1000 ms with the main horizons (continuous lines) and fault sets (dashed lines) interpreted. Superimposed in white and dark blue, the features of the geoelectrical model highlighted in Fig. 3.22h are indicated: the limits of the top of the more resistive layer R1 at -552 to -627 m.a.s.l. and the north-border of the F fault region (modified from Alcalde et al., 2014).

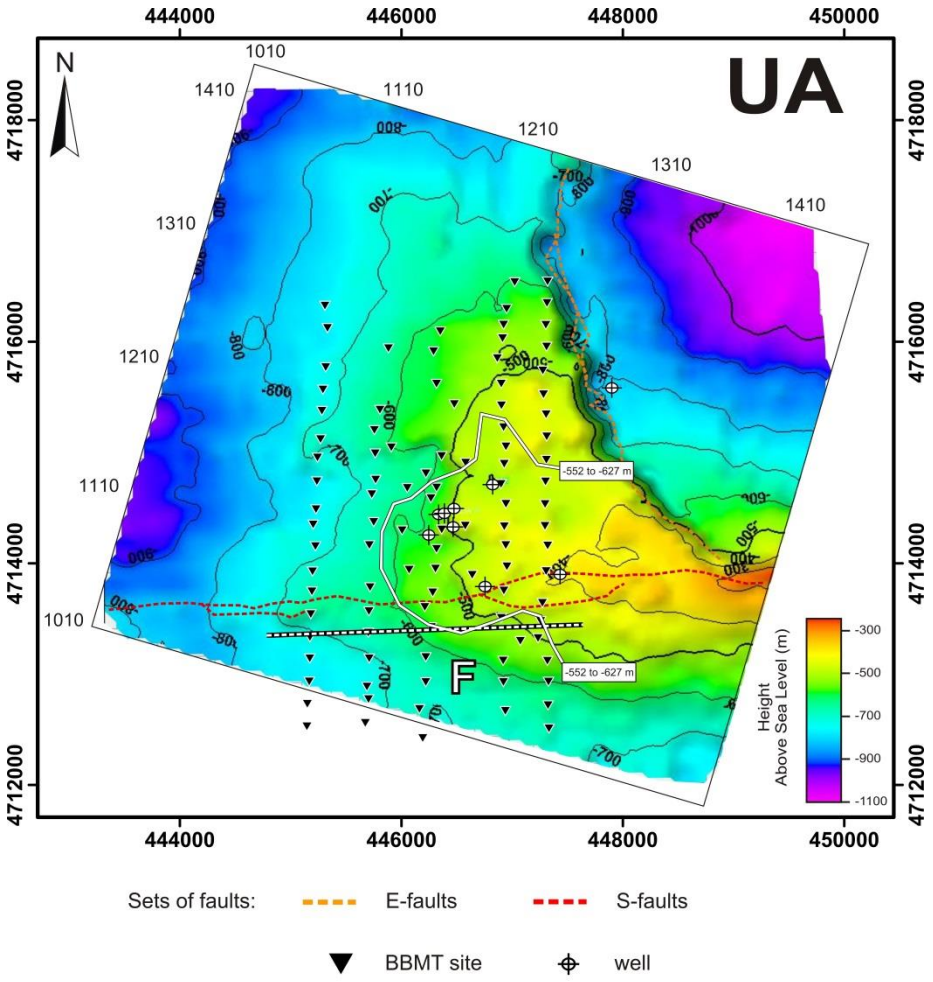

Fig. 3.28. Depth map of the top of the Anhydrite unit (UA) according to the seismic volume interpretation. Dashed lines represent the interpreted E-fault and S-fault sets. Superimposed in white, the features of the geoelectrical model highlighted in Fig. 3.22h are indicated: the limits of the top of the more resistive layer R1 at -552 to -627 m.a.s.l. and the north-border of the F fault region. The depth range at which the R1 top is observed, is indicated (modified from Alcalde et al., 2014).

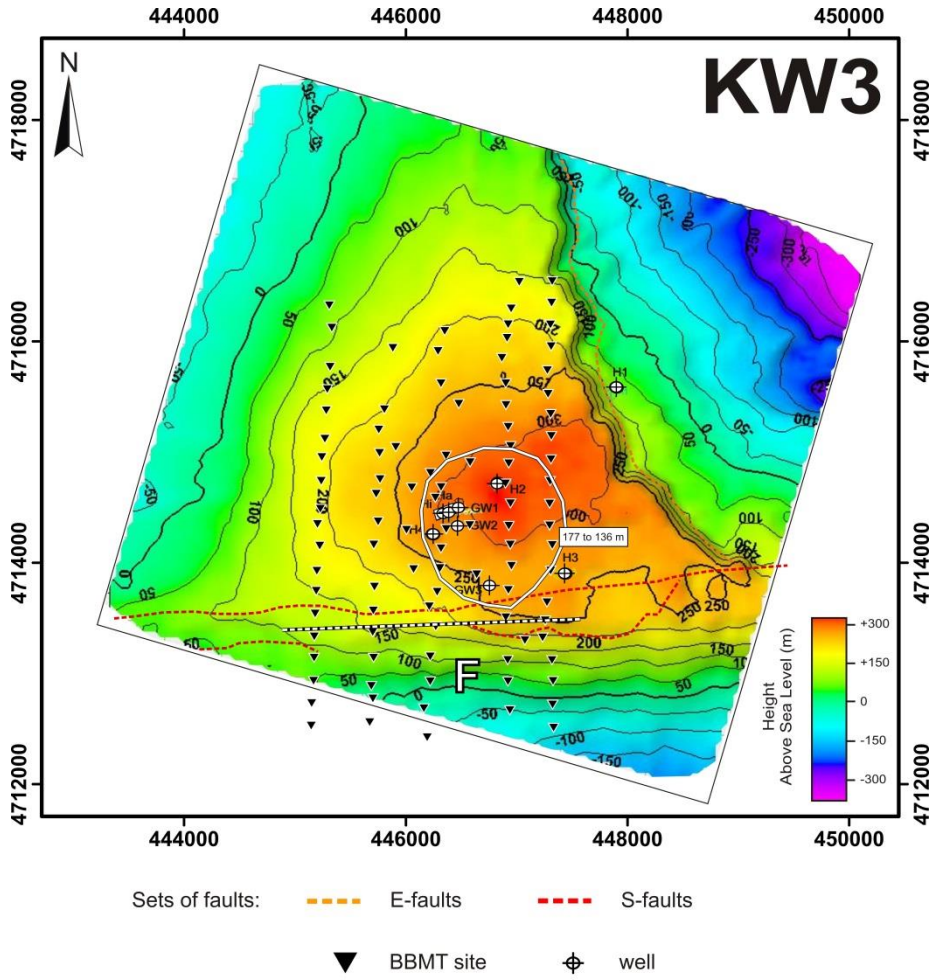

Fig. 3.29. Depth map of the top of the Weald (KW3) according to the seismic volume interpretation. Dashed lines represent interpreted E-fault and S-fault sets. Superimposed in white, the features of the geoelectrical model highlighted in Fig. 3.22d are indicated: the limits of the dome image at 177 to 136 m (within the R2 layer) and the north-border of the F fault region (modified from Alcalde et al., 2014).

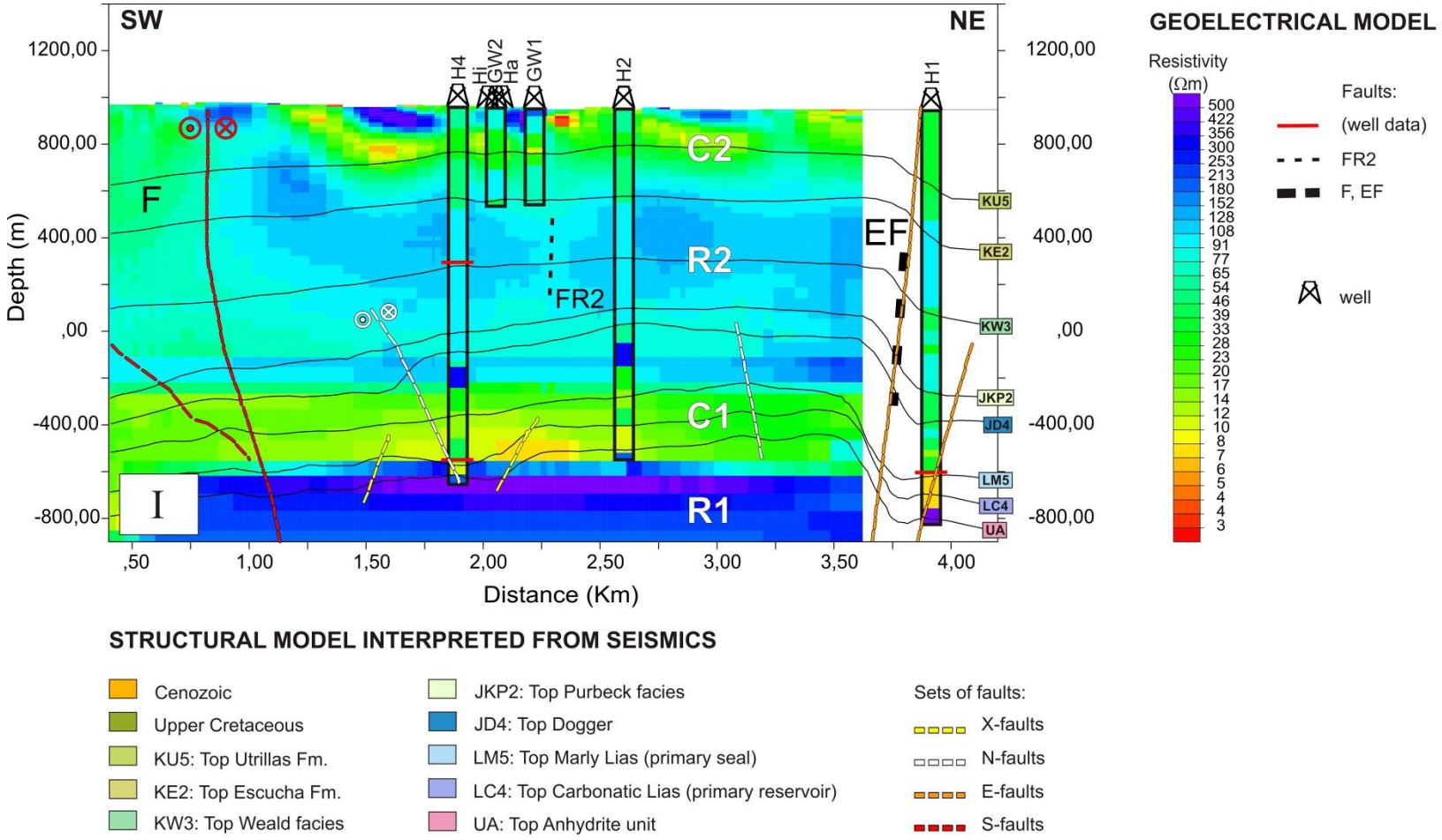

Fig. 3.30. Section I of the geoelectrical model (Fig. 3.21) and superimposed, the α profile of the structural model interpreted from seismics (Alcalde et al., 2014). Geoelectrical model: the main resistive layers (R1, C1, R2 and C2) and F and EF fault regions are indicated. Possible FR2 fracture regions and faults that cross the H wells according to well data, are also specified. The 1D resistivity models derived for each well appear superimposed. Structural model interpreted from seismics: the top of the different units (black lines) and the main fault sets (X-faults, N-faults, E-faults and S-faults) are indicated.

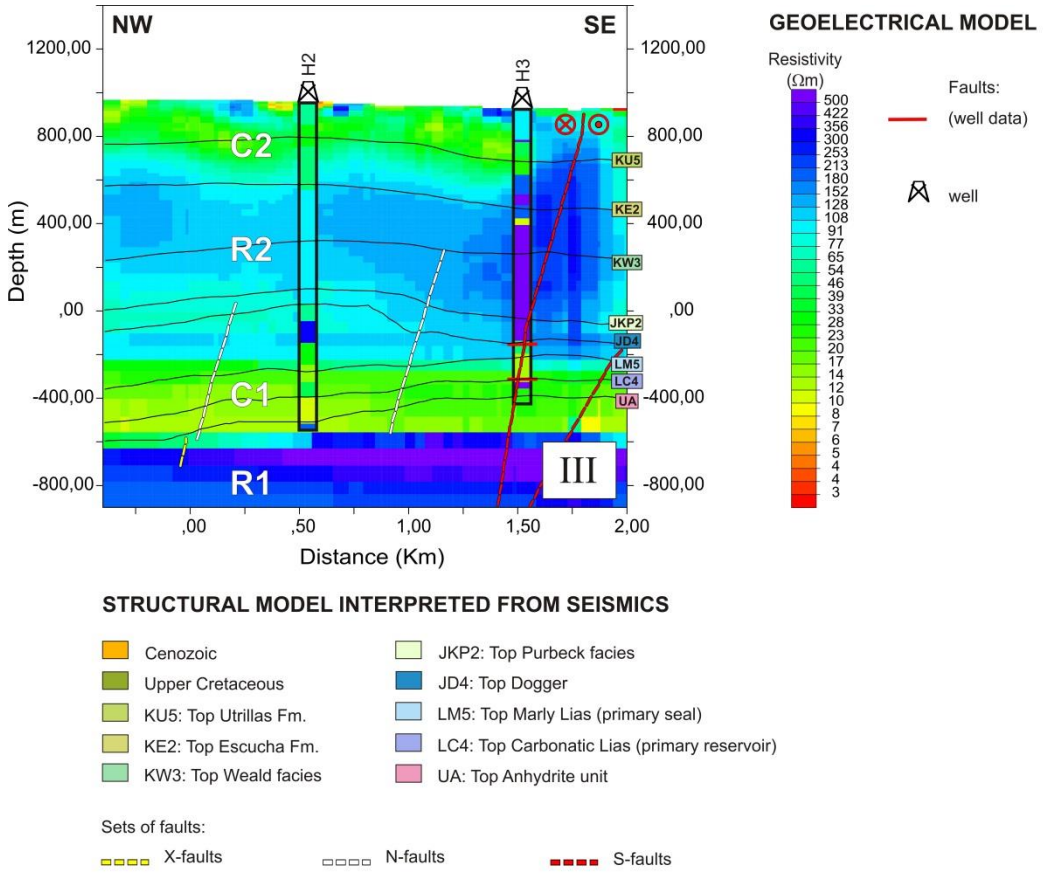

Fig. 3.31. Section III of the geoelectrical model (Fig. 3.21) and superimposed, the β profile of the structural model interpreted from seismics (Alcalde et al., 2014). Geoelectrical model: the main resistive layers (R1, C1, R2 and C2) and F and EF fault regions are indicated. Possible FR2 fracture regions and faults that cross the H wells according to well data, are also specified. The 1D resistivity models derived for each well appear superimposed. Structural model interpreted from seismics: the top of the different units (black lines) and the main fault sets (X-faults, N-faults, E-faults and S-faults) are indicated.

3.5.3. 3D Microgravimetry

A microgravimetric survey was carried out in August-December 2010 at the Hontomín URL (Implemental Systems, 2011). It characterised 4 x 4 km^2 of the site, covering an area similar to that covered by the MT 3D survey.

The results provided by the microgravimetric modelling were correlated with the 3D geoelectrical baseline model. Figure 3.32 shows the Bouguer anomaly map for a density reduction of 2.4 g/cm^3 (Implemental Systems, 2011). The more positive anomalies (red colours) occur in areas with average density greater than the Bouguer reduction density of 2.4 g/cm^3, whereas the more negative anomalies (blue colours) occur in areas of lower density. In this way, the map highlights a large minimum located in the centre-northern part of the study area. In the north, the minimum is limited by a smoother gradient, whereas in the south, it is limited by a strong gradient with an increase of more than 5 mGal in the Bouguer anomaly value. This strong gradient presents a clear ENE-WSW orientation.

In order to correlate the results provided by both geophysical techniques, the features of the 3D geoelectrical model pointed out in Fig. 3.22b were superimposed in Fig. 3.32. Therefore, dashed white lines indicate (i) the more resistive area imaged in the NW region of the model, at around 700 m.a.s.l. (interpreted as the dome crest at that level) and the (ii) the approximate north-border of the F region (EW line). The more resistive region located at 700 m.a.s.l. is observed to agree with the location of the Bouguer anomaly minimum (Fig. 3.32). Likewise, the north-border of the F fault region matches with a strong gradient of the Bouguer anomaly (Fig. 3.32). Thus, the results provided by both techniques are consistent.

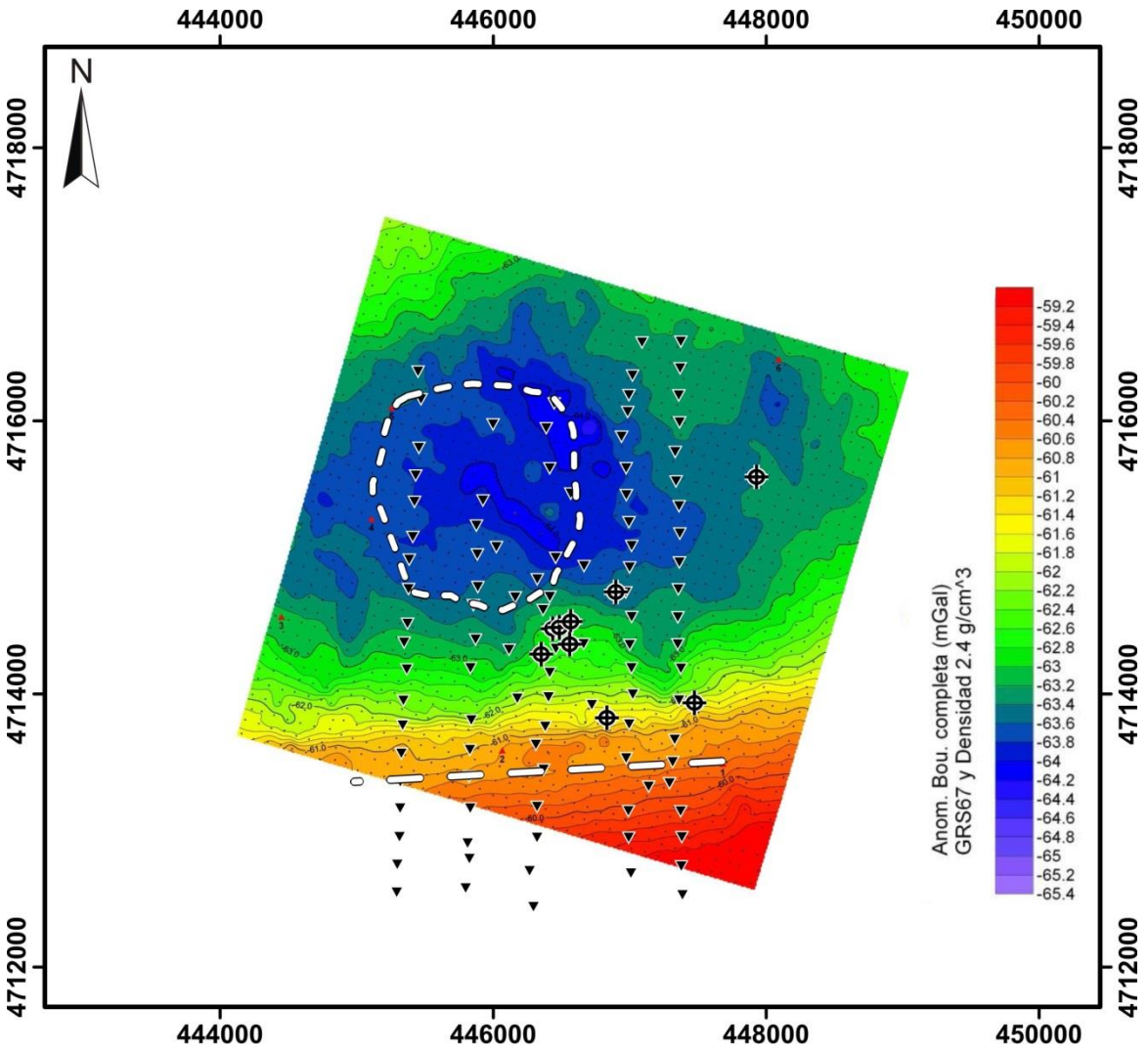

Fig. 3.32. Bouguer anomaly map for a density reduction of 2.4 g/cm^3. Small black dots are microgravimetric stations and red triangles, the gravimetric bases. Superimposed are displayed the wells and the BBMT sites considered for the 3D inversion (black triangles). White dashed lines represent the geoelectrical features interpreted in Fig. 3.22b: the circle located in the NW portion, delimitates the more resistive region imaged in the 3D geoelectrical model at around 700 m.a.s.l. and the EW line indicates the approximate north-border of the F fault region (modified from Implemental Systems, 2011).

3.5.4. Conclusions of the correlation with other geophysical data

The 3D geoelectrical baseline model of the Hontomín site is supported by a variety of geophysical data, which demonstrates its accuracy and reliability. In this section, the model was correlated with results provided by other characterisation surveys undertaken at the URL. Resistivity logs of Hi and Ha wells proved that the 3D geoelectrical baseline model predicted the resistivity structure of both wells, satisfactory reproducing their geoelectrical behaviour. The modelled dome structure was observed in both reflection seismic and microgravimetric results. The north-border of the F fault region matches with set S faults interpreted in the seismic volume and with a strong gradient of the Bouguer anomaly in the microgravimetry.

The structural model obtained from the seismic interpretation correlates reasonably well with the obtained geoelectrical structure. The correlation of the depth map of the anhydrite unit top with the top of the bottom resistive layer R1 demonstrates the coherence of the final resistivity model. The F fault region is observed to alter the geoelectrical behaviour of the different units. Accordingly, the comparison between seismic and magnetotelluric results underscores the importance of combining both techniques in characterisation surveys, especially to better describe faults.

The seismic results show a set of faults in the eastern part of the study area, out of the region modelled by the MT (E-faults). Likewise, the Bouguer anomaly seems to present an orientation similar to the one given by the E-faults in that region. Hence, it would be interesting to acquire a new MT profile in this eastern area in order to study the geoelectrical behaviour of the fault set. Although the profile is outside the URL, it would complete the MT characterisation of the Hontomín site.

In view of these correlation results, an interesting task to face in the future would be to carry out a joint inversion using all the available geophysical data. In order to combine the existing data, a relationship between the different physical parameters should be established. Two possible approaches (Gallardo and Meju, 2011; Moorkamp et al., 2011) involve: (i) to specify a functional relation between the physical parameters (Jegen et al., 2009) or (ii) to impose a structural constrain in order to force similarity between the different properties

distribution (cross-gradient) (Gallardo and Meju, 2003). Joint inversion will improve the resolution of the MT images and enhance the geological model of the URL. Although the correlation of seismic and microgravimetric results is out of the scope of this work, it is worth to point out that could be an interesting task to undertake in the near future.

4 Magnetotelluric monitoring

It has been amply demonstrated that MT is well-established as an EM characterisation technique. However, in reference to monitoring studies, it has been underused compared to other EM methods. In this chapter a new approach is developed to carry out EM monitoring using surface MT: a layer stripping approach. It is an innovative contribution to enhance the resolution of the surface MT data to small resistivity changes.

4.1. Introduction

EM monitoring studies are usually carried out by means of direct-current (DC) (e.g. Kiessling et al., 2010; Bergmann et al., 2012) and CSEM methods (e.g. Becken et al., 2010; Girard et al., 2011; Vilamajó et al., 2013). The MT method is less used for these kinds of surveys mainly because of its natural-source dependence, i.e., uncontrolled and non-repeatable source. However, in recent years some attempts have been undertaken in the following contexts: (i) searching for earthquake precursory resistivity changes (Park, 1996; Svetov et al., 1997; Sholpo, 2006; Hanekop and Simpson, 2006; Park et al., 2007; Kappler et al., 2010) and (ii) in geothermal projects, for both studying the movement of fluids and exploration purposes (Aizawa et al., 2011; Peacock et al., 2012a; Peacock et al., 2012b; Aizawa et al., 2013). In volcanic areas MT monitoring has also been used to investigate the relationship between EM pulses and type of eruption (Aizawa et al., 2010). In all these cases, MT monitoring has been applied either analysing temporal variations in the

magnetotelluric spectra or studying the evolution through time of the impedance tensor $Z_{ij}(\omega)$, the phase tensor, or directly, the MT responses (section 1.5).

Unfortunately, the above mentioned works show that resistivity variations are subtle and can sometimes be hardly detected and quantified using surface MT data because of the resolution of the method. For that reason, in this chapter is proposed a methodology based on the analytical solution of the 1D MT problem. Giving a well-known geoelectrical structure (baseline model), the aim is to remove the effect of the upper, unchanging, structures in order to obtain the MT responses at the target depth. In this way, this technique (called layer stripping hereafter) can enhance the resolution at the target depth making possible to monitor small resistivity variations due to changes in the reservoir.

The layer stripping concept was already used in Baba and Chave (2005) to eliminate the 3D topographic effects from the seafloor MT data. Similarly, in Queralt et al. (2007) it was used to remove the responses of known 3D structures from the observed down-mine AMT responses and in this way, to enhance the resolution of below-mine ore bodies. In both cases, layer stripping was shown to be a useful tool to obtain approximate responses in 3D.

In this chapter is presented the layer stripping method as a MT monitoring technique. The structure of the chapter is as follows: firstly, the method is introduced and validated for CO_2 injection in 1D; then, the methodology is applied to a 1D Earth where the CO_2 injection is simulated by a 3D plume, and finally, the method is tested in a real case study using the geoelectrical baseline model of the Hontomín site (Fig. 3.14) (Ogaya et al., 2014). The methodology is validated through synthetic studies using ModEM (Egbert and Kelbert, 2012), which provided responses on the surface and at depth.

4.2. The method: layer stripping

The methodology proposed (layer stripping) is based on the analytical solution of the 1D MT problem. In a layer-earth (1D Earth), the MT responses are derived using a well-known recursive relation (Srivastava, 1965; Kaufman and Keller, 1981; Ward and Hohmann, 1988; Grandis et al., 1999). The impedance tensor of a given interface z_n is deduced from

the impedance tensor of the next deeper interface z_{n+1} using an expression involving the frequency (ω, EM field characteristic) and the thickness and resistivity of the n-layer (h_n and ρ_n, respectively) (Fig. 4.1), where magnetic permeability is assumed to be the same for each layer (and take the free space value), and the electric permittivity of each layer (i.e., the effects of displacement currents) is ignored. First is determined the impedance tensor at the top of the underlying homogenous halfspace ($\boldsymbol{Z}_N$) (Fig. 4.1), viz.,

$$\boldsymbol{Z}_N = \frac{\omega\mu}{k_N} \qquad (4.1).$$

Moving upwards, it is possible to compute the impedance tensor at the top of each layer,

$$\boldsymbol{Z}_n = \frac{\omega\mu}{k_n} coth\left[coth^{-1}\left(\frac{k_n Z_{n+1}}{\omega\mu}\right) + ih_n k_n\right] \qquad (4.2),$$

where k_n is the layer propagation constant within each layer and is given by

$$k_n = \sqrt{\frac{-i\omega\mu}{\rho_n}} \qquad (4.3).$$

In this way, the impedance tensor Z_1 on the surface of the Earth (at $z = 0$) is calculated. The algorithm used (Eq. 4.2) is based on the one presented in Srivastava (1965) and Grandis et al. (1999).

For the layer stripping methodology, a formulation is proposed founded on Eq. 4.2. Rewriting the equation, it is possible to obtain the inverse recursive relation (move downwards) and calculate responses at the top of the n-layer from responses at the top of the $(n-1)$-layer. Thereby, the formulation for the layer stripping technique can be expressed as

$$\boldsymbol{Z}_n = \frac{\omega\mu}{k_{n-1}} coth\left[coth^{-1}\left(\frac{k_{n-1} Z_{n-1}}{\omega\mu}\right) - ih_{n-1} k_{n-1}\right] \qquad (4.4).$$

Accordingly, using the thickness and the resistivity of each layer, it is possible to calculate $\boldsymbol{Z}_n$ from $\boldsymbol{Z}_1$.

This technique would increase the resolution of surface MT responses to resistivity variations produced at $(n+l)$-layer (layer in grey in Fig. 4.1) removing the effect of the

unchanging upper layers (Fig. 4.1). Therefore, this new methodology is presented as especially useful for monitoring areas where the geoelectrical baseline model of the site is well-known.

It has been seen that in the 1D case the MT responses at depth only depend on the structures located at and below the observation point (i.e., they are independent of any layers located above it)(Kaufman and Keller, 1981). However, in 2D and 3D cases the MT problem is more complex because currents may flow above and below the observation point; this is discussed and shown in detail in Queralt et al. (2007). Consequently, for multidimensional scenarios the layer stripping solution is not as exact as in 1D, but can constitute a useful tool to estimate approximate responses.

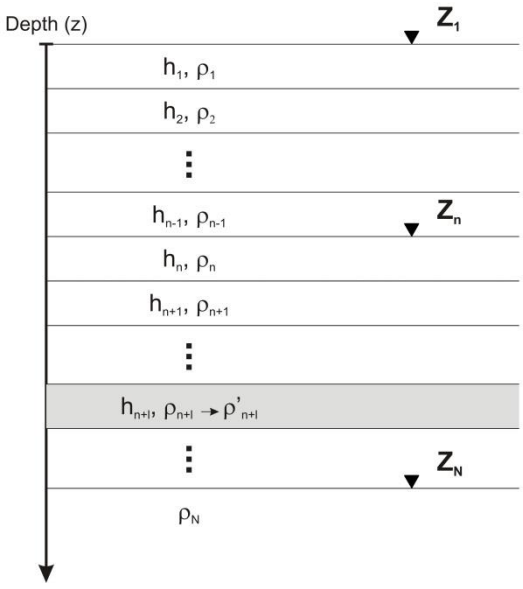

Fig. 4.1. N-layered 1D structure. $\boldsymbol{Z}_1$ is the MT response on the surface of the Earth and $\boldsymbol{Z}_n$, the MT response at top of the n-layer. Each layer has a h_n thickness and a ρ_n resistivity. Resistivity changes from ρ_{n+l} to ρ'_{n+l} are located at $(n+l)$-layer (grey layer). The stack of layers continues down to layer N which is a halfspace of resistivity ρ_N.

4.3. Synthetic data examples

In this section, the layer stripping methodology is validated through two synthetic studies simulating CO_2 injection in 1D and in 3D. The process consisted of applying the layer stripping technique (Eq. 4.4) to surface MT responses provided by ModEM. In the 1D case, results obtained at the top of each layer were compared to those supplied by the 1D analytical solution (Eq. 4.1-Eq. 4.3). In this way, the effects of the gridding in ModEM responses were also evaluated (Appendix 4.1). In the 3D case, stripping results were compared to responses provided by ModEM at depth.

In the synthetic data examples, the 1D model derived from the H2 resistivity log data (Fig. 4.2) (see section 2.3.1) was used as the baseline model of the pre-injection state. The numerical solution was obtained using a mesh of 58x59x81-layer grid with an approximate model extension of 83x83x86 km^3. Due to the discretisation of the model, there existed some small differences between the 1D analytical solution and the ModEM responses. Those differences were eliminated by applying a correction term (see Appendix 4.1).

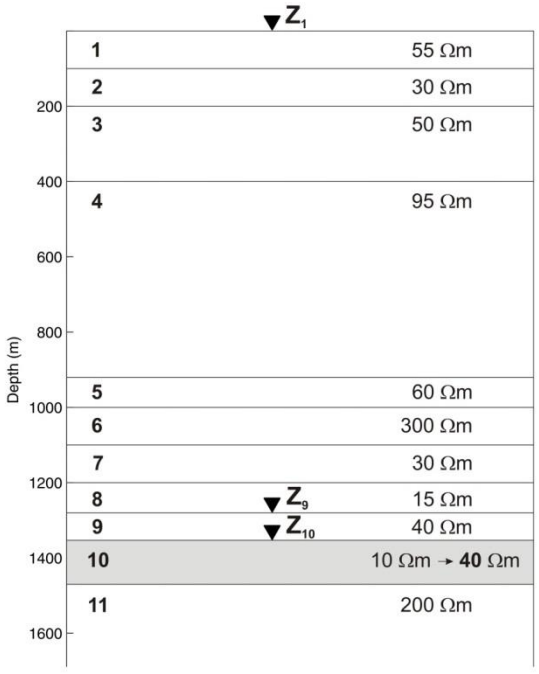

Fig. 4.2. 1D resistivity model derived from H2 resistivity log data (section 2.3.1). In order to simulated a CO_2 injection in 1D, the resistivity of the 10th-layer (reservoir layer) was modified from 10 **Ω**m to 40 **Ω**m, as was estimated in section 2.3.1 for a CO_2 saturation of 50 %. Black triangles indicate the position of the MT measurements shown in Fig. 4.3.

4.3.1. 1D injection of CO_2

The reservoir resistivity (layer number 10) (Fig. 4.2) was modified from 10 Ωm to 40 Ωm to simulate a homogeneous CO_2 saturation of 50 % after injection (see section 2.3.1). Figure 4.3 shows the layer stripping solutions at three different depths. Differences between the pre-injection and the post-injection state (resolution to resistivity changes) increase with the depth at which the data are acquired. Table 4.1 summarizes the maximum apparent resistivity and phase variations observed at the top of each layer of the 1D model. In principle, these are the maximum variations that might be expected since the CO_2 layer is infinite in a 1D case. Therefore, these variations may be greater than in any other 2D or 3D case, since the edge effects of the plume will probably not result in such large changes.

The results demonstrate that the layer stripping methodology is valid for a 1D model. Only small discrepancies due to numerical instabilities are observed in the shorter periods for the deepest layers.

Table 4.1. Maximum apparent resistivity and phase variations between pre-injection and post-injection state, at the top of each layer of the 1D model (Fig. 4.2). Variations were calculated using the 1D analytical solution (Eq. 4.1-Eq. 4.3). Layer number 10 corresponds to the CO_2 reservoir.

Layer (depth in m)	App. Res. Diff. (%)	Phase Diff. (deegres)
1 (0)	28,3	4,9
2 (100)	30,3	5,1
3 (200)	34,0	5,6
4 (400)	40,7	6,3
5 (920)	65,7	9,4
6 (1000)	74,4	10,3
7 (1100)	83,0	11,4
8 (1200)	118,6	14,2
9 (1280)	258,4	18,8
10 (1353)	547,6	14,3
11 (1470)	0	0

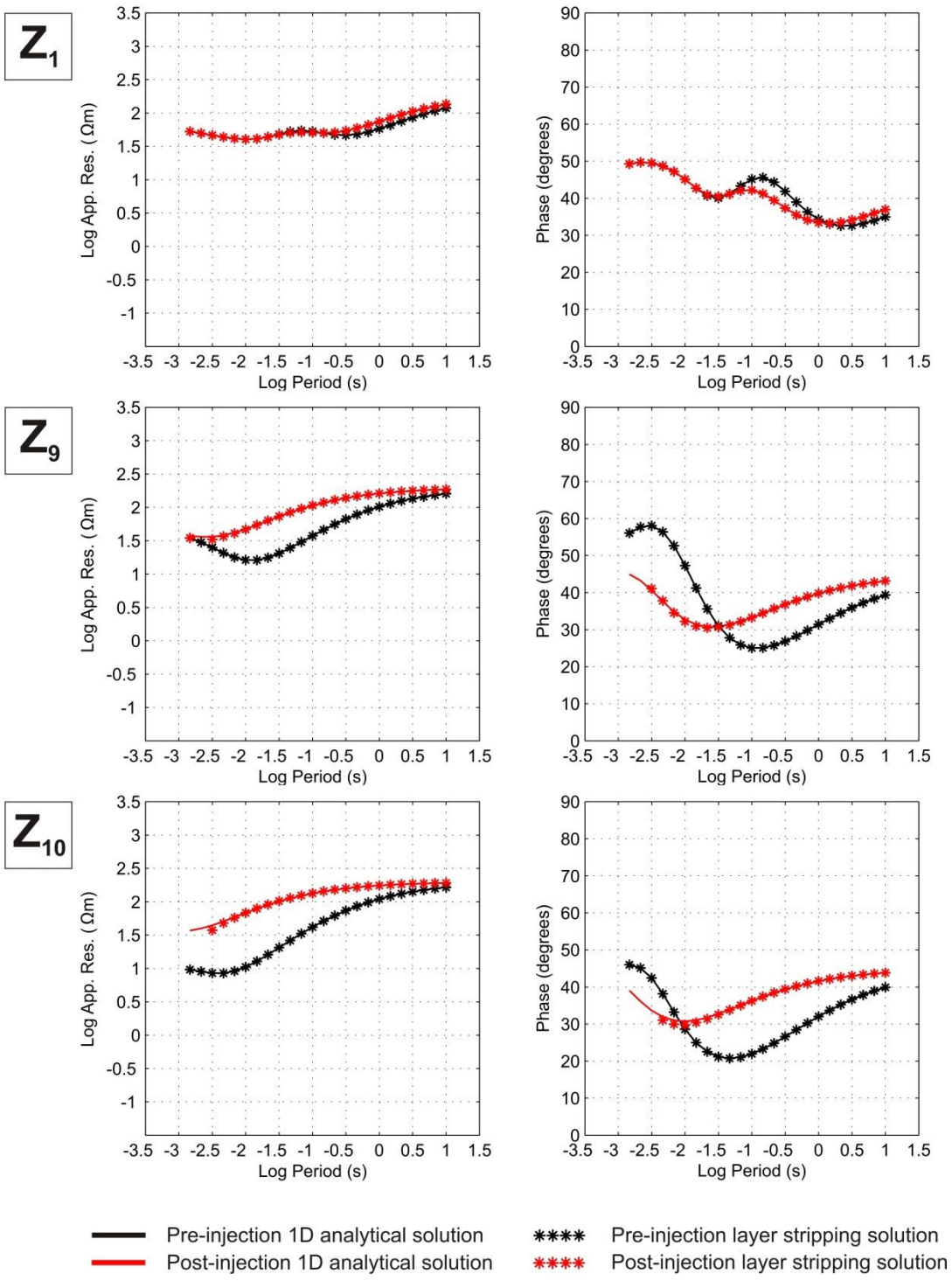

Fig. 4.3. MT responses at the top of layers 1, 9 and 10 (top of the reservoir). The location of the MT measures is indicated by black triangles in Fig. 4.2. In black are displayed the responses of the pre-injection 1D model and in red, the responses of the post-injection 1D model (with CO_2). One-dimensional analytical solutions are plotted with continuous lines whereas the layer stripping results are plotted with small stars.

4.3.2. 3D injection of CO_2

The layer stripping methodology was then applied to a 1D model with a 3D plume. Since an infinite layer of CO_2 does not represent a real CO_2 injection, 3D plume of CO_2 was simulated. Accordingly, a 40 Ωm plume was placed within the reservoir (layer number 10) as is shown in Fig. 4.4.

The minimum volume of CO_2 detectable from surface MT data was determined by carrying out several numerical tests. Table 4.2 summarizes the volumes of the studied plumes and Fig. 4.5 shows the apparent resistivity and phase variations observed at the centre of the plume (position A in Fig. 4.6) for each volume. These variations must be larger than the experimental error assumed in the acquired MT data in order to be detected. In this work, an error floor of 10 % for the apparent resistivity and of 2.865 degrees for the phases was adopted. This error floor was imposed on the off-diagonal components of the Hontomín MT data set for the 3D inversion.

Volume V_5 corresponds to 25 Megatons of CO_2 and involves differences in the surface MT responses larger than the assumed experimental error (Fig. 4.5). It gives an approximate idea of the volume required to detect a resistivity change of the order of the one studied here (from 10 Ωm to 40 Ωm), using surface MT data. Two real examples of injections with a similar amount of CO_2 are: Snøhvit in Norway (offshore deep saline aquifer), with a planned maximum injection of 31-40 Megatons[1] and Sleipner, also in Norway (offshore deep saline formation), with a planned maximum injection of 17 Megatons[2]. In In-Salah, in Algeria, (onshore deep saline formation) about 17 Megatons were planned to be injected during the whole life of the project (Haddadji, 2006), but at present the injection is suspended[3]. Another example but for Enhanced Oil Recovery (EOR) purposes, is The Rangely Oil Field in USA where a total of approximately 23-25 Megatons of CO_2 has been injected since 1986[4].

[1] http://www.globalccsinstitute.com/project/sn%C3%B8hvit-co2-injection (visited February 2014).
[2] http://www.globalccsinstitute.com/project/sleipner%C2%A0co2-injection (visited February 2014).
[3] http://www.globalccsinstitute.com/project/salah-co2-storage (visited February 2014).
[4] http://www.globalccsinstitute.com/project/shute-creek-gas-processing-facility (visited February 2014).

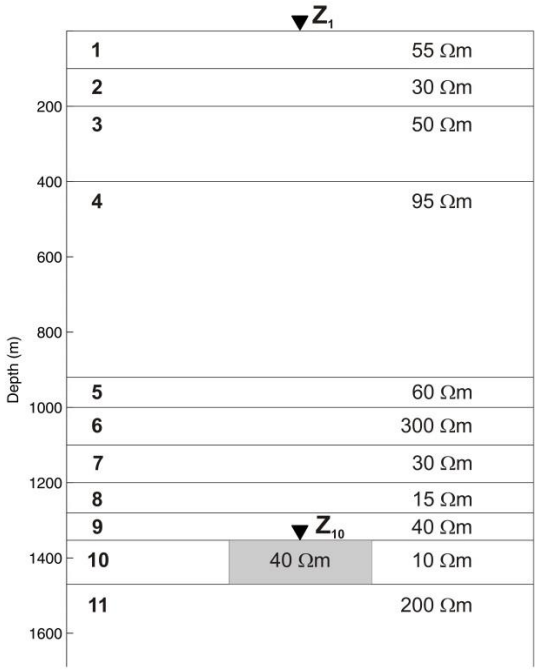

Fig. 4.4. 1D resistivity model derived from H2 resistivity log data (section 2.3.1) and 3D plume of 40 **Ω**m within the reservoir (it represents a homogeneous CO_2 saturation of 50 %).

Table. 4.2. Simulated CO_2 plumes.

	Plume dimensions (km^3)	Stored CO_2 (Megatons)
V_1	0.200 x 0.200 x0.117	0.2
V_2	0.600 x 0.600 x 0.117	1.8
V_3	1.000 x 1.000 x 0.117	5.1
V_4	1.800 x 1.800 x 0.117	16.6
V_5	2.200 x 2.200 x 0.117	25.0

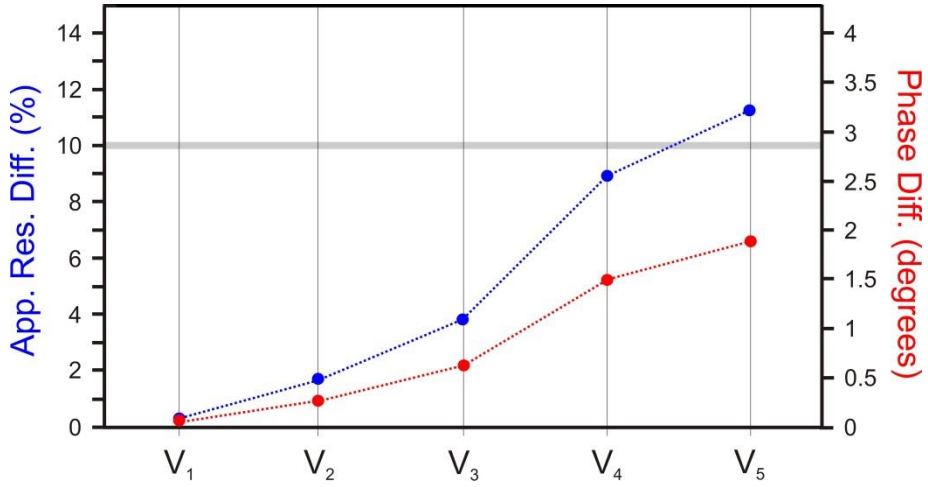

Fig. 4.5. Differences observed in apparent resistivity (blue) and phase (red) responses between the pre-injection 1D model and the post-injection model, for each of the CO_2 volumes shown in Table 4.2. A homogeneous saturation of 50 % was assumed, which results in a post-injection resistivity of 40 Ωm. The MT responses were obtained at the centre of the plume (position A in Fig. 4.6); consequently, both XY and YX polarisations are equal for symmetry arguments. The grey line indicates the assumed experimental error in the data (10 % for the apparent resistivity and 2.865 degrees for the phases). Volume V_5, which corresponds to 25 Megatons of CO_2, is the only volume that produces differences larger than the assumed experimental error.

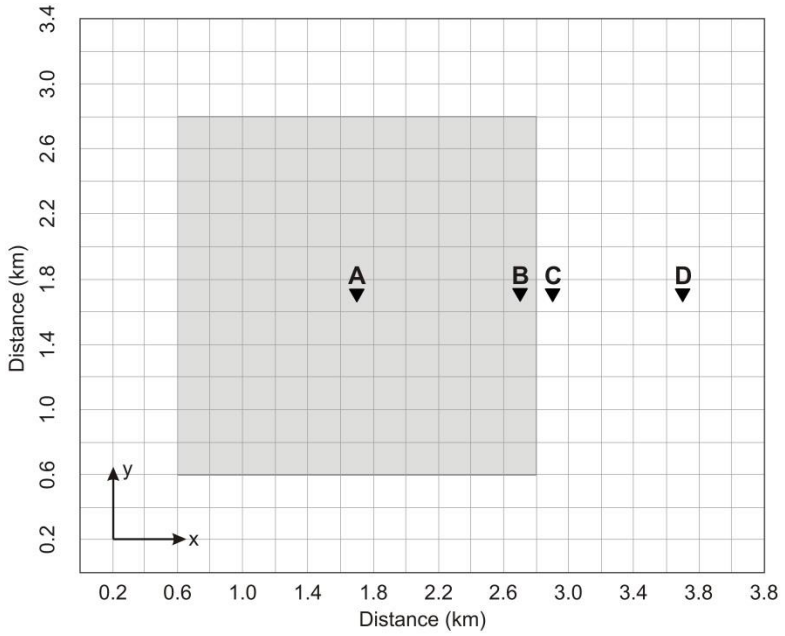

Fig. 4.6. MT responses were calculated at four different positions: A, B, C and D. The plume shown corresponds to volume V_5 in Table 4.2.

For volume V_1, the variation observed in the surface MT responses is very small and layer stripping does not noticeably improve the resolution to changes produced in the reservoir (Fig. 4.7). Differences obtained at the reservoir depth are above 4 % for the apparent resistivity and 0.65 degrees for the phases (values below the imposed error floor). Thus the resistivity variation produced in such small volumes of CO_2 is practically undetectable for surface MT and also, difficult to observe with the layer stripping methodology. On the contrary, for volume V_2, which means a variation at surface of 1.6 % for the apparent resistivity and of 0.3 degrees for the phases, the layer stripping at the reservoir depth shows variations greater than 35 % for apparent resistivity and 5 degrees for phases (Fig. 4.8).

In the case of plume V_5, MT responses were calculated at four different positions: A, B, C and D (see Fig. 4.6). Figures 4.9- 4.12 illustrate, at each of these positions, the ModEM responses and the layer stripping solutions on the surface and at the top of the reservoir for both XY and YX polarisations. The results show slight discrepancies between the ModEM responses and layer stripping solutions at the reservoir depth, with the differences being more significant in the phases than in the apparent resistivities. For apparent resistivity, layer stripping recovers reasonably well the ModEM responses at depth. At the B and C positions (Fig. 4. 10 and Fig. 4.11), the YX apparent resistivities show larger differences because edge effects are more important in that mode. In general, the layer stripping solutions are more accurate at the longest periods where they tend to agree with the responses provided by ModEM.

Although the methodology does not recover exactly the responses expected at the reservoir depth, it does make possible enhanced resolution with apparent resistivity and phase variations far greater than the ones observed on the surface. The evolution of the responses along the different sites (A, B, C and D positions) facilitates location of the plume and approximate delineation of its limits. Moreover, by studying the variations at more than one single site it may be possible to distinguish true resistivity variations from EM noise, allowing one to monitor smaller volumes of CO_2.

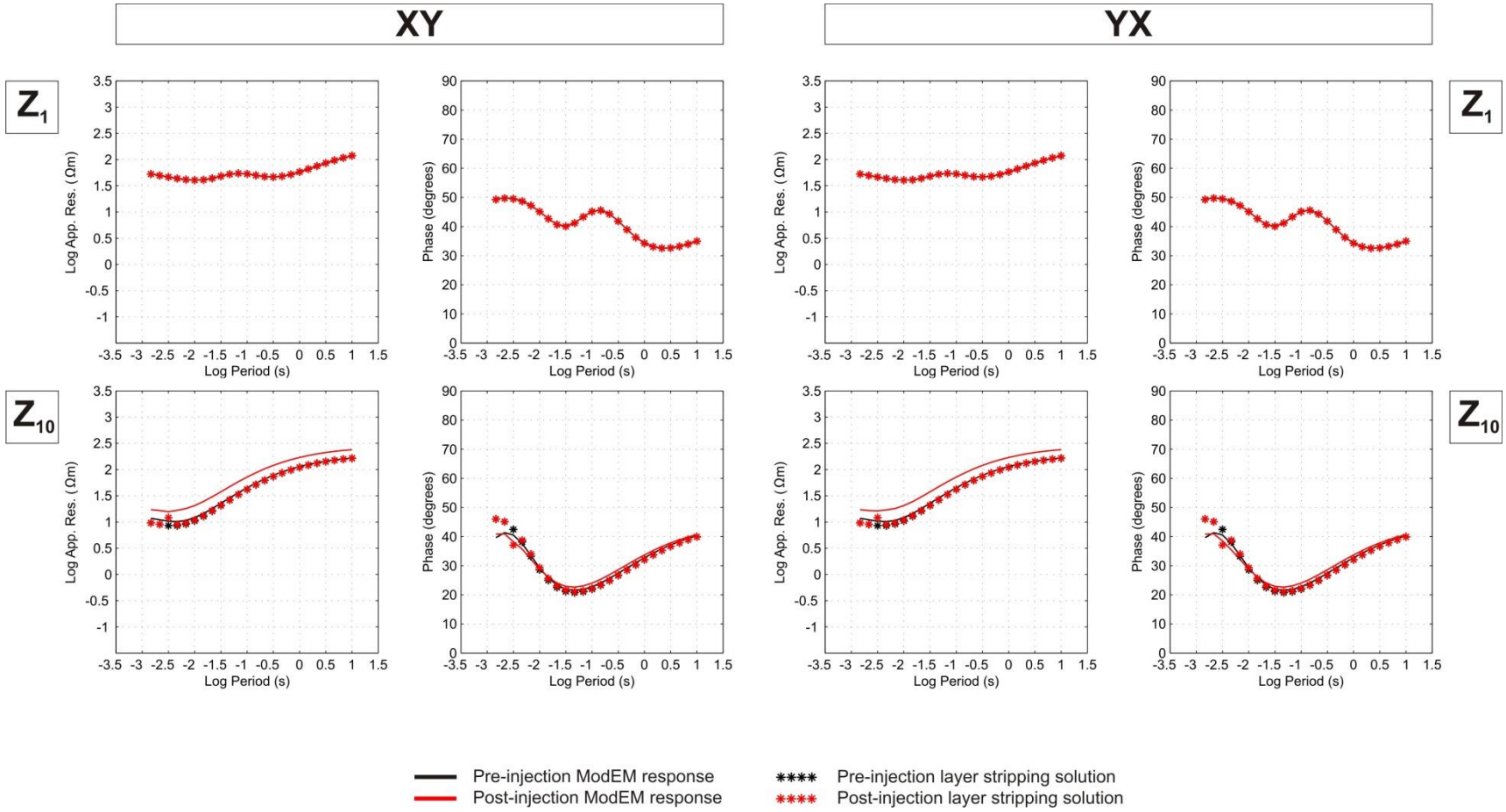

Fig. 4.7. Layer stripping for volume V_1. Both MT responses on the surface ($\boldsymbol{Z_1}$) and at the top of 10-layer (above the reservoir, $\boldsymbol{Z_{10}}$) are shown. In black are displayed the responses of the pre-injection model and in red, the responses of post-injection model. ModEM responses are plotted with continuous lines whereas the layer stripping solutions are plotted with small stars. XY and YX polarisations are similar since the MT responses were obtained at the centre of the plume.

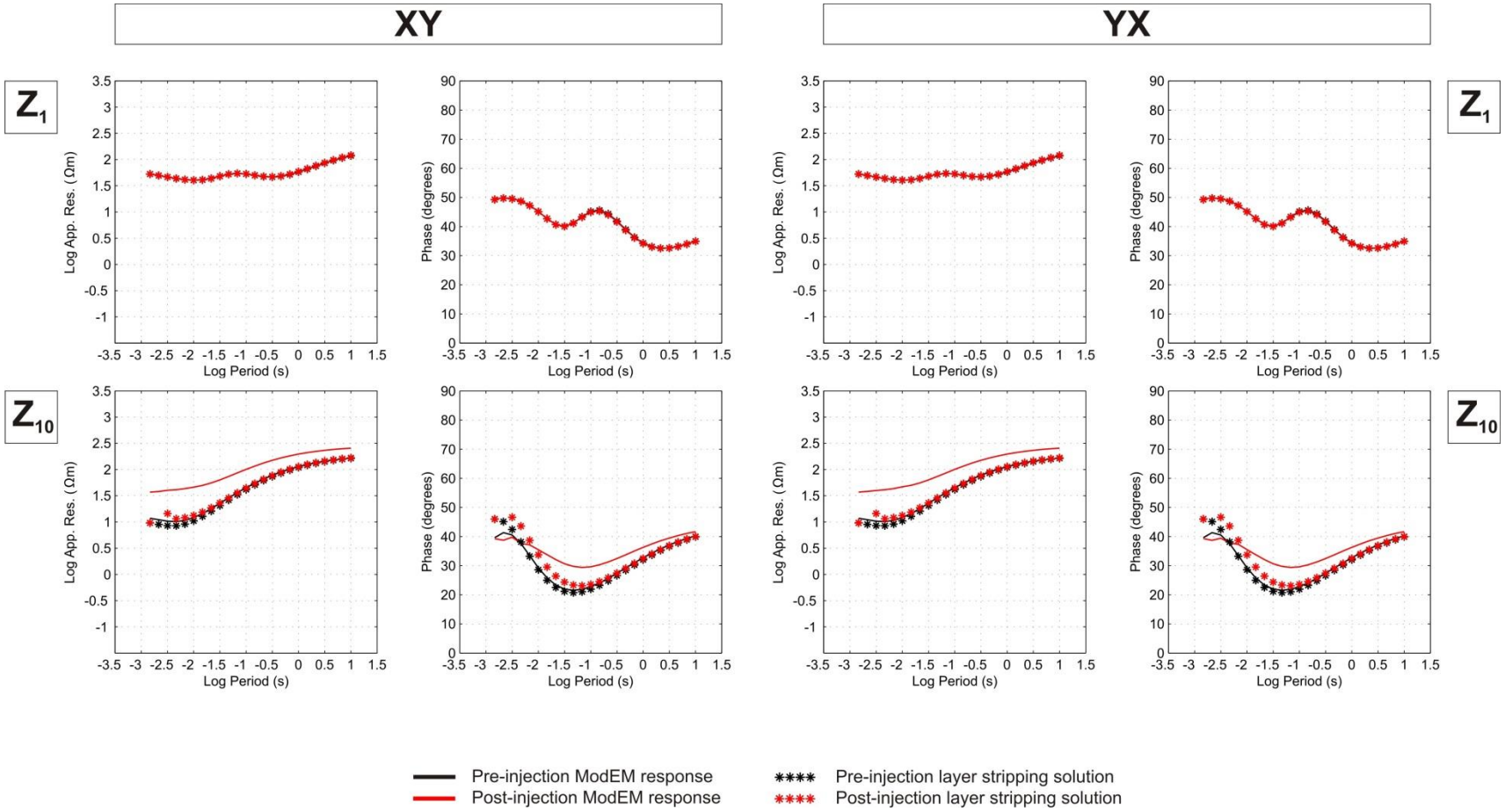

Fig. 4.8. Layer stripping for volume V_2. Both MT responses on the surface ($\boldsymbol{Z_1}$) and at the top of 10-layer (above the reservoir, $\boldsymbol{Z_{10}}$) are shown. In black are displayed the responses of the pre-injection model and in red, the responses of the post-injection model. ModEM responses are plotted with continuous lines whereas the layer stripping solutions are plotted with small stars. XY and YX polarisations are similar since the MT responses were obtained at the centre of the plume.

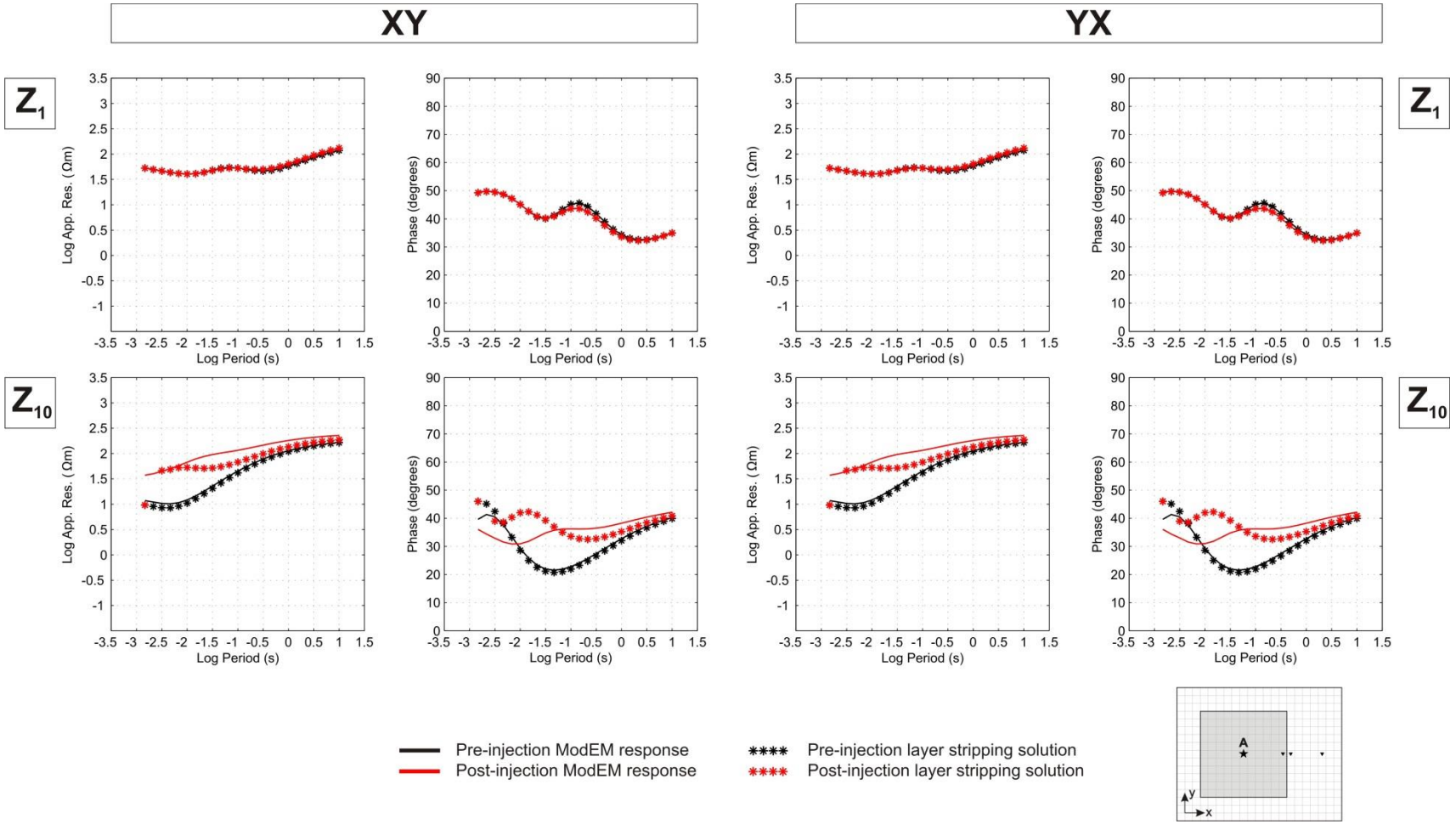

Fig 4.9. Layer stripping for volume V_5 at position A (Fig. 4.6). Both MT responses on the surface ($\boldsymbol{Z_1}$) and at the top of 10-layer (above the reservoir, $\boldsymbol{Z_{10}}$) are shown. In black are displayed the responses of the pre-injection model and in red, the responses of the post-injection model. ModEM responses are plotted with continuous lines whereas the layer stripping solutions are plotted with small stars. XY and YX polarisations are similar since the MT responses were obtained at the centre of the plume.

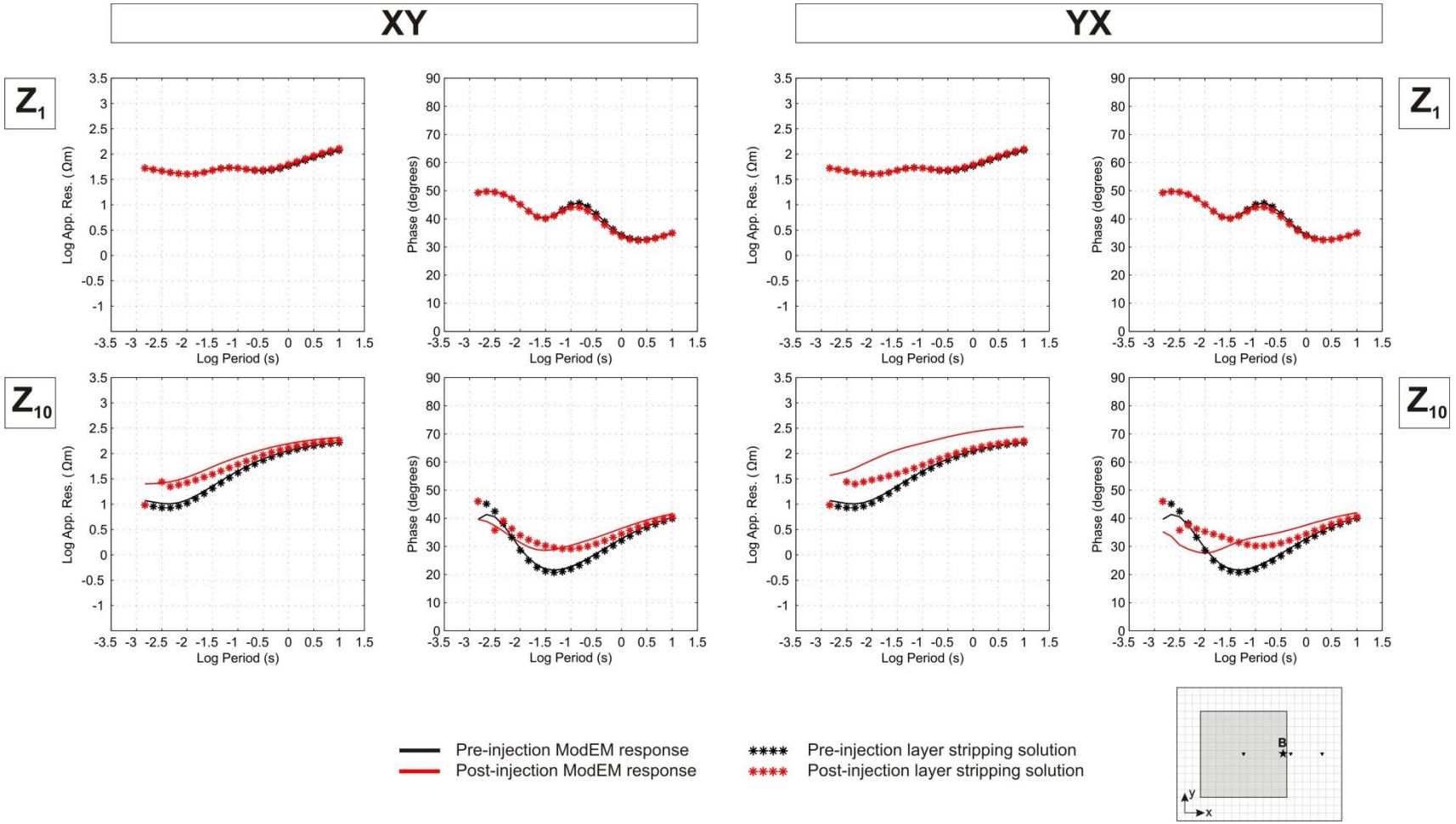

Fig. 4.10. Layer stripping for volume V_5 at position B (Fig. 4.6). Both MT responses on the surface ($\boldsymbol{Z_1}$) and at the top of 10-layer (above the reservoir, $\boldsymbol{Z_{10}}$) are shown. In black are displayed the responses of the pre-injection model and in red, the responses of the post-injection model. ModEM responses are plotted with continuous lines whereas the layer stripping results are plotted with small stars.

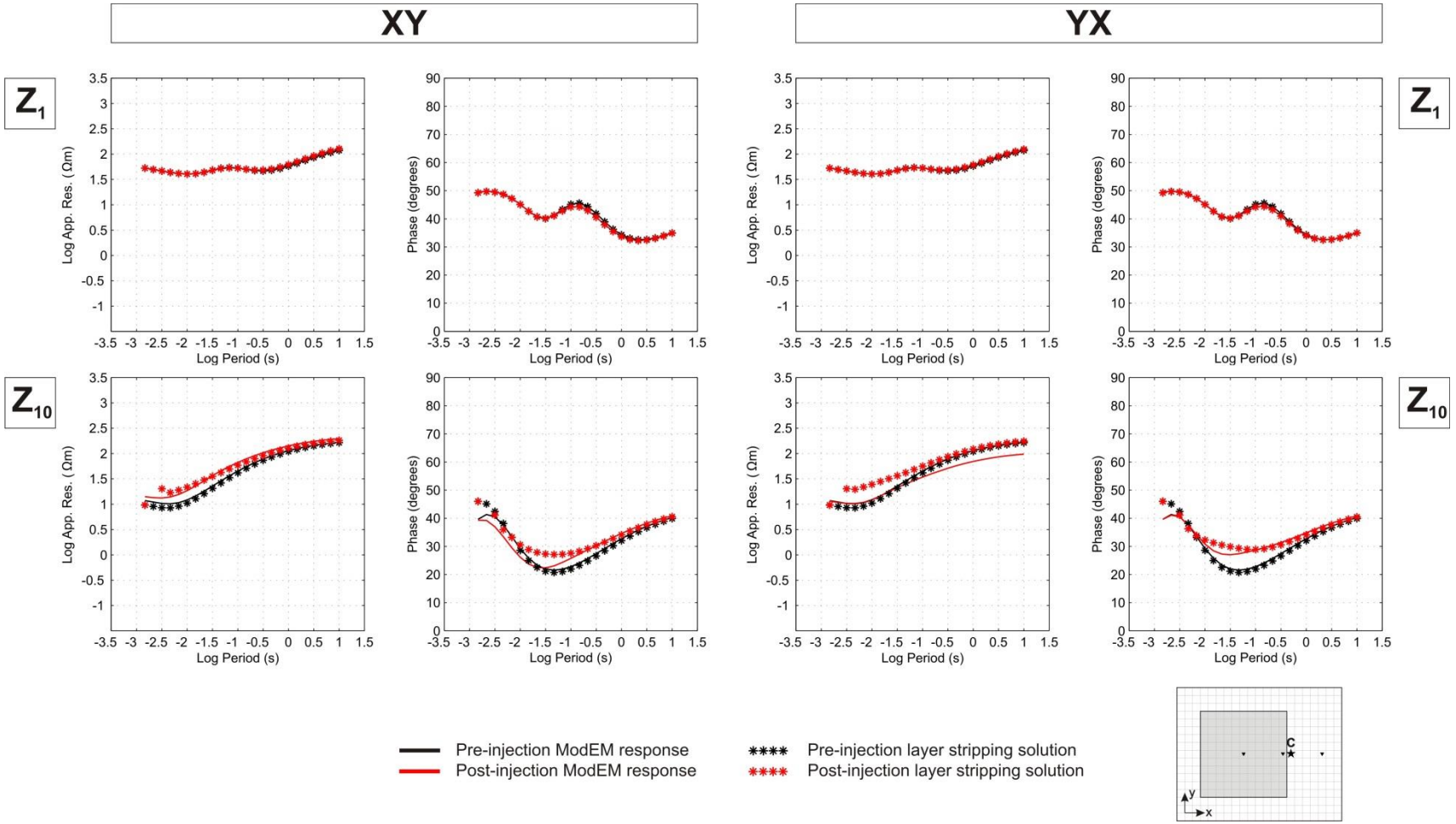

Fig. 4.11. Layer stripping for volume V_5 at position C (Fig. 4.6). Both MT responses on the surface ($\boldsymbol{Z_1}$) and at the top of 10-layer (above the reservoir, $\boldsymbol{Z_{10}}$) are shown. In black are displayed the responses of the pre-injection model and in red, the responses of the post-injection model. ModEM responses are plotted with continuous lines whereas the layer stripping results are plotted with small stars.

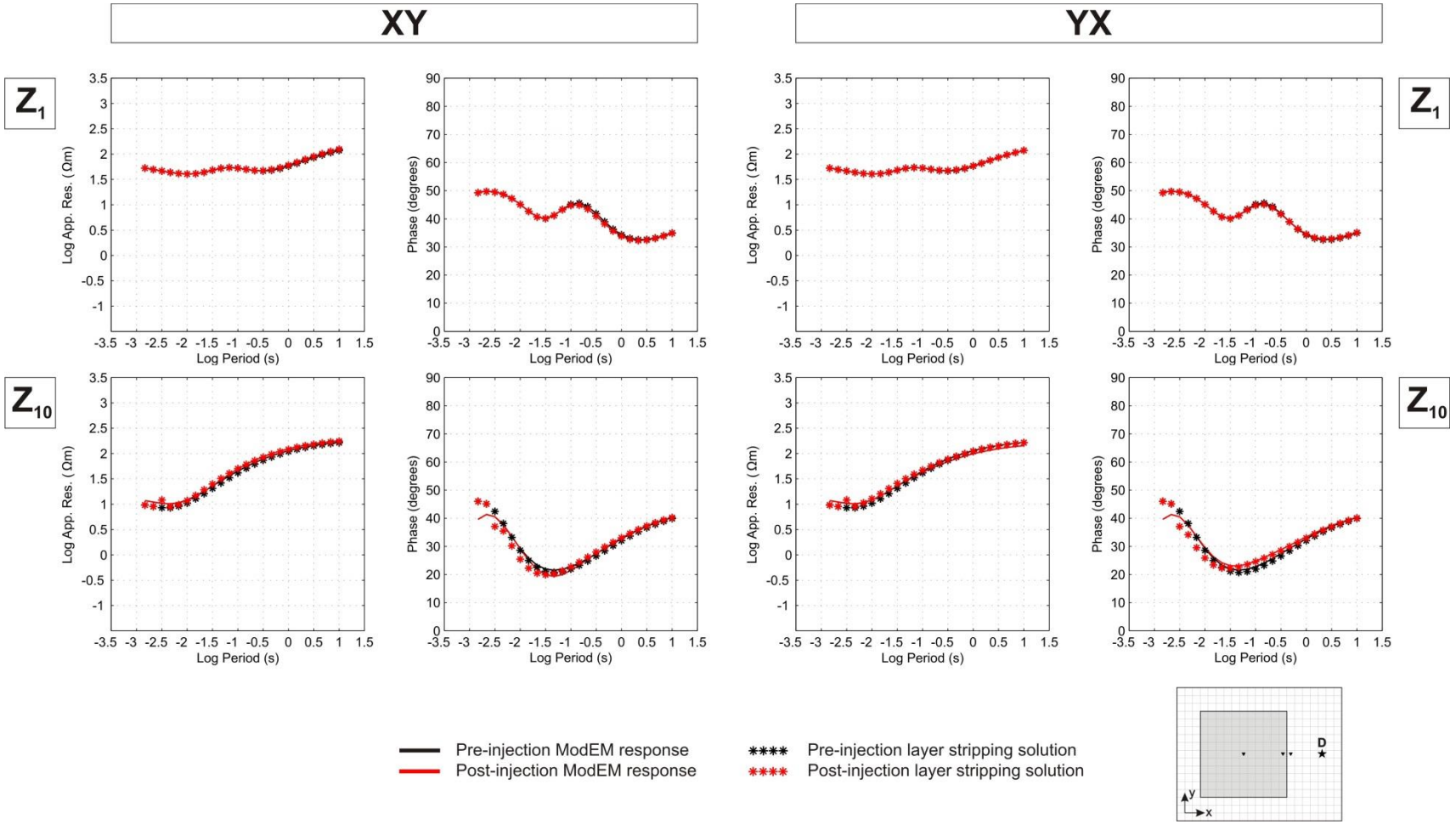

Fig. 4.12. Layer stripping for volume V_5 at position D (Fig. 4.6). Both MT responses on the surface ($\boldsymbol{Z_1}$) and at the top of 10-layer (above the reservoir, $\boldsymbol{Z_{10}}$) are shown. In black are displayed the responses of the pre-injection model and in red, the responses of the post-injection model. ModEM responses are plotted with continuous lines whereas the layer stripping results are plotted with small stars.

4.4. Case study: the Hontomín CO_2 storage site

To study the feasibility of the layer stripping methodology in a real case study, the volume V_5 of CO_2 (Table 4.2) was considered as the injection volume at the Hontomín URL. As the structure of the Hontomín facility is well-known, layer stripping was applied taking into account the geoelectrical baseline model of the site (Fig. 3.14) (Ogaya et al., 2014). For this study, the MT responses were calculated using ModEM.

The influence of the medium above the level of data acquisition was evaluated through a test that consisted of replacing all layers located above the reservoir by air-layers. Model A (Fig. 4.13) is the baseline model of the Hontomín site and model B (Fig. 4.13) is the baseline model with air-layers overlying the reservoir. The bottom of the air layers is at -408 m.a.s.l.. Figure 4.13 compares the responses of both models inside the reservoir (-478 m.a.s.l.) at the Hi well location (for description of well location see section 2.3). In Hontomín, the main reservoir-seal system is located in the period range of 0.1 to 1 seconds (section 2.3.1) (Ogaya et al., 2013). From dimensionality analysis of the MT data (section 3.4.1) (Ogaya et al., 2012), it was concluded that the responses at those periods were mainly 3D. However, Fig 4.13 shows that the overlying air-layers do not affect responses inside the reservoir significantly. Consequently, it is acceptable to perform a 1D assumption for the layer stripping at the Hontomín site.

The 1D model that best fitted the surface responses of the baseline model at Hi well position was sought. With this aim, first was considered the 1D model provided by the column of the 3D baseline model located at Hi well position (model called Hi model hereafter) (presented in section 3.5.1, Fig. 3.25). In Fig. 4.14 are displayed in black the responses of the 3D baseline model, and in grey the responses of the Hi model (Fig. 4.15). It is observed that both responses are not equivalent. Thus, more suitable 1D models were pursued for each polarisation using the Hi model as a starting model. Figure 4.15 shows the Hi model in grey and the 1D models that best fit the XY and YX polarisations of the 3D baseline model responses in blue and in red, respectively. The responses of the blue and red models are illustrated in Fig. 4.14. It is observed that their responses are coincident with the baseline model ones. Hence layer stripping was applied using these XY and YX 1D models.

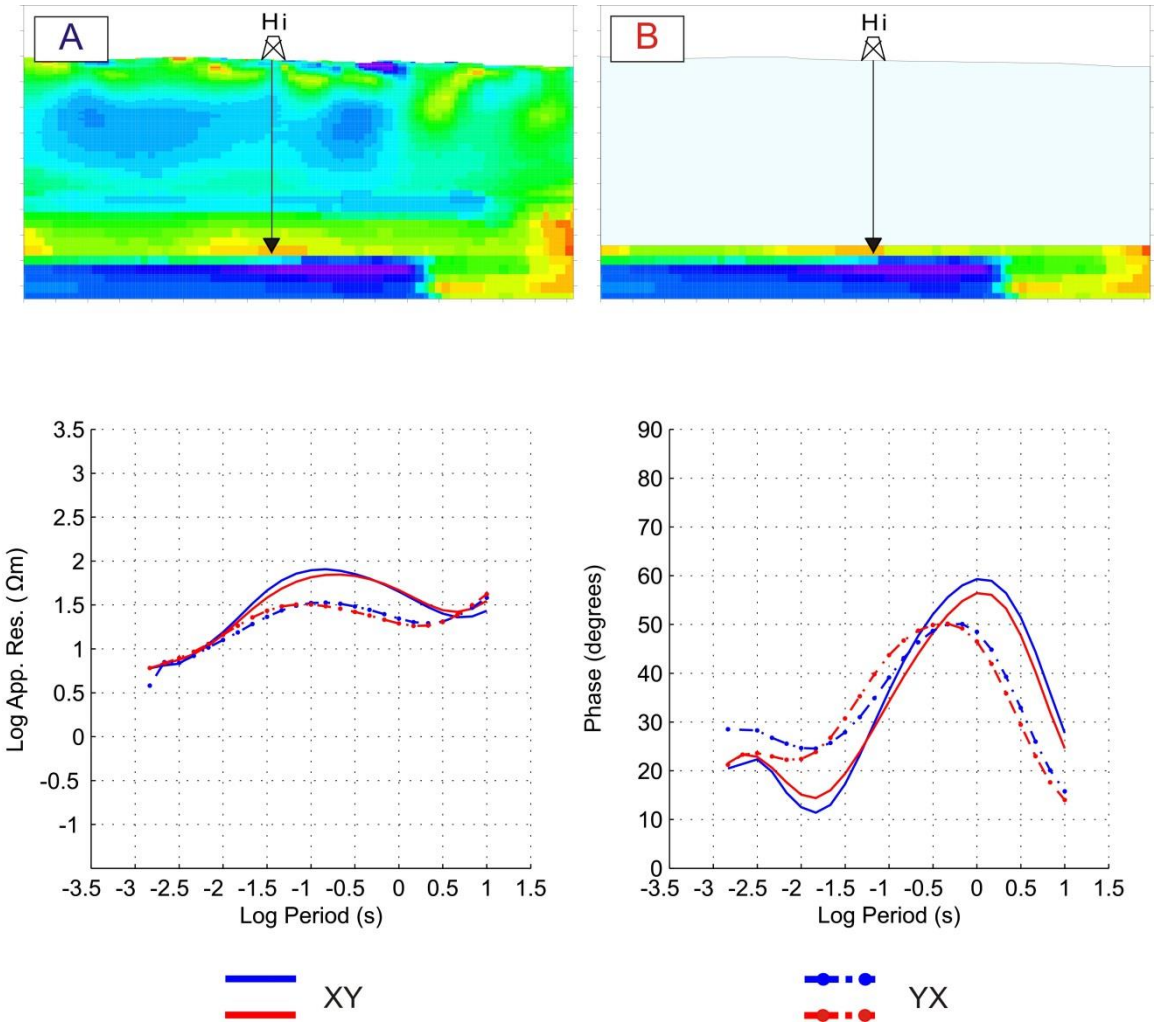

Fig. 4.13. Comparison of the MT responses inside the reservoir (at -478 m.a.s.l.) between two models: model A is the baseline model of the Hontomín site and model B is the baseline model with air-layers overlying the reservoir, the bottom of the air layers is at -408 m.a.s.l.. Model A responses are plotted in blue, and model B responses are plotted in red. Continuous lines display XY polarisation whereas dotted-dashed lines display YX polarisation. Responses were calculated at Hi well position.

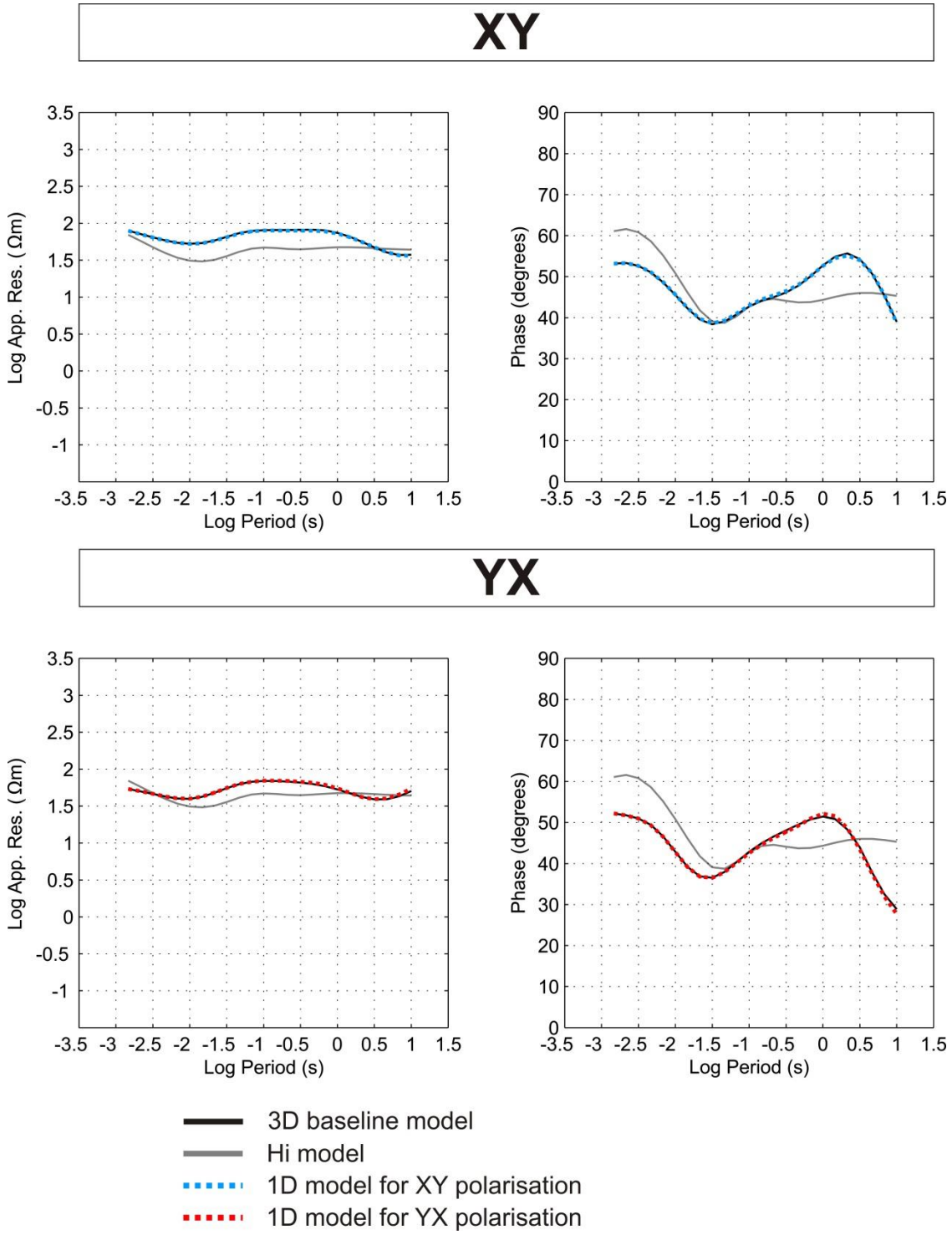

Fig. 4.14. Comparison between the surface MT responses of the 3D geoelectrical baseline model at Hi well position (black), the Hi model (1D model provided by the column of the 3D baseline model located at Hi well position) (grey) and the 1D models that best fitted XY and YX polarisations of the 3D baseline model (blue and red, respectively). Models are plotted in Fig. 4.15.

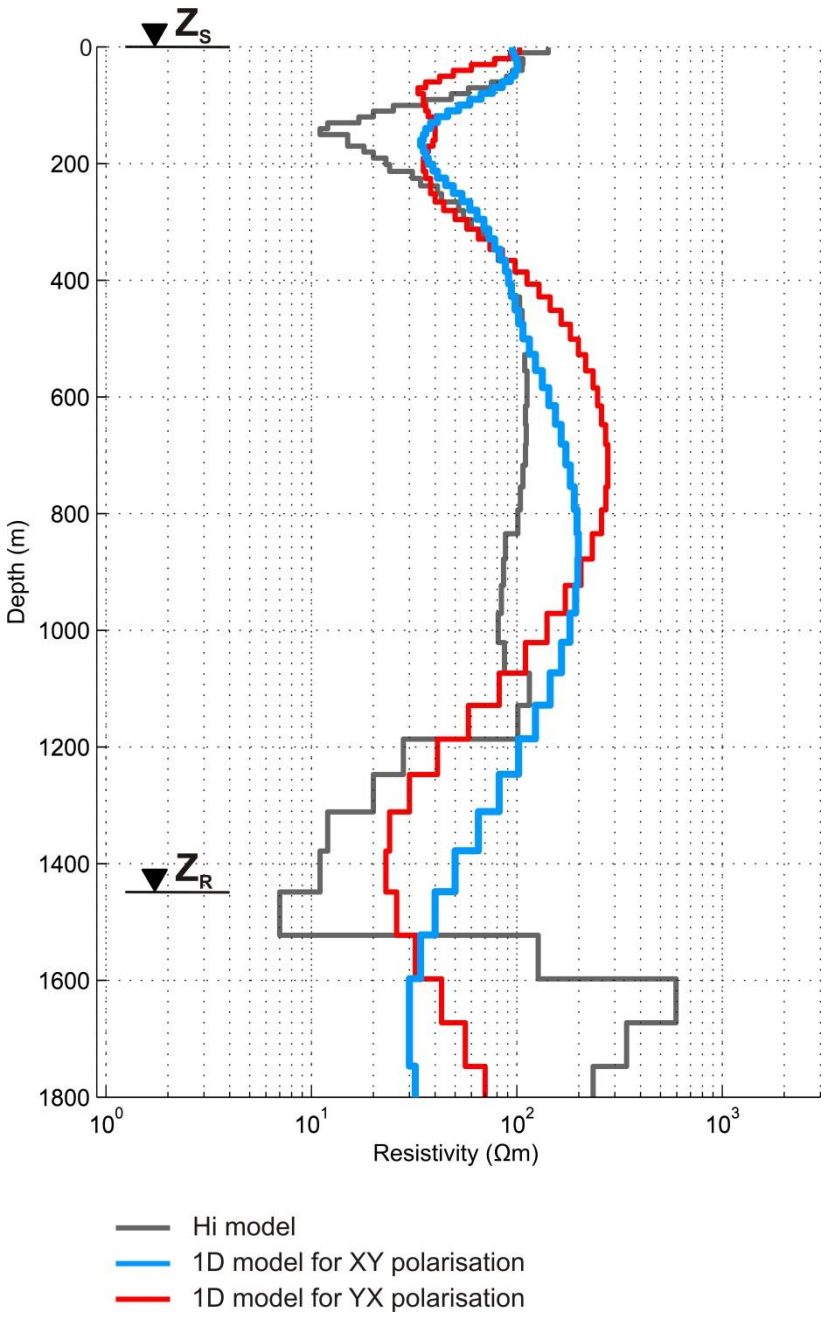

Fig. 4.15. Hi model (grey) and the 1D models that best fitted XY and YX polarisations of the 3D baseline model response at Hi well position (blue and red, respectively). Responses of those models are shown in Fig. 4.14. The 1D models were pursued using the Hi model as a starting model. For the layer stripping, the MT responses at Hi well position were calculated at the indicated depths: on surface ($\boldsymbol{Z}_S$) and in the reservoir (at -478 m.a.s.l., which means 1448 m TVD)($\boldsymbol{Z}_R$).

Then an injection of a volume V_5 of CO_2 at the Hontomín site was simulated. The MT responses at Hi well position were calculated at two different depths: at surface $\boldsymbol{Z}_S$, and in the reservoir $\boldsymbol{Z}_R$ (at -478 m.a.s.l., which means 1448 m TVD). Both positions are indicated in Fig. 4.15. The effect of the upper layers was removed from the surface MT responses using the 1D models obtained for each polarisation (Fig. 4.14); Fig. 4.16 shows the results.

Post-injection layer stripping solutions (red stars in Fig. 4.16) are scattered for some short periods whereas for the longest ones they tend to overlap the pre-injection layer stripping solution (black stars) and agree with the ModEM responses. The results for the YX polarisation are better than the ones obtained for the XY polarisation. This fact could be due to the 1D model used in each case. In general, responses provided by ModEM in the reservoir are not recovered by the layer stripping method. However, this simulation highlights the improvement observed in the resolution of the MT responses to the resistivity changes produced in the reservoir.

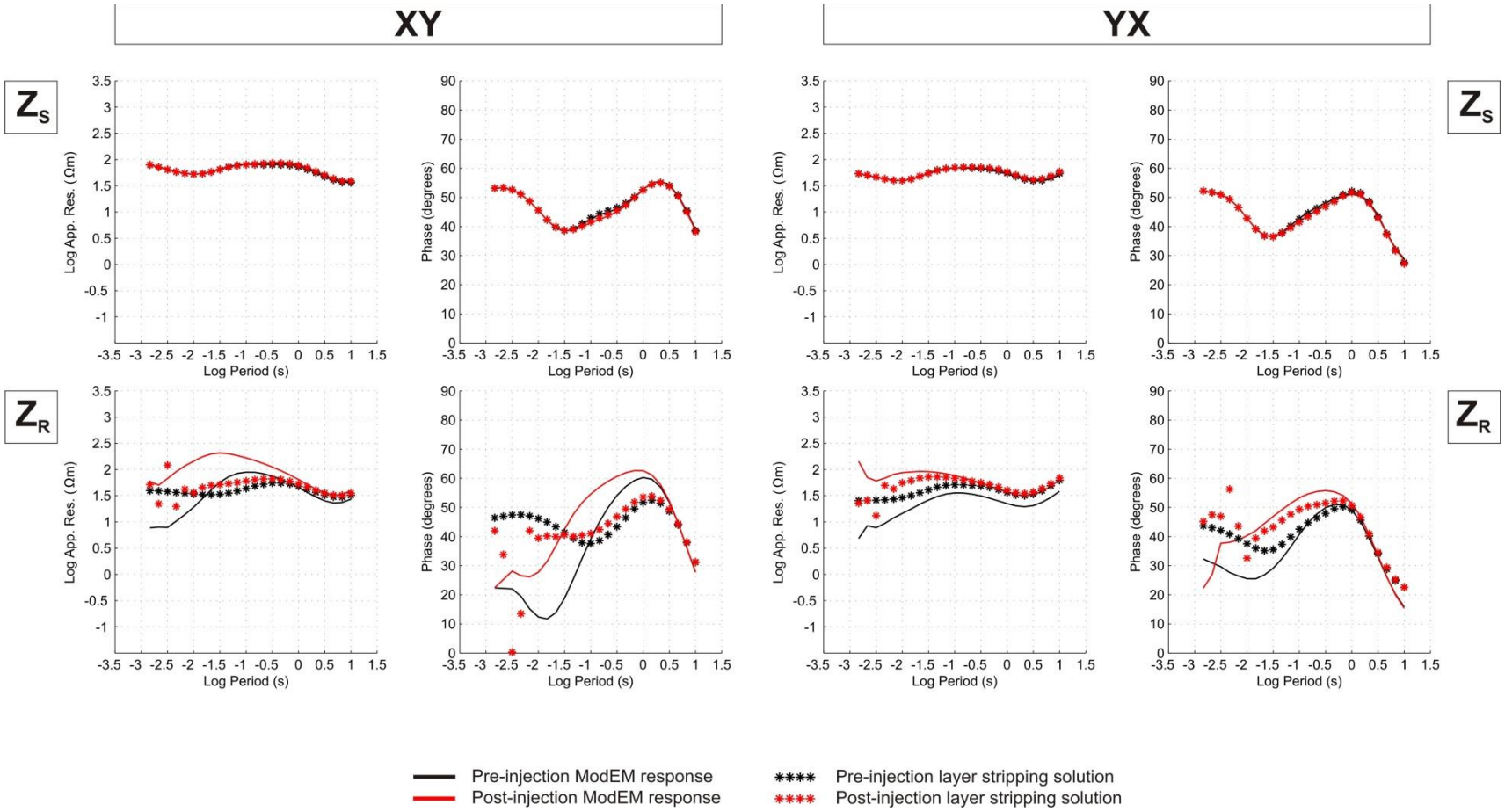

Fig. 4.16. Layer stripping for a simulated injection of CO_2 of a volume V_5 at the Hontomín site. Both MT responses on the surface ($\boldsymbol{Z}_S$) and in the reservoir ($\boldsymbol{Z}_R$) are shown. ModEM responses are plotted with continuous lines whereas the layer stripping results are plotted with small stars. In black are displayed the responses of the baseline model and in red, the responses with volume V_5 of CO_2 (Table 4.2).

4.5. Discussion

The magnetotelluric method allows monitoring huge volumes of CO_2 injection using surface data. However, the method can be insensitive to changes produced by small fluid volumes. For that reason, a new methodology is proposed, namely layer stripping. This approach aims to remove the effect of the upper layers from surface MT responses and enhance the resolution to resistivity changes produced in the reservoir.

Layer stripping is based on the recursive relation for deriving MT responses in a 1D Earth (Eq. 4.4). For monitoring purposes, this formulation has allowed obtaining more accurate results than other formulations, since the effect of the upper layers, not affected by the fluid injection, is removed. In Baba and Chave (2005) the stripping concept was applied to eliminate the topographic effects from the observed MT responses assuming the theoretical relationship

$$\boldsymbol{Z} = \boldsymbol{Z}_t \boldsymbol{Z}_m \quad (4.5),$$

where $\boldsymbol{Z}$ was the seafloor MT response which included the influence of the topography, $\boldsymbol{Z}_t$ was tensor describing the topographic effect, and $\boldsymbol{Z}_m$ was the responses without topography. If Eq. 4.5 is applied for monitoring resistivity changes located at $(n+l)$-layer (Fig. 4.1), the impedance tensor on the surface would be approached by

$$\boldsymbol{Z}_1 = \boldsymbol{Z}_{1n} \boldsymbol{Z}_n \quad (4.6),$$

where $\boldsymbol{Z}_{1n}$ would include the MT responses of the layers comprised between the surface and the n-layer, and $\boldsymbol{Z}_n$ would be the MT response on the top of the n-layer. Then, both $\boldsymbol{Z}_{1n}$ and $\boldsymbol{Z}_n$would be affected by resistivity variations produced at $(n+l)$-layer according to Eq. 4.2. Thus, whereas the stripping of $\boldsymbol{Z}_{1n}$ (Eq. 4.6) would also remove part of the effect of the fluid injection, with the formulation used in this work (Eq. 4.4) is possible to totally recover, to within experimental error, the effect of the injected fluid in 1D.

In 3D, layer stripping was demonstrated to work well and provide good approximate responses. Despite solutions that differed from the ones provided by ModEM (basically at

short periods), an important increase of the resolution with depth was observed, suggesting the suitability of the method for monitoring purposes.

Apart from the ability of monitoring smaller volumes of CO_2, the layer stripping methodology offers the advantage of avoiding repetition of complete 3D MT acquisition surveys. To have an overall control of the area, only a precise 3D baseline model of the study region is required. Once the baseline model is determined, the acquisition can be reduced to those sites most sensitive to the expected resistivity changes. However, special care should be taken when seeking equivalent 1D models to apply the layer stripping to the surface data. The conductance estimation (electrical conductivity and thickness product) can be inaccurate, placing the changes at incorrect depths (Peacock et al., 2012a). Thus, it is important to take into account the baseline model of the site to properly define the corresponding 1D models.

Synthetic MT responses calculated at depth show an important enhancement of the resolution compared to surface responses. This fact exhibits the potential of the Vertical Gradient Magnetometry (VGM). The method was already proposed some decades ago (Jones, 1983a; Spitzer 1993; Patella and Siniscalchi, 1994; Vellante, 1997; Schmucker et al., 2009) but has not been applied. Moreover, this method could offer the advantage of being affected by a lower EM noise level because the measure is acquired at depth.

At the Hontomín URL, it was estimated that the minimum volume of CO_2 detectable from surface MT data corresponds to 25 Megatons, since the involved differences in the MT surface responses are larger than the assumed experimental error (10 % for the apparent resistivity and 2.865 degrees for the phases). This constitutes the minimum volume required to detect resistivity variations from 10 Ωm to 40 Ωm (for an homogeneous CO_2 saturation of 50 %). Nevertheless, it was demonstrated that layer stripping would enhance the resolution of surface responses allowing monitoring of smaller volumes down to the order of 1.8 Megatons. Applying the layer stripping methodology to more than a single site may be possible to distinguish small resistivity variations from EM noise. Unfortunately, the layer stripping method could not enhance the resolution to those really small variations not detectable from surface data (CO_2 volumes on the order of 0.2 Megatons). Thereby, the

expected volume of CO_2 at the Hontomín site (no more than 0.02 Megatons) should be monitored using CSEM or other EM techniques.

Facing a real MT monitoring survey, it is advisable to have good control of the EM noise in order to obtain high-quality data. In the light of the experience acquired in the characterisation surveys of the Hontomín URL, it will be essential to use remote reference techniques (Ogaya et al., 2013). In addition, integration with other monitoring techniques could help to understand data variations. The In-SAR studies to control the ground deformation may help to link deformations to changes in the MT measurements. Aizawa et al. (2011) observed that a deformation of the ground can lead to a tilt of the coils, and as a consequence, to a variation of the impedance tensor. It could be also interesting to compare MT data to micro-seismicity results since micro fractures can produce changes in pore connectivity which may invoke changes in the rock resistivity. On the other hand, seasonal and diurnal weather conditions (e.g., rainfall and temperature changes) can also have small effects on the data (Aizawa et al., 2011; Aizawa et al., 2013).

4.6. Conclusions

Layer stripping is presented as an innovative methodology based on the analytical solution of the 1D MT problem. It aims to remove the effect of the well-known overlying structures in order to enhance the resolution at a giving depth. The method has been validated through synthetic studies for a 1D and 3D CO_2 plumes and tested in the Hontomín URL using the geoelectrical baseline model of the site. Obtained results demonstrate that the method can theoretically be applied in real monitoring surveys. In 3D, layer stripping does not recover the response predict by ModEM at depth but provides valuable approximate responses. The results suggest that layer stripping may improve the resolution of surface MT response being able to detect smaller resistivity changes. To analyse data from more than a single site will help to both (i) distinguish noise from true resistivity variation in those cases located in the detectability limit and (ii) locate the resistivity variations in space. Layer stripping methodology will simplify monitoring surveys avoiding carrying out periodic 3D

acquisitions. Additionally, synthetic MT responses at depth demonstrate the potential of borehole MT measurements and suggest the VGM method as a monitoring technique.

In the Hontomín URL, the minimum volume of CO_2 detectable from surface data corresponds to 25 Megatons, assuming a resistivity variations from 10 Ωm to 40 Ωm (homogeneous CO_2 saturation of 50 %). Nevertheless, using the layer stripping methodology it is possible to monitor smaller injection volumes on the order of 1.8 Megatons. For variations undetectable from surface data (e.g. the one expected at the Hontomín site), geoelectrical monitoring should be carry out using CSEM techniques. The development of the VGM is suggested.

Appendix 4.1. Correction term

It was found that there existed some small differences between the 1D analytical solution (Eq. 4.1-4.3) and ModEM responses. The observed discrepancies decreased with finer gridding. Thereby, those differences were attributed to the discretisation of the model. For the 58x59x81-layer grid (one of the meshes used in this work), the apparent resistivity and phase curves seem visually to overlap each other. However, when the difference between both of them was calculated, discrepancies smaller than 0.5 % for the apparent resistivity and 0.45 degrees for the phases were observed. Those differences were taken into account before applying the layer stripping to the surface data. Otherwise, the MT responses would not have been corresponded to the model that was actually being stripped away.

Accordingly, a correction term was applied to the ModEM responses that consisted of calculating the difference between the response of the code and its corresponding 1D analytical solution, for each of the 1D pre-injection model (baseline model). The same correction term was then applied to both the pre-injection model (without CO_2) and the post-injection model (with CO_2).

5 Conclusions and future work

In this thesis, the magnetotelluric method was used to characterise and monitor a geological reservoir of CO_2. Specifically, it was applied at the Hontomín site (Spain) where the CO_2 injection is planned to be into a deep saline aquifer. In agreement with the structure of the thesis, and according to the proposed objectives (section 1.7), the conclusions are organised in two sections. The first part is related to the magnetotelluric characterisation of the Hontomín site (main body of the thesis) and the second part, to the magnetotelluric monitoring. As is detailed below, the aims and objectives outlined at the beginning of the work have been achieved. Furthermore, some perspectives for future work are enumerated at the end of the chapter.

Magnetotelluric characterisation

The 3D geoelectrical baseline model of the Hontomín site is the major contribution of this thesis. The MT method has been demonstrated to be an appropriate geophysical technique to characterise the study area and to provide a 3D resistivity model of the URL.

The 1D analysis of all existing wells' resistivity log data allowed forming a general idea of the Hontomín structure, correlating different lithologies to electrical properties, and describing the electrical behaviour of the reservoir and seal units. The results showed that the primary reservoir-seal system was sensed in the period range of 0.1 to 1 s. Thereby, 1D resistivity models helped to design the fieldwork according to the characteristics of the study area and provided indispensable information for the modelling and inversion of the MT data.

The EM characterisation of the Hontomín site was divided into two stages: a 2D MT data acquisition carried out in Spring 2010 (MTD profile, modelled in Ogaya et al., 2013) and a 3D MT data acquisition undertaken in Autumn 2010 (Ogaya et al., 2012; Ogaya et al., 2014). The first 2D survey demonstrated the validity of the MT method to characterise the study area, showed the importance of using remote reference techniques to derive optimal MT responses, and provided a 2D geoelectrical model of the URL. The subsequent 3D survey completed the MT characterisation of the site and supplied the 3D geoelectrical baseline model of the URL.

The 2D resistivity model imaged a geoelectrical structure composed of four main layers: a resistive bottom layer (below -600 m.a.s.l.) linked to Keuper facies and to the Anhydrite unit; a conductive layer (below -200 m.a.s.l. and thickness up to 400 m) containing the primary reservoir and seal units; a resistive middle layer (between +700 m.a.s.l. and -200 m.a.s.l.) containing the secondary reservoir-seal system, and a conductive top layer (above +700 m.a.s.l.) linked to Upper Cretaceous sequences. In the southern part of the model, a fault region (F region) was imaged related to the Ubierna Fault. The F structure revealed an important conductive fluid circulation along the fracture region, unknown prior to the MT survey. The electrical resistivity obtained for the primary reservoir ranges between 8 and 25 Ωm, which means a porosity of between 9 % and 17 % according to Archie's law.

In general, the electrical responses of each formation in the 3D resistivity model coincide with the ones imaged in the previous 2D model. However, the 3D model provides the 3D spatial characterisation of the different units, showing the dome-like structure of the Hontomín site. The model images different fracture regions as well as the EW prolongation of the F fault. The F fault region affects all the layers of the model but does not outcrop at surface. A more conductive behaviour of the F fault is imaged in the eastern part of the study area that, according to hydrogeochemical studies (Buil et al., 2012; Nisi et al., 2013), could be indicative of a mixing process between deep and shallow aquifer waters. On the contrary, the western part of the fault is less conductive and seems to be imaged by a set of faults.

The 3D resistivity model is supported by a variety of multidisciplinary data. The resistivity structure of the Hi and Ha wells are reasonably well predicted by the model. The observed

dome structure is coherent with the structure observed in both microgravimetric (Implemental Systems, 2011) and 3D seismic results (Alcalde et al., 2013b; Alcalde et al., 2014). Likewise, the northern border of the F fault region spatially correlates with a set of faults interpreted in the 3D seismic volume and with a strong gradient of the Bouguer anomaly in the microgravimetry data. Thus, independent data sets were proven to provide coherent and reliable information.

During the monitoring of the URL, special attention should be paid to possible faults imaged in the secondary reservoir-seal system, neighbouring Hi well, and to the eastern part of the F fault region. Nevertheless, it is important to highlight that the volume of CO_2 expected in the Hontomín site is going to be small (less than 20 kilotons), which means that none of the above mentioned geoelectrical structures likely constitute an important leakage pathway.

The detailed geoelectrical characterisation presented here is an important contribution to CO_2 geological storage projects for two main reasons: (i) it demonstrates the valuable information that a 3D geoelectrical baseline model can provide, and (ii) it shows the importance of a high-resolution reference model to define the monitoring requirements. Three-dimensional magnetotelluric surveys are complementary to other 3D characterisation studies, such as reflection seismics and gravimetrics, and, due to electrical conductivity's sensitivity to fluid flow, makes for a method with superior resolution to particular aspects of interest and importance for CO_2 storage and long-term monitoring.

Magnetotelluric monitoring

In this thesis, the MT method has also been evaluated as a monitoring technique, carrying out different synthetic studies and sensitivity tests. Synthetic studies showed that differences between the pre-injection and the post-injection state (resolution to resistivity changes) increase with the depth at which data are acquired. Accordingly, an innovative methodology was developed, called layer stripping, based on the analytical solution of the 1D MT problem. The approach consists of enhancing the resolution of surface MT responses to resistivity variations produced at a given depth, removing the effect of the time-invariant upper layers of the structure. The geoelectrical structure of the study area has to be well

known to apply the proposed methodology; thus, an accurate geoelectrical baseline model of the study area is required.

The methodology was validated through synthetic studies and tested theoretically at the Hontomín URL. In 3D, layer stripping solutions did not recover exactly the MT responses expected at depth but provided valuable approximate responses. The method made possible enhanced resolution with apparent resistivity and phase variations far greater than the ones observed on the surface. Facing a real case study, to analyse data from more than a single site will help to distinguish noise from small resistivity variation and to locate the resistivity variations in the space.

Theoretically, in the Hontomín URL, the minimum volume of CO_2 detectable from surface data corresponds to 25 Megatons, assuming resistivity variations from 10 Ωm to 40 Ωm (homogeneous CO_2 saturation of 50 %). Nevertheless, using the layer stripping methodology it will be possible to monitor smaller injection volumes on the order of 1.8 Megatons.

Future work

Finally, some perspectives of future work are enumerated. In reference to the characterisation work, the acquisition of a new MT profile in the eastern part of the modelled region is proposed to study the geoelectrical behaviour of the fault set located in the east. Although the fault set is outside the limits of the URL, the new profile would complete the MT characterisation of the Hontomín site.

According to the encouraging results obtained in the correlation of the 3D model with the other geophysical data acquired at the URL, an attractive, but challenging, task to face in the future would be to carry out a joint inversion of all the available geophysical data. In particular, joint inversion combining magnetotelluric and seismic data will be interesting to better describe the different fault sets. In addition, it would be interesting to study to what extent 3D density and 3D velocity models can be derived from the 3D resistivity model using the available log data.

On the other hand, the development of the Vertical Gradient Magnetometry (VGM) is suggested. Not only to be applied as a monitoring technique, but also as a high-resolution characterisation technique.

In reference to the layer stripping approach, to test the technique with real post-injection data would be fundamental in order to further develop the methodology.

References

Aizawa, K., Kanda, W., Ogawa, Y., Iguchi, M., Yokoo, A., Yakiwara, H., Sugano, T., 2011. Temporal changes in electrical resistivity at Sakurajima volcano from continuous magnetotelluric observations. Journal of Volcanology and Geothermal Research 199, 165-175.

Aizawa, K., Koyama, T., Uyeshima, M., hace, H., Hashimoto, T., Kanda, W., Yoshimura, R., Utsugi, M., Ogawa, Y., Yamazaki, K., 2013. Magnetotelluric and temperature monitoring after the 2011 sub-Plinian eruptions of Shinmoe-dake volcano. Earth Planets Space 65, 539-550, doi: 10.5047/eps.2013.05.008.

Aizawa, K., Yokoo, A., Kanda, W., Ogawa, Y., Iguchi, M., 2010. Magnetotelluric pulses generated by volcanic lightening at Sakurajima volcano, Japan. Geophysical Research Letters 37, L17301, doi: 10.1029/2010GL044208.

Alcalde, J., Martí, D., Calahorrano, A., Marzán, I., Ayarza, P., Carbonell, R., Juhlin, C., Pérez-Estaún, A., 2013a. Active seismic characterization experiments of the Hontomín research facility for geological storage of CO_2, Spain. International Journal of Greenhouse Gas Control 19, 785-795, doi: 10.1016/j.ijggc.2013.01.039.

Alcalde, J., Martí, D., Juhlin, C., Malehmir, A., Sopher, D., Saura, E., Marzán, I., Ayarza, P., Calahorrano, A., Pérez-Estaún, A., Carbonell, R., 2013b. 3-D reflection seismic imaging of the Hontomín structure in the Basque-Cantabrian basin (Spain). Solid Earth 4, 481-496, doi: 10.5194/se-4-481-2013.

Alcalde, J., Marzán, I., Saura, E., Martí, D., Ayarza, P., Juhlin, C., Pérez-Estaún, A., Carbonell, R., 2014. 3D geological characterization of the Hontomín CO2 storage site, Spain: multidisciplinary approach from seismics, well-logging and regional data. Tectonophysics (Accepted).

Alemu, B.L., Aker, E., Soldal, M., Johnsen, Ø., Aagaard, P., 2011. Influence of CO2 on rock physics properties in typical reservoir rock: A CO2 flooding experiment of brine saturated sandstone in a CT-scanner. Energy Proceedia 4, 4379-4386, doi: 10.1016/j.egypro.2011.02.390.

Álvarez, C., 1994. Hydrocarbons in Spain – exploration and production. First Break 12, Volume 1, doi: 10.3997/1365-2397.1994004

Álvarez de Buergo, E., García, A., 1996. Cálculo de reservas remanentes de hidrocarburos en zonas estructuralmente complejas: aplicación al campo de "Ayoluengo". Geogaceta 20, 161-164.

Andréis, D., MacGregor, L., 2011. Using CSEM to monitor production from a complex 3D gas reservoir- A synthetic case study. The Leading Edge 30(9), 1070-1079.

Archie, G.E., 1942. The electrical resistivity log as an aid in determining some reservoir characteristics. Transactions of AIME 146, 54–67.

Arrhenius, S., 1896. On the Influence of Carbonic Acid in the Air upon the Temperature of the Ground. Philosophical Megazine and Journal of Science 5(41), 237-276.

Avdeev, D.B., 2005. Three-dimensional electromagnetic modelling and inversion from theory to application. Surveys in Geophysics 26(6), 767-799, doi: 10.1007/s10712-005-1836-2.

Baba, K., Chave, A., 2005. Correction of seafloor magnetotelluric data for topographic effects during inversion. Journal of Geophysical Research 110, B12105, doi: 10.1029/2004JB003463.

Bachu, S., 2000. Sequestration of CO2 in geological media: criteria and approach for site selection in response to climate change. Energy Conversion and Management 41(9), 953-970, doi: 10.1016/S0196-8904(99)00149-1.

Bachu, S., 2003. Screening and ranking of sedimentary basins for sequestration of CO2 in geological media in response to climate change. Environmental Geology 44, 277-289, doi: 10.1007/s00254-003-0762-9.

Bahr,K., 1988. Interpretation of the magnetotelluric impedance tensor: regional induction and local telluric distortion. Journal of Geophysics 62, 119-127.

Batzle, M., Wang, Z. 1992. Seismic properties of pore fluids. Geophysics 57, 1396-1408.

Beamish, D., Travassos, J.M., 1992. The use of D^+ solution in magnetotelluric interpretation. Journal of Applied Geophysics 29, 1-19, doi: 10.1016/0926-9851(92)90009-A.

Becken, M., Ritter, O., Burkhardt, H., 2008. Mode separation of magnetotelluric responses in three-dimensional environments. Geophysical Journal International 172, 67-86, doi: 10.1111/j.1365-246X.2007.03612.x.

Becken, M., Streich, R., Krüger, K., Ritter, O., 2010. Exploration and monitoring of CO_2 storage sites using controlled-source electromagnetic: results of a feasibility study at Ketzin, Germany. XL385 EGU2010-7966, EGU General Assembly 2010.

Bedrosian, P.A., 2007. MT+, Integrating Magnetotellurics to Determine Earth Structure, Physical State, and Processes. Surveys in Geophysics 28, 121–167, doi: 10.1007/s10712-007-9019-6.

Benjumea, B., Macau, A., Figueres, S., Gabàs, S., Sendra, R., Marzán, I., 2012. Testificación geofísica de los sondeos de investigación hidrogeológica de Hontomín (Burgos). IGC – Institut Geològic de Catalunya Technical Report, GA-002/12, Generalitat de Catalunya, 36 pp.

Berdichevsky, M.N., Bezruk, I.A., Chinavera, O.M., 1973. Magnetotelluric sounding with the use of mathematical filters. Izv. Akad. Nauk. SSSR. Fiz. Zeml. 3, 72-92.

Berdichevsky, M.N., Dmitriev, V.I., 1976a. Distortion of magnetic and electric fields by near-surface lateral inhomogeneities. Acta. Geodaet., Geophys. Et montanist Acad. Sci. Hung. 11, 447-483.

Berdichevsky, M.N., Dmitriev, V.I., 1976b. Principles of interpretation of magnetotelluric sounding curves, in: Adam, A. (Ed.), Geoelectric and geothermal studies, KAPG geophysical monograph, pp. 165-221. Akadémiai Kiadó, Budapest.

Berdichevsky, M.N., Dmitriev, V.I., 2008. Models and Methods of Magnetotellurics. Springer, 563 pp, ISBN: 978-3-540-77811-0.

Bergmann, O., Ivandic, M., Norden, B., Rücker, C., Kiessling, D., Lüth, S., Schmidt-Hattenberger, C., Juhlin, C., 2014. Combination of seismic reflection and constrained resistivity inversion with an application to 4D imaging of the CO_2 storage site, Ketzin, Germany. Geophysics 97(2), B37-B50, doi: 10.1190/geo2013-0131.

Bergmann, P., Lengler, U., Schmidt-Hattenberger, C., Giese, R., Norden, B., 2010. Modelling the geoelectric and seismic reservoir response caused by carbon dioxide injection based on multiphase flow simulation: results from the CO_2SINK project. Chemie der Erde 70 (S3), 173-183, doi: 10.1016/j.chemer.2010.05.007.

Bergmann, P., Schmidt-Hattenberger, C., Kiessling, D., Rücker, C., Labitzke, T., Henninges, J., Baumann, G., Schütt, H., 2012. Surface-downhole electrical resistivity tomography applied to monitoring of CO_2 storage at Ketzin, Germany. Geophysics 77, B253-B267, doi: 10.1190/geo2011-0515.1.

Beroiz, C., Permanyer, A., 2011. Hydrocarbon habitat of the Sedano trough, Basque-Cantabrian Basin, Spain. Journal of Petroleum Geology 34(4), 387-409, doi: 10.1111/j.1747-5457.2011.00511.x

Berre, I., Lien, M., Mannseth, T., 2011. Identification of three-dimensional electric conductivity changes from time-lapse electromagnetic observations. Journal of Computational Physics 230, 3915-3928, doi: 10.1016/j.jcp.2011.02.015.

Bhuyian, A.H., Landrø, M., Johansen, S.E., 2012. 3D CSEM modelin and time-lapse sensitivity analysis for subsurface CO_2 storage. Geophysics 77(5), E343-E355, doi: 10.1190/geo2011-0452.1.

Black, N., Zhdanov, M.S., 2009. Monitoring of hydrocarbon reservoirs using marine CSEM method. SEG Tech. prog. Expanded Abstracts 28(1), 850-854, doi: 10.1190/1.3255884.

Blanchard, T. D., 2011. Time-lapse seismic attenuation as a tool for monitoring hydrocarbons and CO_2 in geological materials. PhD Thesis, The University of Leeds, School of Earth and Environment, UK, 275 pp.

Boerner, D.E., 1992. Controlled source electromagnetic deep sounding: theory, results and correlation with natural source results. Surveys in Geophysics 13, 435-488.

Boillot, G., Capdevila, R., 1977. The Pyrenees: subduction and collision? Earth and Planetary Science Letters 35, 151-160.

Boillot, G., Malod, J., 1988. The North and North-West Spanish continental margin. Revista de la Sociedad Geológica de España 1, 295-316.

Börner, R.U., 2010. Numerical Modelling in Geo-Electromagnetics: Advances and Challenges. Surveys in Geophysics 31(2), 225-245, doi: 10.1007/s10712-009-9087-x.

Börner, J.H., Herdengen, V., Repke, J.U., Spitzer, K., 2013. The impact of CO2 on the electrical properties of water bearing porous madia-laboratory experiments with respect to carbon capture and storage. Geophysical Prospecting 61(Suppl. 1), 446-460, doi: 10.1111/j.1365-2478.2012.01129.x.

Bourgeois, B., Girard, J.F., 2010. First modelling results of the em response of a CO_2 storage in the Paris basin. Oil & Gas Science and Technological Review – IFP 65(4), 597–614, doi: 10.2516/ogst/2009076.

Breen, S.J., Carrigan, C.R., LaBrecque, D.J., Detwiler, R.L., 2012. Bench-scale experiments to evaluate electrical resistivity tomography as a monitoring tool for geologic CO_2 sequestration. International Journal of Greenhouse Gas Control 9, 484-494, doi: 10.1016/j.ijggc.2012.04.009.

Bryant, E., 1997. Climate process and change. Cambridge University Press, Cambridge, ISBN: 9780521484404.

Buil, B., Gómez, P., Peña, J., Garralón, A., Galarza, C., Durán, J.M., Domínguez, R., Escribano, A., Turrero, M.J., Robredo, L.M., Sánchez, L., 2012. Caracterización y monitorización hidrogeoquímica de los acuíferos superiores a la formación almacenamiento de CO_2 (Hontomín, Burgos) y actualización de la caracterización de aguas superficiales. Technical report CIEMAT/DMA/2G010/1/2012.

Cagniard, L., 1953. Principe de la métode magnéto-tellurique, nouvelle méthode de prospection géophysique. Annales de Géophysique 9(2), 95-125.

Caldwell, T.G., Bibby, H.M., Brown, C., 2004. The magnetotelluric phase tensor. Geophysical Journal International 158, 457-469, doi: 10.1111/j.1365-246X.2004.02281.x.

Canal, J., Delgado, J., Falcón, I., Yang, Q., Juncosa, R., Barrientos, V., 2013. Injection of CO_2-saturated water through a siliceous sandstone plug from the Hontomin Test Site (Spain): experiments and modeling. Environmental Science & Technology 47(1), 159-167, doi: 10.1021/es3012222.

Carola, E., Tavani, S., Ferrer, O., Granado, P., Quintà, A., Butillé, M., Muñoz, J. A., 2013. Along-strike extrusion at the transition between thin- and thick-skinned domains in the Pyrenean Orogen (northern Spain), in: Nemcok, M., Mora, A.R., Cosgrove, J.W. (Eds.), Thin-Skin-Dominated Orogens: From initial Inversion to Full Acretion. Geological Society, London, Special Publications 377(1), 119-140, doi: 10.1144/SP377.3.

Carrigan, C.R., Ramirez, A.L., Newmark, R.L., Aines, R., Friedman, S.J., 2009. Application Of ERT For Tracking CO_2 Plume Growth And Movement At The SECARB Cranfield Site. 8th Annual Conference on CARBON Capture & Sequestration Pittsburgh, PA, United States, 4-7 May 2009.

Carrigan, C.R., Yang, X., LaBrecque, D.J., Larsen, D., Freeman. D., Ramirez, A.L., Daily, W., Aines, R., Newmark, R., Friedman, J., Hovorka, S., 2013. Electrical resistance tomographic monitoring of CO_2 movement in deep geologic reservoirs. International Journal of Greenhouse Gas Control 18, 401-408, doi: 10.1016/j.ijggc.2013.04.016.

Chave, A.D., 2012. Estimation of the magnetotelluric response function, in: Chave, A. D., Jones, A. G. (Eds.), The Magnetotelluric Method: Theory and Practice, Chapter 4, pp. 165-218. Cambridge University Press, Cambridge (UK), ISBN: 978-0-521-81927-5.

Chave A.D., Jones, A.G., 1997. Electric and magnetic field distortion decomposition of BC87 data. Journal of Geomagnetism and Geoelectricity 49, 767-789.

Chave, A.D., Jones, A.G., 2012. The magnetotelluric method: Theory and Practice. Cambridge University Press, Cambridge (UK), 570 pp., ISBN: 978-0-521-81927-5.

Chave, A.D., Thomson, D.J., 2004. Bounded influence magnetotelluric response function estimation. Geophysical Journal International 157, 988–1006, doi: 10.1111/j.1365-246X.2004.02203.x.

Christensen, N.B., Sherlock, D., Dodds, K., 2006. Monitoring CO_2 injection with crosshole electrical resistivity tomography. Exploration Geophysics 37, 44-49.

CO2CRC, 2008. Storage Capacity Estimation, Site Selection and Characterisation for CO2 Storage Projects. Cooperative Research Centre for Greenhouse Gas Technologies, Canberra, CO2CRC Report No. RPT08-1001, 52 pp.

Constable, S.C., 1990. Marine electromagnetic induction studies. Surveys in Geophysics 11(2-3), 303-327.

Constable, S., 2010. Ten years of marine CSEM for hydrocarbon exploration. Geophysics 75(5), 75A67-75A81.

Constable, S., Srnka, L.J., 2007. An introduction to marine controlled source electromagnetic methods for hydrocarbon exploration. Geophysics 72(2), WA3-WA12.

de Groot-Hedlin, C., Constable, S., 1990. Occam's inversion to generate smooth, two-dimensional models from magnetotelluric data. Geophysics 55, 1613-1624.

Directive 2009/31/EC of the European Parliament and of the Council of 23 April 2009 on the geological storage of carbon dioxide and amending Council Directive 85/337/EEC, European Parliament and Council Directives 2000/60/EC, 2001/80/EC, 2004/35/EC, 2006/12/EC, 2008/1/EC and Regulation (EC) No 1013/2006.

Edwards, N., 2005. Marine controlled source electromagnetics: principles, methodologies, future commercial applications. Surveys in Geophysics 26, 675-700.

Egbert, G.D., Booker, J.R., 1986. Robust estimation of Geomagnetic transfer functions. Geophysical Journal of the Royal Astronomical Society 87, 173–194.

Egbert, G.D., Kelbert, A., 2012. Computational Recipes for EM Inverse Problems. Geophysical Journal International 189(1), 251-267, doi: 10.1111/j.1365-246X.2011.05347.x.

Elío, J., 2013. Estrategias de monitorización de CO_2 y otros gases en los estudios de análogos naturales. PhD Thesis. Universidad Politécnica de Madrid, Madrid, Spain, 416 pp.

Elío, J., Nisi, B., Ortega, M.F., Mazadiego, L.F., Vaselli, O., Grandia, F., 2013. CO_2 soil flux baseline at the technological development plant for CO_2 injection at Hontomin (Burgos, Spain). International Journal of Greenhouse Gas Control 18, 224-236, doi: 10.1016/j.ijggc.2013.07.013.

Escalas, M., Queralt, P., Ledo, J., Marcuello, A., 2013. Polarisation analysis of magnetotelluric time series using a wavelet-based scheme: A method for detection and characterisation of cultural noise sources. Physics of the Earth and Planetary Interiors 218, 31-50, doi: 10.1016/j.pepi.2013.02.006.

Farquharson, C.G., Craven, J.A., 2009. Three-dimensional inversion of magnetotelluric data for mineral exploration: An example from the McArthur River uranium deposit, Saskatchewan, Canada. Journal of Applied Geophysics 68(4), 450-458, doi: 10.1016/j.jappgeo.2008.02.002.

Gallardo, L. A., Meju, M. A., 2003. Characterization of heterogeneous near-surface materials by joint 2D inversion of DC resistivity and seismic data. Geophysical Research Letters 30(13), 1658, doi: 10.1029/2003GL017370.

Gallardo, L. A., Meju, M. A., 2011. Structure-coupled multiphysics imaging in geophysical sciences. Reviews of Geophysics 49, RG1003, doi: 10.1029/2010RG000330.

Gamble, T.D., Goubau, W.M., Clarke, J., 1979. Magnetotellurics with a remote magnetic reference. Geophysics 44, 53–68.

García Lobón, J.L., Reguera García, M.I., Martín León, J., Rey Moral, C., Berrezuerta Alvarado, E.R., Pérez Ortiz, I., 2011. Resumen ejecutivo del 'Plan de selección y caracterización de áreas y estructuras favorables para el almacenamiento geológico de CO_2 en España', Fondo Documental del IGME, Informe SID 64055, Madrid.

García-Mondéjar, J., 1996. Plate reconstruction of the Bay of Biscay. Geology 24(7), 635–638, doi: 10.1130/0091-7613(1996)024.

García-Ríos, M., Luquot, L., Soler, J. M., and Cama, J., 2013.Laboratory scale interaction between CO2-rich brine and reservoir rocks (limestone and sandstone). Procedia Earth and Planetary Science 7, 109–112.

Ghaedrahmati, R., Moradzadeh, A., Fathianpour, N., Lee, S.K., Porkhial, S., 2013. 3-D inversion of MT data from the Sabalan geothermal field, Ardabil, Iran. Journal of Applied Geophysics 93, 12-24, doi: 10.1016/j.jappgeo.2013.03.006.

Giese, R., Henninges, J., Lüth, S., Morozova, D., Schmidt-Hattenberger, C., Würdemann, H., Zimmer, M., Cosma, C., Juhlin, C., CO2SINK Group, 2009. Monitoring at the CO_2SINK Site: A Concept Integrating Geophysics, Geochemistry and Microbiology. Energy Procedia 1, 2251-2259, doi: 10.1016/j.egypro.2009.01.293.

Girard, J.F., Coppo, N., Rohmer, J., Bourgeois B., Naudet, V., Schmidt-Hattenberger, C., 2011. Time-lapse CSEM monitoring at Ketzin (Germany) CO_2 injection using 2xMAM configuration. Energy Procedia 4, 3322-3329.

Global CCS Institute, 2011. The global status of CCS: 2011, Canberra, Australia, ISBN: 978-0-9871863-0-0.

Glover, P.W.J., Hole, M.J., Pous, J., 2000. A modified Archie's law for two conducting phases. Earth and Planetary Science Letters 180, 369-383.

Grandis, H., Menvielle, M., Roussignol, M., 1999. Bayesian inversion with Markov chains-I. The magnetotelluric on-dimensional case. Geophysical Journal International 138(3), 757-768.

Groom, R.W., Bailey, R.C., 1989. Decomposition of magnetotelluric impedance tensor in the presence of local three-dimensional galvanic distortion. Journal of Geophysical Research 94, 1913-1925.

Haddadji, R., 2006. The In-Salah CCS experience, Sonatrach, Algeria. The First International Conference on the Clean Development Mechanism, 19-21 September 2006, Riyadh, Saudi Arabia.

Hagrey, S.A., 2011. CO_2 plume modelling in deep saline reservoirs by 2D ERT in boreholes. The Leading Edge 30(24), 24-33, doi: 10.1190/1.3535429.

Hagrey, S.A., Strahser, M., Rabbel, W., 2013. Seismic and geoelectric modeling studies of parameters controlling CO_2 geostorage in saline formations. International Journal of Grennhouse Gas Control 19, 796-806, doi: 10.1016/j.ijggc.2013.01.041.

Hanekop, O., Simpon, F., 2006. Error propagation in electromagnetic transfer functions: what role for the magnetotelluric method in detecting earthquake precursors? Geophysical Journal International 165, 763-774, doi: 10.1111/j.1365-246X.2006.02948.x.

Harris, P., MacGregor, L., 2006. Determination of reservoir properties from the integration of CSEM and seismic data. First Break 24, 15-21.

Harris, P., Du, Z., MacGregor, L., Olsen, W., Shu, R., Cooper, R., 2009. Joint interpretation of seismic and CSEM data using well log constraints: an example from Luva Field. First Break 27, 73-81.

He, Z., Hu, Z., Luo, W., Wang, C., 2010. Mapping reservoirs based on resistivity and induced polarization derived from continuous 3D magnetotelluric profiling: Case study from Qaidim basin, China. Geophysics 75(1), B25-B33, doi: 10.1190/1.3279125.

Heise, W., Caldwell, T.G., Bibby, H.M., Bannister, S.C., 2008. Three-dimensional modeling of the magnetotelluric data from the Rotakawa geothermal field, Taupo Volcanic Zone, New Zeland. Geophysical Journal International 173, 740-750, doi: 10.1111/j.1365-246X.2008.03737.x.

Hoversten, G.M., Gasperikova, E., 2005. Non-seismic geophysical approaches to monitoring, in: Thomas, D.C., Benson, S.M. (Eds.), Carbon Dioxide Capture for Storage in Deep Geologic Formations. Elsevier Ltd., Oxford, UK, Volume 2, 1071-1112.

Hoversten, G.M., Gritto, R., Washbourne, J., Daley, T., 2003. Pressure and fluid saturation prediction in a multicomponent reservoir using combined seismic and electromagnetic imaging. Geophysics 68 (5), 1580-1591, doi: 10.1190/1.1620632.

IEA-International Energy Agency, 2012. CO2 emissions from fuel combustion: Highlights, UEA Publications, Paris, France.

Implemental Systems, 2011. Informe de la campaña gravimétrica para el "Proyecto de microgravimetría en la Plataforma Burgalesa". Technical report CIUDEN Exp.1977/2010.

Ingham, M.R., Bibby, H.M., Heise, W., Jones, K.A., Cairns, P., Dravitzki, S., Bennie, S.L., Caldwell, T.G., Ogawa, Y., 2009. A magnetotelluric study of Mount Ruapehu volcano, New Zealand. Geophysical Journal International 179(2), 887-904, doi: 10.1111/j.1365-246X.2009.04317.x.

IPCC – Intergovernmental Panel on Climate Change, 2005. IPCC Special Report on Carbon Dioxide Capture and Storage. Prepared by Working Group III of the Intergovernmental Panel on Climate Change [Metz, B., O. Davidson, H. C. de Coninck, M. Loos, and L. A. Meyer (Eds.)]. Cambridge University Press, Cambridge, United Kingdom and New York, NY, USA.

JafarGandomi, A., Curtis, A., 2011. Detectability of petrophysical properties of subsurface CO_2-saturated aquifer reservoirs using surface geophysical methods. The Leading Edge 30(10), 1112-1121.

Jegen, M. D., Hobbs, R.W., Tarits, P., Chave, A., 2009. Joint inversion of marine magnetotelluric and gravity data incorporating seismic constraints. Preliminary results of sub-basalt imaging off the Faroe Shelf. Earth Planetary Scientific Letters 282, 47-55.

Jiracek, G., 1990. Near-surface and topographic distortions in electromagnetic induction. Surveys in Geophysics 11(2-3), 163-203, doi: 10.1007/BF01901659.

Jones, A.G, 1983a. A passive Natural-Source Twin-Purpose Borehole Technique: Vertical Gradient Magnetometry (VGM). Journal of Geomagnetism and Geoelectricity 35, 473-490, ISSN: 0022-1392.

Jones, A.G., 1983b. The problem of the current channelling: a critical review. Geophysical Surveys 6, 79-122.

Jones, A. G., 2011. Three-dimensional galvanic distortion of three-dimensional regional conductivity structures: Comment on "Three-dimensional joint inversion for magnetotelluric resistivity and static shift distributions in complex media" by Yutaka Sasaki and Max A. Meju. Journal of Geophysical Research 16, B12104, doi: 10.1029/2011JB008665.

Jones, A.G., 2012. Distortion of magnetotelluric data: its identification and removal, in: Chave, A. D., Jones, A. G. (Eds.), The Magnetotelluric Method: Theory and Practice, Chapter 6, pp. 219-302. Cambridge University Press, Cambridge (UK), ISBN: 978-0-521-81927-5.

Jones, A.G., Chave, A.D., Egbert, G., Auld, D., Bahr, K., 1989. A comparison of Techniques for Magnetotelluric Response Function Estimation. Journal of Geophysical Research 94(B10), 14201-14213, doi: 10.1029/JB094iB10p14201.

Kang, S., Jee Seol, S., Byun, J., 2012. A feasibility study of CO_2 sequestration monitoring using the mCSEM method at a deep brine aquifer in a shallow sea. Geophysics 77(2), E117-E126, doi: 10.1190/geo2011-0089.

Kappler, K.N., Frank Morrison, H., Egbert, G.D., 2010. Long-term monitoring of ULF electromagnetic fields at Parkfield, California. Journal of Geophysical Research 115, B04406, doi: 10.1029/2009JB006421.

Kaufman, A., Keller, G.V., 1981. The magnetotelluric sounding method. Methods in Geochemistry and Geophysics 15, 583 pp.

Key, K., 2012. Marine electromagnetic studies of seafloor resources and textonics. Surveys in Geophysics 33, 135-167.

Kiessling, D., Schmidt-Hattenberger, C., Schuett, H., Schilling, F., Krueger, K., Schoebel, B., Danckwardt, E., Kummerow, J., CO2SINK Group, 2010. Geoelectrical methods for monitoring geological CO_2 storage: First results from cross-hole and surface-downhole measurements from the CO2SINK test site at Ketzin (Germany). International Journal of Greenhouse Gas Control 4(5), 816-826, doi: 10.1016/j.ijggc.2010.05.001.

Kiyan, D., Jones, A.G., Vozar, J., 2014. The inability of magnetotelluric off-diagonal impedance tensor elements to sense oblique conductors in 3-D inversion. Geophysical Journal International 196, 1351-1364, doi:10.1093/gji/ggt470.

Ledo, J., 2006. 2-D versus 3-D magnetotelluric data interpretation. Surveys in Geophysics 27(5), 511-543.

Ledo, J., Jones, A.G., 2005. Upper mantle temperature determined from combining mineral composition, electrical conductivity laboratory studies and magnetotelluric field observations: application to the intermontane belt, Northern Canadian Cordillera. Earth and Science Letters 236, 258–268, doi: 10.1016/j.epsl.2005.01.044.

Ledo, J., Queralt, P., Martí, A., Jones, A.G., 2002. Two-dimensional interpretation of three-dimensional magnetotelluric data: an example of limitations and resolution.

Gephysical Journal International 150(1), 127-139, doi: 10.1046/j.1365-246X.2002.01705.x.

Le Pichon, X., Sibuet, J. C., 1971.Western extension of boundary between European and Iberian plates during the Pyrenean orogeny. Earth Planetary Scientific Letters 12, 83-88.

Lien, M., Mannseth, T., 2008. Sensitivity study of marine CSEM data reservoir production monitoring. Geophysics 73(4), F151-F163, doi: 10.1190/1.2938512.

Liu, Z., Moysey, S.M.J., 2012. The Dependence of Electrical Resistivity-Saturation Relationships on Multiphase Flow Instability. ISRN Geophysics 2012, 1-10, doi: 10.5402/2012/270750.

Lumley, D., 2010. 4D seismic monitoring of CO2 sequestrattion. The Leading Edge 29 (2), 150-155, doi: 10.1190/1.3304817.

Lupion, M., Diego, R., Loubeau, L., Navarrete, B., 2011a. CIUDEN CCS project: Status of the CO2 capture technology development plant in power generation. Energy Procedia 4, 5639-5646.

Lupion, M., Navarrete, B., Otero, P., Cortés, V.J., 2011b. Experimental programme in CIUDEN's CO2 capture technology development plant for power generation. Chemical Engineering Research and Design 89 (9), 1494-1500.

MacGregor, L., 2012. Integrating seismic, CSEM, and well log data for reservoir characterization. The Leading Edge 31(3), 268–277.

Mackie, R. L., Madden, T. R., 1993. Three dimensional magnetotelluric inversion using conjugate gradients. Geophysical Journal International 115, 215-229, doi: 10.1111/j.1365-246X.1993.tb05600.x

Magee, J.W., 1991. Thermophysical properties of CO_2 and CO_2-rich mixtures, in: Bruno, T.J. Ely, J.F (Eds.), Supercritical Fluid Technology. CRC Press, Boca Raton, FL, Chapter 8, 329 pp.

Márquez, M., Jurado, M.J., 2011. Petrophysical characterization of a CO_2 storage reservoir using well logs. Geophysical Research Abstracts, vol. 13, EGU2011-6891-3. EGU General Assembly 2011.

Martí, A., Queralt, P., Ledo, J., 2009. WALDIM: A code for the dimensionality analysis of magnetotelluric data using rotational invariants of the magnetotelluric tensor. Computer & Geosciences 35(12), 2295-2303, doi: 10.1016/j.cageo.2009.03.004.

McNeice, G.W., Jones, A.G., 2001. Multisite, multifrequency tensor decomposition of magnetotelluric data, Geophysics 66 (1), 158-173.

Merten, R., 2006. Petroleum exploration and production in Spain. Zeitschrift der Deutschen Gesellschaft Für Geowissenschaften 157, 717-732

Metcalf, A., Granados, A., Delgado-Huertas, A., 2013. Determining seasonal natural effects over isotopic baselines for CO_2 storage monitoring. Energy Procedia (Accepted).

Miensopust, M.P., 2010. Multidimensional Magnetotellurics: A 2D Case Study and a 3D Approach to Simultaneously Invert for Resistivity Structure and Distortion Parameters. PhD thesis, National University of Ireland, Galway, Ireland, 353 pp.

Miensopust, M.P., Queralt, P., Jones, A.G. and the 3D MT modellers, 2013. Magnetotelluric 3D inversion – a recapitulation of two successful workshops on forward and inversion code testing and comparison. Geophysical Journal International 193(3), 1216-1238, doi: 10.1093/gji/ggt066.

Montadert, L., de Charpal, O., Roberts, D., Guennoc, P., Sibuet, J.C., 1979. Northeast Atlantic passive continental margins: rifting and subsidence processes, in: Talwani, M., Hay, W., Ryan, W.B.F. (Eds.), Deep Drilling Results in the Atlantic Ocean: Continental Margins and Paleoenvironment. Maurice Ewing Ser., vol. 3. AGU, Washington, DC, 154-186, doi: 10.1029/ME003p0154.

Moorkamp, M., Heincke, B., Jegen, M., Roberts, A.W., Hobbs, R., W., 2011. A framework for 3-D joint inversion of MT, gravity and seismic refraction data. Geophysical Journal International 184(1), 477-493, doi: 10.1111/j.1365-246X.2010.04856.x.

Muñoz, J.A., 1992. Evolution of a continental collision belt: ECORS-Pyrenees crustal balanced section, in: McClay, K.R. (Ed.), Thrust Tectonics. Chapman and Hall, London, 370-385.

Muñoz, J.A., 2002. The Pyrenees, in: Gibbons, W., Moreno, T. (Eds.), The Geology of Spain. Geological Society, London, pp. 370–385.

Myer, L.R., 2001. Laboratory measurement of geophysical properties for monitoring of CO2 sequestration. 1st National Conference on Carbon Sequestration, Morgantown, West Virginia, Session 6A, p. LBNL-47643.

Nakatsuka, Y., Xue, Z., Garcia, H., Matsuoka, T., 2010. Experimental study on CO_2 monitoring and quantification of stored CO_2 in saline formations using resistivity measurements. International Journal of Greenhouse Gas Control 4, 209–216, doi: 10.1016/j.ijggc.2010.01.001.

NETL- National Energy Technology Laboratory, 2009. Best practices for: Monitoring, Verification, and Accounting of CO_2 Stored in Deep Geologic Formations. U.S. Department of Energy, DOE/NETL-311/081508.

Newman, G.A., Gasperikova, E., Hoversten, G.M., Wannamaker, P.E., 2008. Three-dimensional magnetotelluric characterization of the Coso geothermal field. Geothermics 37, 369-399, doi: 10.1016/j.geothermics.2008.02.006.

Newman, G.A., Recher, S., Tezkan, B., Neubauer, M., 2003. 3D inversion of a scalar radio magnetotelluric field data set. Geophysics 68(3), 791-802, doi: 10.1190/1.1581032.

Nisi, B., Vaselli, O., Tassi, F., Elío, J., Delgado Huertas, A., Mazadiego, L.P., Ortega, M.F., 2013. Hydrogeochemistry of surface and spring waters in the surroundings of the CO_2 injection site at Hontomín-Huermeces (Burgos, Spain). International Journal of Greenhouse Gas Control 14, 151-168, doi: 10.1016/j.ijggc.2013.01.012.

Ogaya, X., Ledo, J., Queralt, P., Marcuello, A., Quintà, A., 2013. First geoelectrical image of the subsurface of the Hontomín site (Spain) for CO_2 geological storage: A magnetotelluric 2D characterization. International Journal of Greenhouse Gas Control 13, 168-179, doi: 10.1016/j.ijggc.2012.12.023.

Ogaya, X., Queralt, P., Ledo, J., Marcuello, A., Jones, A.G., 2012. Preliminary results of the 3-D magnetotelluric characterization of the subsurface of the Technology Demonstration Plant of Hontomín (Burgos, Spain) for geological storage of CO_2, In: Zurutuza, J. (Ed.) 7AHPGG: Proceedings. Portuguese-Spanish Assembly of Geodesy and Geophysics, pp. 703-708, ISBN: 978-84-941323-1-5.

Ogaya, X., Queralt, P., Ledo, J., Marcuello, A., Jones, A.G., 2014. Geoelectrical baseline model of the subsurface of the Hontomín site (Spain) for CO_2 geological storage in a deep saline aquifer: a 3D magnetotelluric characterisation. International Journal of Greenhouse Gas Control 27, 120-138, doi: 10.1016/j.ijggc.2014.04.030.

Orange, A., Key, K., Constable, S., 2009. The feasibility of reservoir monitoring usingtime-lapse marine CSEM. Geophysics 74(2), F21-F29, doi: 10.1190/1.3059600.

Palacky, G.J., 1987. Resistivity characteristics of geological targets, in: Nabighian, M.N. (Ed.), Electromagnetic methods in applied geophysics. Society of Exploration Geophysicists, Tulsa, Oklahoma, EEUU, Volume 1, Chapter 3, 53-129.

Park, S.K., 1996. Precursors to earthquakes: Seismoelectromagnetic signals. Surveys in Geophysics 17(4), 493-516.

Park, S.K., Dalrymple, W., Larsen, J.C., 2007. The 2004 Parkfield earthquake: Test of the electromagnetic precursor hypothesis. Journal of Geophysical Research 112, B5, doi: 10.1029/2005JB004196.

Parker, R.L., 1980. The inverse problem of electromagnetic induction: Existence and construction of solutions based on incomplete data. Journal of Geophysical Research 85 (B8), 4421–4428, doi: 10.1029/JB085iB08p04421.

Parker, R.L., Whaler, K.A., 1981. Numerical methods for establishing solutions to the inverse problem of electromagnetic induction. Journal of Geophysical Research 86 (B10), 9574–9584, doi: 10.1029/JB086iB10p09574.

Patella, D., Siniscalchi, A., 1994. Two-level magnetovariational measurements for the determination of underground resistivity distributions. Geophysical Prospecting 42, 417-444, doi: 10.1111/j.1365-2478.1994.tb00219.x.

Peacock, J.R., Thiel, S., Reid, P., Heinson, G., 2012a. Magnetotelluric monitoring of a fluid injection: Example from an enhanced geothermal system. Geophysical Research Letters 39, L18403, doi: 10.1029/2012GL053080.

Peacock, J., Thiel, S., Reid, P., Messellier, M., Heinson, G., 2012b. Monitoring enhanced geothermal fluids with magnetotellurics, test case: Paralana, South Australia. PROCEEDINGS, Thirty-Seventh Workshop on Geothermal Reservoir Engineering. Stanford University, Stanford, California, January 30- February 1, 2012, SGP-TR-194.

Pérez-Estaún, A., Gómez, M., Carrera, J., 2009. El almacenamiento geológico de CO_2, una de las soluciones al efecto invernadero./Geological storage of CO_2, one of the solutions to the greenhouse effect. Enseñanza de las Ciencias de la Tierra 17(2), 179-189, ISSN: 1132-9157.

Permanyer, A., Márquez, G., Gallego, J.R., 2013. Compositional variability in oils and formation waters from the Ayoluengo and Hontomín fields (Burgos, Spain). Implications for assessing biodegradation and reservoir compartmentalization. Organic Geochemistry 54, 125-139, doi: 10.1016/j.orggeochem.2012.10.007.

Piña-Varas, P., Ledo, J., Queralt, P., Marcuello, A., Bellmunt, F., Hidalgo, R., Messeiller, R., 2014. 3-D Magnetotelluric Exploration of Tenerife Geothermal System (Canary Islands, Spain). Surveys in Geophysics (In Press) doi: 10.1007/s10712-014-9280-4.

Piña-Varas, P., Ledo, J., Queralt, P., Roca, E., García-Lobón, J.L., Ibarra, P., Biete, C., 2013. Two-dimensional magnetotelluric characterization of the El Hito Anticline (Loranca Basin, Spain). Journal of Applied Geophysics 95, 121-134, doi: 10.1016/j.jappgeo.2013.06.002

Prado, J., Campos, R., Ruiz, C., Pelayo, M., recreo, F., Lomba, L., Hurtado, A., Egulior, S., Pérez del Vilar, L., 2008. Almacenamiento geológico de CO_2: selección de formacions favorables. 9º Congreso Nacional de Medio Ambiente, comunicación técnica, 30 p.

Pujalte, V., Robles, S., García-Ramos, J.C., Hernández, J. M., 2004. El Malm-Barremiense no marinos de la Cordillera Cantábrica, in: Vera, J.A. (Ed.), Geología de España. SGE-IGME, Madrid, 288-291.

Pujalte, V., Robles, S., Valles, J.C., 1988. El Jurásico marino de las zonas de alto sedimentario relativo al borde SW de la Cuenca Vasco-Cantábrica (Rebolledo de la Torre, Palencia). III Coloquio de Estratigrafía y Paleogeografía del Jurásico de España: libro guía de las excursiones: Logroño, 10-19 septiembre 1988. Ciencias de la Tierra, Instituto de Estudios Riojanos 11, 85-94.

Queralt, P., Jones, A.G., Ledo, J., 2007. Electromagnetic imaging of a complex ore layer: 3D forward modelling, sensitivity tests, and down-mine measurements. Geophysics 72(2), F85-F95, doi: 10.1190/1.2437105.

Quesada, S., Robles, S., Pujalte, V., 1991. Correlación secuencial y sedimentológica entre registros de sondeos y series de superficie de Jurásico Marino de la Cuenca de Santander (Cantabria, Palencia y Burgos). Geogaceta 20, 176-179.

Quesada, S., Robles, S., Pujalte, V., 1993. El Jurásico marino del margen suroccidental de la Cuenca Vasco-Cantábrica y su relación con la exploración de hidrocarburos. Geogaceta 13, 92-96.

Quesada, S., Robles, S., Rosales, I., 2005. Depositional architecture and transgressive–regressive cycles within Liassic backstepping carbonate ramps in the Basque-Cantabrian basin, northern Spain. Journal of the Geological Society 162 (3), 531–538.

Quintà, A., 2013. El patrón de fracturación alpina en el sector suroccidental de los Pirineos Vascos. PhD Thesis. Universitat de Barcelona, Barcelona, Spain, 153 pp.

Quintà, A., Tavani, S, 2012. The foreland deformation in the south-western Basque-Cantabrian Belt (Spain). Tectonophysics 576-577, 4-19, doi: 10.1016/j.tecto.2012.02.015.

Quintà, A., Tavani, S., Roca, E., 2012. Fracture pattern analysis as a tool for constraining the interaction between regional and diapir-related stress fields: Poza de la Sal Diapir (Basque Pyrenees, Spain), in: Alsop, G.I., Archer, S.G., Hartley, A.J., Grant, N.T., Hodkinson, R. (Eds.), Salt Tectonics, Sediments and Prospectivity. Geological Society, London, Special Publication 363(1), 521-532.

Ramirez, A. L., Newmark, R. L., Daily, W.D., 2003. Monitoring Carbon Dioxide Floods Using Electrical resistence Tomography (ERT): Sensitivity Studies. Journal of Environmental and Engineering Geophysics 8(3), 187-208.

Rikitake, T., 1951. Changes in earth current and their relation to the electrical state of the earth's crust. Bull. Earthq. Res. Inst., University of Tokyo 29, 271-276.

Robles, S., Pujalte, V., Valles, J.C., 1989. Sistemas sedimentarios del Jurasico de la parte occidental de la Cuenca Vasco-Cantábrica. Cuadernos de Geología Ibérica 13, 185-198, ISSN: 0378-102X.

Robles, S., Quesada, S., Rosales, I., Aurell, M., García-Ramos, J. C., 2004. El Jurásico marino de la Cordillera Cantábrica, in: Vera, J.A. (Ed.), Geología de España. SGE-IGME, Madrid, 279-285.

Roca, E., Muñoz, J.A., Ferrer, O., Ellouz, N., 2011. The role of the Bay of Biscay Mesozoic extensional structure in the configuration of the Pyrenean orogeny: Constraints from MARCONI deep seismic reflection survey. Tectonics 30(2), TC2001.

Rodi, W., Mackie, R.L., 2001. Non linear conjugate gradients algorithm for 2D magnetotelluric inversion. Geophysics 66, 174-187.

Rodi, W., Mackie, R.L., 2012. The inverse problem, in: Chave, A. D., Jones, A. G. (Eds.), The Magnetotelluric Method: Theory and Practice, Chapter 8, pp. 347-420. Cambridge University Press, Cambridge (UK), ISBN: 978-0-521-81927-5.

Roest, W.R., Srivastava, S. P., 1991. Kinematics of the plate boundaries between Eurasia, Iberia, and Africa in the North Atlantic from the Late Cretaceous to the present. Geology 6, 613-616.

Rosales, I., Quesada, S., Robles, S., 2006. Geochemical arguments for identifying second-order sea-level changes in hemipelagic carbonate ramp deposits. Terra Nova 18(4), 233-240.

Rosell, O., Martí, A., Marcuello, A., Ledo, J., Queralt, P., Campanyà, J., 2011. Deep electrical resistivity structure of the northern Gibraltar Arc (western mediterranean): evidence of lithospheric slab break-off. Terra Nova 23(3), 179-186, doi: 10.1111/j.1365-3121.2011.00996.x.

Rubio, F.M., Ayala, C., Gumiel, J.C., Rey, C., 2011. Caracterización mediante campo potencial y teledetección de la estructura geológica seleccionada para planta de desarrollo tecnológico de almacenamiento geológico de CO_2 en Hontomín (Burgos). IGME- Instituto Geológico y Minero de España Technical Report, 182 pp.

Ruiz, C., Recreo, F., Prado, P., Campos, R., Pelayo, M., de la Losa, A., Hurtado, A., Lomba, L., Pérez del Villar, L., Martínez, R., Ortiz, G., Satre, J., 2007. Almacenamiento Geológico de CO_2. Criterios de selección de emplazamientos. Informe Técnico CIEMAT 1085, 99 pp.

Rutqvist, J., 2012. The geomechanics of CO2 storage in deep sedimentary formations. Geotechnical and Geological Engineering 30 (3), 525-551, doi: 10.1007/s10706-011-9491-0.

Samouëlian, A., Cousin, I., Tabbagh, A., Bruand, A., Richard, G., 2005. Electrical resistivity survey in soil science: a review. Soil and Tillage Research 83, 173-193, doi: 10.1016/j.still.2004.10.004.

Sato, K., Mito, S., Horie, T., Ohkuma, H., Saito, H., Watanabe, J., Yoshimura, T., 2011. Monitoring and simulation studies for assessing macro- and meso-scale migration of CO2 sequestered in an onshore aquifer: Experiences from the Nagaoka pilot site, Japan. International Journal of Greenhouse Gas Control 5, 125-137, doi: 10.1016/j.ijggc.2010.03.003.

Schamper, C., Rejiba, F., Tabbagh, A., Spitz, S., 2011. Theoretical analysis of long offset time-lapse frequency domain controlled source electromagnetic signals using the method of moments: Application to the monitoring of a land oil reservoir. Journal of Geophysical Research: Solid Earth 116, B3, doi: 10.1029/2009JB007114.

Schmucker, U., Spitzer, K., Steveling, E., 2009. An electromagnetic sounding experiment in Germany using the vertical gradient of geomagnetic variations observed in a deep borehole. Geophysical Journal International, 178(3), 1273-1288, doi: 10.1111/j.1365-246X.2009.04199.x.

Serrano, A., Martínez del Olmo, W., 1990. Tectónica salina en el Dominio Cántabro–Navarro: evolución, edad y origen de las estructuras salinas, in: Orti, F., Salvany, J. M. (Eds.), Formaciones evaporíticas de la Cuenca del Ebro y cadenas periféricas, y de la zona de Levante. Nuevas Aportaciones y Guía de Superficie. Empresa Nacional De Residuos Radiactivos S.A, ENRESA-GPPG, Barcelona, 39–53.

Sholpo, M.E., 2006. Monitoring of Relative Changes in the Electrical Conductivity of Rocks from Observations of the Magnetotelluric Apparent Resistivity (Numerical Modelling). Physics of the Solid Earth 42(4), 323-329, ISSN 1069-3513.

Simpson, F., Bahr, K., 2005. Practical Magnetotellurics. Cambridge University Press, 254 pp, ISBN 0-521-81727-7.

Siripunvaraporn, W., 2012. Three-dimensional Magnetotelluric Inversion: An introductory guide for Developers and Users. Surveys in Geophysics 33(1), 5-27, doi: 10.1007/s10712-011-9122-6.

Siripunvaraporn, W., Egbert, G., 2000. An efficient data-subspace inversion method for 2-D magnetotelluric data. Geophysics 65, 791-803.

Siripunvaraporn, W., Egbert, G., Lenbury, Y., Uyeshima, M., 2005. Three-dimensional magnetotelluric inversion: data-space method. Physics of the Earth and Planetary Interiors 150, 3–14, doi: 10.1016/j.pepi.2004.08.023.

Spitzer, K., 1993. Observations of geomagnetic pulsations and variations with a borehole magnetometer down to depths of 3000m. Geophysical Journal International 115(3), 839-848, doi: 10.1111/j.1365-246X.1993.tb01496.x.

Srivastava, S.P., 1965. Method of interpretation of magnetotelluric data when source field is considered. Journal of Geophysical Research 70(4), 945-954.

Stangeland, A., 2007. A model for the CO2 capture potencial. International Journal of Greenhouse Gas Control 1(4), 418-429, doi: 10.1016/S1750-5836(07)00087-4.

Streich, R., Becken, M., Ritter, O., 2010. Imaging of CO_2 storage sites, geothermal reservoirs, and gas shales using controlled-source magnetotellurics: Modeling studies. Chemie der Erde-Geochemistry 70(3), 63-75, doi: 10.1016/j.chemer.2010.05.004.

Streimikiene, D., 2012. The impact of international GHG trading regimes on penetration of new energy technologies and feasibility to implement EU Energy and Climate Package targets. Renewable and Sustainable Energy Reviews 16(4), 2172-2177, doi: 10.1016/j.rser.2012.01.042.

Svetov, B.S., Karinskij, S.D., Kuksa, Y.I., Odintsov, V.I., 1997. Magnetotelluric monitoring of geodynamic processes. Annali de Geofisica XL(2), 435-443.

Tavani, S., 2012. Plate kinematics in the Cantabrian domain of the Pyrenean orogen. Solid Earth 3, 265-292.

Tavani, S., Carola, C., Granado, P., Quintà, A., Muñoz, J. A., 2013. Transpressive inversion of a Mesozoic extensional forced fold system with an intermediate décollement level in the Basque-Cantabrian Basin (Spain). Tectonics 32(2), 146-158, doi: 10.1002/tect.20019.

Tavani, S., Muñoz, J. A., 2012. Mesozoic rifting in the Basque-Cantabrian Basin (Spain): Inherited faults, transversal structures and stress perturbation. Terra Nova 24, 70-76.

Tavani, S., Quintà, A., Granado, P., 2011. Cenozoic right-lateral wrench tectonics in the Western Pyrenees (Spain): The Ubierna Fault System. Tectonophysics 509, 238-253.

Tikhonov, A.N., 1950. On determining electrical characteristics of the deep layers of the Earth's crust. Dokl. Akad. Nauk. SSSR 73, 295-297.

Tuncer, V., Unsworth, M.J., Siripunvaraporn, W., Craven, J.A., 2006. Exploration for unconformity-type uranium deposits with audiomagnetotellurics data: A case study from the McArthur River mine, Saskatchewan, Canada. Geophysics 71(6), B201-B209, doi: 10.1190/1.2348780.

Turkenburg, W.C., 1997. Sustainable development, climate change, and carbon dioxide removal (CDR). Energy Conversion and Management 38(Supplement), S3-S12, doi: 10.1016/S0196-8904(96)00237-3.

Ugalde, A., Villaseñor, A., Gaite, B., Casquero, S., Martí, D., Calahorrano, A., Marzán, I., Carbonell, R., Estaún, A.P., 2013. Passive seismic monitoring of an experimental CO_2 geological storage site in Hontomín (Northern Spain). Seismological Research Letters 84(1), 75-84, doi: 10.1785/0220110137.

Vellante, M., 1997. Some theoretical aspects of the two-level magnetovariational method. Annali di Geofisica Vol. XL, N. 6, doi: 10.4401/ag-3838.

Vera. J.A., 2004. Geología de España. SGE-IGME, Madrid, ISBN: 978-84-7840-546-6.

Vialle, S., Contraires, S., Zinzsner, B., Clavaud, J.-B., Mahiouz, K., Zuddas, P., Zamora, M., 2014. Percolation of CO_2-rich fluids in a limestone simple: Evolution of Hysraulic, electrical, chemical, and structural properties. Journal of Geophysical Research: Solid Earth 119, doi: 10.1002/2013JB010656.

Vilamajó, E., Queralt, P., Ledo, J., Marcuello, A., 2013. Feasibility of monitoring the Hontomín (Burgos, Spain) CO_2 storage site using deep EM source. Surveys in Geophysics 34, 441-461, doi: 10.1007/s10712-013-9238-y.

Vozoff, K., 1991. The magnetotelluric method, in: Nabighian, M.N. (Ed.), Electromagnetic Methods in Applied Geophysics, pp. 641-711. Society of Exploration Geophysicists, Tulsa, Oklahoma, EEUU.

Wagner, F.M., Möller, M., Schmidt-Hattenberger, C., Kempka, T., Maurer, H., 2013. Monitoring freshwater salinization in analog transport models by time-lapse electrical resistivity tomography. Journal of Applied Geophysics 89, 84-95, doi: 10.1016/j.jappgeo.2012.11.013.

Wang, Z., Cates, M., Langan, R., 1998. Seismic monitoring of a CO2 flood in a carbonate reservoir: A rock physics study. Geophysics 63, 1604-1617.

Ward, S.H., Hohmann, G.W., 1988. Electromagnetic theory for geophysical applications, in: Nabighian, M.N., Corbett, J.D. (Eds.), Electromagnetic methods in applied geophysics: theory, SEG Monograph 1, 131-313.

Weaver, J.T., Agarwal, A.K., Lilley, F.E.M., 2000. Characterisation of the magneto-telluric tensor in terms of its invariants. Geophysical Journal International 141(2), 321–336, doi: 10.1046/j.1365-246X.2000.00089.x.

Whittal, K.P., Oldenburg, D.W., 1992. Inversion of Magnetotelluric Data for a One-Dimensional Conductivity. Geophysical Monograph Series No.5, Society of

Exploration Geophysicists, Tulsa, Oklahoma, EEUU, ISBN 10: 1560800585 / ISBN 13: 9781560800583.

Wirianto, M., Mulder, W.A., Slob, E.C., 2010. A feasibility study of land CSEM reservoir monitoring in a complex 3D model. Geophysical Journal Internationanl 181(2), 741-755.

Wright, D., Ziolkowski, A., Hobbs, B., 2002. Hydrocarbon detection and monitoring with multicomponent transient electromagnetic (MTEM) survey. The Leading Edge 21(9), 852-864, doi: 10.1190/1.1508954.

Xiao, Q., Cai, X., Xu, X., Liang, G., Zhang, B., 2010. Application of the 3D magnetotelluric inversion code in a geologically complex area. Geophysical Prospecting 58(6), 1177-1192, doi: 10.1111/j.1365-2478.2010.00896.x.

Zhdanov, MS., Endo, M., Black, N., Spangler, L., Fairweather, S., Hibbs, A., Eiskamp, G.A., Will, R., 2013. Electromagnetic monitoring of CO_2 sequestration in deep reservoris. First Break 31(2), 85-92.

Zhdanov, M.S., Wan, L., Gribenko, A., Čuma, M., Key, K., Constable, S., 2011. Large-scale 3D inversion of marine magnetotelluric data: Cse study from the Gemini prospect, Gulf of Mexico. Geophysics 76(1), F77-F87, doi: 10.1190/1.3526299.

Zieglar, P.A., 1988. Late Jurassic-Early Cretaceous Central Atlantic sea-floor spreading, closure of Neo-Tethys, and opening of Canada Basin, in: Ziegler, P.A. (Ed.), Evolution of the Artic-North Atlantic and Western Tethys. American Association of Petroleum Geologists Memoirs 43, Tulsa, pp. 63-82.

Ziegler, P. A., 1989. Evolution of the North Atlantic: An Overview, in Tankard, A. J., Balkwill, H.R. (Eds.), Extensional Tectonics and Stratigraphy of the North Atlantic Margins. AAPG Memoir 46, 111-129.

Ziolkowski, A., Wright, A., 2012. The potential of the Controlled Source Electromagnetic Method: A Powerful Toll for Hydrocarbon Exploration, Appraisal, and Reservoir Charcaterization. IEEE Signal Processing Magazine 29(4), 36-52, doi: 10.1109/MSP.2012.2192529.

Supplementary figures

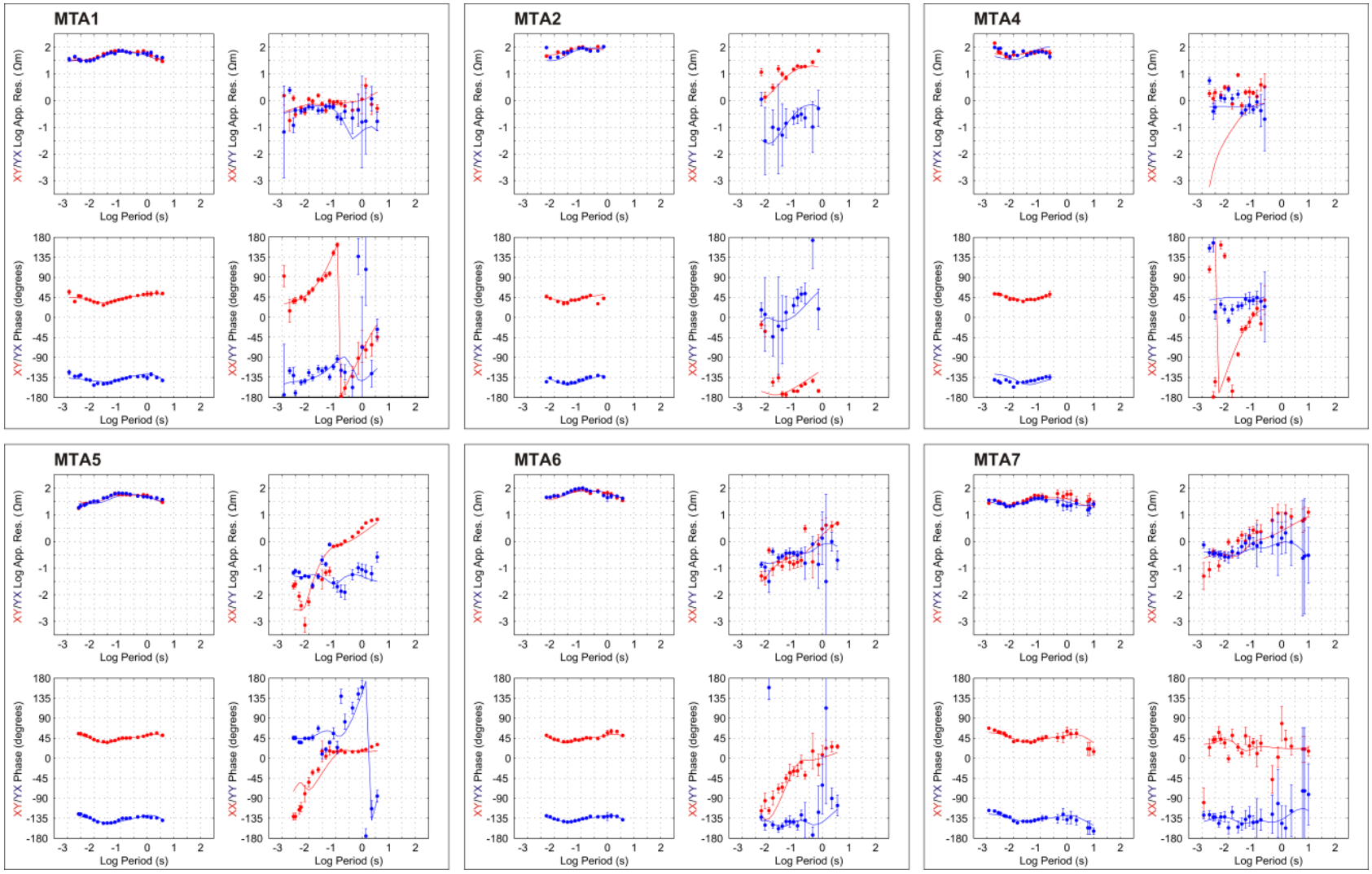

Fig. S1. Observed data and model responses at sites MTA1, MTA2, MTA4, MTA5, MTA6 and MTA7.

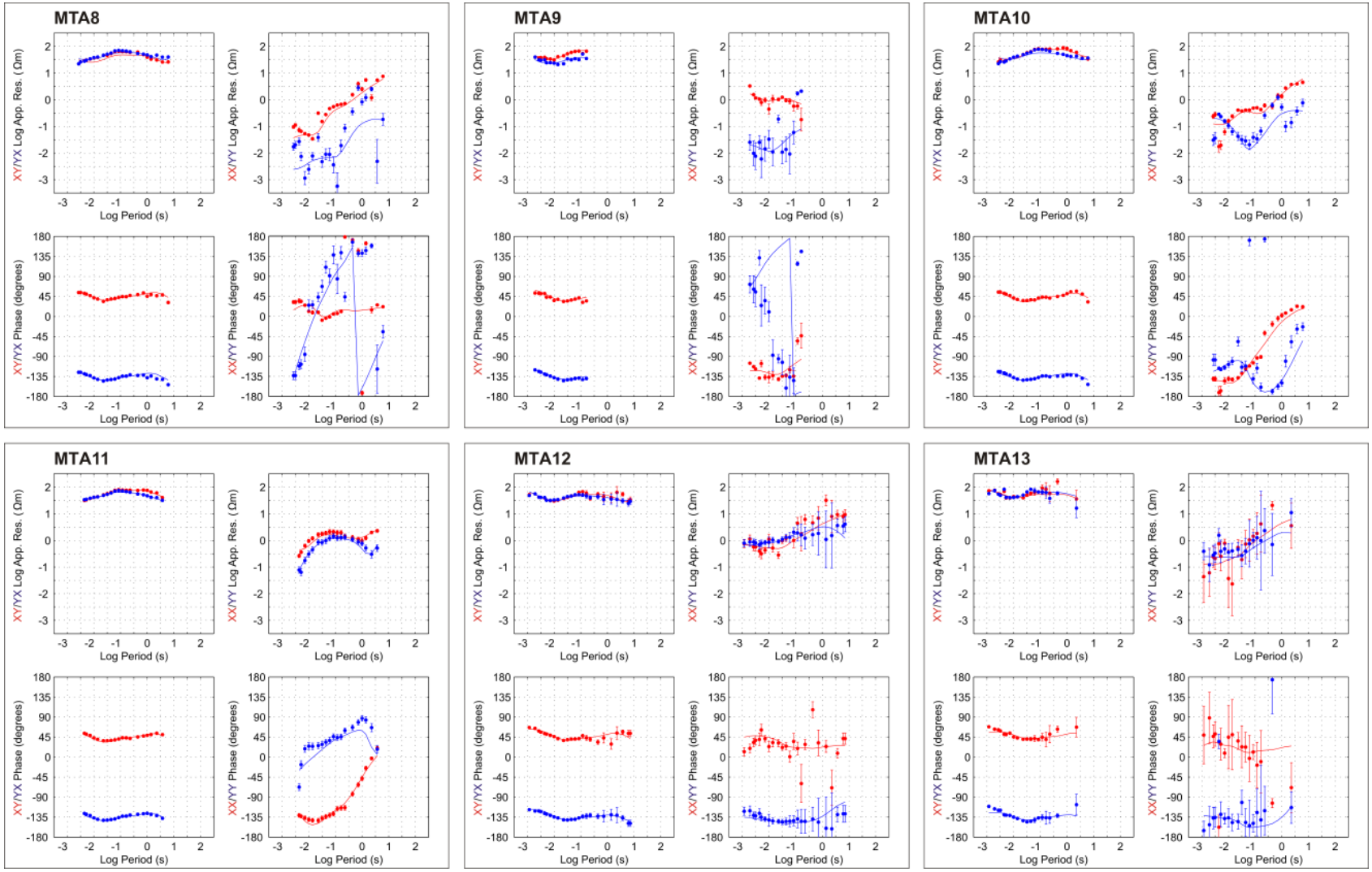

Fig. S2. Observed data and model responses at sites MTA8, MTA9, MTA10, MTA11, MTA12 and MTA13.

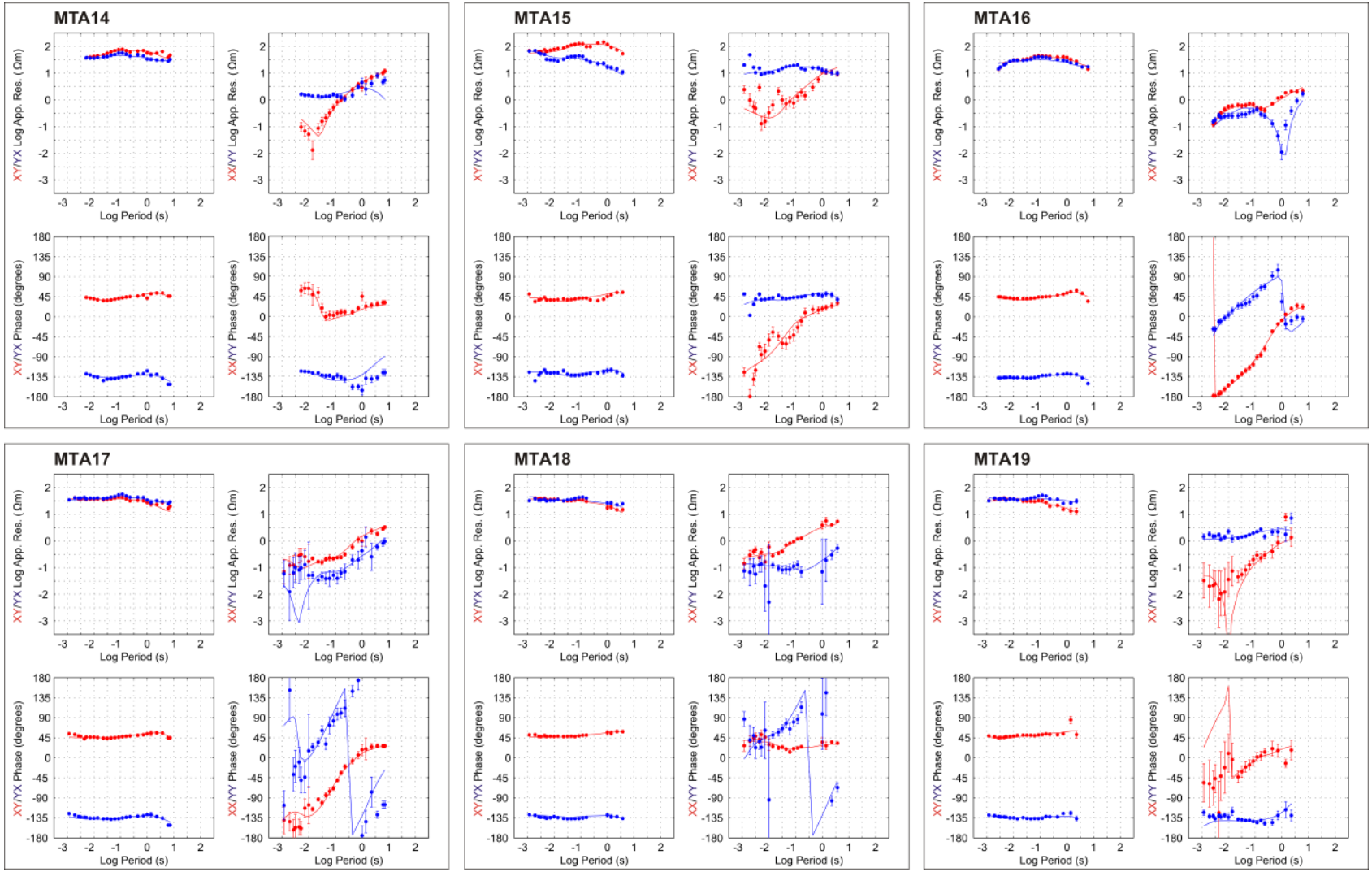

Fig. S3. Observed data and model responses at sites MTA14, MTA15, MTA16, MTA17, MTA18 and MTA19.

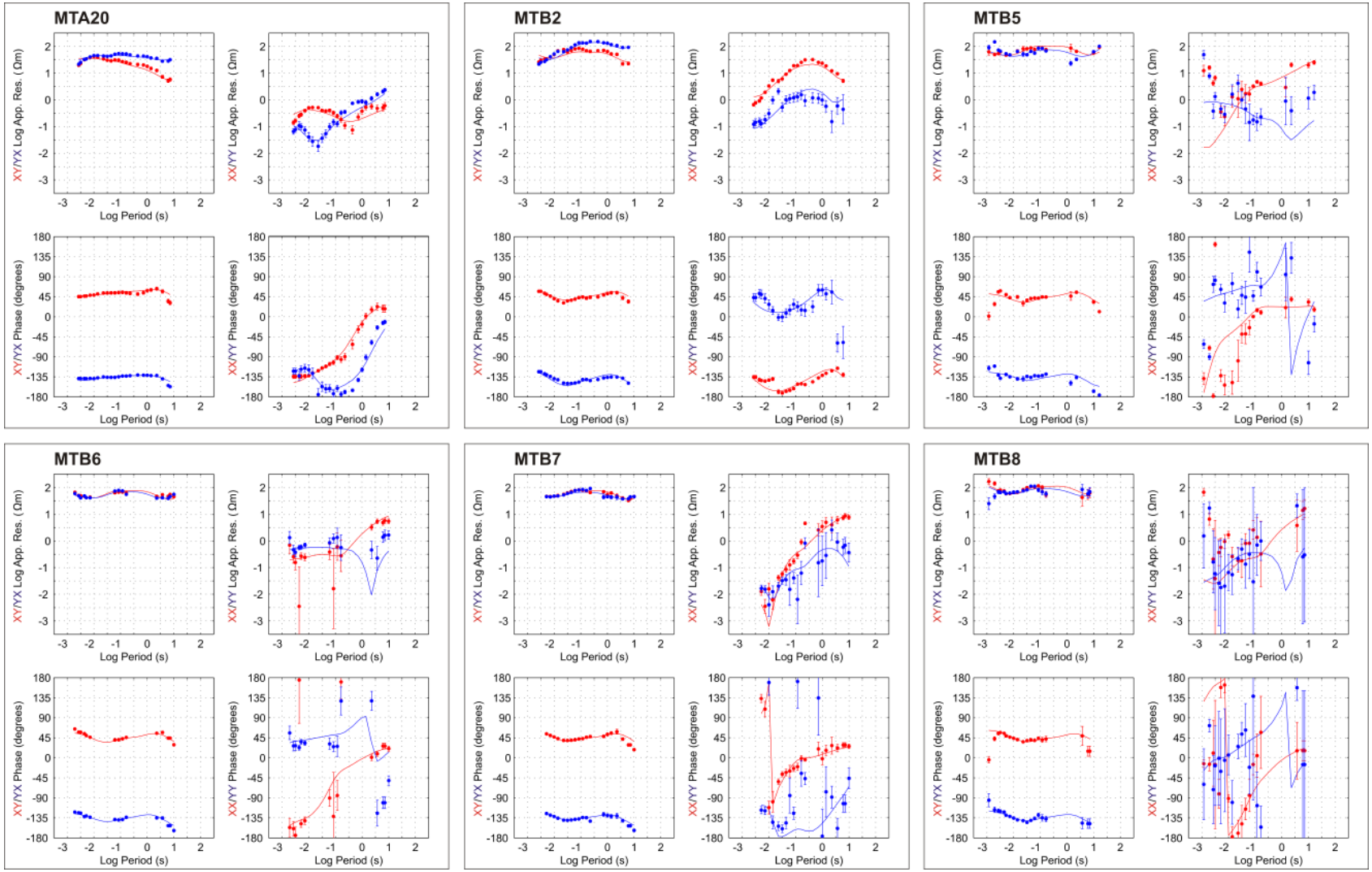

Fig. S4. Observed data and model responses at sites MTA20, MTB2, MTB5, MTB6, MTB7 and MTB8.

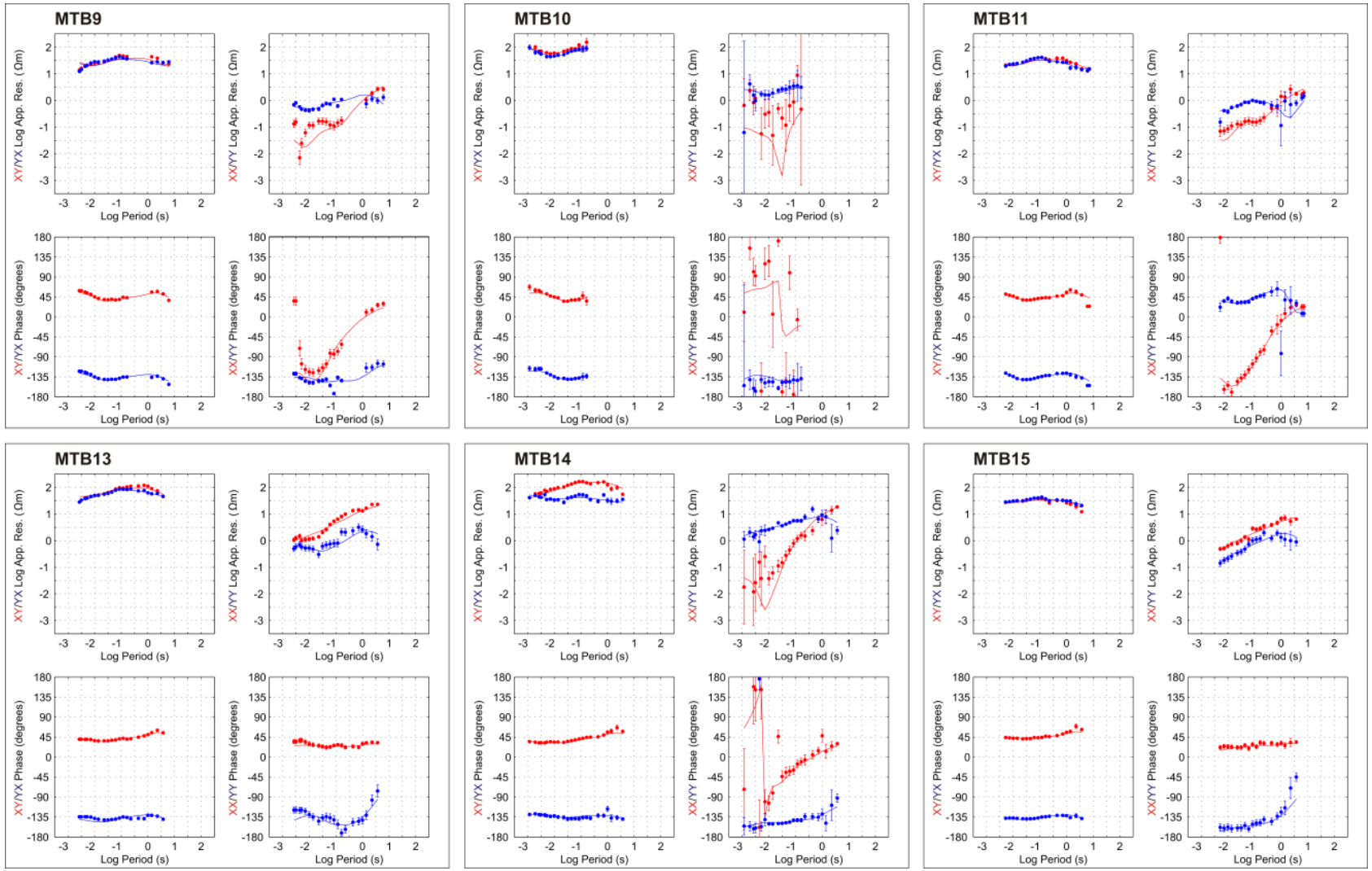

Fig. S5. Observed data and model responses at sites MTB9, MTB10, MTB11, MTB13, MTB14 and MTB15.

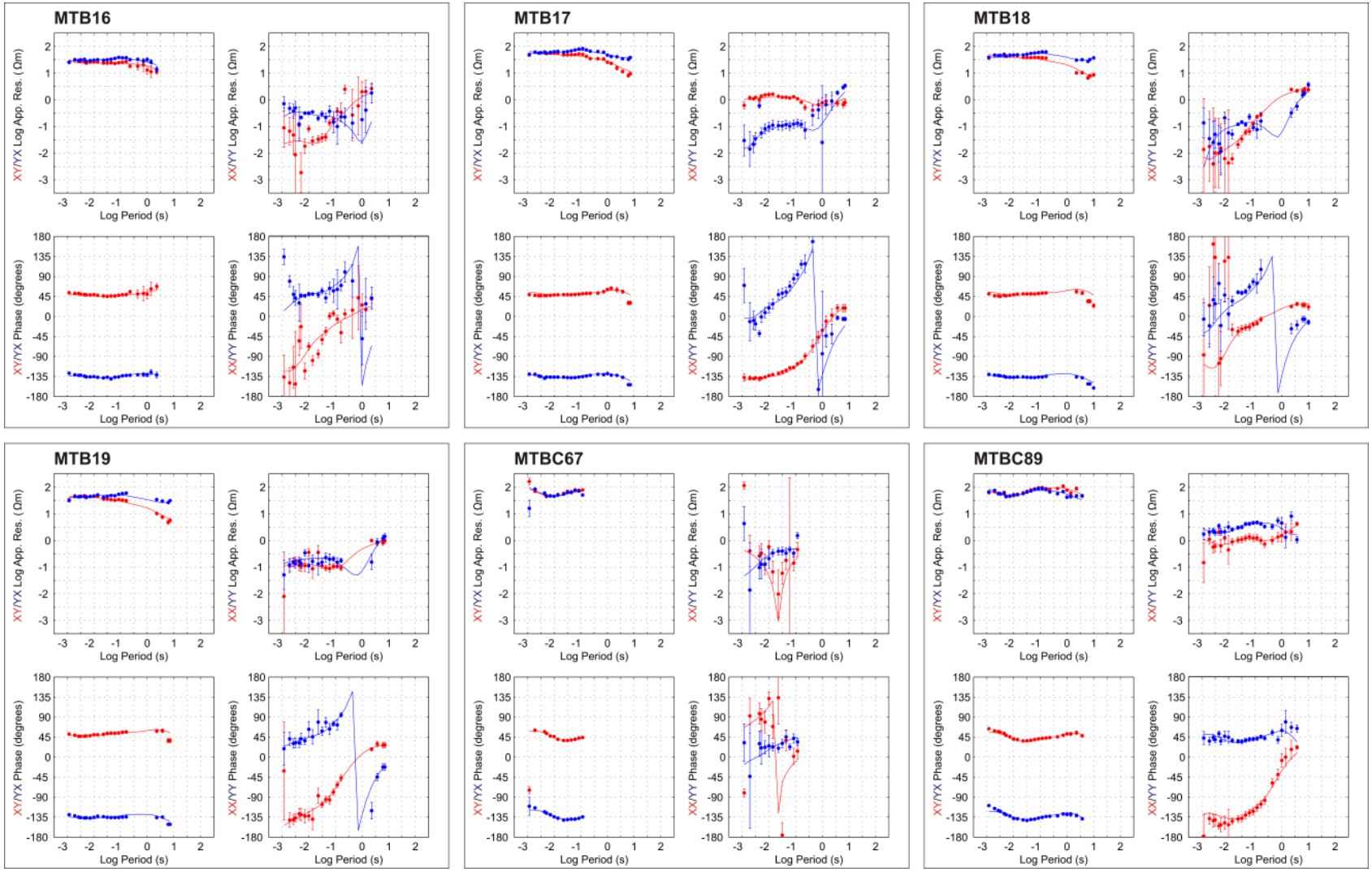

Fig. S6. Observed data and model responses at sites MTB16, MTB17, MTB18, MTB19, MTBC67 and MTBC89.

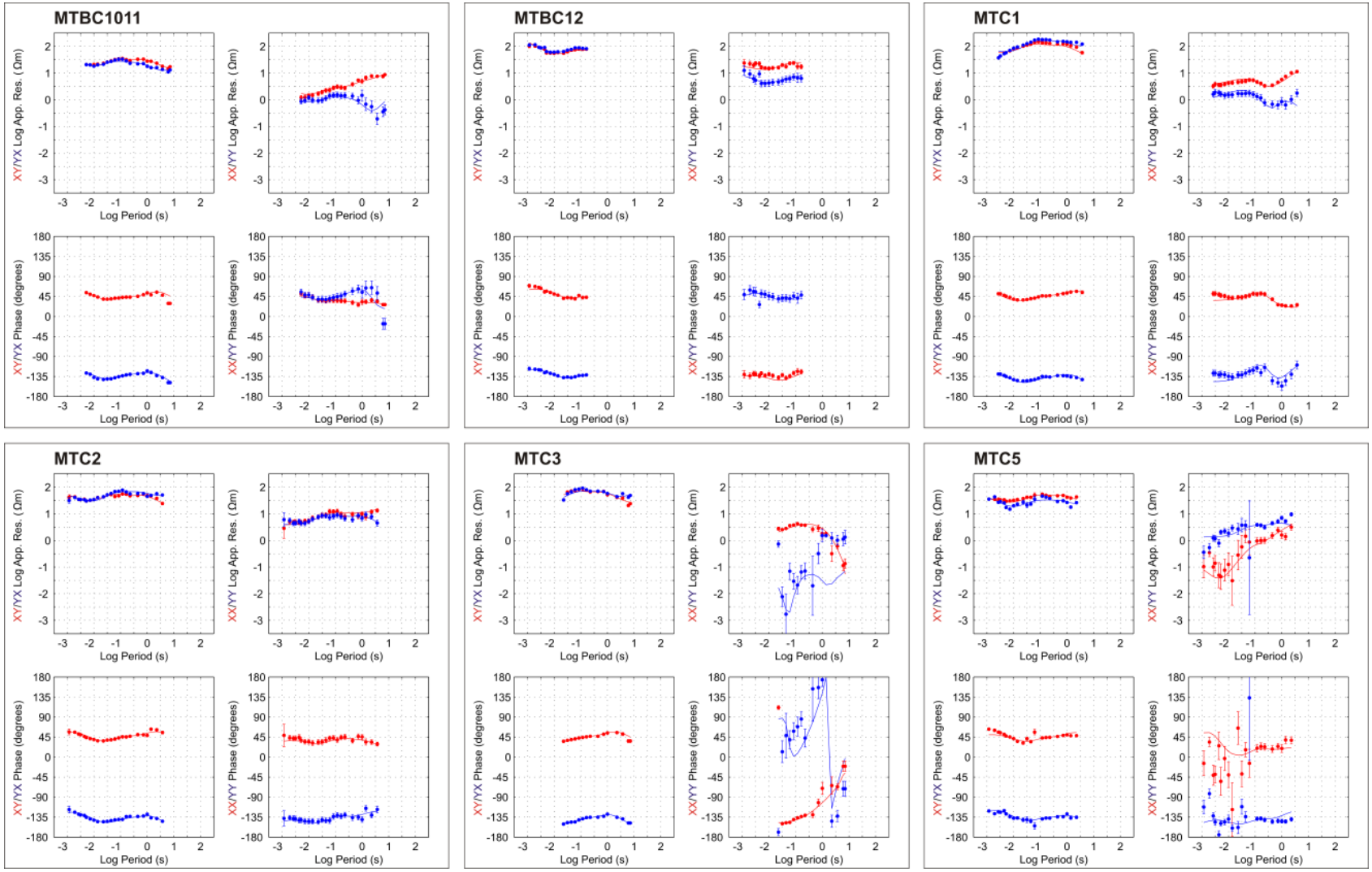

Fig. S7. Observed data and model responses at sites MTBC1011, MTBC12, MTC1, MTC2, MTC3 and MTC5.

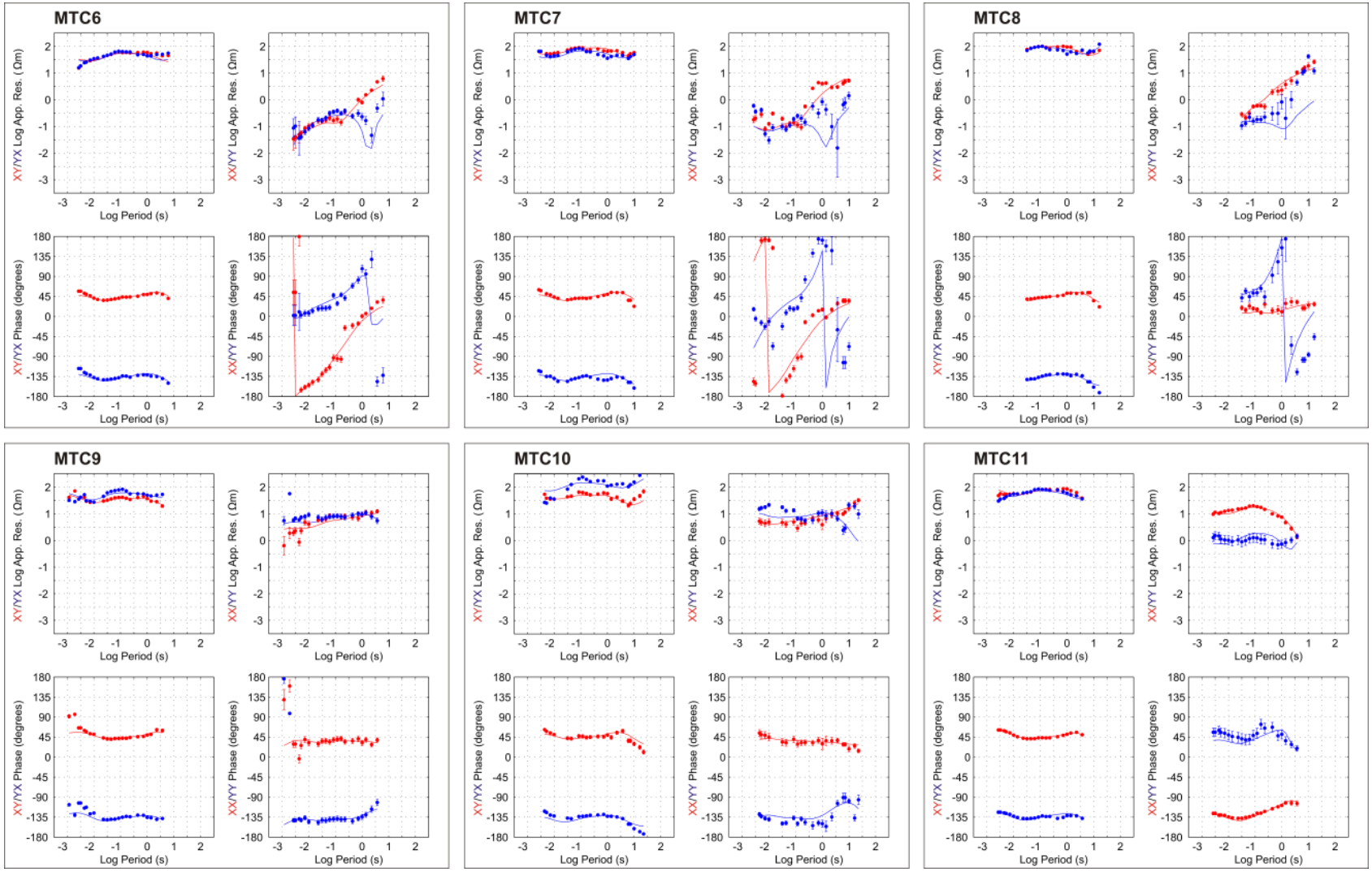

Fig. S8. Observed data and model responses at sites MTC6, MTC7, MTC8, MTC9, MTC10 and MTC11.

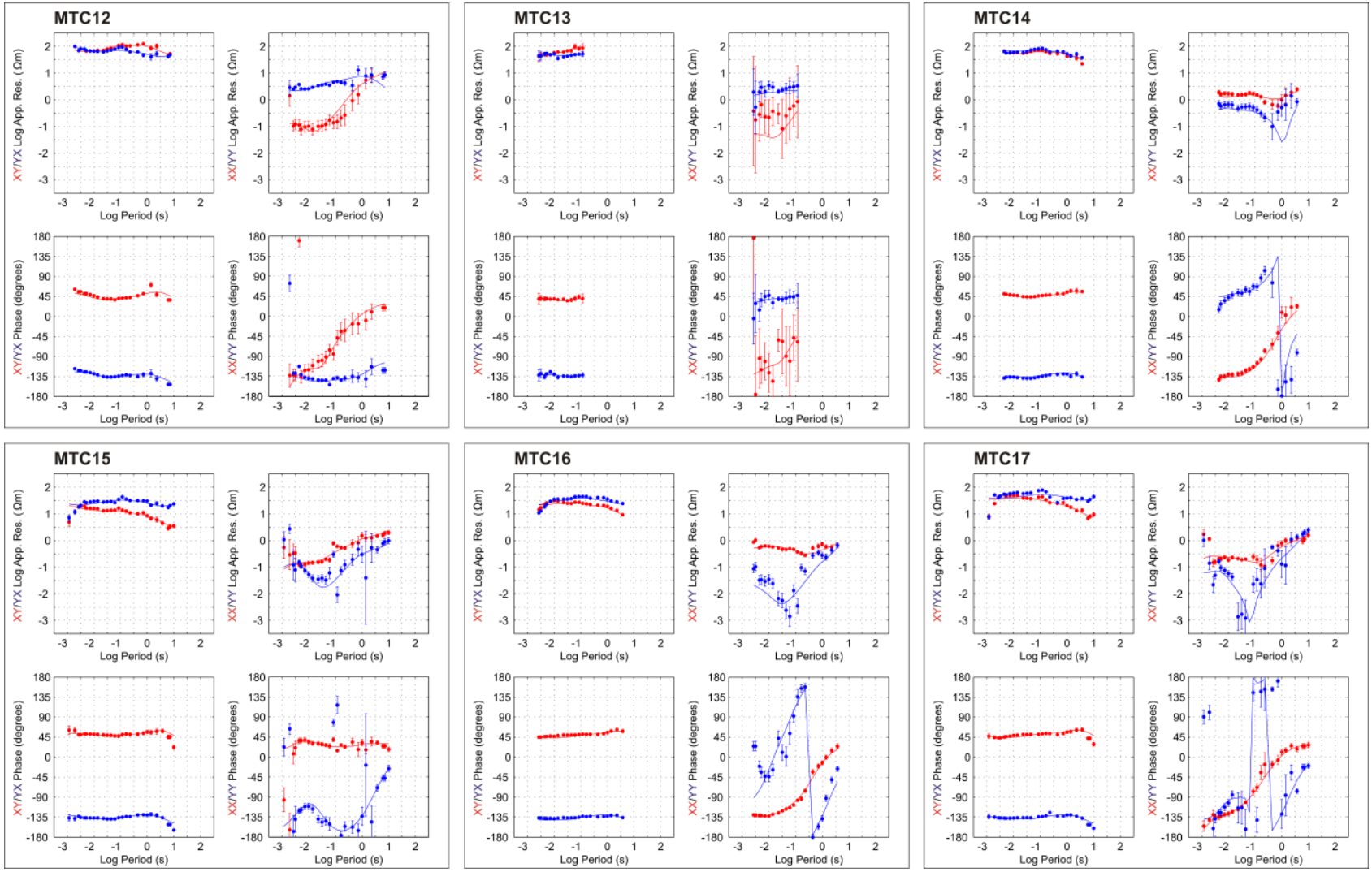

Fig. S9. Observed data and model responses at sites MTC12, MTC13, MTC14, MTC15, MTC16 and MTC17.

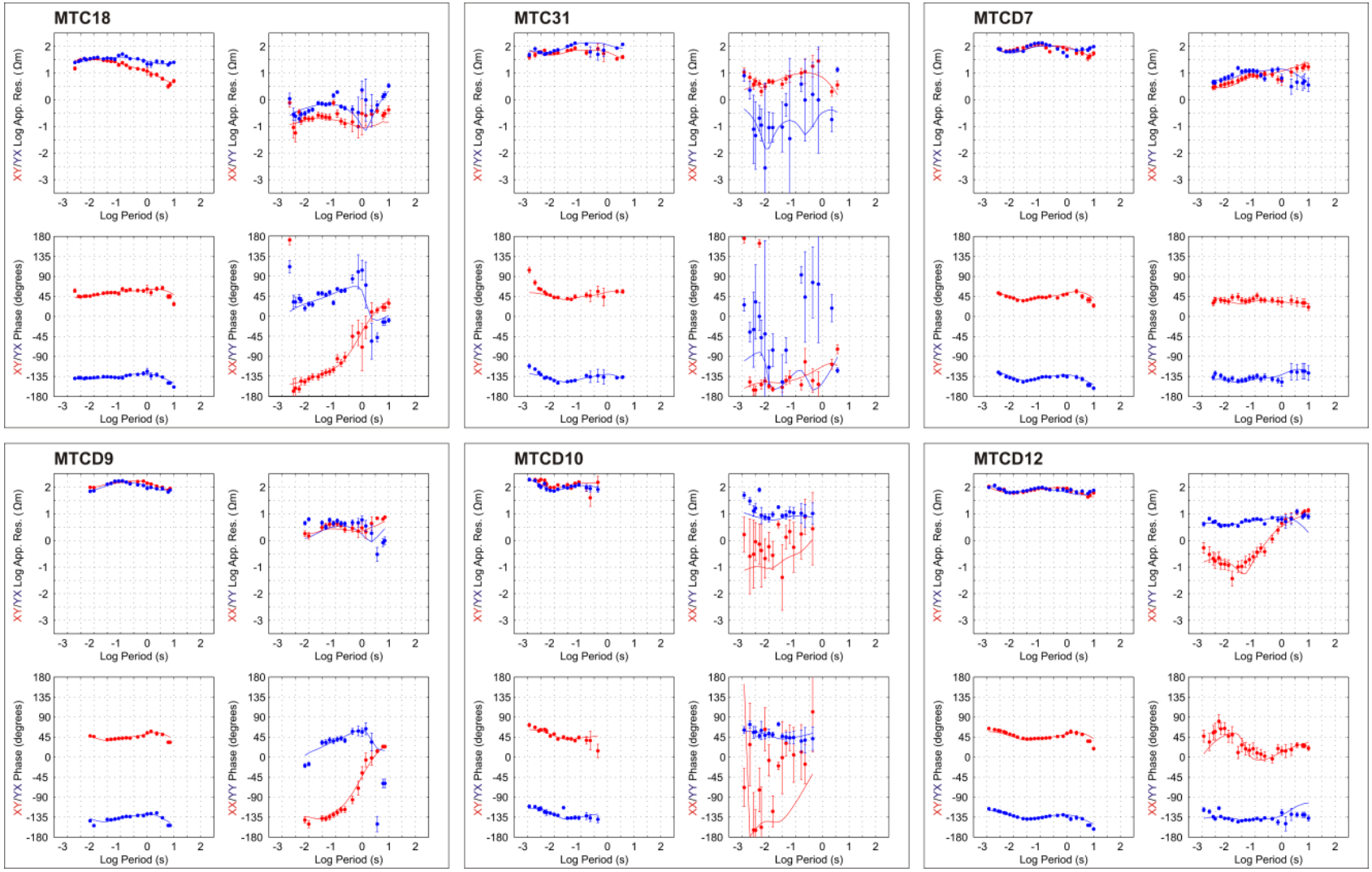

Fig. S10. Observed data and model responses at sites MTC18, MTC31, MTCD7, MTCD9, MTCD10 and MTCD12.

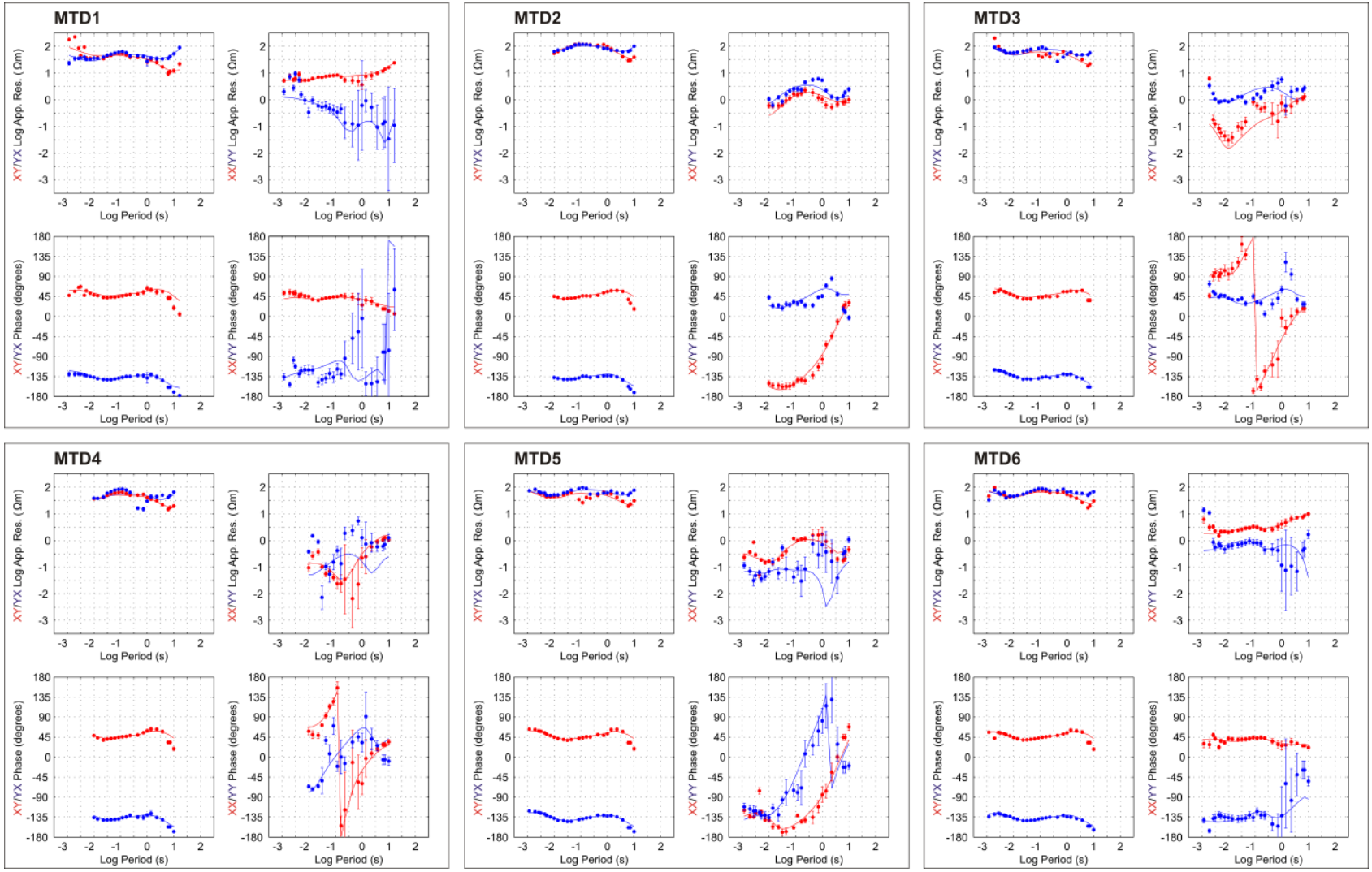

Fig. S11. Observed data and model responses at sites MTD1, MTD2, MTD3, MTD4, MTD5 and MTD6.

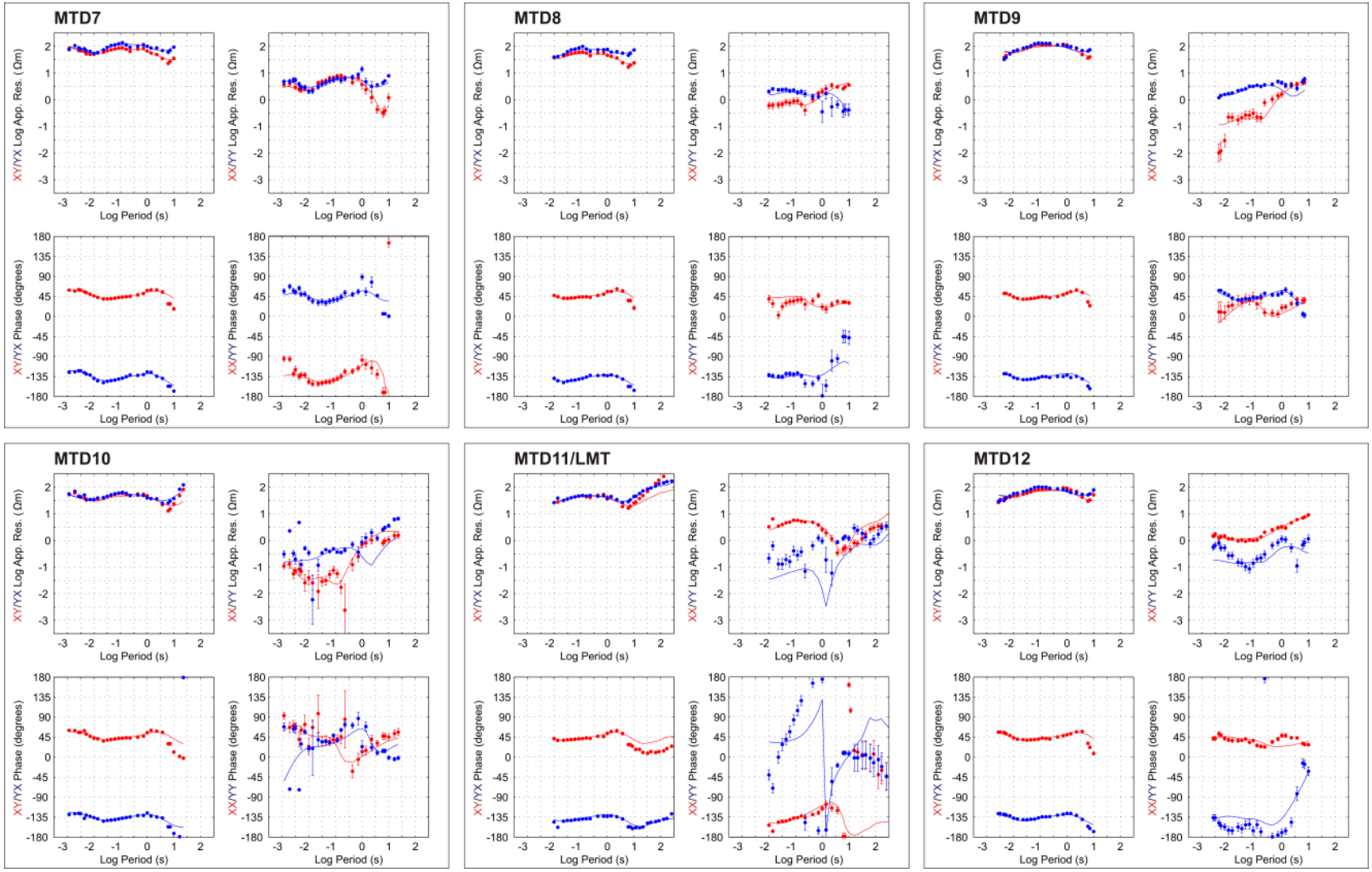

Fig. S12. Observed data and model responses at sites MTD7, MTD8, MTD9, MTD10, MTD11 (includes LMT data in the period range of 10 to 340 s) and MTD12.

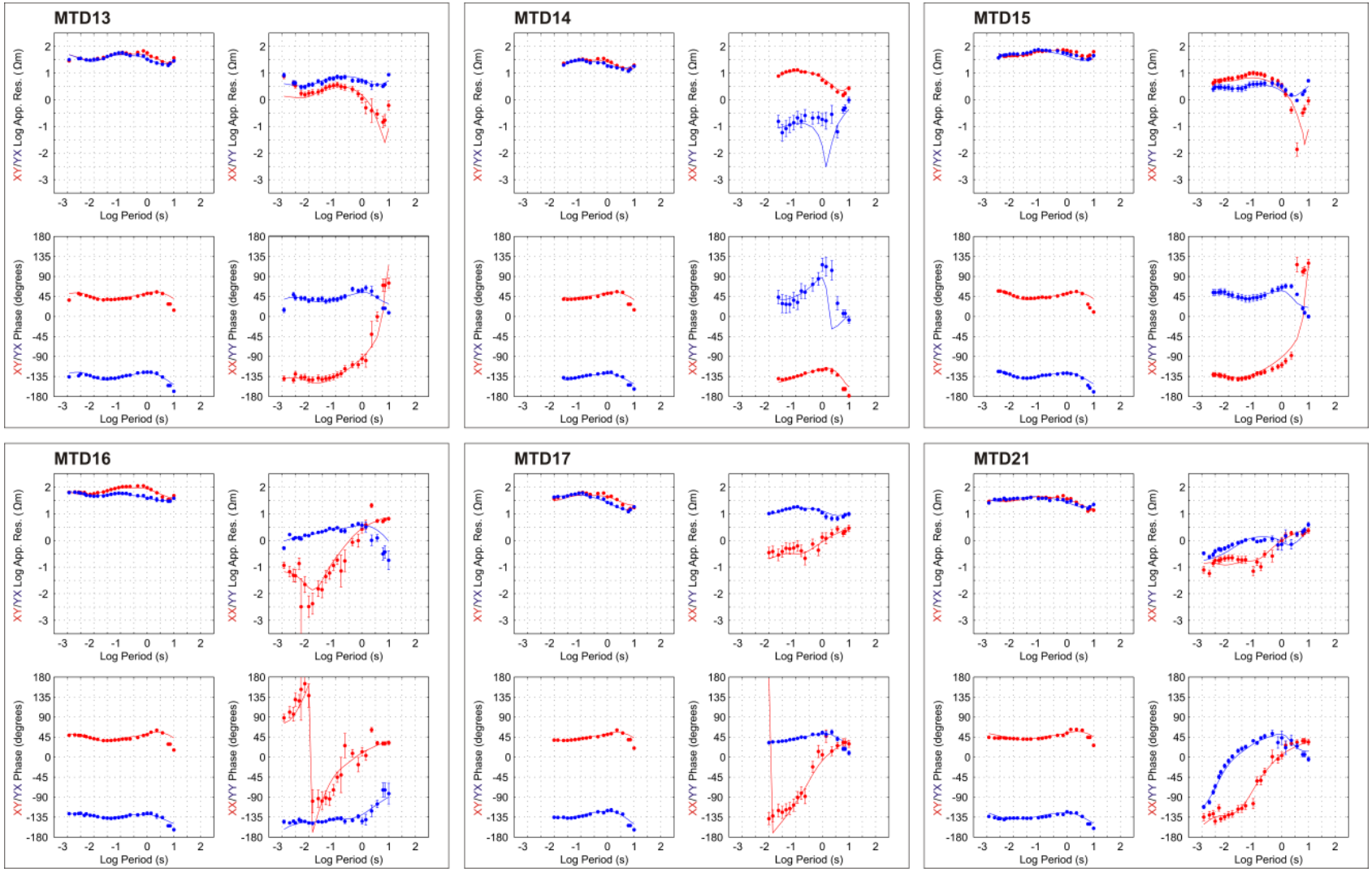

Fig. S13. Observed data and model responses at sites MTD13, MTD14, MTD15, MTD16, MTD17 and MTD21.

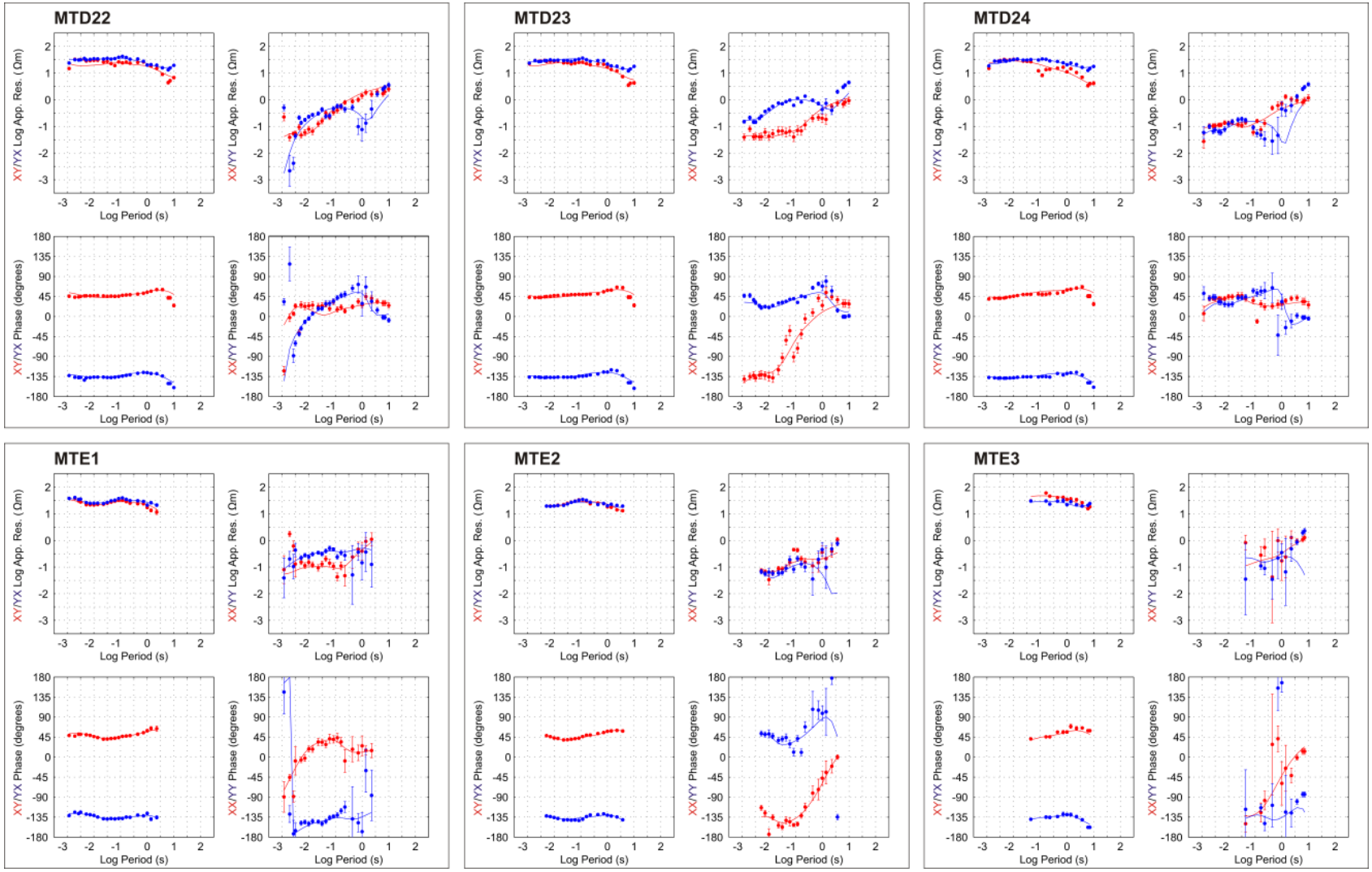

Fig. S14. Observed data and model responses at sites MTD22, MTD23, MTD24, MTE1, MTE2 and MTE3.

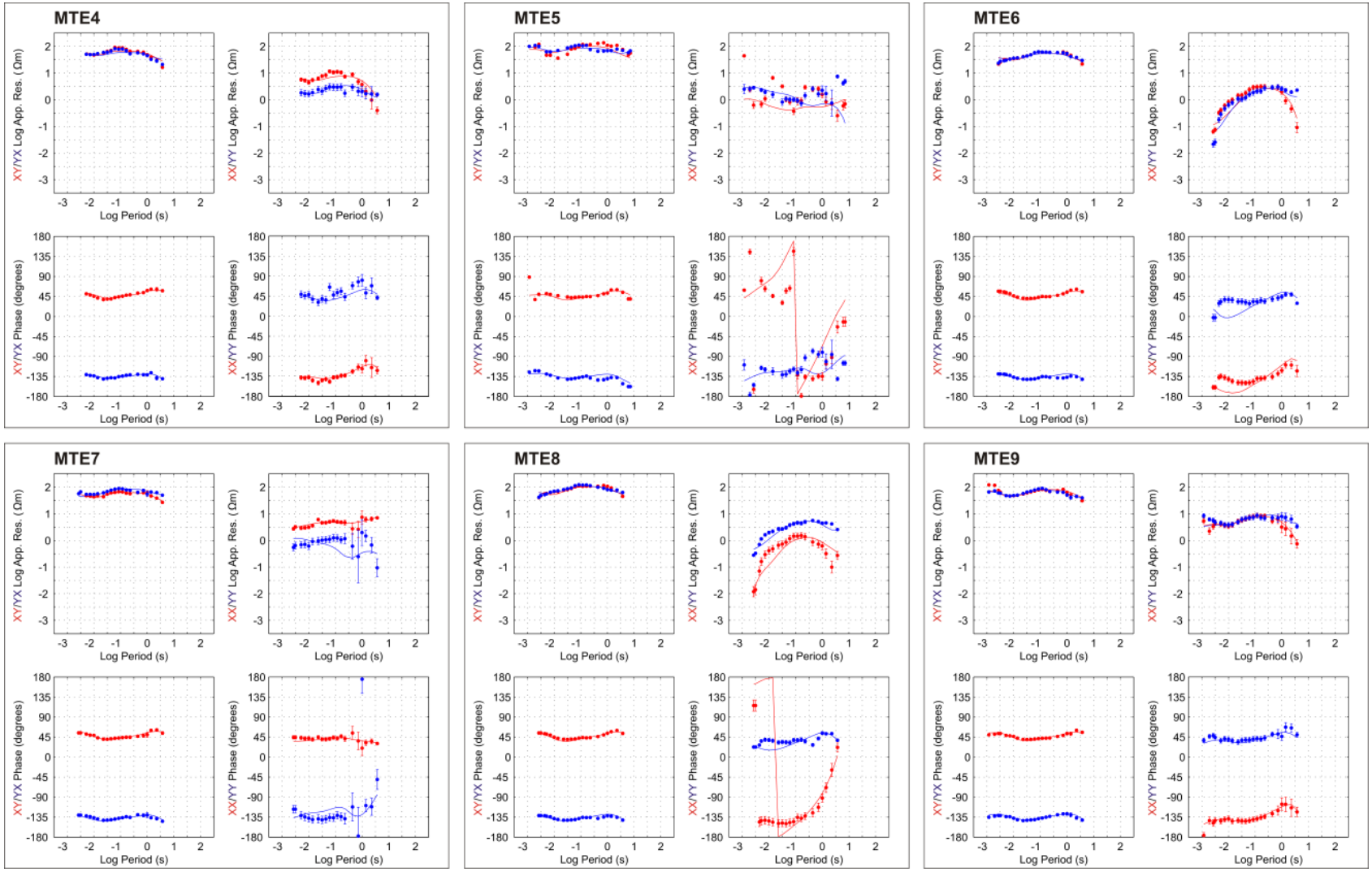

Fig. S15. Observed data and model responses at sites MTE4, MTE5, MTE6, MTE7, MTE8 and MTE9.

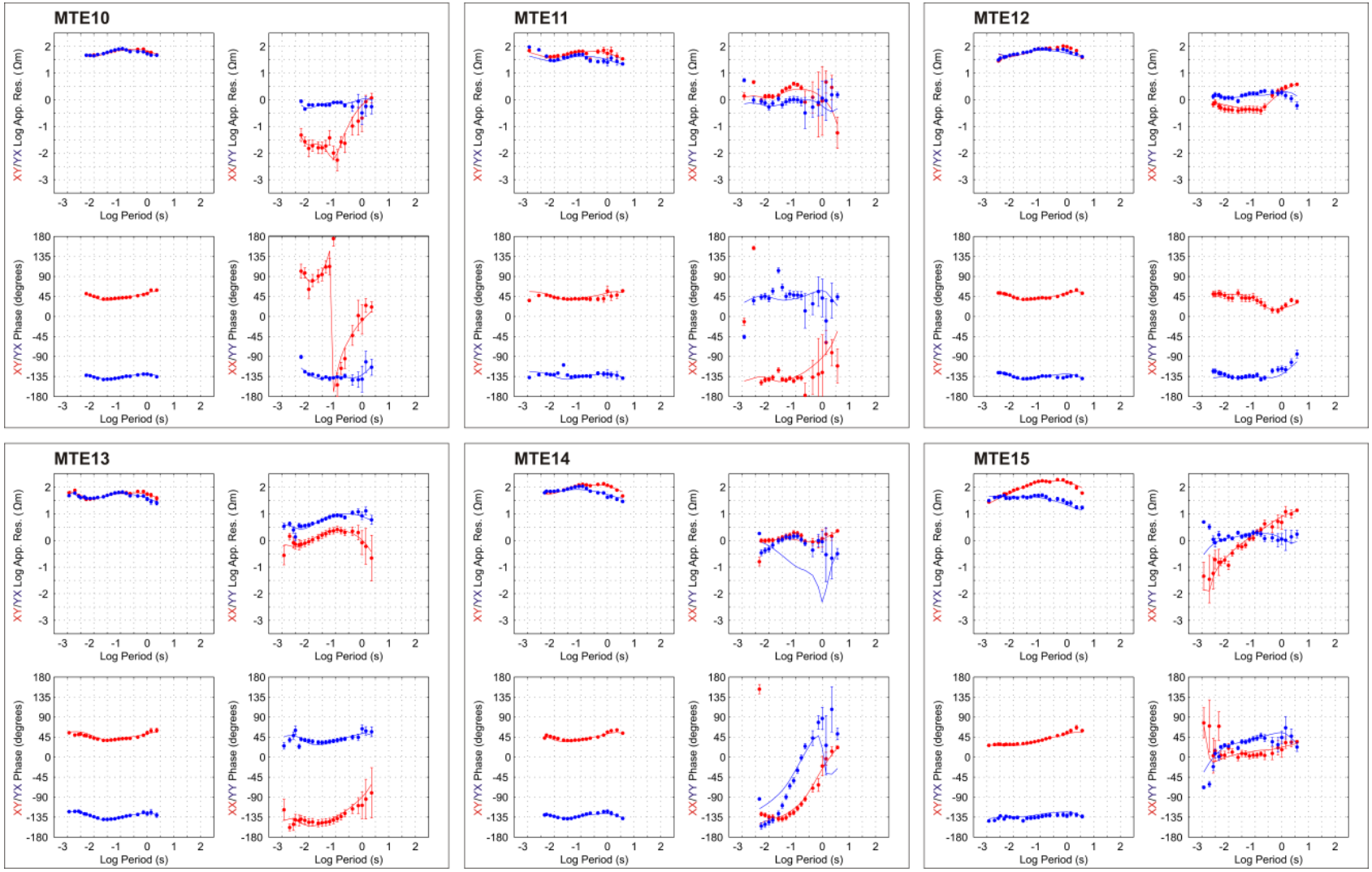

Fig. S16. Observed data and model responses at sites MTE10, MTE11, MTE12, MTE13, MTE14 and MTE15.

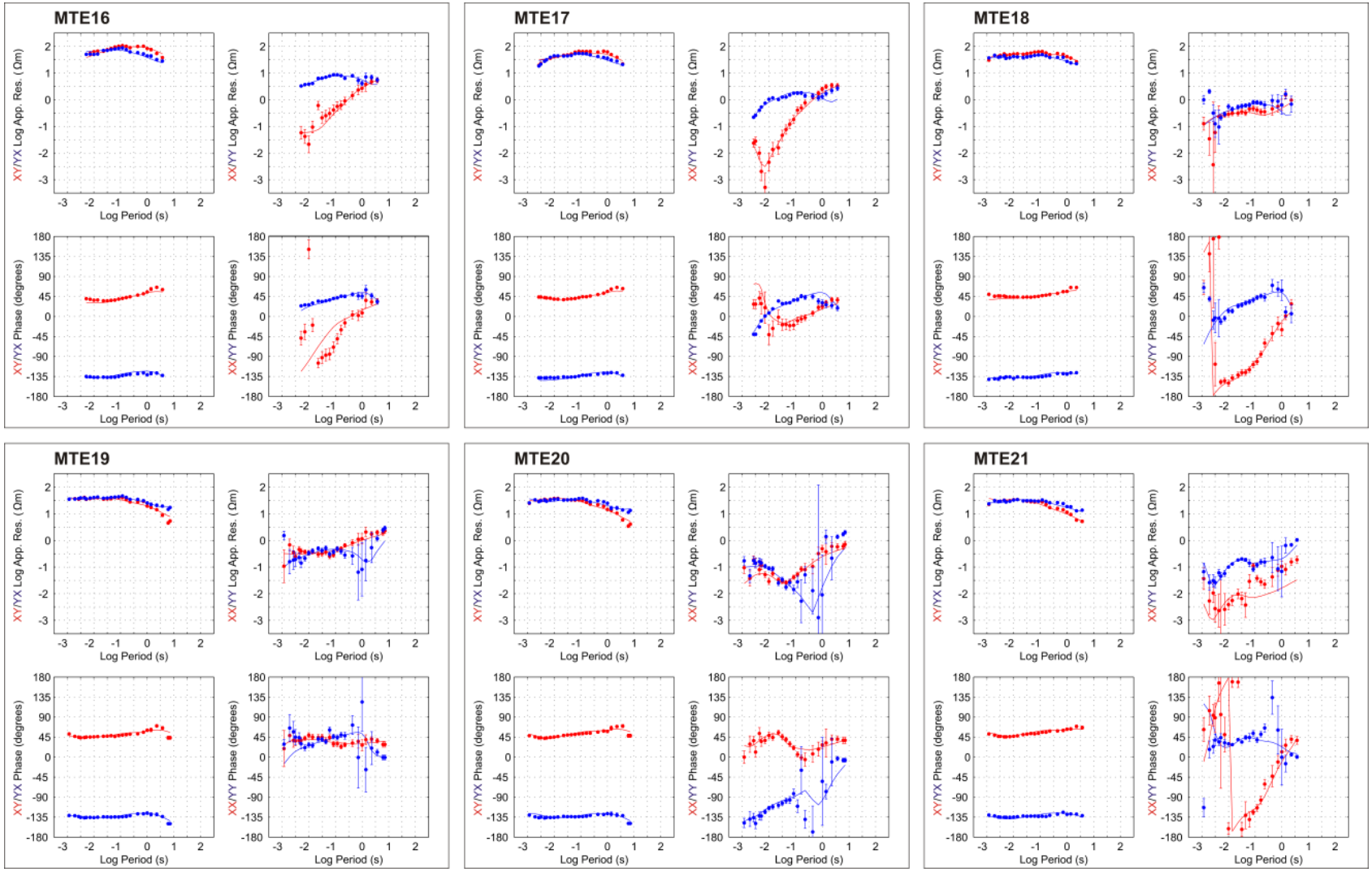

Fig. S17. Observed data and model responses at sites MTE16, MTE17, MTE18, MTE19, MTE20 and MTE21.

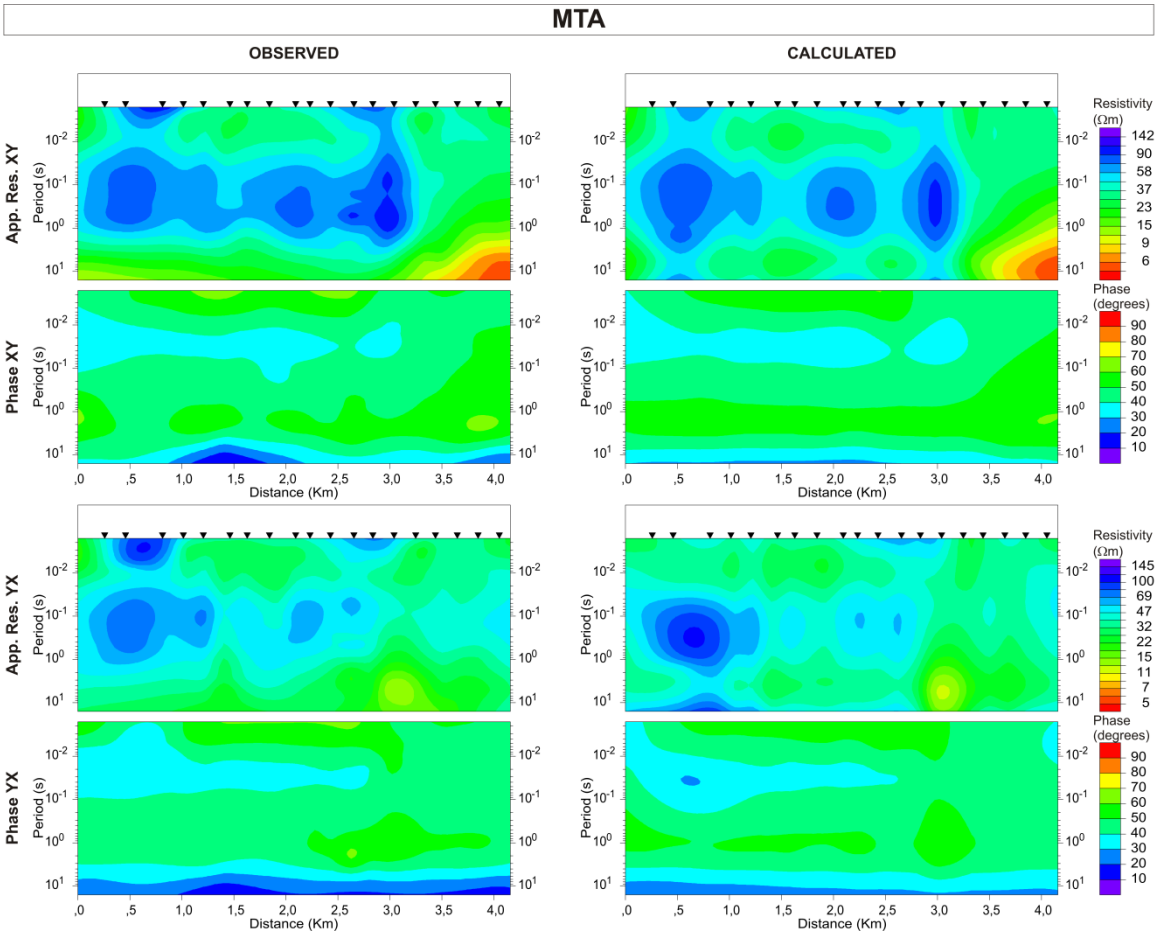

Fig. S18. Pseudosections of MTA profile: Apparent resistivity and phase for observed data and model responses. The position of the BBMT sites is marked as black triangles.

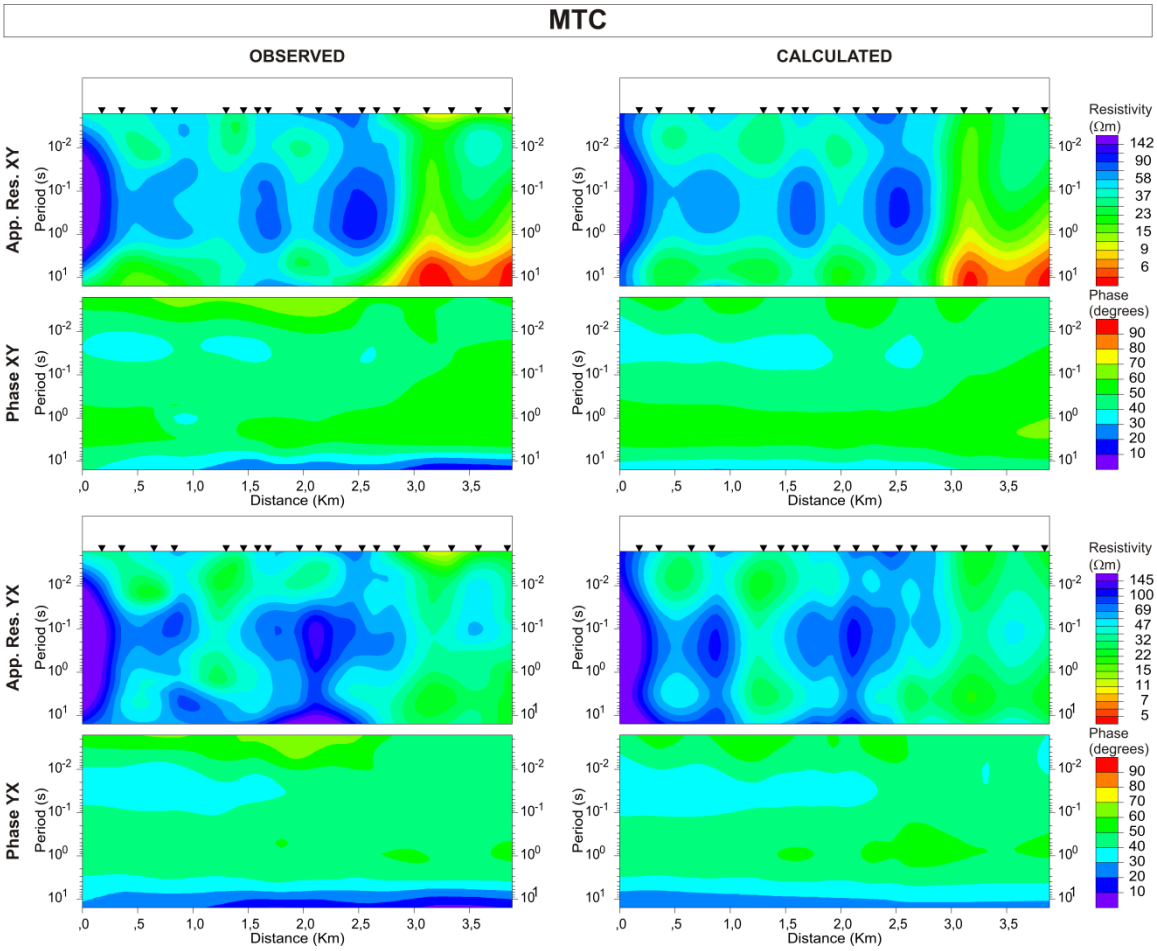

Fig. S19. Pseudosections of MTC profile: Apparent resistivity and phase for observed data and model responses. The position of the BBMT sites is marked as black triangles.

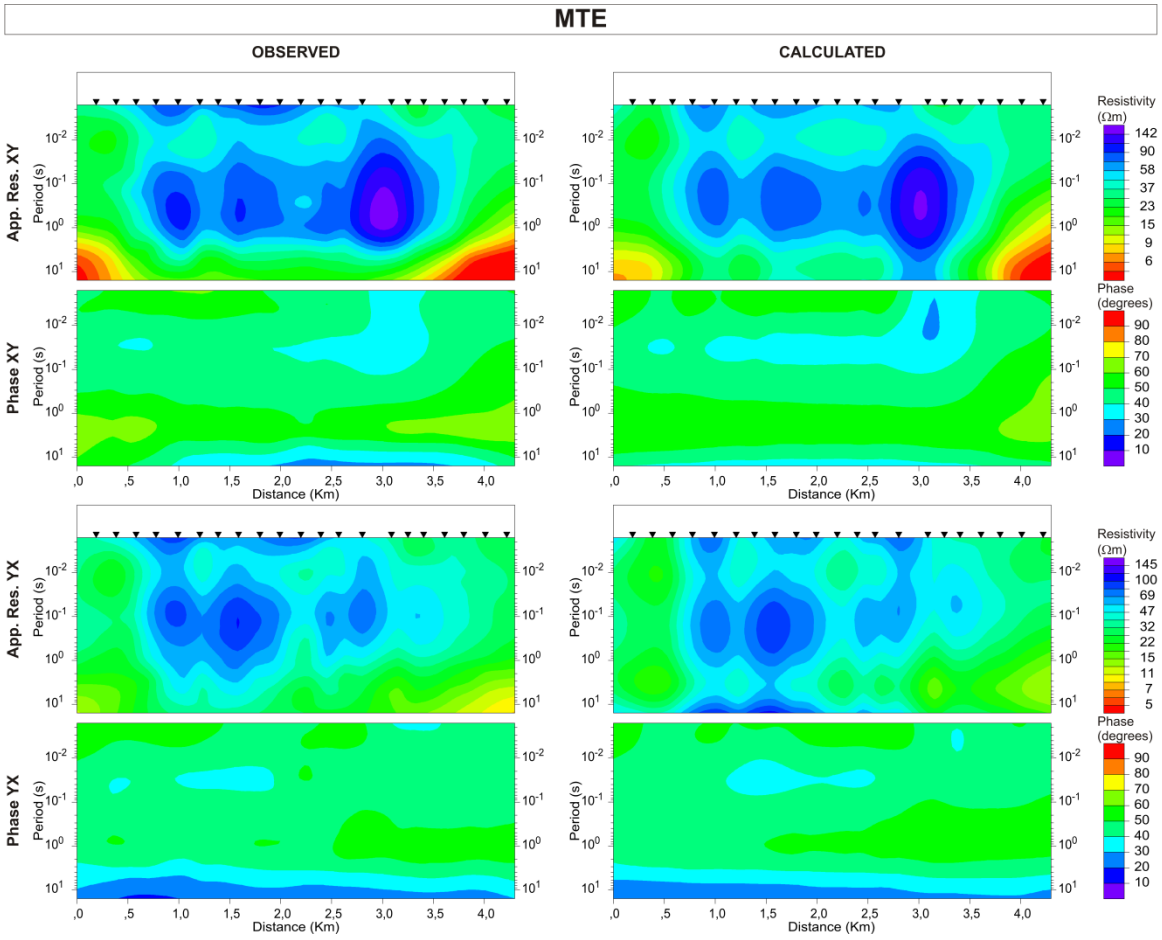

Fig. S20. Pseudosections of MTE profile: Apparent resistivity and phase for observed data and model responses. The position of the BBMT sites is marked as black triangles.

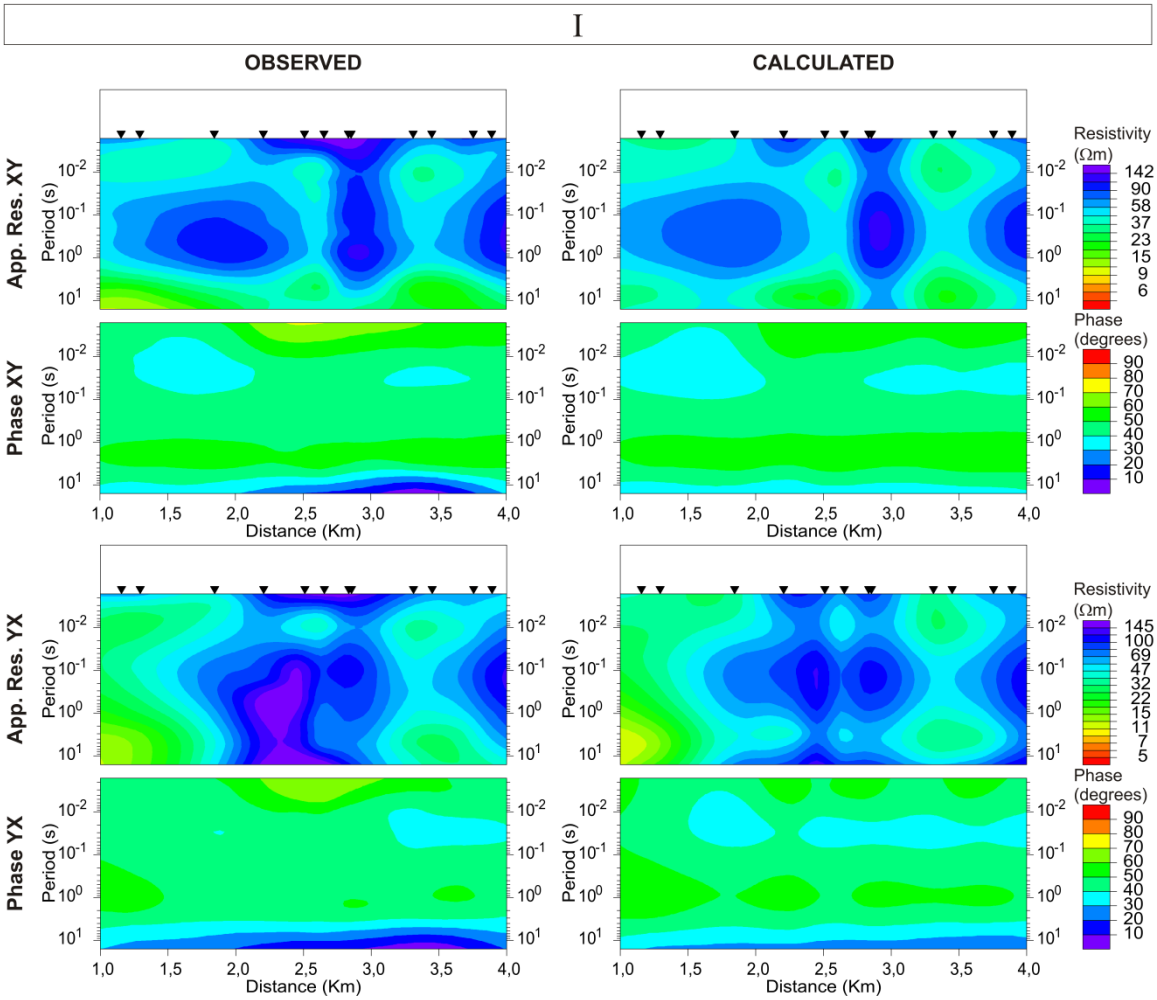

Fig. S21. Pseudosections of profile I: Apparent resistivity and phase for observed data and model responses. The position of the BBMT sites is marked as black triangles.

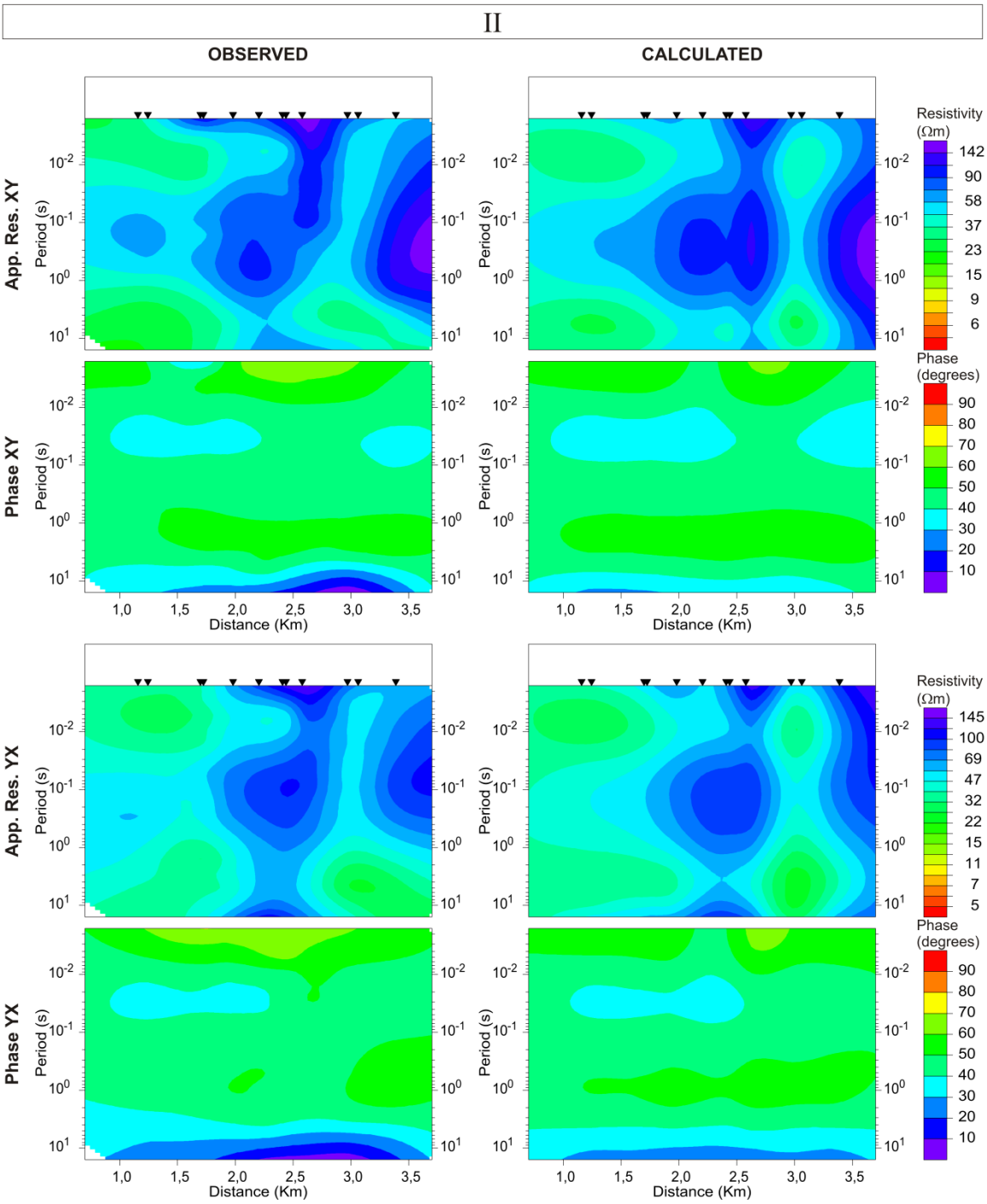

Fig. S22. Pseudosections of profile II: Apparent resistivity and phase for observed data and model responses. The position of the BBMT sites is marked as black triangles.

PEER reviewed papers

1

Ogaya, X., Ledo, J., Queralt, P., Marcuello, A., Quintà, A., 2013. First geoelectrical image of the subsurface of the Hontomín site (Spain) for CO_2 geological storage: A magnetotelluric 2D characterization. International Journal of Greenhouse Gas Control 13, 168-179, doi: 10.1016/j.ijggc.2012.12.023.

2

Ogaya, X., Queralt, P., Ledo, J., Marcuello, A., Jones, A.G., 2014. Geoelectrical baseline model of the subsurface of the Hontomín site (Spain) for CO_2 geological storage in a deep saline aquifer: A 3D magnetotelluric characterisation. International Journal of Greenhouse Gas Control 27, 120-138, doi: 10.1016/j.ijggc.2014.04.030.

1

Ogaya, X., Ledo, J., Queralt, P., Marcuello, A., Quintà, A., 2013. First geoelectrical image of the subsurface of the Hontomín site (Spain) for CO_2 geological storage: A magnetotelluric 2D characterization. International Journal of Greenhouse Gas Control 13, 168-179, doi: 10.1016/j.ijggc.2012.12.023.

International Journal of Greenhouse Gas Control 13 (2013) 168–179

Contents lists available at SciVerse ScienceDirect

International Journal of Greenhouse Gas Control

journal homepage: www.elsevier.com/locate/ijggc

First geoelectrical image of the subsurface of the Hontomín site (Spain) for CO_2 geological storage: A magnetotelluric 2D characterization

Xènia Ogaya[a,b,*], Juanjo Ledo[a], Pilar Queralt[a], Álex Marcuello[a], Anna Quintà[a]

[a] Institut de Recerca, Centre Mixt d'Investigació GEOMODELS, Group of Geodynamics and Basin Analysis, Dept. Geodinàmica i Geofísica, Universitat de Barcelona (UB), Spain
[b] Fundación Ciudad de la Energía (CIUDEN), Ponferrada, Spain

ARTICLE INFO

Article history:
Received 13 April 2012
Received in revised form 16 October 2012
Accepted 24 December 2012
Available online 18 January 2013

Keywords:
Geophysical imaging
CO_2 geoelectrical baseline model
Magnetotellurics
Electrical resistivity

ABSTRACT

Magnetotelluric (MT) data provided a two-dimensional (2-D) resistivity model of the subsurface of the Technology Demonstration Plant (TDP) located in Hontomín (Burgos, Spain) for geological storage of CO_2 in a deep saline aquifer. A first north–south profile of 22 broadband MT soundings was acquired to study the viability of the method to characterize the TDP subsurface. Stations were deployed at approximately 200-m intervals and the data were recorded in the period range of 0.001–100 s. The dimensionality analysis proved the validity of the 2-D assumption, and therefore a joint 2-D inversion of the TE and TM modes was undertaken constraining the modelling process according to a vintage resistivity log acquired for oil exploration. The 2-D model provides the first geoelectrical image of the structure and links the different lithologies to electrical properties. Results locate the main reservoir and seal units in the period range of 0.1–1 s. Thereby it is proved the validity of the method to supply a high resolution baseline model able to fully image the geoelectrical structure of the Hontomín site in the pre-injection state.

1. Introduction

Currently, carbon capture and storage (CCS) is considered a potential mitigation technique for climate change. It aims to trap and transport the carbon dioxide (CO_2) emitted from large point sources to suitable storage sites. There, the CO_2 is stored into the porous of a permeable formation (reservoir) which is capped by another impermeable formation (seal) that prevents it from migration to the surface (IPCC, 2005). The gas is injected at depths below 800 m, where CO_2 reaches supercritical conditions (T_c = 31.1 °C and P_c = 7.38 MPa). At these conditions, CO_2 behaves still like a gas filling all the available volume, but with a liquid-like density. With the same volume, at supercritical state it is able to store more quantity of CO_2 because the density is higher. Thereby increasing the density, the storage of CO_2 in the pore space is more efficient and becomes safer since buoyancy forces decrease (Bachu, 2003).

In Spain, saline aquifers offer the most suitable scenario for CO_2 geological storage (Pérez-Estaún et al., 2009). For this reason, the Fundación Ciudad de la Energía – CIUDEN has established a Technology Demonstration Plant (TDP) for CO_2 storage in a deep saline aquifer. The project is partly funded by the Spanish Government and co-financed by the European Union through the European Energy Programme for Recovery. The Research Laboratory is located in Hontomín (Spain) and this work presents a component of the on-going project.

To date, geological storage of CO_2 is being carried out offshore and onshore and both at pilot – an industrial-scale (Global CCS Institute, 2011). Monitoring the whole process is essential in order to image the migration of the CO_2 plume within the reservoir during and after the injection and detect any possible leak. It is a valuable tool to support the required safety conditions providing information about the evolution of the injected gas. As the migration takes place at various scales, there is no single technique able to fully characterize the CO_2 plume together with reservoir and seal behaviours. For this reason, a huge number of methods are being implemented in a complementary manner in order to resolve ambiguities and overcome the existing gaps (Giese et al., 2009; Sato et al., 2011; JafarGandomi and Curtis, 2011). The hydrocarbon exploration activity has provided experience on this field (Hoversten et al., 2003; Harris and MacGregor, 2006; Harris et al., 2009).

Geophysical techniques are presented as the most useful tool to characterize and monitor the reservoir complex and the seal and reservoir integrities. Among them, electrical and electromagnetic methods are very suitable for monitoring purposes since they offer a high degree of complementarity to study the different scales of interest in reservoirs and are sensitive to electrical conductivity. In aqueous fluids (saline aquifers), the electrical conductivity is strongly dependent on fluid salinity, temperature, porosity, pore connectivity, saturation and, to some extent, on pressure

* Corresponding author at: Facultat de Geologia, Dept. Geodinàmica i Geofísica, C/Martí i Franqués s/n, 08028 Barcelona, Spain. Tel.: +34 934034028; fax: +34 934021340.
E-mail address: xeniaogaya@ub.edu (X. Ogaya).

1750-5836/$ – see front matter © 2012 Elsevier Ltd. All rights reserved.
http://dx.doi.org/10.1016/j.ijggc.2012.12.023

(Bedrosian, 2007). In the specific case of CO_2 storage in a saline aquifer, these relationships are even more relevant since the presence of the gas inside the pore replaces a fraction of saline fluid reducing the effective volume available for ionic transport (Bourgeois and Girard, 2010; Nakatsuka et al., 2010). As a consequence, the bulk electrical resistivity of the rock is expected to increase strongly enabling to properly detect the CO_2 saturation in the porous of the formation by electrical and electromagnetic (EM) methods (Nakatsuka et al., 2010; MacGregor, 2012).

At present, many studies about the viability of monitoring by EM methods are being carried out using: electrical resistivity tomography (ERT) or its extension, cross-hole ERT; control-source electromagnetic (CSEM) and control-source magnetotellurics (CSMT). The applicability of cross-hole ERT has been evaluated through synthetic studies (e.g. Ramirez et al., 2003; Christensen et al., 2006; Carrigan et al., 2009; Hagrey, 2011) and it has provided interesting results at Ketzin pilot site (Kiessling et al., 2010) since the electrodes distribution along wells allows to reach deeper penetration. Moreover, CSEM is getting growing attention in the monitoring process because the incorporation of the source to the method makes possible to control and minimize the man-made EM noise. During last decades, the method has been used in marine context to monitor hydrocarbon extraction and injection and working in this line, some viability studies have been presented (Lien and Mannseth, 2008; Black and Zhdanov, 2009; Orange et al., 2009). Recently, the method has been introduced to terrestrial contexts. Some synthetic studies analysing the propagation of EM fields and evaluating different configurations of sources and receivers are Bourgeois and Girard (2010) and Wirianto et al. (2010). Some of the experiments undertaken in Ketzin are reported in Becken et al. (2010) and Girard et al. (2011). Regarding to CSMT, some synthetic works exploring and evaluating the possibilities of the method in monitoring processes have also been presented (Streich et al., 2010). The MT method is typically used to characterize structures at regional and crustal scale (e.g. Bedrosian, 2007). However, its main drawback is its dependence to a natural-source. Thus CSMT technique is presented as a solution allowing a major control of the EM noise.

Effectiveness of any monitoring technique must be assessed on site-by-site basis. All works agree on highlighting the importance of a previous characterization of the area to assure the success of the monitoring process. To perceive and quantify any change owing to the CO_2 injection will be essential to know in detail the structure in the pre-injection state. Hence a reliable and realistic baseline geoelectrical model is imperative to design a proper monitoring set up.

This work will focus on the first stage of the geoelectrical characterization of the Spanish TDP for CO_2 geological storage in Hontomín. The characterization work will be carried out by means of the magnetotelluric method since it is the only EM method that can provide an image of the electrical resistivity distribution at the required depths. Nevertheless, as the study area is surrounded by wind turbines and DC power-supply lines together with other EM-noise sources, further considerations have to be taken. Thus, prior to carry out a full three-dimensional (3-D) survey, a two-dimensional (2-D) MT survey has been undertaken and presented in this work. The aim is to study the viability of the method in the area as well as to obtain a first geoelectrical image of the subsurface of the Hontomín TDP.

2. Geological setting

The study area is located in Hontomín, in the southern sector of the Basque-Cantabrian Basin (Western Pyrenees, north Spain), between the Sierra de Cantabria Frontal Thrust and the Ubierna Fault (Fig. 1). Basque-Cantabrian Basin is an Upper Jurassic-Lower Cretaceous extensional basin related with the opening of North Atlantic and Gulf of Biscay (Le Pichon and Sibuet, 1971; Montadert et al., 1979; Ziegler, 1988; Vera, 2004). This basin was filled with a thick sequence of Mesozoic sediments, which overlays a package of Upper-Triassic evaporites. From late Cretaceous, the opening of south Atlantic produces the convergence and collision of Iberian and Eurasian tectonic plates, which generates the Pyrenean orogen (Boillot and Capdevila, 1977; Boillot and Malod, 1988; Roest and Srivastava, 1991; Muñoz, 1992). During this period, previous Mesozoic basins were inverted and incorporated to the Pyrenean orogen.

Exploration activities have provided geological and geophysical information of the study area since early 60s. Vintage seismics and well logs neighbouring the Hontomín structure show that is a dome anticline structure cored by Upper Triassic evaporates (Keuper facies), which folds the overlying Mesozoic and Cenozoic sequence. Concretely, it is constituted by Jurassic carbonates (dolostones, limestones and marls), Lower Cretaceous sandstones, shales and conglomerates, Upper Cretaceous limestones and marls, and finally, Cenozoic detritic materials (conglomerates, sandstones and shales).

The stratigraphic sequence shows several reservoir and seal units at different ages. On one hand, exploration activity in Hontomín reveals the existence of a hydrocarbon reservoir in Jurassic limestones sealed by Jurassic marls. On the other hand, in Ayoluengo oil field, there is hydrocarbon extraction from Lower Cretaceous sandstones composing the Purbeck paleochannels. The seal is constituted by clays from Purbeck and Weald formations. Moreover, there exist more reservoir levels such as Utrillas formation and other Upper Cretaceous limestone levels; however, in Hontomín, they are located at shallow depths.

Thereby, in Hontomín, the injection is planned to be in the basal part of the carbonate reservoir system, which is located about 1500 m depth. Consequently, the saline aquifer constituted by more than 100-m-thick sequence of Lower Jurassic limestones (Sopeña Formation and the upper part of the Puerto de la Palombera Formation, underneath it) will act as a primary reservoir. In this way, four black-shale levels interbedded in the Lower Jurassic marls (Camino Formation) will offer a primary seal. Upwards, Purbeck and Weald facies (Upper Jurassic-Lower Cretaceous) constituted by intercalations of conglomerates, sandstones and shales will represent a feasibly secondary reservoir-seal system. They may act as suitable stratigraphic trap ensuring the stop of the CO_2 upwards migration.

For this survey, it is worth to point out well Hontomín-2 (H2) drilled in 1968 for the mentioned oil exploration purposes. The well crosses the centre of the dome and is placed around 100 m away from the acquired MT profile (Fig. 1). Its resistivity log data provided a one-dimensional (1-D) model that supplied a starting resistivity model and helped to constrain the MT data inversion process. Moreover, it made possible to link the stratigraphy of the study area to the electrical properties of the different lithologies and formations (Fig. 2).

3. Main reservoir: the saline aquifer

The primary reservoir rock is mainly constituted of calcite (around 97%) and dolomite (around 1%) and the porosity estimation obtained from the vintage well logs of the area ranges from 0% to 18% (Márquez and Jurado, 2011). The salinity is over 20 g/l. CIEMAT – *Centro de Investigaciones Energéticas, Medioambientales y Tecnológicas* – carried out a survey to describe the subsurface waters in the Hontomín area (Buil et al., 2012). In order to characterize the

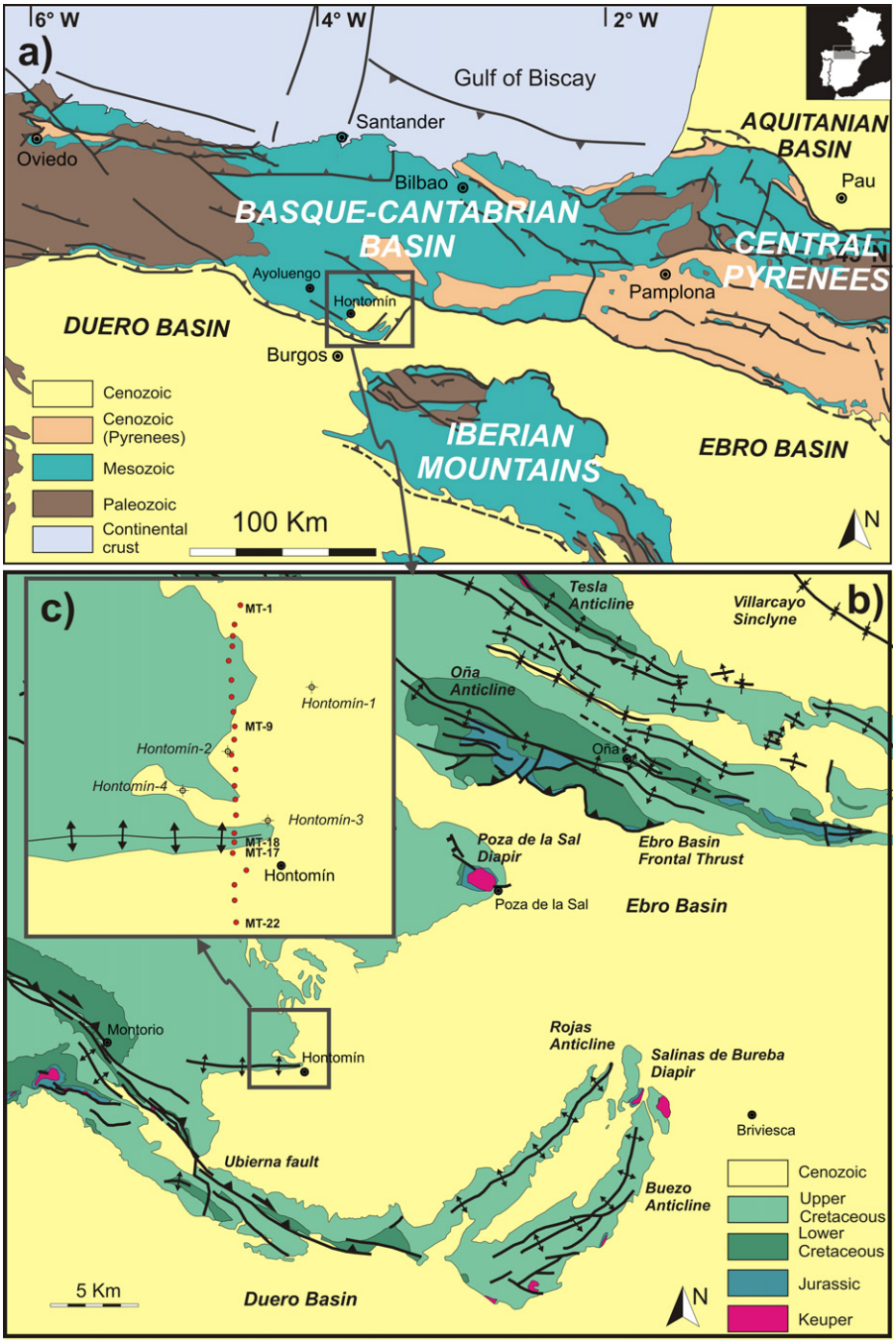

Fig. 1. Geological map. (a) Geological map of the Basque-Cantabrian Basin and the location of the study area (modified from Muñoz, 2002). (b) Geological map of Hontomín surrounding area with the location of the Hontomín structure. (c) Red dots indicated the location of the acquired MT soundings (MT1, MT2, . . .). The location of the four vintage exploration wells is also indicated. (For interpretation of the references to color in this figure legend, the reader is referred to the web version of the article.)

saline aquifer, several samples were acquired in H2 well at 1355 m depth. The results of this study reveal that the pH of the brine has a median value of 7.3 and the average electrical conductivity is 47 mS/cm which means a resistivity of 0.22 Ω m. Approximately, the chemical composition of the acquired samples is: 17,390 mg/l of chlorides (Cl^-); 244 mg/l of bicarbonates (HCO_3^-); 1782 mg/l of sulphates (SO_4^-); 8832 mg/l of Na; 431 mg/l of K; 773 mg/l of Mg and 1676 mg/l of Ca.

Since the saline aquifer of Hontomín is characterized by low resistivity brine (0.22 Ω m) and low clay content, the Archie's law (Archie, 1942) is useful to first estimate the resistivity change due to the CO_2 injection. It describes the resistivity behaviour of sedimentary porous rocks as a function of the most significant variables (Eq. (1)):

$$\rho = a \cdot \frac{\rho_w}{\phi^m \cdot S_w^n}, \quad (1)$$

water resistivity (ρ_w), water saturation (S_w) and rock porosity (ϕ). m is the cementation factor; n, the saturation exponent and a, a proportionality constant. This law describes reasonably well the conductivity when this is dominated by the electrolytic conduction due to brine ions; as a consequence, it is not valid in the presence of clays.

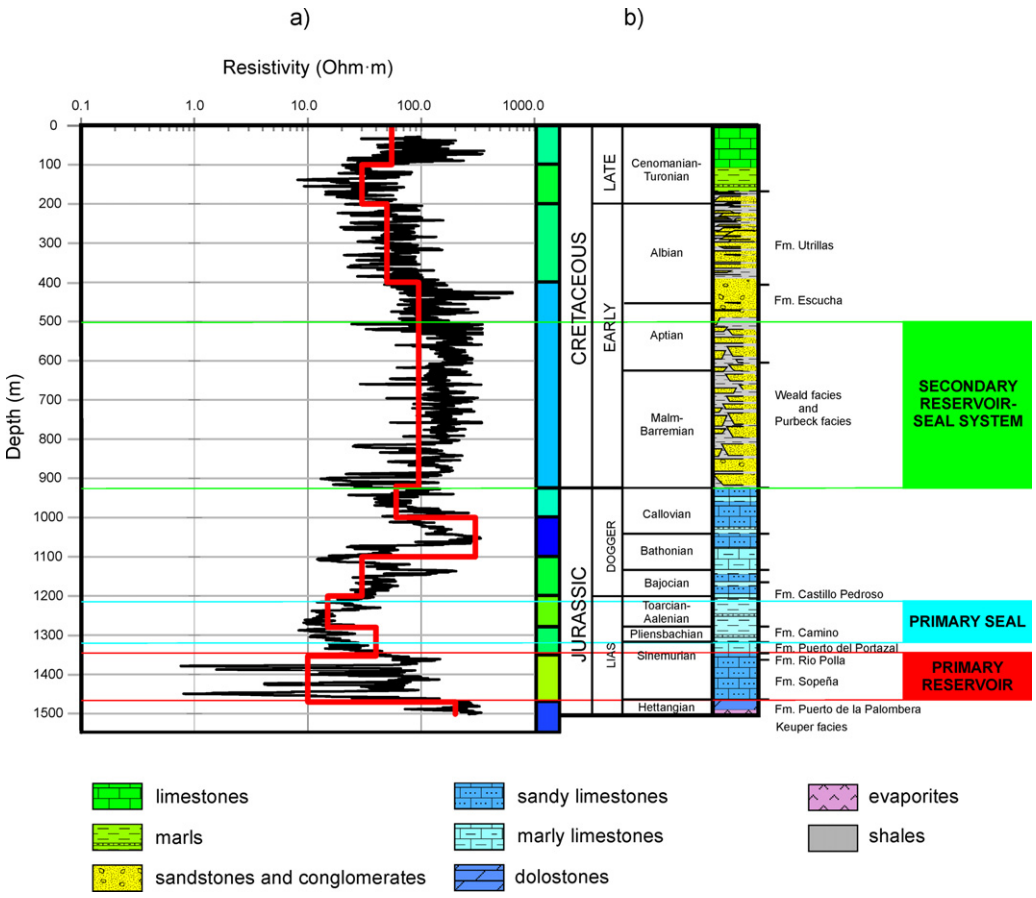

Fig. 2. Hontomín-2 (H2) resistivity well log and stratigraphic column. (a) The black line shows the Deep Induction Standard Processed Resistivity (resistivity log data) of H2 well and the red line displays the 11-layer earth model with the same MT response at the surface. On the right, the 1-D model in the color scale used in the final 2-D resistivity model (Fig. 5). (b) Stratigraphic column showing Triassic to Cretaceous materials. Primary and secondary reservoir-seal systems are indicated. (For interpretation of the references to color in this figure legend, the reader is referred to the web version of the article.)

Assuming just two fluid phases (the initial brine and the injected CO_2) within the reservoir formation and that the CO_2 does not interact with the rock (no dissolution, no precipitation; porosity remains constant), the pre-injection and post-injection resistivities of the bulk rock can be related in a simpler manner (Eq. (2)):

$$\frac{\rho}{\rho_0} = (1 - S_w)^{-n} \tag{2}$$

For the particular case of the Hontomín site, it is assumed an n value equal to 2 (clean sand). In this way, a homogenous saturation of 50% results in an expected post-injection resistivity equal to 4 times the pre-injection reservoir resistivity. As it is a non-commercial project the injection is limited to 100,000 tonnes. In fact, no more than 20,000 tonnes are planned to be injected in the Hontomín site which will correspond to a volume of 135 m × 135 m × 25 m given the pressure and temperature conditions at the reservoir depth.

4. MT method

The MT method is a natural-source electromagnetic technique able to infer the electrical conductivity distribution of the subsurface. It is based on the simultaneous measurement of the natural EM field variations at the Earth's surface. The origins of the method for geophysical exploration are attributed to Tikhonov (1950) and Cagniard (1953) who established the theoretical bases. Some fundamentals aspects of the method are going to be introduced in this work; for an extended explanation, see review papers on MTNet – www.mtnet.info.

In magnetotellurics, the incident EM field is treated as plane waves propagating downwards. In the conducting Earth, EM waves propagate diffusively and their penetration depends on both its oscillation frequency (ω) and the conductivity (σ) of the penetrated medium. The skin-depth (δ; Eq. (3)) is a reasonable measure of the inductive scale length which is the depth at which EM fields are attenuated to e of their amplitudes at the Earth's surface:

$$\delta = \sqrt{\frac{2}{\mu\sigma\omega}} \tag{3}$$

μ is the magnetic permeability typically assumed equal to its free space value μ_0. Thus high-frequency waves penetrate shallow depth while low-frequency waves are able to reach the mantle.

The field variations measured at the Earth's surface are then transformed to the frequency domain. The impedance tensor $Z_{ij}(\omega)$ is a complex second-rank tensor function of frequency. It contains the amplitude and phase relations between the measured horizontal components of the electric (E) and magnetic ($H = B/\mu_0$) fields (Eq. (4)),

$$\begin{bmatrix} E_x \\ E_y \end{bmatrix} = \begin{bmatrix} Z_{xx}(\omega) & Z_{xy}(\omega) \\ Z_{yx}(\omega) & Z_{yy}(\omega) \end{bmatrix} \begin{bmatrix} H_x \\ H_y \end{bmatrix} \tag{4}$$

From each element of the impedance tensor can be derived the MT response functions, apparent resistivity (ρ_{aij}) and phase (φ_{ij}), defined as it is shown in Eqs. (5) and (6), respectively:

$$\rho_{aij}(\omega) = \frac{1}{\mu\omega}\left|Z_{ij}(\omega)\right|^2 \tag{5}$$

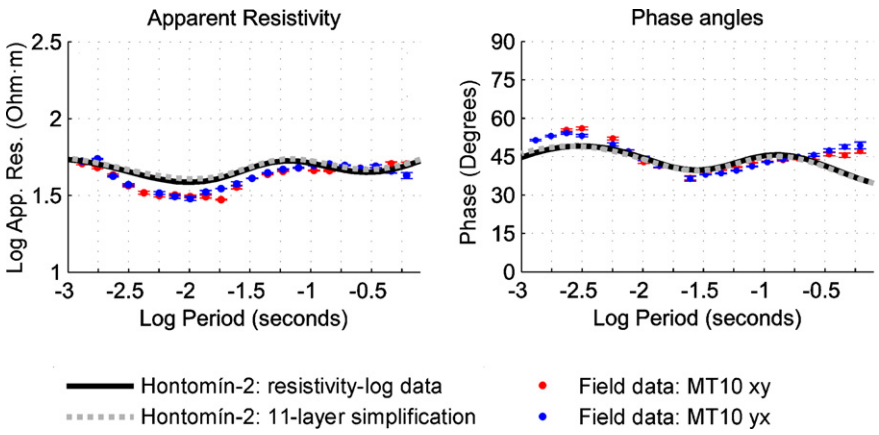

Fig. 3. MT responses at H2 well and MT10 sounding. The black solid line reproduces the MT response of H2 resistivity-log data. The grey dotted line shows the MT response of the 11-layer simplification of H2 (1-D model). Both MT responses at the surface are the same. Dots displayed the two polaritzation of the MT data acquired at MT10 sounding (located close to H2). The figure shows data from 0.001 to 0.9 s because the end of the well is approximately reached at 0.9 s.

$$\varphi_{ij}(\omega) = \tan^{-1}\left[\frac{Im\,Z_{ij}(\omega)}{Re\,Z_{ij}(\omega)}\right] \quad (6)$$

The form of the impedance tensor is related to the dimensionality of geoelectrical structures. In a 2-D earth, conductivity varies along one lateral direction and in depth. Thereby, it is defined a strike direction along which electrical conductivity remains constant. In this particularly case, electric and magnetic fields are mutually orthogonal and the equivalent impedance tensor can be decoupled into two independent modes. One of these modes is referred to as the transverse electric TE mode and describes the response of the electric currents flowing along the structure. The other mode is known as the transverse magnetic TM mode and describes the responses for the currents flowing across the structure. In this way, TM and TE modes satisfy the principle of complementary information and reliable and comprehensive information on the earth's conductivity can be obtained by means of joint TM and TE mode interpretations.

Regarding to the processing of the data, the remote reference (RR) technique helps in the improvement of the acquired data quality in areas with a non-contemptible level of EM noise. The RR method was introduced by Gamble et al. (1979) and consists on the simultaneous recording of local and remote magnetic fields. It aims to eliminate uncorrelated noise in the recorded fields assuming that the uncontaminated (natural) part of the induced field is expected to be coherent over large distances whereas noise is generally random and incoherent.

5. Previous geoelectrical information

Due to a former hydrocarbon exploration activity in the study area, there existed some a priori information that helped to construct an initial idea of the geoelectrical structure of Hontomín (Fig. 2). H2 well was chosen over the other wells because of its emplacement in reference to the MT profile. Consequently, its Deep Induction Standard Processed Resistivity (resistivity log data) was used to derive a 1-D model.

Taking into account the MT response at the surface, H2 resistivity log data was simplified to an 11-layer earth model. Fig. 3 shows that apparent resistivity and phase present the same behaviour in both cases. The end of the well is reached at approximately 0.9 s which corresponds to a depth of 1500 m according to the skin depth equation – Eq. (3) – and assuming a homogenous earth of 10 Ω m (resistivity of the most conductive layer of the well). In agreement with the available information (Fig. 2), the main reservoir-seal system is imaged in the range of 0.5–0.8 s by a relative minimum in the apparent resistivity curve. It can be detected earlier in the phases as is displayed by a maximum in the range of 0.1–0.6 s. Thus this study provided a 1-D model that helped to estimate the skin-depth of the study area and consequently, defined the range of periods that should be recorded in the field work.

6. Magnetotelluric data and 2-D inversion

In spring 2010, the first stage of the geoelectrical characterization of Hontomín was carried out. In total, 22 broadband magnetotelluric (BBMT) soundings (named MT1, MT2, ...) were acquired along a north–south profile taking into account the rather constant E–W trend of geological structures and crossing the main faults and folds. The total length of the profile was around 4 km and the stations were deployed at approximately 200-m intervals (Fig. 4). The data was recorded in the period range of 0.001–100 s: assuming a homogenous earth of 50 Ω m as it is derived from H2 resistivity log data (Fig. 3), and according to the skin depth equation (Eq. (3)), this period range allows characterizing depths between 112 m and 11 km. In the most conservative case of a homogenous earth of 10 Ω m (average H2 resistivity log data at the reservoir depth), the penetration depth ranges from 5 m to 5 km. Consequently, this period range fully characterizes the target region. The instrumentation consisted of Metronix ADU06, Metronix ADU07 and Phoenix V8. The *x*-axis was oriented in the magnetic north–south (N–S) direction pointing the north, and *y*-axis in the east–west (E–W) direction pointing the east. The EM noise was dealt with both, long time series (to minimize its effects by statistics) and RR acquisition methods and robust processing algorithm (to remove the incoherent part of the signal). Thereby the data was recorded during 48 h and a RR station was placed around 20 km away from the middle of the profile.

Different robust processing codes (Gamble et al., 1979; Egbert and Booker, 1986) using remote reference methods were tested and used at all stations of the profile to derive optimal MT responses (such as apparent resistivity and phase). Due to the important presence of wind turbines, DC power-supply lines and other electrical-noise sources in the area, the RR technique was essential to improve the quality of the MT data between 0.5 and 10 s. Fig. 5 summarizes the processing of the data; subfigures a and b show the improvement provided by the RR technique. Fig. 3 compares the MT data acquired at site MT10 (located close to H2 well) to the H2 well log data for periods shorter than 0.9 s. It is observed that the apparent resistivity and phase present the same behaviour as the resistivity log. At periods exceeding 10 s, the analysis of the MT responses highlights the presence of noise with phases decreasing

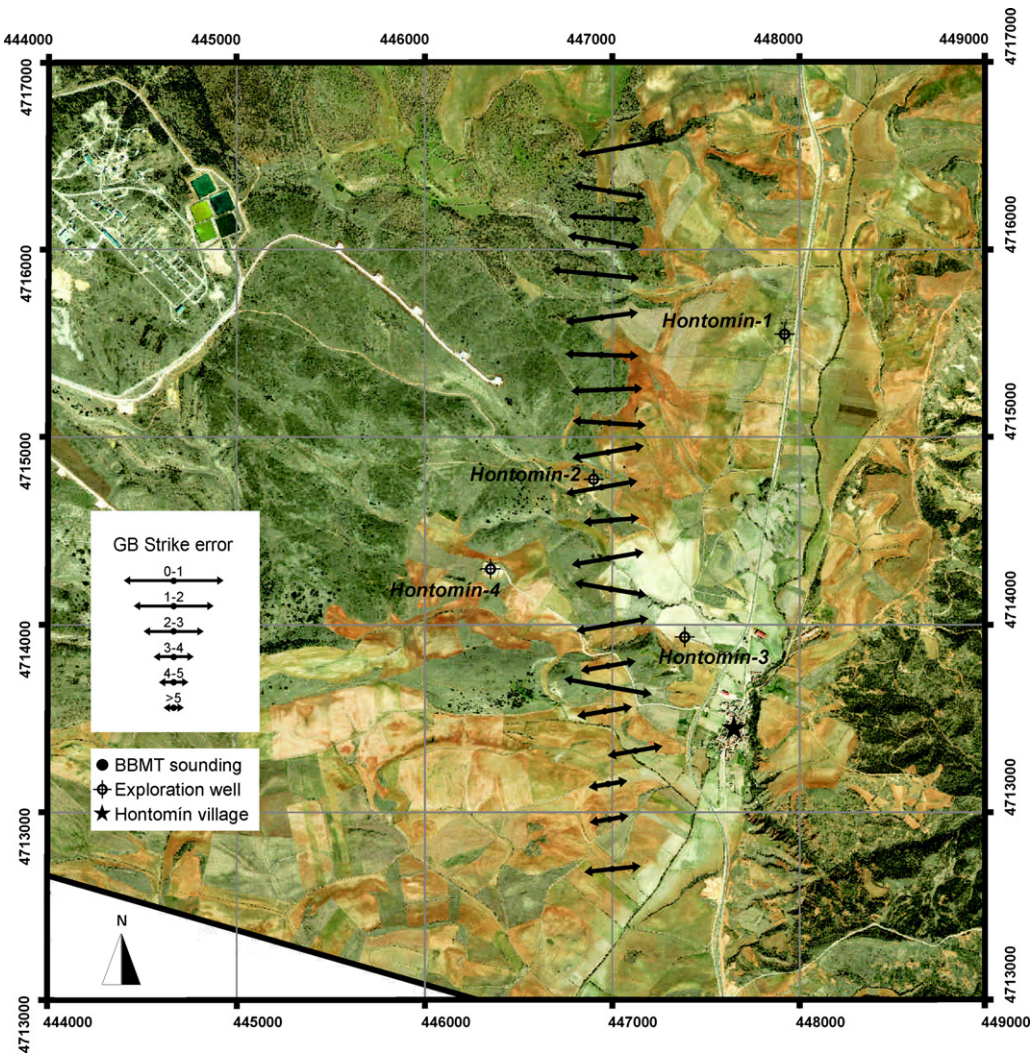

Fig. 4. Geoelectrical strike angle for the period range of 0.001–10 s with an error floor of 5% on the impedance tensor components. Black dots indicate the location of the BBMT soundings and arrows indicate the GB strike angle. Their length is associated with the compatibility of the data with the 2-D assumption. The best-fit average multi-site, multi-frequency GB regional strike is N86°E. The location of the four wells drilled in the past is also indicated.

to 0° and apparent resistivities showing slopes of 45° (Fig. 5). Consequently, all the following studies were undertaken in the period range of 0.001–10 s.

Prior to any geophysical interpretation of the MT responses, the MT dimensionality of the acquired data was computed using the distortion decomposition method of Groom and Bailey (1989; GB), which is implemented in the STRIKE code of McNeice and Jones (2001). This method facilitates the estimation of the regional impedance tensor by detecting and removing most of the effects caused by local near-surface heterogeneities. The strike direction ambiguity of 90° was fixed considering the orientation of the main geological units of the zone. Fig. 4 displays the best geoelectrical strike direction determined from the data at each site for the period range of 0.001–10 s with an error floor of 5% on the impedance tensor components. The arrows indicate the strike direction of each site and their length is associated with the compatibility of the data with the 2-D assumption. It can be seen that all sites of the profile display misfits to the GB distortion model with an RMS (root mean square) less than 2.0. Thus responses along the profile are consistent with the 2-D assumption and therefore, suitable for the 2-D modelling. The best-fit average multi-site, multi-frequency GB regional strike is N86°E, which represents a dominant East–West strike direction consistent with the pre-existing geological and geophysical information of the area. Consequently, the data was rotated −4°N as it is observed in Fig. 5c.

Small-scale geological inhomogeneities near the surface may produce galvanic distortion (Chave and Jones, 2012) resulting, for a 2-D case with axis oriented along and across the strike direction, in a vertical displacement of the apparent resistivity data. In our survey, this was overcome using the resistivity log data provided by well H2. The resistivity log data fixed the resistivity values at shallow depth defining the reference level for the apparent resistivity curves. As the first meters of the earth are mainly 1-D, both polarizations flow together at short periods. In all the BBMT soundings the correction was smaller than a cycle. Fig. 5c shows the static shift correction at site MT16.

Finally, it was studied the physical consistency of the data through the D^+ model solutions (Parker, 1980; Parker and Whaler, 1981). The method consists of analysing the physical validity of the MT responses finding the 1-D earth which best fits both apparent resistivity and phase curves. This technique has demonstrated to be valid for most 2-D cases and for some 3-D cases (Beamish and Travassos, 1992). Using an estimated error data of 10% in the apparent resistivity and in the phase, the D^+ solution allowed the detection and removal of the outliers and noisy points whose apparent resistivity and phase values did not show a coherent

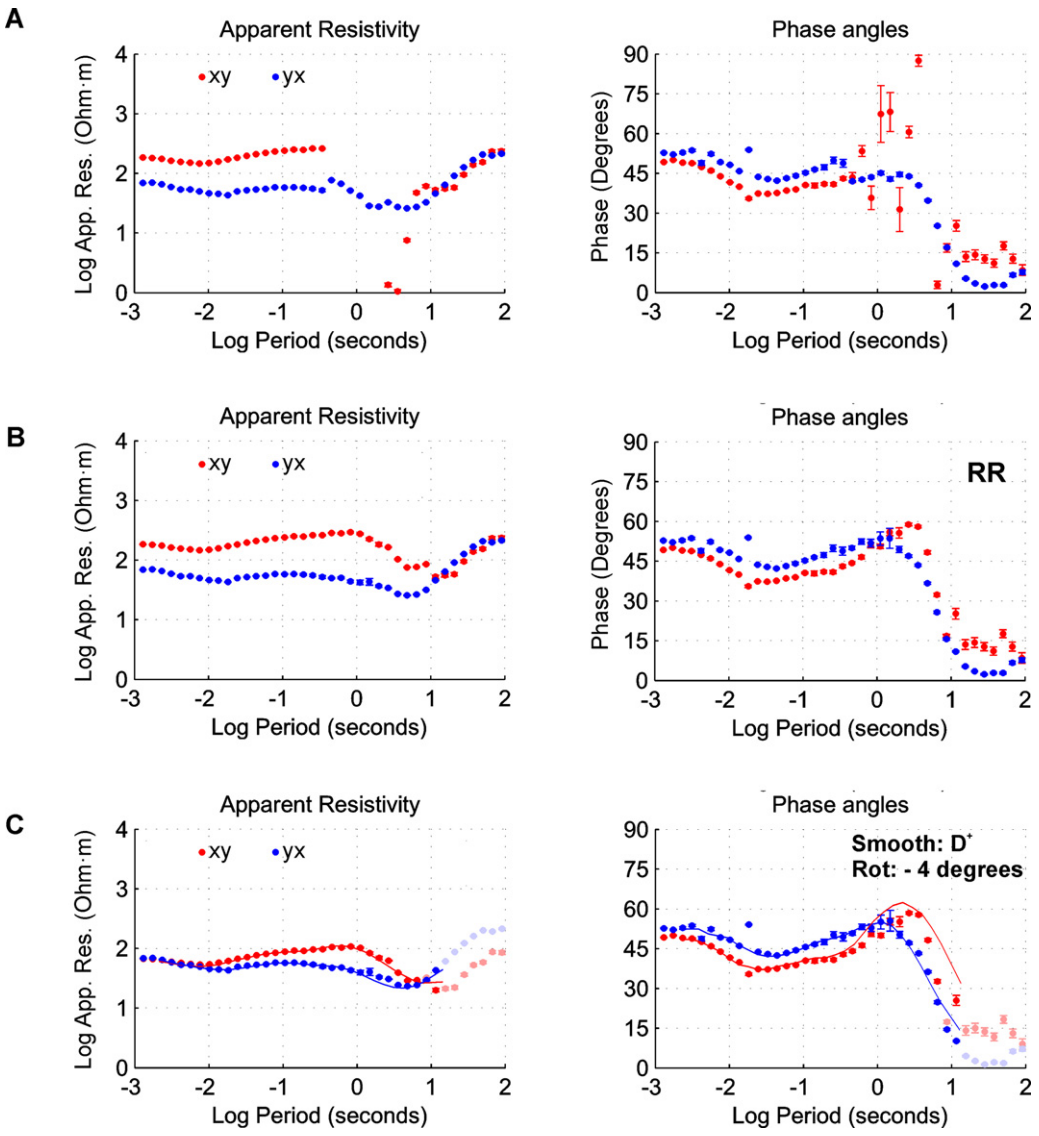

Fig. 5. MT responses at site MT16. (a) Robust processing not using the remote reference technique. (b) Robust processing using the remote reference technique. (c) Final MT responses at site MT16 after using the RR technique, rotating the data according to the regional strike and correcting the static shift. The smoothed curves (D^+ solution) are plotted using solid lines. Outliers and noisy points (removed data) are indicated by lighter colors. Since the rotation of the axes is small, there does not exist an appreciable change in the apparent resistivity and phase curves.

behaviour. In this way, the D^+ solution provided the smoothing of the data shown in Fig. 5c. In total, around 25% of the MT data was discarded (this percentage includes 10 to 100-s MT data – noisy region).

According to the results of the dimensionality analysis, which prove that the 2-D model is valid and appropriate, a joint 2-D inversion of the smoothed TE and TM apparent resistivity and phase data along the profile was undertaken rotating the *z*. The TE mode was identified with *yx* polarization and TM mode, with *xy* polarization. The 2-D inversion code used is that of Rodi and Mackie (2001). The algorithm searches for the model that trades off the lowest overall RMS misfit with the smallest lateral and vertical conductivity gradients in a regularized manner. The starting model was the 11-layer earth based on the simplification of the resistivity log provided by well H2. According to this imposition, cells of the model associated to this well were fixed during the inversion and modelling processes. The topography on the profile was also considered.

On average, the model fits the smoothed data with an RMS misfit of 1.29. The error floor for the phases was 1.45°, and 5% for the apparent resistivity. The final model together with the 11-layer simplification of H2 well resistivity log is shown in Fig. 6. Comparisons between data and model responses for the apparent resistivities and phases of both modes are shown in Fig. 7 (TE mode) and in Fig. 8 (TM mode). As is illustrated, the residuals between the observed data and the model responses are random and small, and no strong feature in the data is unexplained. Thus the fit between the data and model responses is highly satisfactory.

7. Interpretation and discussion

The magnetotelluric data inverted in the period range of 0.001–10 s produce a reliable resistivity image from near-surface to over 1800-m depth imaging the main reservoir (saline aquifer) and the main seal, as well as the secondary reservoir-seal system. All depths are given in terms of sea level since the topography has been taken into account (see Fig. 6). The resistivity distribution is composed by four main layers (from bottom to top): (1) a resistive layer (region R1) present below −600 m (bottom of the model); (2) a very conductive layer (area C1) imaged below −200 m with a thickness up to 400 m; (3) a resistive middle layer, between +700 m and

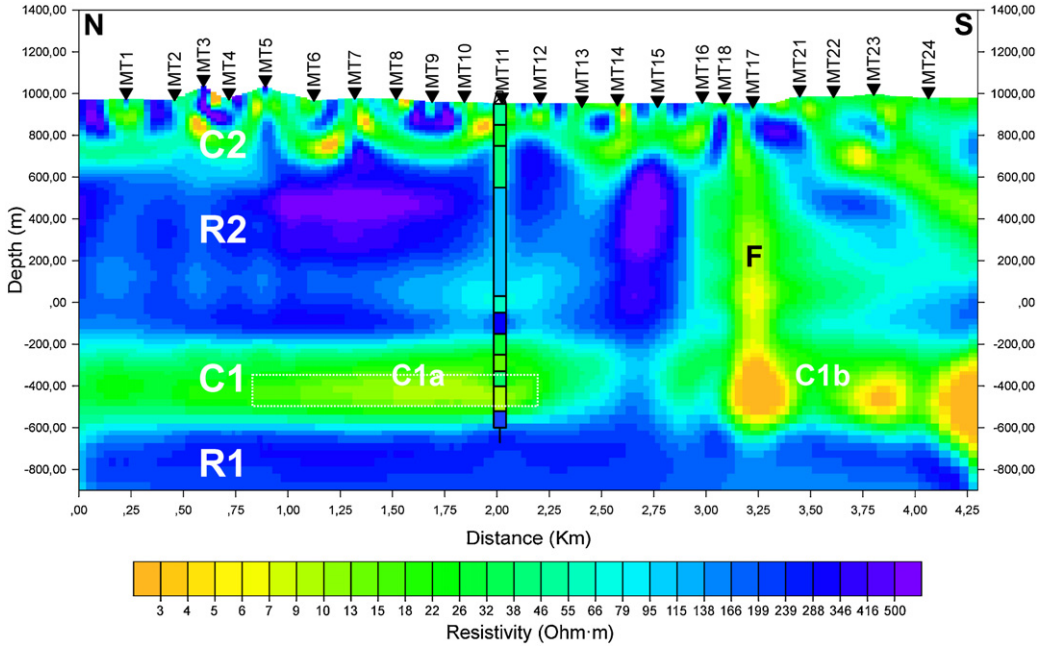

Fig. 6. 2-D resistivity model. The model fits the data with an RMS misfit of 1.29. Superimposed appears the 1-D model provided by the resistivity-log data of H2 well. MT soundings' position is marked as black triangles. The four main layers of the resistivity distribution are (from bottom to top): R1, C1, R2 and C2. The deep saline aquifer (main reservoir) and the main seal are within the conductive unit C1. A more resistive area beneath sites MT14 and MT15 divided this layer in two regions: C1a (where the injection is planned) and C1b. The secondary reservoir and seal system is contained in region R2. F indicates a vertical low resistivity structure disrupting R2 layer (a fault). Dotted line indicates the homogenous structure used to compute non linear sensitivity tests in the main reservoir region (see text for further information).

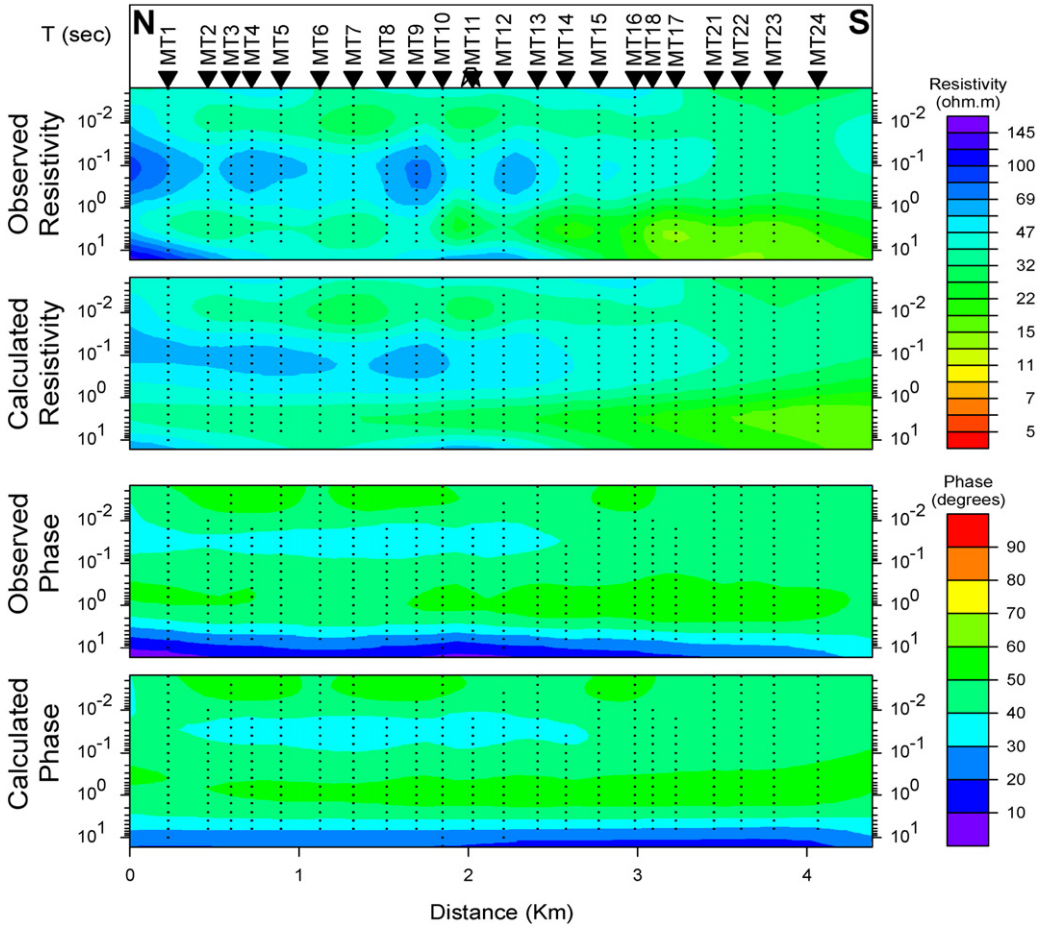

Fig. 7. Pseudosections of TE mode: Comparison of apparent resistivity and phase for the observed and model responses of TE mode. MT soundings position is marked as black triangles.

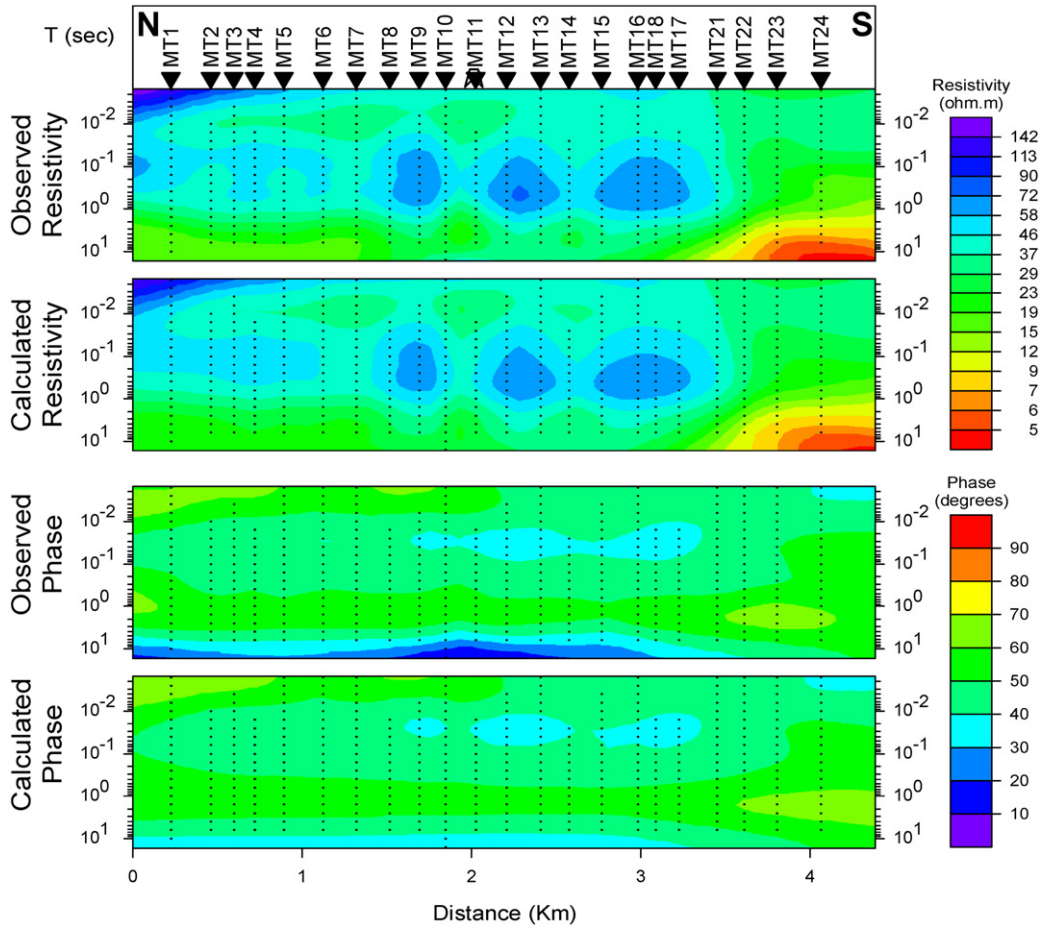

Fig. 8. Pseudosections of TM mode: Comparison of apparent resistivity and phase for the observed and model responses of TM mode. MT soundings position is marked as black triangles.

−200 m corresponding to region R2; (4) a conductive top layer (C2) with more resistive and conductive scattered small bodies evident from surface to +700-m horizon. H2 well makes possible to link these electrical properties to the different lithologies.

The resistive layer at the bottom of the model (R1) is required by the increase of the apparent resistivity data at around 1 s and coincides with the resistive Upper Triassic unit (Keuper facies) (Fig. 2). This is an impermeable and resistive unit which may constitute an interesting bottom seal (below the main reservoir).

The deep saline aquifer (primary reservoir) and the main seal are located within the conductive unit C1. The resistivity value of these structures is very similar and cannot be separately resolved only from surface MT measurements. Data from the H2 well log allows to better associate the small changes of electrical resistivity values within C1 to the different lithological units. This layer is divided into two regions (labelled C1a and C1b to facilitate the comprehension of the following discussion) by a more resistive area beneath sites MT14 and MT15. At −450 m, inside region C1a, it is imaged a more conductive area (9–11 Ω m) associated to Lower Jurassic (Lias) rocks that corresponds to the main reservoir. Above the main reservoir, the primary seal is imaged as a layer with resistivity values of 18–23 Ω m, due to the presence of thin layers of black shales belonging to the Camino Fm. The top of C1 is composed by the lower part of the Dogger marly limestones. This C1 layer corresponds to the period range of 0.1–1 s.

Region R2 is the thickest of the model and contains the secondary reservoir-seal system (Early Cretaceous). This system is formed by sandstones, conglomerates and shales from Purbeck facies. The limit between region R2 and C2 is situated on the upper part of the Lower Cretaceous materials and marks the top of the Utrillas Fm (Fig. 2). In the southern part of the model, within sites MT16 and MT21, region R2 is disrupted by a near vertical low resistivity structure indicated by an 'F' in Fig. 6. F constitutes a fault associated with the Ubierna Fault (Fig. 1) as it is also imaged by subsequent 3-D seismic studies (Alcalde et al., 2012). The resistivity distribution suggests an important conductive fluid circulation along the fracture region since the signal is too powerful to be generated by a thin accumulation of clays along the fault. Further studies have been undertaken to evaluate if the presence of this fault could suggest a possible leakage pathway. Mazadiego et al. (2012) after determining the baseline of CO_2 flux in the soil–atmosphere interface concluded affirming that the flow gas in the fault region is as low as in other regions without fractures. However, Buil et al. (2012) acquired some surface water samples in the eastern part of the fault with a higher content of sulphates and chlorides and higher electrical conductivity suggesting its mixing with deeper waters. In any case, due to the non-commercial character of the project, no more than 20 kilotons are planned to be injected. This represents an approximate volume of 130 m × 130 m × 25 m at the reservoir depth assuming a homogenous saturation of 50%. As the injection is planned in C1a region, the probability of the injected gas reaching the C1b region and consequently the fault is low. Moreover, underneath MT14 and MT15 sites the connection between C1a and C1b seems to be sealed (resistive area).

Finally C2 region are Cenomanian and Coniacian limestones and marls (Upper Cretaceous) which dominates the surface of the study area.

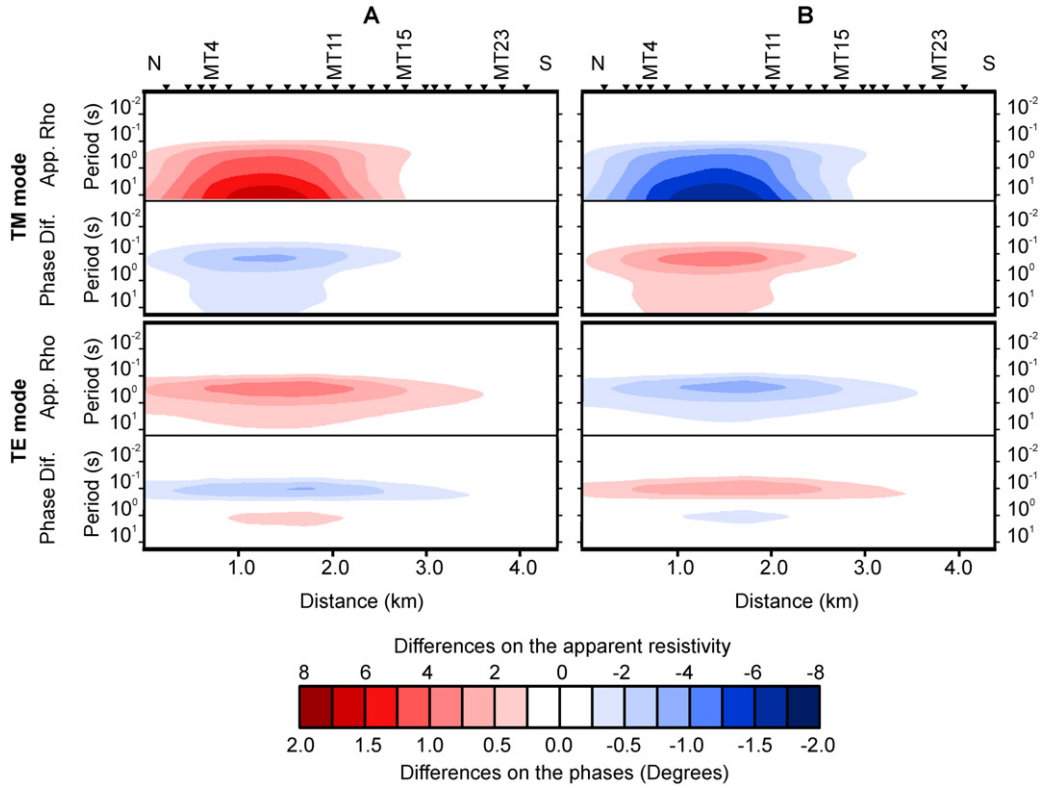

Fig. 9. Non linear sensitivity tests to find the precision in determining the reservoir resistivity. The figure displays the difference between the responses of the final model and the modified assuming a homogenous structure of 8 Ω m (A) and 25 Ω m (B) at the reservoir depth. It is observed that apparent resistivity of TM mode reached in both cases (A and B) a value of 5% of difference which means that the main reservoir electrical resistivity ranges between 8 and 25 Ω m. Periods are displayed on a logarithmic scale.

An overall view of the model shows a very smooth dome-shape structure with the axis of the anticline located close to H2 well (MT11 sounding). As it is also observed in the preliminary 3-D seismic images of the Hontomín site (Alcalde et al., 2012), the anticlinal structure is softer than it was expected from vintage seismics and exploration wells.

The primary reservoir is imaged as the most conductive region inside C1a. The saline aquifer is linked to the lowest resistivity values of the model as reported by the resistivity log data provided by well H2; thanks to the well constraint, the position of the units and their resistivity values are well determined. In order to check the upper and lower resistivity limits of the saline aquifer compatible with the measured surface data, non linear sensitivity tests (Ledo and Jones, 2005) were computed. Thus it was assumed a homogeneous structure (indicated in Fig. 8) with constant resistivity at the reservoir depth. The electrical resistivity of this structure was increased and decreased from the original value till the difference between the responses of the final model and the modified one reached a value of 5% for the apparent resistivities and/or 1.45° in the phases. Thereby it was concluded that the primary reservoir electrical resistivity ranges between 8 and 25 Ω m (see Fig. 9). This result made possible to estimate the reservoir porosity using the Archie's law (Eq. (1)): assuming 100% water saturation ($S_W = 1$), $m = 2$ and $a = 1$, the porosity of the main reservoir is comprised between 9% and 17%. This porosity range agrees with the first estimation obtained by Márquez and Jurado (2011) from the vintage well logs of the area (from 0% to 18%).

Feasibility of monitoring the CO_2 plume by means of the MT method was also performed using non-linear sensitivity tests. Archie's law predicts that in the unfavourable case of just 50% of saturation, the post-injection resistivity will increase 4 times (Eq. (2)). If it is assumed 10 Ω m as the resistivity of the reservoir, the post-injection resistivity is 40 Ω m. Consequently, in agreement with the results obtained in this 2-D study, large amount of CO_2 can be monitored using the MT method. However, in the particular case of the Hontomín TDP, the plume will be too small (130 m × 130 m × 25 m at the reservoir temperature and pressure conditions) to be detected. To determine properly the minimum detectable size of the plume further studies in 3-D will be needed.

8. Conclusions

The magnetotelluric (MT) method has shown to be an appropriate technique to characterize the study area and provide a high resolution geoelectrical baseline model. The 2-D resistivity model highlights the viability of the method in the Hontomín site in spite of the EM noise, which has been successfully minimized and removed from the acquired MT data. Facing the second stage of the geoelectrical characterization, this work suggests some manners to deal with this EM noise and underlines the importance of using remote reference techniques as a way to eliminate uncorrelated signal from the acquired data. On the analysis of both the acquired MT data and H2 resistivity log data is observed that the primary system (primary reservoir and seal) is imaged in the range of 0.1–1 s whereas EM noise in the area appears in periods longer than 10 s.

The 2-D resistivity model presented in this work constitutes the first geoelectrical image of the Hontomín site. Thus it contributes to understand the geoelectrical structure of the area and makes possible to correlate the different lithologies and formations to electrical resistivities. It confirms a clear contrast between electrical properties of the primary reservoir-seal system, more conductive as it contains the saline aquifer, and the more resistive character of the secondary reservoir-seal system. The electrical

resistivity of the primary reservoir ranges between 8 and 25 Ω m which means, according to Archie's law, a porosity between 9% and 17%. The model images an EW fault in the southern part associated to the Ubierna Fault and probably linked to an important fluid circulation. However, it is expected that this fault does not constitute an important leakage pathway. On one hand, the injection well is projected close to H2 well (centre of the dome) which means far from the fault region. One the other hand, no more than 20,000 CO_2 tonnes are planned to be injected which implies a small plume of 130 m × 130 m × 25 m given the pressure and temperature conditions at the reservoir depth and assuming a homogenous saturation of 50%.

The constrained inversion carried out using well log data provided a high quality geoelectrical model. An interesting task to face in the future will be to improve the resolution of the MT images also taking into account the 3-D seismic acquired in the area. Thus the surfaces of the main formations could be placed on the resistivity model to enhance the inversion.

Acknowledgements

The authors sincerely thank the Associate Editor Ziqiu Xue and the anonymous reviewers for their useful comments. This Project has been partly financed by funds coming from the Spanish Ministry of Industry, Tourism and Trade, through the CIUDEN-UB Geomodels agreement related to the Development and Adaptation of Electromagnetic Techniques: Characterization of Storage Sites. This project is co-financed by the European Union through the Technology Demonstration Plant of Compostilla OXYCFB300 Project (European Energy Programme for Recovery). The sole responsibility of this publication lies with the author. The European Union is not responsible for any use that may be made of the information contained therein. This work was also developed in the framework of the Spanish MCI project PIER-CO2 (CGL2009-07604). It is a contribution of the Research Group of Geodynamics and Basin Analysis (2009SGR1198) of the Generalitat de Catalunya and the Research Institute GEOMODELS. Xènia Ogaya is being currently supported by the Fundación Ciudad de la Energía (CIUDEN) research training program. We sincerely thank EXES-UB group for their help in the MT data acquisition and Modesto Montoto and Andrés Pérez-Estaún for their continuous support.

References

Alcalde, J., Martí, D., Juhlin, C., Malehmir, A., Sopher, D., Calahorrano, A., Ayarza, P., Marzán, I., Pérez-Estaún, A., Carbonell, R., 2012. 3D seismic imaging of a geological storage of CO_2 site: Hontomín, Spain. In: Symposium Abstract Volume. The 15th International Symposium on Deep Seismic Profiling of the Continents and their Margins.

Archie, G.E., 1942. The electrical resistivity log as an aid in determining some reservoir characteristics. Transactions of AIME 146, 54–67.

Bachu, S., 2003. Screening and ranking of sedimentary basins for sequestration of CO_2 in geological media in response to climate change. Environmental Geology 44, 277–289, http://dx.doi.org/10.1007/s00254-003-0762-9.

Beamish, D., Travassos, J.M., 1992. The use of the D^+ solution in magnetotelluric interpretation. Journal of Applied Geophysics 29, 1–19, http://dx.doi.org/10.1016/0926-9851(92)90009-A.

Becken, M., Streich, R., Krüger, K., Ritter, O., 2010. Exploration and monitoring of CO_2 storage sites using controlled-source electromagnetic: results of a feasibility study at Ketzin, Germany. XL385 EGU2010-7966, EGU General Assembly 2010.

Bedrosian, P.A., 2007. MT+, integrating magnetotellurics to determine earth structure, physical state, and processes. Surveys in Geophysics 28, 121–167, http://dx.doi.org/10.1007/s10712-007-9019-6.

Black, N., Zhdanov, M.S., 2009. Monitoring of hydrocarbon reservoirs using marine CSEM method. SEG Technical Program Expanded Abstracts 28 (1), 850–854, http://dx.doi.org/10.1190/1.3255884.

Boillot, G., Capdevila, R., 1977. The Pyrenees: subduction and collision? Earth and Planetary Science Letters 35, 151–160.

Boillot, G., Malod, J., 1988. The North and North–West Spanish continental margin. Revista de la Sociedad Geológica de España 1, 295–316.

Bourgeois, B., Girard, J.F., 2010. First modelling results of the em response of a CO_2 storage in the Paris basin. Oil & Gas Science and Technological Review – IFP 65 (4), 597–614, http://dx.doi.org/10.2516/ogst/2009076.

Buil, B., Gómez, P., Peña, J., Garralón, A., Galarza, C., Durán, J.M., Domñinguez, R., Escribano, A., Turrero, M.J., Robredo, L.M., Sánchez, L., 2012. Caracterización y monitorización hidrogeoquímica de los acuíferos superiores a la formación almacenamiento de CO_2 (Hontomín, Burgos) y actualización de la caracterización de aguas superficiales. Technical report CIEMAT/DMA/2G010/1/2012.

Carrigan, C.R., Ramirez, A.L., Newmark, R.L., Aines, R., Friedman, S.J., 2009. Application of ERT for tracking CO_2 plume growth and movement at the SECARB cranfield site. In: 8th Annual Conference on CARBON Capture & Sequestration, Pittsburgh, PA, United States, May 4–7, 2009.

Christensen, N.B., Sherlock, D., Dodds, K., 2006. Monitoring CO_2 injection with crosshole electrical resistivity tomography. Exploration Geophysics 37, 44–49.

Cagniard, L., 1953. Principe de la métode magnéto-tellurique, nouvelle méthode de prospection géophysique. Annales de Geophysique 9, 95–125.

Chave, A.D., Jones, A.G. (Eds.), 2012. The Magnetotelluric Method: Theory and Practice. Cambridge University Press, Cambridge, UK, 552 pp., ISBN: 9780521819275.

Egbert, G.D., Booker, J.R., 1986. Robust estimation of Geomagnetic transfer functions. Geophysical Journal of the Royal Astronomical Society 87, 173–194.

Gamble, T.D., Goubau, W.M., Clarke, J., 1979. Magnetotellurics with a remote magnetic reference. Geophysics 44, 53–68.

Giese, R., Henninges, J., Lüth, S., Morozova, D., Schmidt-Hattenberger, C., Würdemann, H., Zimmer, M., Cosma, C., Juhlin, C., CO2SINK Group, 2009. Monitoring at the CO_2SINK site: a concept integrating geophysics, geochemistry and microbiology. Energy Procedia 1, 2251–2259, http://dx.doi.org/10.1016/j.egypro.2009.01.293.

Girard, J.F., Coppo, N., Rohmer, J., Bourgeois, B., Naudet, V., Schmidt-Hattenberger, C., 2011. Time-lapse CSEM monitoring at Ketzin (Germany) CO_2 injection using 2×MAM configuration. Energy Procedia 4, 3322–3329.

Global CCS Institute, 2011. The Global Status of CCS: 2011. Global CCS Institute, Canberra, Australia, ISBN: 978-0-9871863-0-0.

Groom, R.W., Bailey, R.C., 1989. Decomposition of magnetotelluric impedance tensors in the presence of local three-dimensional galvanic distortion. Journal of Geophysical Research 94, 1913–1925.

Hagrey, S.A., 2011. CO_2 plume modelling in deep saline reservoirs by 2D ERT in boreholes. The Leading Edge 30 (24), 24–33, http://dx.doi.org/10.1190/1.3535429.

Harris, P., MacGregor, L., 2006. Determination of reservoir properties from the integration of CSEM and seismic data. First Break 24, 15–21.

Harris, P., Du, Z., MacGregor, L., Olsen, W., Shu, R., Cooper, R., 2009. Joint interpretation of seismic and CSEM data using well log constraints: an example from Luva Field. First Break 27, 73–81.

Hoversten, G.M., Gritto, R., Washbourne, J., Daley, T., 2003. Pressure and fluid saturation prediction in a multicomponent reservoir using combined seismic and electromagnetic imaging. Geophysics 68 (5), 1580–1591, http://dx.doi.org/10.1190/1.1620632.

IPCC – Intergovernmental Panel on Climate Change, 2005. IPCC Special Report on Carbon Dioxide Capture and Storage. Cambridge University Press, Cambridge, UK, pp. 195–276 (Chapter 5).

JafarGandomi, A., Curtis, A., 2011. Detectability of petrophysical properties of subsurface CO_2-saturated aquifer reservoirs using surface geophysical methods. The Leading Edge 30 (10), 1112–1121.

Kiessling, D., Schmidt-Hattenberger, C., Schuett, H., Schilling, F., Krueger, K., Schoebel, B., Danckwardt, E., Kummerow, J., CO2SINK Group, 2010. Geoelectrical methods for monitoring geological CO_2 storage: first results from cross-hole and surface-downhole measurements from the CO_2SINK test site at Ketzin (Germany). International Journal of Greenhouse Gas Control 4 (5), 816–826, http://dx.doi.org/10.1016/j.ijggc.2010.05.001.

Le Pichon, X., Sibuet, J.C., 1971. Western extension of boundary between European and Iberian plates during the Pyrenean opening. Earth and Planetary Science Letters 12, 83–88.

Ledo, J., Jones, A.G., 2005. Upper mantle temperature determined from combining mineral composition, electrical conductivity laboratory studies and magnetotelluric field observations: application to the intermontane belt, Northern Canadian Cordillera. Earth and Science Letters 236, 258–268, http://dx.doi.org/10.1016/j.epsl.2005.01.044.

Lien, M., Mannseth, T., 2008. Sensitivity study of marine CSEM data reservoir production monitoring. Geophysics 73 (4), F151–F163, http://dx.doi.org/10.1190/1.2938512.

MacGregor, L., 2012. Integrating seismic, CSEM, and well log data for reservoir characterization. The Leading Edge 31 (3), 268–277.

Márquez, M., Jurado, M.J., 2011. Petrophysical characterization of a CO_2 storage reservoir using well logs. Geophysical Research Abstracts, vol. 13, EGU2011-6891-3. EGU General Assembly 2011.

Mazadiego, L.F., Grandia, F., Elio, J., Missi, B., Vasseli, O., Ortega, M., Caballero, J., Vilanova, E., Chacn, E., Llamas, J., 2012. Baseline of soil-atmosphere CO_2 flux in the Hontomin site (Burgos, Spain). In: CO_3-Monitoring and Detection, Third EAGE CO_2 Geological Storage Workshop.

McNeice, G.W., Jones, A.G., 2001. Multisite, multifrequency tensor decomposition of magnetotelluric data. Geophysics 66 (1), 158–173.

Montadert, L., de Charpal, O., Roberts, D., Guennoc, P., Sibuet, J.C., 1979. Northeast Atlantic passive continental margins: rifting and subsidence processes. In: Talwani, M., Hay, W., Ryan, W.B.F. (Eds.), Deep Drilling Results in the Atlantic Ocean:

Continental Margins and Paleoenvironment. Maurice Ewing Ser., vol. 3. AGU, Washington, DC, pp. 154–186, http://dx.doi.org/10.1029/ME003p0154.
Muñoz, J.A., 1992. Evolution of a continental collision belt: ECORS-Pyrenees crustal balanced cross-section. In: McClay, K.R. (Ed.), Thrust Tectonics. Chapman and Hall, London, pp. 235–246.
Muñoz, J.A., 2002. The Pyrenees. In: Gibbons, W., Moreno, T. (Eds.), The Geology of Spain. Geological Society, London, pp. 370–385.
Nakatsuka, Y., Xue, Z., Garcia, H., Matsuoka, T., 2010. Experimental study on CO_2 monitoring and quantification of stored CO_2 in saline formations using resistivity measurements. International Journal of Greenhouse Gas Control 4, 209–216, http://dx.doi.org/10.1016/j.ijggc.2010.01.001.
Orange, A., Key, K., Constable, S., 2009. The feasibility of reservoir monitoring using time-lapse marine CSEM. Geophysics 74 (2), F21–F29, http://dx.doi.org/10.1190/1.3059600.
Parker, R.L., 1980. The inverse problem of electromagnetic induction: existence and construction of solutions based on incomplete data. Journal of Geophysical Research 85, 4421–4428.
Parker, R.L., Whaler, K.A., 1981. Numerical methods for establishing solutions to the inverse problem of electromagnetic induction. Journal of Geophysical Research 86, 9574–9584.
Pérez-Estaún, A., Gómez, M., Carrera, J., 2009. El almacenamiento geológico de CO_2, una de las soluciones al efecto invernadero (Geological storage of CO_2, one of the solutions to the greenhouse effect). Enseñanza de las Ciencias de la Tierra 17 (2), 179–189, ISSN: 1132-9157.
Ramirez, A.L., Newmark, R.L., Daily, W.D., 2003. Monitoring carbon dioxide floods using electrical resistance tomography (ERT): sensitivity studies. Journal of Environmental and Engineering Geophysics 8 (3), 187–208.
Rodi, W., Mackie, R.L., 2001. Non linear conjugate gradients algorithm for 2D magnetotelluric inversion. Geophysics 66, 174–187.
Roest, W.R., Srivastava, S.P., 1991. Kinematics of the plate boundaries between Eurasia, Iberia, and Africa in the North Atlantic from the Late Cretaceous to the present. Geology 6, 613–616.
Sato, K., Mito, S., Horie, T., Ohkuma, H., Saito, H., Watanabe, J., Yoshimura, T., 2011. Monitoring and simulation studies for assessing macro- and meso-scale migration of CO_2 sequestered in an onshore aquifer: experiences from the Nagaoka pilot site, Japan. International Journal of Greenhouse Gas Control 5, 125–137, http://dx.doi.org/10.1016/j.ijggc.2010.03.003.
Streich, R., Becken, M., Ritter, O., 2010. Imaging of CO_2 storage sites, geothermal reservoirs, and gas shales using controlled-source magnetotellurics: modeling studies. Chemie der Erde – Geochemistry 70 (3), 63–75, http://dx.doi.org/10.1016/j.chemer.2010.05.004.
Tikhonov, A.N., 1950. On determining electrical characteristics of the deep layers of the Earth's crust. Doklady Akademii Nauk SSSR 73, 295–297.
Vera, J.A., 2004. Geología de España. SGE-IGME, Madrid, ISBN: 978-84-7840-546-6.
Wirianto, M., Mulder, W.A., Slob, E.C., 2010. A feasibility study of land CSEM reservoir monitoring in a complex 3D model. Geophysical Journal International 181 (2), 741–755.
Ziegler, P.A., 1988. Late Jurassic–Early Cretaceous Central Atlantic sea-floor spreading, closure of Neo-Tethys, and opening of Canada Basin. In: Ziegler, P.A. (Ed.), Evolution of the Arctic–North Atlantic and the Western Tethys. American Association of Petroleum Geologists Memoirs 43, Tulsa, pp. 63–82.

2

Ogaya, X., Queralt, P., Ledo, J., Marcuello, A., Jones, A.G., 2014. Geoelectrical baseline model of the subsurface of the Hontomín site (Spain) for CO_2 geological storage in a deep saline aquifer: A 3D magnetotelluric characterisation. International Journal of Greenhouse Gas Control 27, 120-138, doi: 10.1016/j.ijggc.2014.04.030.

International Journal of Greenhouse Gas Control 27 (2014) 120–138

Contents lists available at ScienceDirect

International Journal of Greenhouse Gas Control

journal homepage: www.elsevier.com/locate/ijggc

Geoelectrical baseline model of the subsurface of the Hontomín site (Spain) for CO_2 geological storage in a deep saline aquifer: A 3D magnetotelluric characterisation

Xènia Ogaya[a,*], Pilar Queralt[a], Juanjo Ledo[a], Álex Marcuello[a], Alan G. Jones[b]

[a] Departament de Geodinàmica i Geofísica, Facultat de Geologia, GEOMODELS Research Institute, Universitat de Barcelona, C/ Martí i Franquès s/n, 08028 Barcelona, Spain
[b] Dublin Institute for Advanced Studies, School of Cosmic Physics, Dublin 2, Ireland

ARTICLE INFO

Article history:
Received 18 January 2014
Received in revised form 26 March 2014
Accepted 29 April 2014

Keywords:
CO_2 storage
Geoelectrical baseline model
Geophysical imaging
3D modelling
Magnetotellurics
Electrical resistivity

ABSTRACT

The magnetotelluric (MT) method was used to characterise the underground research laboratory (URL) for CO_2 storage in a deep saline aquifer at Hontomín (Spain). A total grid of 109 closely-spaced broadband MT sites was acquired in the study area covering an areal extent of 3×5 km^2. Different three-dimensional (3D) inversion codes were employed to invert the MT data in the period range of 0.001–10 s (frequency range 1000–0.1 Hz), with all of them giving similar results. The final preferred 3D model validates a previously published two-dimensional (2D) MT study and is supported by a variety of multidisciplinary data (e.g., well log, 3D seismic and hydrogeochemistry data). The 3D model constitutes the baseline electrical resistivity model of the site that will be used for the future time-lapse electromagnetic (EM) monitoring experiments of the URL. The 3D resistivity distribution shows the dome-like structure of the saline aquifer and images fracture regions, thus identifying the most likely leakage pathways and consequently, the monitoring requirements of the Hontomín site.

1. Introduction

Monitoring of CO_2 storage sites permits control of gas injection and storage operations, detection of possible leakage, and support of the required safety conditions (IPCC, 2005; NETL, 2009). Different geophysical techniques are presented as suitable for monitoring purposes and a number of multidisciplinary monitoring schemes have been designed to study and control the evolution of the injected CO_2 plume (Hoversten and Gasperikova, 2005; IPCC, 2005; Giese et al., 2009; NETL, 2009; JafarGandomi and Curtis, 2011; Sato et al., 2011). Electric and electromagnetic (EM) methods have been demonstrated to be valuable as they constrain the electrical conductivity of the storage complex and offer a high degree of complementarity between their different techniques to study the different scales and depths of interest in a storage site (Kiessling et al., 2010; Streich et al., 2010; Girard et al., 2011; Bergmann et al., 2012; Vilamajó et al., 2013). The electrical conductivity of the Earth materials (also commonly defined in terms of its inverse, electrical resistivity) is essentially a transport property of the medium, compared to the propagation velocity of elastic waves which is a property that is associated to the transmission of mechanical energy. It has a far wider range of variation than seismic velocity or rock density (Bedrosian, 2007) and is more sensitive to CO_2 saturation compared to other techniques (Lumley, 2010; MacGregor, 2012). Electrical conductivity is a physical property sensitive to the nature of the rock constituents (mineralogy composition of the rock) but also to the characteristics of the pore space; it depends on fluid salinity, temperature, porosity, pore connectivity, saturation and pressure (Bedrosian, 2007). Archie's law (Archie, 1942) describes reasonably well the bulk electrical conductivity of the rock as a function of these parameters. In the context of CO_2 monitoring, the estimation of some of these parameters is critical to locate the gas plume and understand CO_2 migration (Bourgeois and Girard, 2010; Nakatsuka et al., 2010; Alemu et al., 2011; MacGregor, 2012; Börner et al., 2013).

For most techniques, the changes produced by the injection of the CO_2 are identified and quantified carrying out a comparative analysis with the reference pre-injection state (monitoring based on repeated time-lapse studies). For that reason, a thorough characterisation must be taken first to define a high-resolution baseline

* Corresponding author at: Facultat de Geologia, Dept. Geodinàmica i Geofísica, C/Martí i Franquès s/n, 08028 Barcelona, Spain. Tel.: +34 934034028; fax: +34 934021340.
E-mail addresses: xeniaogaya@ub.edu, xeniaogaya@gmail.com (X. Ogaya).

http://dx.doi.org/10.1016/j.ijggc.2014.04.030
1750-5836/

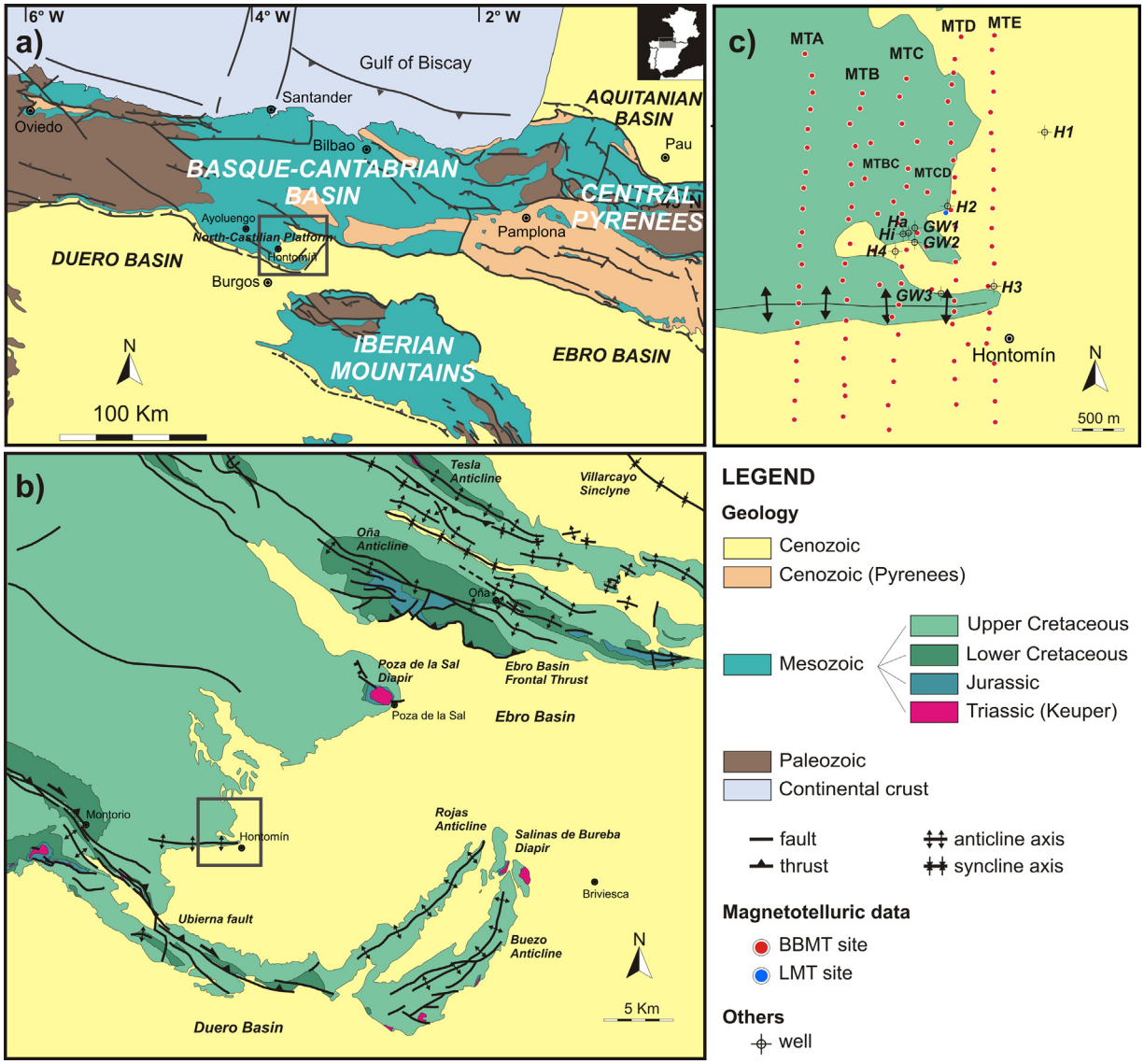

Fig. 1. Geological maps of the study area: (a) geological map of the Basque-Cantabrian Basin indicating the North-Castilian Platform and the location of the study area (modified from Muñoz, 2002); (b) geological map of the Hontomín surrounding area indicating the location of the Hontomín structure; (c) red and blue dots show the location of the broadband MT (BBMT) and long period MT (LMT) sites, respectively. Also indicated are the acronyms of the various profiles (MTA-MTE) and the locations of the wells H1–H4, GW1–GW3 and Hi-Ha. (For interpretation of the references to colour in this figure legend, the reader is referred to the web version of this article.)

model of the storage site subsurface. In the underground research laboratory (URL) for CO_2 storage in a deep saline aquifer of Hontomín (Spain; described below), a large number of multidisciplinary experiments are being undertaken to characterise the subsurface in order to be able to monitor the expected CO_2 plume evolution (e.g., Rubio et al., 2011; Buil et al., 2012; Benjumea et al., 2012; Ogaya et al., 2012; Alcalde et al., 2013a,b; Canal et al., 2013; Elío et al., 2013; Nisi et al., 2013; Ogaya et al., 2013; Quintà, 2013; Ugalde et al., 2013; Vilamajó et al., 2013). Since the applicability and sensitivity of monitoring techniques depends on the site characteristics, diverse EM techniques are being assessed for different purposes according to their resolution and penetration depth.

The magnetotelluric (MT) method has demonstrated its validity to characterise the subsurface of the Hontomín site providing the first two-dimensional (2D) geoelectrical model of the URL (Ogaya et al., 2013). Controlled-source EM (CSEM) techniques have indicated their feasibility to monitor the Hontomín site and detect small volumes of CO_2 (Vilamajó et al., 2013). Moreover, the EM noise of the study area has been analysed and characterised (Escalas et al., 2013) in order to design strategies to deal with it.

This work addresses the extension of the MT characterisation presented in Ogaya et al. (2013). In general, the MT method has been used in both regional (e.g., Rosell et al., 2011) and local (e.g., Ogaya et al., 2013) characterisation work since it is the only EM technique with a penetration depth ranging from tens of metres to hundreds of kilometres. Moreover, its tensorial character enables determination of the dominant directionality of geological structures and subsurface processes, and their variation with depth. In the past years, thanks to the progress made in 3D MT inversion algorithms (Avdeev, 2005; Siripunvaraporn, 2012), a number of MT studies have been undertaken in 3D in order to overcome the limitations of 2D interpretation (Ledo et al., 2002). Some of these investigations were focussed on near surface structures demonstrating the suitability of the method in a variety of contexts: mineral exploration (Tuncer et al., 2006; Farquharson and Craven, 2009; Xiao et al., 2010); waste site characterisation (Newman et al., 2003); volcano and geothermal studies (Heise et al., 2008; Newman et al., 2008; Ingham et al., 2009; Ghaedrahmati et al., 2013) and hydrocarbon exploration (He et al., 2010; Zhdanov et al., 2011). In CO_2 geological storage contexts,

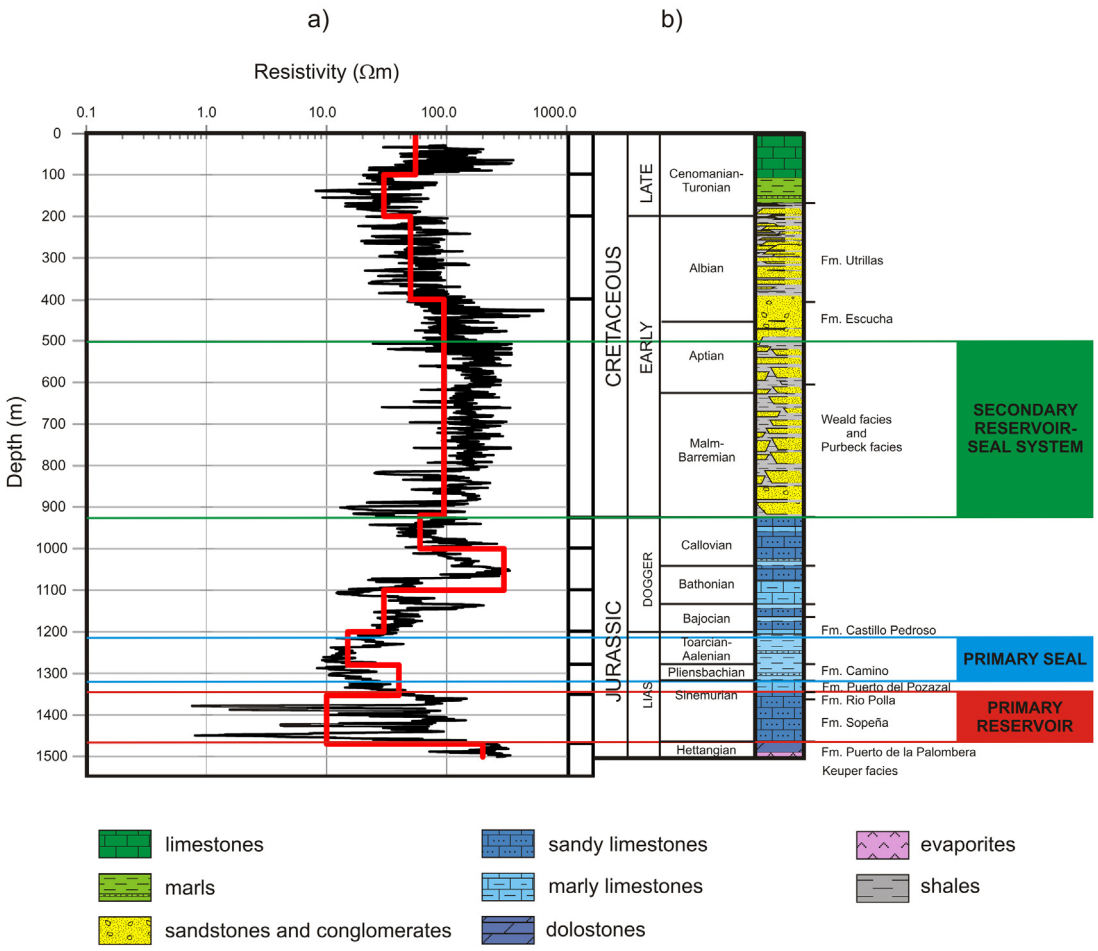

Fig. 2. Electrical resistivity of the different facies and formations: (a) in black, H2 resistivity log data and in red, H2 one-dimensional resistivity model (Ogaya et al., 2013); (b) stratigraphic column of the Hontomín site at H2 well showing Triassic to Cretaceous materials. Primary and secondary reservoir-seal systems are indicated. Depths are given in terms of true vertical depth (TVD).

this work constitutes the first 3D MT characterisation survey of an URL.

In agreement with the results of the dimensionality analysis presented in Ogaya et al. (2012), 3D inversion and forward modelling of the complete MT data set was undertaken, combining the inverse code described by Mackie and Madden (1993) subsequently developed and implemented by Geosystem, and the ModEM inverse code presented by Egbert and Kelbert (2012). The process was also corroborated using the WSINV3DMT inverse code (Siripunvaraporn et al., 2005). The final 3D model defines the geoelectrical baseline model of the Hontomín URL subsurface that will establish the point of comparison for subsequent EM monitoring surveys of the site.

2. The Hontomín site

The Hontomín URL is a Technological Development Plant (TDP) for CO_2 storage in a deep saline aquifer; the project is led by the Fundación Ciudad de la Energía – CIUDEN. The Hontomín site is a non-commercial project and the injection is limited to 100 kilotons by regulation. However, no more than 20 kilotons are planned to be injected which corresponds to an approximate volume of $135 \times 135 \times 25\ m^3$ at 1500 m TVD (true vertical depth). The volume was estimated according to the variation of CO_2 density with depth, for hydrostatic pressure and a geothermal gradient of 25 °C/km from 15° at the surface (Fig. 5.2 in IPCC, 2005)

The URL is located in the southern sector of the Basque-Cantabrian Basin (Western Pyrenees, Spain; Fig. 1). The boundaries of the Hontomín structure are the Ubierna Fault to the south (Tavani et al., 2011), the Ebro basin to the east and the Duero basin to the west (Fig. 1). The geological setting of the study area pertinent to EM studies was described in detail in Ogaya et al. (2013) and will be summarised below.

Former hydrocarbon exploration activity in the region provided 2D seismic profiles and well-log data (H1, H2, H3 and H4; Fig. 1c). These geological and geophysical data, as well as recent studies including 3D reflection seismics (Alcalde et al., 2013a,b), gravimetry (Rubio et al., 2011) and magnetotellurics (Ogaya et al., 2013), indicate that the Hontomín site is a smooth Jurassic domed anticline structure cored by Upper Triassic evaporites (Keuper facies; Quintà, 2013; Fig. 2). The overall lateral extent of the structure is $3 \times 5\ km^2$.

Two wells are planned in the URL (Fig. 1c): the injection well (Hi) and the monitoring well (Ha). They will be placed on the crest of the Jurassic dome according to the geological interpretation derived from the available well-log data and the seismic studies (Alcalde et al., 2013a,b; Quintà, 2013). The injection is projected to occur in the basal part of the Lower Jurassic carbonates at about 1500 m TVD (Fig. 2). The primary reservoir is constituted by a dolostone unit (upper part of Puerto de la Palombera Fm.) and an oolitic limestone unit (Sopeña Fm., Fig. 2). The reservoir has a thickness of more than 100 m and the porosity estimate, according to vintage well logs, ranges from 0% to 18% (Márquez and Jurado, 2011). From the 2D resistivity model a porosity value of between 9% and 17% was derived using Archie's Law (Ogaya et al., 2013).

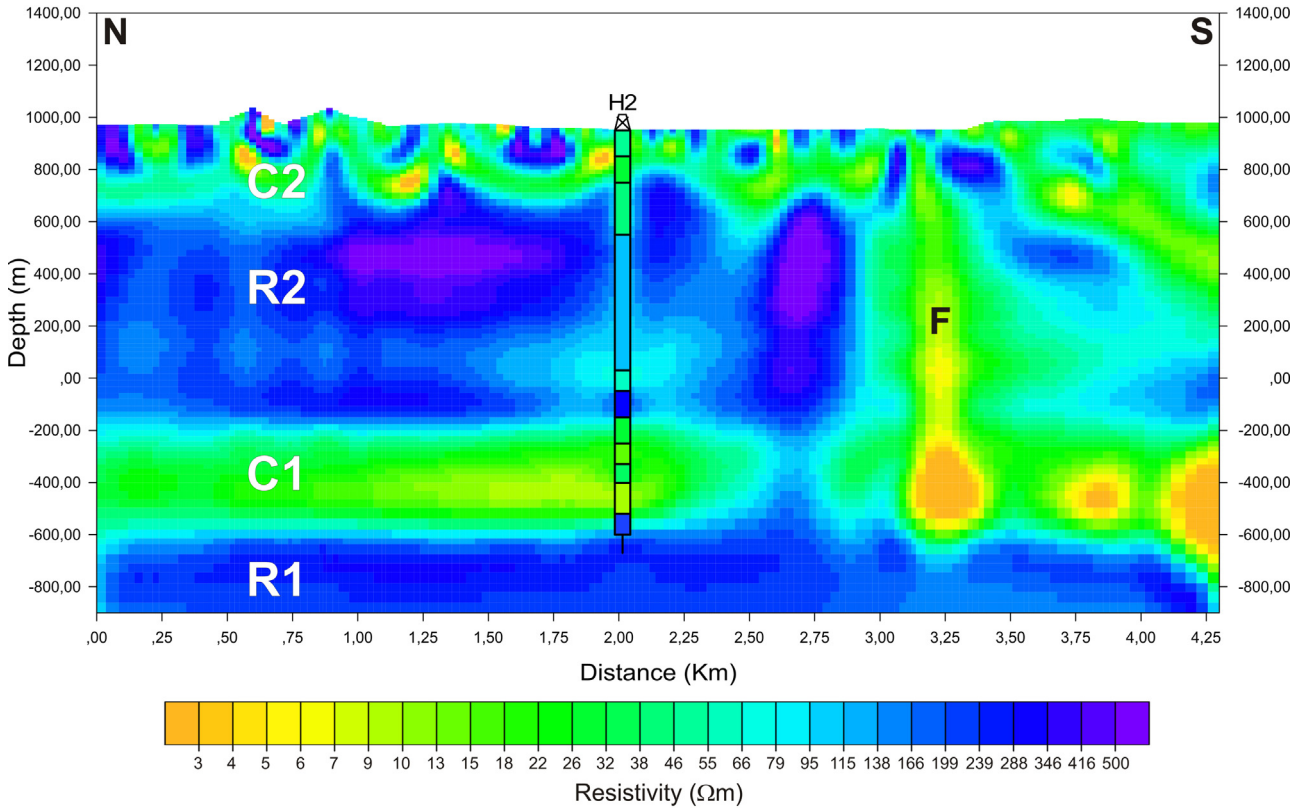

Fig. 3. 2D resistivity model of the MTD-profile data (reproduced from Ogaya et al., 2013). The four main layers of the resistivity distribution are (from bottom to top): R1, C1, R2 and C2. F indicates the fault region located in the southern part of the model. Superimposed is the 1D resistivity model of the H2 well. Depths are given in terms of metres above sea level (m.a.s.l.).

The primary seal comprises four black-shale levels interbedded in Lower Jurassic marls (Camino Fm., Fig. 2). A suitable secondary reservoir-seal system is represented by the intercalations of conglomerates, sandstones and shales from the Purbeck and Weald facies (Upper Jurassic-Lower Cretaceous).

The electrical behaviour of the different units is shown in Fig. 2 (inferred from the H2 well data; Ogaya et al., 2013). The primary reservoir is a saline aquifer and corresponds to the most conductive unit (10 Ωm in H2 well). The average electrical conductivity of the saline water is 47 mS/cm (a resistivity of 0.22 Ωm; Buil et al., 2012). The primary seal also has a conductive behaviour, whereas the secondary reservoir-seal system is resistive.

2.1. 1D models from the resistivity log-data

Fig. 1c shows the location of all drilled wells. H1, H2, H3 and H4 were drilled for oil exploration purposes (H1 and H2 in the late nineteen-sixties; H3 in 1991 and H4 in 2007) and their depths range up to 1769 m TVD. GW1, GW2 and GW3 are hydrogeological boreholes and were drilled recently (2012) to carry out groundwater studies; their depths range between 150 m and 405 m TVD (Benjumea et al., 2012). Following the procedures used in Ogaya et al. (2013) for the H2 well, where the resistivity log data were smoothed into the minimum number of layers required to describe the subsurface, an equivalent one-dimensional (1D) resistivity model was sought for each of the existing wells. These 1D models produce the same MT responses at the surface, as those ones obtained from forward modelling using the logged resistivities. Since the H4 well (drilled to a depth of 1610 m TVD) lacked resistivity log data, its 1D resistivity model was inferred using the H2-well data to correlate the different lithologies to electrical properties. It constitutes a good approximation as the two wells are located in the centre of the dome and, consequently, they are expected to show a similar pattern. The distance between the two wells is 707 m.

2.2. 2D resistivity model

The previous 2D resistivity model from the MTD profile in Fig. 1c (Ogaya et al., 2013) imaged a resistivity structure composed of four main layers (Fig. 3; all depths are given in terms of metres above sea level, m.a.s.l.): (i) R1 resistive bottom layer (below −600 m.a.s.l.) linked to Keuper facies; (ii) C1 conductive layer (below −200 m.a.s.l. and thickness up to 400 m) containing the primary reservoir and seal units; (iii) R2 resistive middle layer (between +700 m.a.s.l. and −200 m.a.s.l.) containing the secondary reservoir-seal system, and (iv) C2 conductive top layer (above +700 m.a.s.l.) linked to Upper Cretaceous materials. In the southern part of the model a fault region (labelled as F) was imaged that is related to the Ubierna Fault. The F structure revealed an important conductive fluid circulation along the fracture region.

3. Magnetotelluric method

A description of the MT method was given in Ogaya et al. (2013) and here is only briefly summarised. The MT method infers the electrical conductivity structure of the subsurface using the naturally occurring time variation of the EM field. EM waves propagate diffusively through the conducting Earth and their penetration depends on its period (T) and the electrical resistivity of the penetrated medium (ρ). The skin-depth ($\delta = 503\sqrt{\rho T}$ in SI units) is a reasonable estimate of the inductive scale length: the distance over which EM fields are attenuated to $1/e$ of their amplitudes at the Earth's surface in a uniform medium. Thereby, the longer the period, the deeper is the penetration depth.

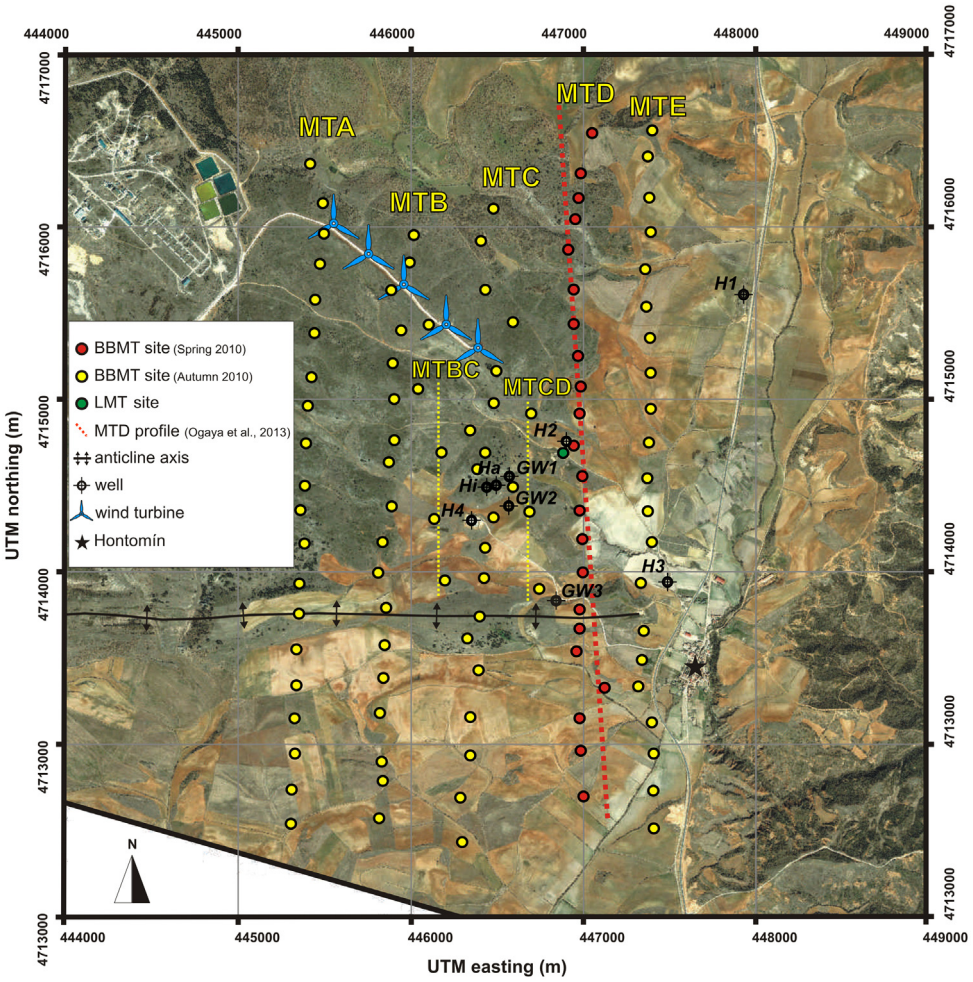

Fig. 4. Locations of the BBMT and LMT sites. In red, the BBMT sites collected in Spring 2010; in yellow, the BBMT sites collected in Autumn 2010 and in green, the single LMT site collected during a third phase of the fieldwork acquisition. Indicated are the acronyms of the profiles as well as the orientation of the 2D model presented in Ogaya et al. (2013; Fig. 3). Small yellow dotted lines indicated MTBC and MTCD profiles. Also shown are the positions of the wells and wind turbines (major EM noise source within the study area). (For interpretation of the references to colour in this figure legend, the reader is referred to the web version of this article.)

The orthogonal electric and magnetic field variations recorded at the Earth's surface are related to each other through the impedance tensor $Z_{ij}(\omega)$, function of oscillation frequency ω. From the impedance tensor are derived the MT response functions: apparent resistivity (ρ_{aij}) and phase (φ_{ij}). The form of this complex second-rank tensor is related to the dimensionality of geoelectrical structures. For that reason, a thorough dimensionality analysis of the MT data is necessary to determine which approach is more adequate: 1D, 2D or 3D. The dimensionality analysis yields information about the direction along which the electrical resistivity remains constant (geoelectric strike direction) and makes it possible to correct the MT data by detecting and removing most of the possible galvanic distortion effects. Nowadays, different approaches are commonly used: (i) Groom-Bailey distortion decomposition method for a regionally 2D geoelectrical subsurface (Groom and Bailey, 1989); (ii) analysis of the set of rotational invariants of the impedance tensor presented by Weaver et al. (2000), and (iii) the study of the phase tensor which relates the real and imaginary parts of the impedance tensor (Caldwell et al., 2004). For an extended description and comparison of the different existing methologies, see Jones (2012) in the recent book on MT by Chave and Jones (2012).

Different 3D MT inversion algorithms have been developed in the last years although 3D inversion requires further development and understanding of the advantages and limitations. For a test and comparison of the current available codes see the compilation of Miensopust et al. (2013). In this Hontomín work, three different 3D inversion codes were used: the code described by Mackie and Madden (1993) subsequently developed and implemented by Geosystem (called Geosystem code hereafter); WSINV3DMT (Siripunvaraporn et al., 2005) and ModEM (Egbert and Kelbert, 2012). The first one is a commercial code and uses a truncated non-linear conjugate gradient approach. The second, WSINV3DMT, is based on a data-space variant of the Occam's approach. Finally, ModEM, is a modular system of computer codes for different EM problems and the inversion algorithm is also based on a non-linear conjugate gradient scheme. For a comprehensive explanation about 3D inversion and modelling, see the following reviews: Avdeev (2005), Börner (2010) and Siripunvaraporn (2012).

4. Magnetotelluric data and dimensionality analysis

The EM characterisation of the Hontomín site was divided into two stages: first, a 2D acquisition was carried out in Spring 2010 (profile presented in Ogaya et al., 2013 and renamed to MTD in this work; red dots in Fig. 4), and then, a 3D acquisition was undertaken in Autumn 2010 (yellow dots in Fig. 4). Eighty-seven new broadband magnetotelluric (BBMT) sites were acquired in the second fieldwork to complement the 22 made in the first fieldwork, making a total of 109 BBMT sites on a grid covering

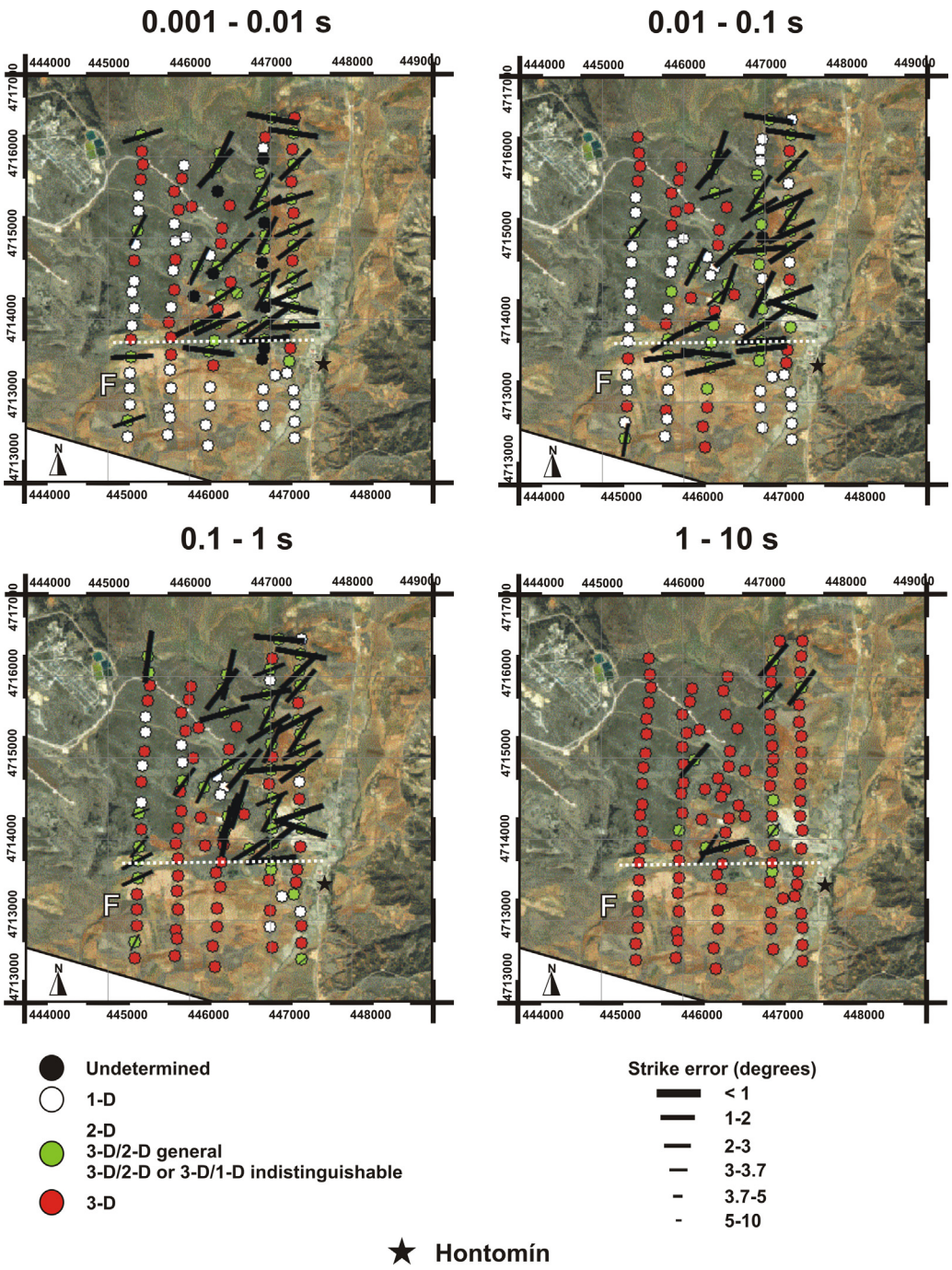

Fig. 5. Map of dimensionality analysis using the WALDIM code for four different period ranges: 0.001–0.01 s, 0.01–0.1 s, 0.1–1 s (primary reservoir-seal system) and 1–10 s. White dots infer 1D geoelectrical structures. Green dots group all inferred 2D cases: purely 2D case, 3D/2D general case with 2D structures affected by galvanic distortion and indistinguishable cases 3D/2D and 3D/1D, where the galvanic distortion makes impossible to determine the strike direction. Red dots designate the inferred 3D cases. Geoelectric strike is indicated by black lines of length inversely proportional to its error. The white dotted line shows the approximate north-border of the F region. The location of Hontomín village is indicated. (For interpretation of the references to colour in this figure legend, the reader is referred to the web version of this article.)

an approximately extent of $3 \times 5\,km^2$. The data were mainly organised along five NS profiles: MTA, MTB, MTC, MTD and MTE (Figs. 1c and 4). To refine the grid in the injection area (Hi region), two smaller NS profiles were acquired: MTBC and MTCD (indicated with yellow dotted lines in Fig. 4). All profiles were perpendicular to the EW trend of geological structures and crossed the EW fault imaged in the previous 2D resistivity model (F fault, Fig. 3). The length of each profile was around 4 km and the average distance between them was approx. 500 m. The stations were distributed on 200 m intervals along the profiles. The instrumentation consisted of Metronix ADU06, Metronix ADU07 and Phoenix V8 recorders with induction coil magnetometers and NaCl-type electrodes with a typical electrode line length of 70 m. The *x*-axis was oriented in the magnetic NS direction with the positive direction pointing to the north, and the *y*-axis in the EW direction pointing to the east. The data were acquired in the period range of 0.001–100 s (1000–0.01 Hz frequency range). The processing and quality control of the new data was the same as the one described in Ogaya et al. (2013). The data were recorded during 24 h and a permanent remote reference (RR) station was placed 20 km away from the H2

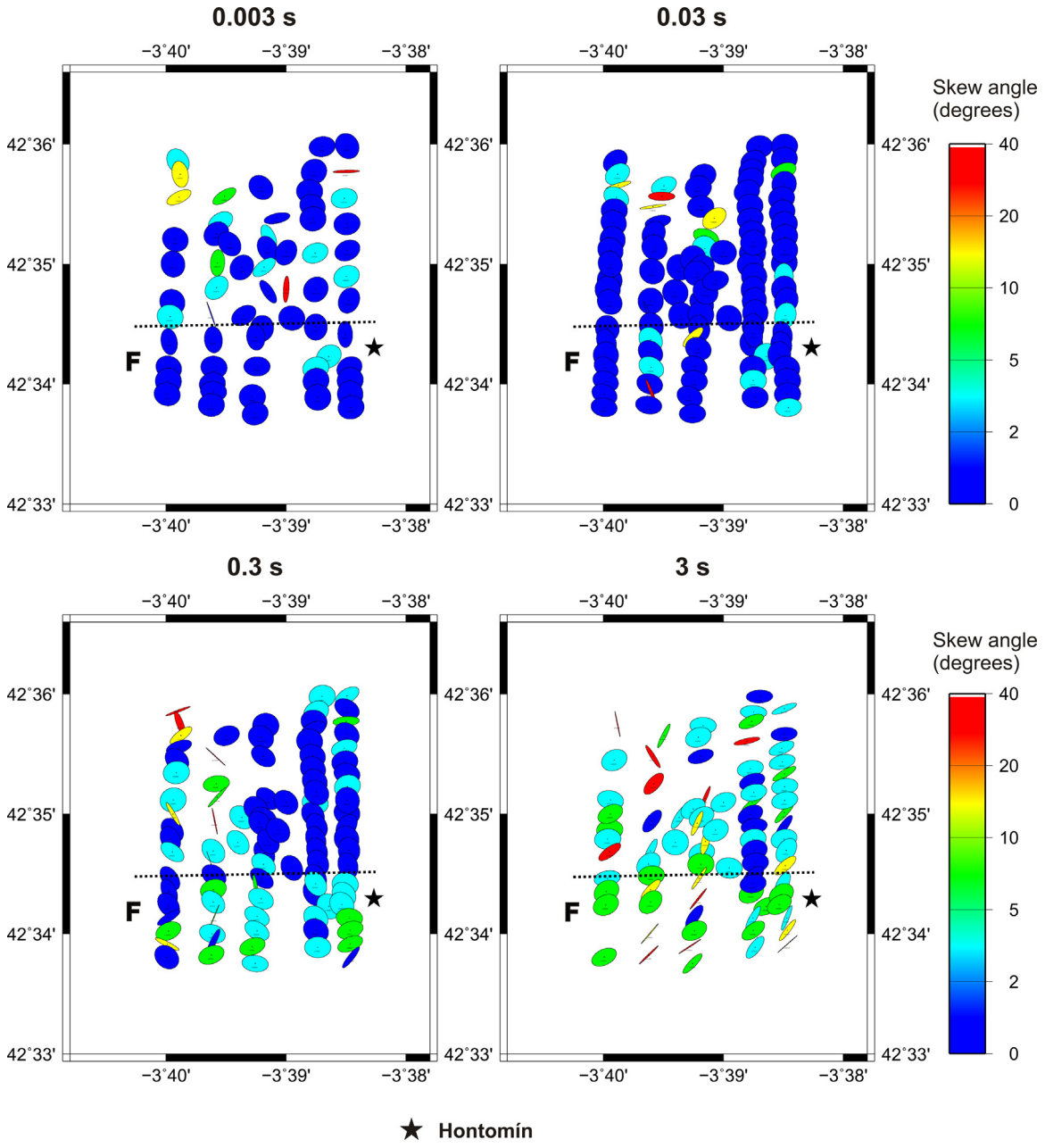

Fig. 6. Phase tensor at each site for four different periods: 0.003 s, 0.03 s, 0.3 and 3 s. The azimuth of the semi-major axis corresponds to the strike direction and the difference between the length of the semi-major and semi-minor axis gives an estimate of the dimensional complexity of the geoelectrical structure (i.e., a circle matches with the 1D case). The colour of the ellipse shows the skew angle β which indicates the 3D character of the resistivity distribution ($\beta = 0$ for a 2D case). As the plot corresponds to four single periods, some of the sites do not have data. The black dotted line shows the approximate north-border of the F region. The location of Hontomín village is indicated.

well to improve the quality of the longest periods (same location as in Ogaya et al., 2013). Moreover, BBMT acquisition was designed in a manner that at least 4 stations were recording at the same time to minimise the effects of the EM noise using also local multiple RR techniques. During a third phase of fieldwork acquisition, a single long period magnetotelluric (LMT) data set was collected to obtain information about the deeper structures (green dot in Fig. 4). The LMT data were acquired in the period range of 16–20000 s using a LEMI system (Lviv Centre of Institute of Space Research).

Robust processing codes employed to derive the BBMT responses were the ones that demonstrated their validity in the previous 2D survey (Egbert and Booker, 1986). The RR technique (Gamble et al., 1979) was used at all stations to improve the quality of the BBMT data between 0.5 and 10 s. The implementation of the local RR technique was crucial for improving the data collected near the wind turbine region (shown on Fig. 4) and consisted of undertaking RR with sites located in the southern part of the study region (less noisy area). At periods exceeding 10 s, ambient noise dominated the natural signal and consequently, the studies were undertaken in the period range of 0.001–10 s (1000–0.1 Hz). The LMT data were processed using Birrp.5 (Chave and Thomson, 2004).

The dimensionality analysis of the acquired MT data was evaluated using (i) the WALDIM code of Martí et al. (2009) based on the Weaver impedance invariants (Weaver et al., 2000), and (ii) studying the phase tensor (Caldwell et al., 2004). Fig. 5 shows the results obtained using the WALDIM code at each site for four different period ranges: 0.001–0.01 s, 0.01–0.1 s, 0.1–1 s and 1–10 s. The assigned error level in the impedance components was of 5% and the thresholds set for the invariants were: $\tau = 0.19$ for invariants I_3–I_7 and $\tau_Q = 0.10$ for invariant Q. For short periods (shallow

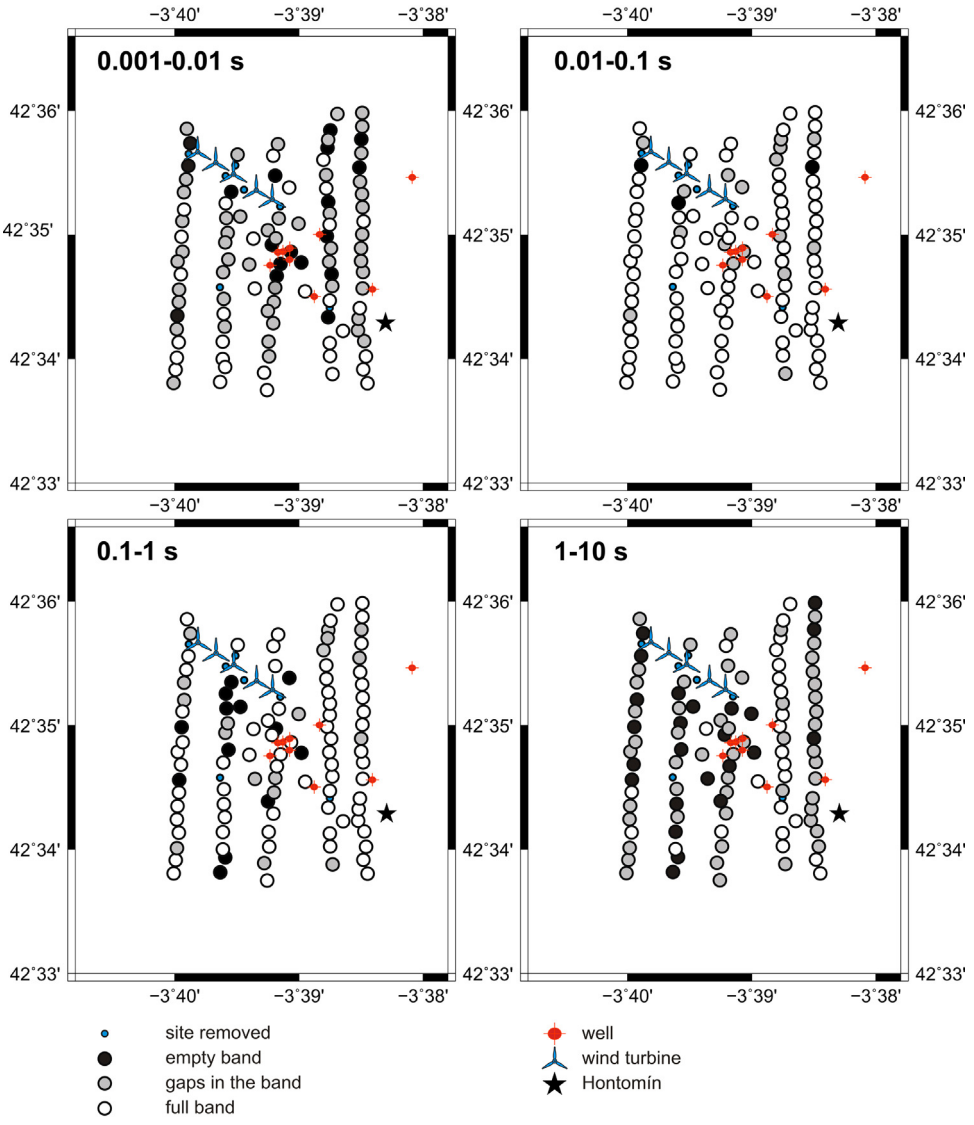

Fig. 7. Quality of the BBMT data. White big dots indicate sites with information in the whole range of periods whereas large black dots indicate sites without any data in the range. Intermediate cases with gaps in the period range are indicated by grey dots. Small blue dots represent the excluded noisy sites. The positions of the wells and the wind turbines, main EM noise source of the study area, are indicated. (For interpretation of the references to colour in this figure legend, the reader is referred to the web version of this article.)

depths), the results indicate 1D/2D conductivity, being mainly 1D in the F region (in the south). On the contrary, when increasing the period (equivalent to increasing the depth of penetration), geoelectrical structures become more complex and present a 3D behaviour.

Fig. 6 plots the phase tensor at each site for four different periods: 0.003 s, 0.03 s, 0.3 and 3 s. As the phase tensor is independent of the electric effects of galvanic distortion, this analysis aimed to determine if there existed an important galvanic distortion in the WALDIM results and, in this way, to estimate to what extent this distortion was perturbing the data. Results indicate that the geoelectrical structure becomes more complex with increasing the period, as showed for the WALDIM analysis.

Thereby, the dimensionality analysis corroborated that a 3D inversion of all the BBMT data set was necessary to avoid misinterpretation of the geoelectrical structure of the Hontomín URL at periods longer than 0.1 s (Ogaya et al., 2012). Moreover, it was concluded that galvanic distortion in the study area was small, since results of the phase tensor study were consistent with the ones obtained using the WALDIM code.

The internal self-consistency of the *XY* and *YX* BBMT data apparent resistivity and phase curves was analysed through D^+ model solutions (Parker, 1980; Parker and Whaler, 1981). This method facilitates detecting and removing outliers and noisy points by analysing the physical validity of the MT responses. Thus, using an estimated data error of 10% for the apparent resistivity and phase, less than 30% of the BBMT data was discarded. This fraction included data from all sites in the range of 10–100 s – the noisy region. Seven BBMT sites were excluded from the inversion because they were considered too noisy with a high and linearly polarised signal (Escalas et al., 2013). Almost all of them were near the wind turbine region. Fig. 7 summarises the quality of the BBMT data, indicating: complete period bands (white); period bands with gaps (grey); empty period bands (black) and excluded sites (blue). Most of the grey cases correspond to curves with shortest periods longer than 0.001 s and/or longest periods shorter than 10 s. This defines the data set for the 3D inversion.

For the data set for the inversion, the minor static effects of galvanic distortion were dealt prior to the inversion using the available

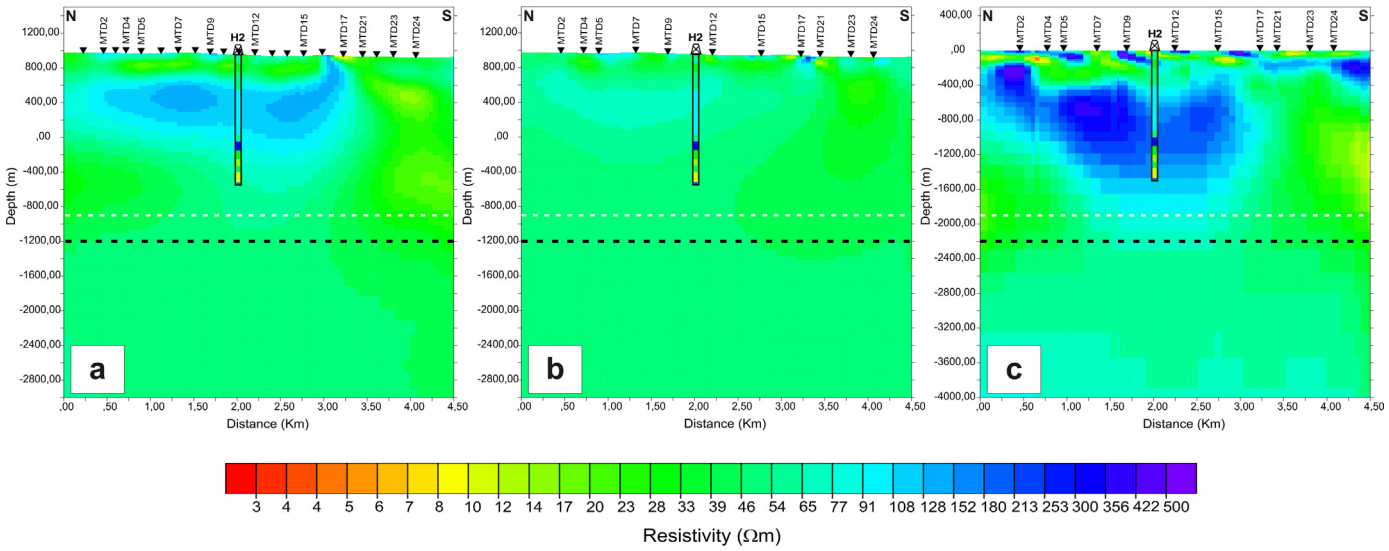

Fig. 8. Equivalent section to the MTD profile modelled in Ogaya et al. (2013) for each of the three initial inversions from a uniform 50 Ωm halfspace: (a) model Ø, (b) ModEM and (c) WSINV3DMT. The black dashed line indicates the approximate depth at which the resistivity increase is observed (depths are given in terms of m.a.s.l. in (a) and (b) cases, and in terms of TVD in (c) case). The white dashed line indicates the bottom of the 2D model shown in Fig. 3. Superimposed appears the 1D resistivity model of the H2 well (Fig. 2a). BBMT sites are marked by black triangles.

resistivity log data to fix the resistivity values at shallow depths. In general terms, the static shift corrections were smaller than a logarithmic decade. Static shift correction could imply a loss of information but related to near surface structures that are not the target of this study.

Giving the predominant 3D behaviour of the geoelectrical structures for periods longer than 0.1 s, the diagonal components of the impedance tensor were considered for the inversion. The importance of including the diagonal components in 3D inversion was recently emphasised by Kiyan et al. (2014). For the shortest periods, the amplitude of the apparent resistivity of the diagonal components at most sites is two to three decades smaller than the off-diagonal components. However, for the longest periods, the difference of amplitude between the diagonal and off-diagonal components is less than a decade. In general, the diagonal component data are of reasonable quality and their apparent resistivity and phase curves are not scattered; their amount of error is relatively low (see supplementary Figs. S1–S17).

Supplementary material related to this article can be found, in the online version, at doi:10.1016/j.ijggc.2014.04.030.

5. 3D inversion of the MT data

5.1. General aspects (setup)

The work flow for 3D inversion consisted in improving a preliminary model provided by Geosystem (Mackie and Madden, 1993; model Ø hereafter; Fig. 8a) using the ModEM code (Egbert and Kelbert, 2012). WSINV3DMT (Siripunvaraporn et al., 2005) was also used to undertake some testing and to study the consistency of the models.

The topography of the study area is relatively gentle: elevations range from 919 to 1040 m.a.s.l. with the highest ones to the NW area (wind turbine region). As the target regions are located at depths below the surface no greater than 1800 m TVD, it was considered important to incorporate topography in the model. To

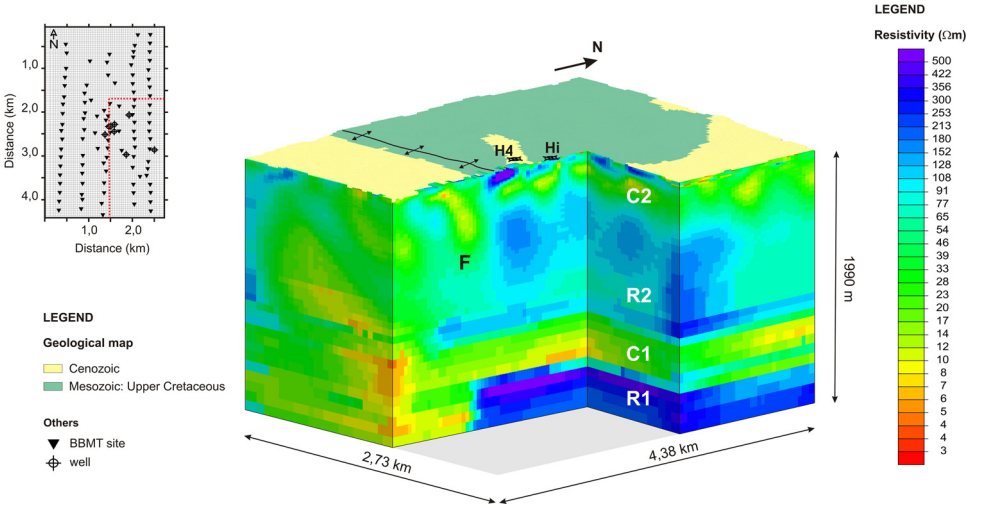

Fig. 9. Final 3D resistivity model of the Hontomín URL subsurface with a cutout (red dotted lines indicate the location of the NS and EW cuts). The geological map of the study area is shown and the positions of the wells and BBMT sites are marked. The F region and the main resistivity layers (R1, C1, R2 and C2) are also indicated. Depths are given in terms of m.a.s.l. (For interpretation of the references to colour in this figure legend, the reader is referred to the web version of this article.)

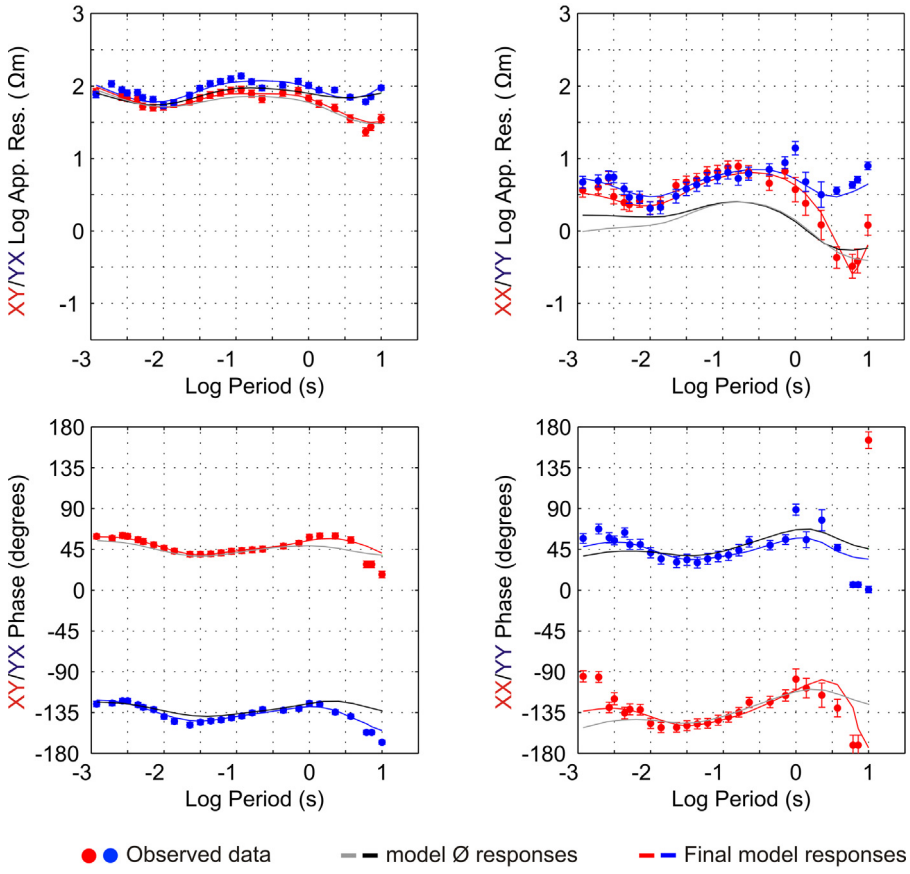

Fig. 10. Responses of the model Ø and the final 3D model at site MTD7.

avoid sharp boundaries between the air and earth cells, a smooth topography was implemented. The mesh was a $73 \times 114 \times 113$-layer grid including topography for Geosystem and ModEM's cases (an approximate model extension of $61 \times 63 \times 54\,km^3$). For WSINV3DMT's test cases, the mesh was a $52 \times 68 \times 60$-layer grid but excluded topography (an approximate model extension of $70 \times 72 \times 52\,km^3$).

The final inversions were undertaken using up to 29 periods of the full impedance tensor for the 102 BBMT sites in the range of 0.001–10 s. The error floor set was 5% for the off-diagonal components (2.865 degrees for the phases and 10% for apparent resistivity) and 10% for the diagonal components (5.73 degrees and 20% for the apparent resistivity). Missing data periods were interpolated and included but had assigned large error bars.

The models were run on the Stokes cluster of the Irish Centre for High-End Computing (ICHEC) and on the Mallet and Lehmann clusters from Dublin Institute for Advanced Studies (DIAS). The main aspects of the inversion process are detailed below.

5.2. Initial 3D inversions

Some initial inversions were run using ModEM and WSINV3DMT codes to validate the initial model Ø used and to assess its geological consistency. The initial model was for both cases a halfspace of 50 Ωm (as for Geosystem's inversion) which agrees with the average resistivity value of the H2 well log data (Fig. 2). The inversions were undertaken using the full impedance tensor. However, in order to assure the convergence of these initial models, first iterations were undertaken using only 50 sites uniformly distributed and covering all the area, and the off-diagonal components. Once the main structures were defined, more sites and components were included in the inversion. The greater was the amount of data incorporated to the inversion, the greater was the definition and resolution of the imaged structures. As was also seen in Ingham et al. (2009), the resistivity structure obtained from the first inversions with only a small number of sites was basically the same as that obtained with the whole data set, i.e., the existence of conductivity structures is a robust first-order feature in the data set. The data fit was better doing a correction of the static shift prior to the inversion.

Fig. 8 shows a section of the 3D model coincident with the MTD 2D profile modelled in Ogaya et al. (2013), for each of the three initial inversions from a uniform halfspace: (a) model Ø, (b) ModEM and (c) WSINV3DMT. The 3D models fit the data with an RMS misfit of 1.36, 2.25 and 2.05, respectively. Despite the discrepancies related to topography, as it is included in (a) and (b) cases and not included in (c) case, the results from the initial 3D inversions confirmed that the three models are equivalent in the sense that all of them recovered the same main resistivity features. Moreover, the obtained electrical resistivity distribution resembles the one imaged in the previous 2D model (Ogaya et al., 2013; Fig. 3), proving the geological consistence of the models. Thus, it was considered appropriate to define the model Ø as the initial model for the subsequent inversions with the ModEM code.

Nevertheless, comparing the obtained models to both the 2D model (Ogaya et al., 2013; Fig. 3) and the resistivity well logs existing in the area, it was noticed that none of the inversions recovered the resistive structure located at 1600 m TVD (R1 in Fig. 3). The models only imaged a slight increase in the resistivity at around 2200 m TVD (at −1200 m.a.s.l. for models with topography). This depth is indicated by a black dashed line in Fig. 8. Therefore, the fitting of the deepest part needed to be improved.

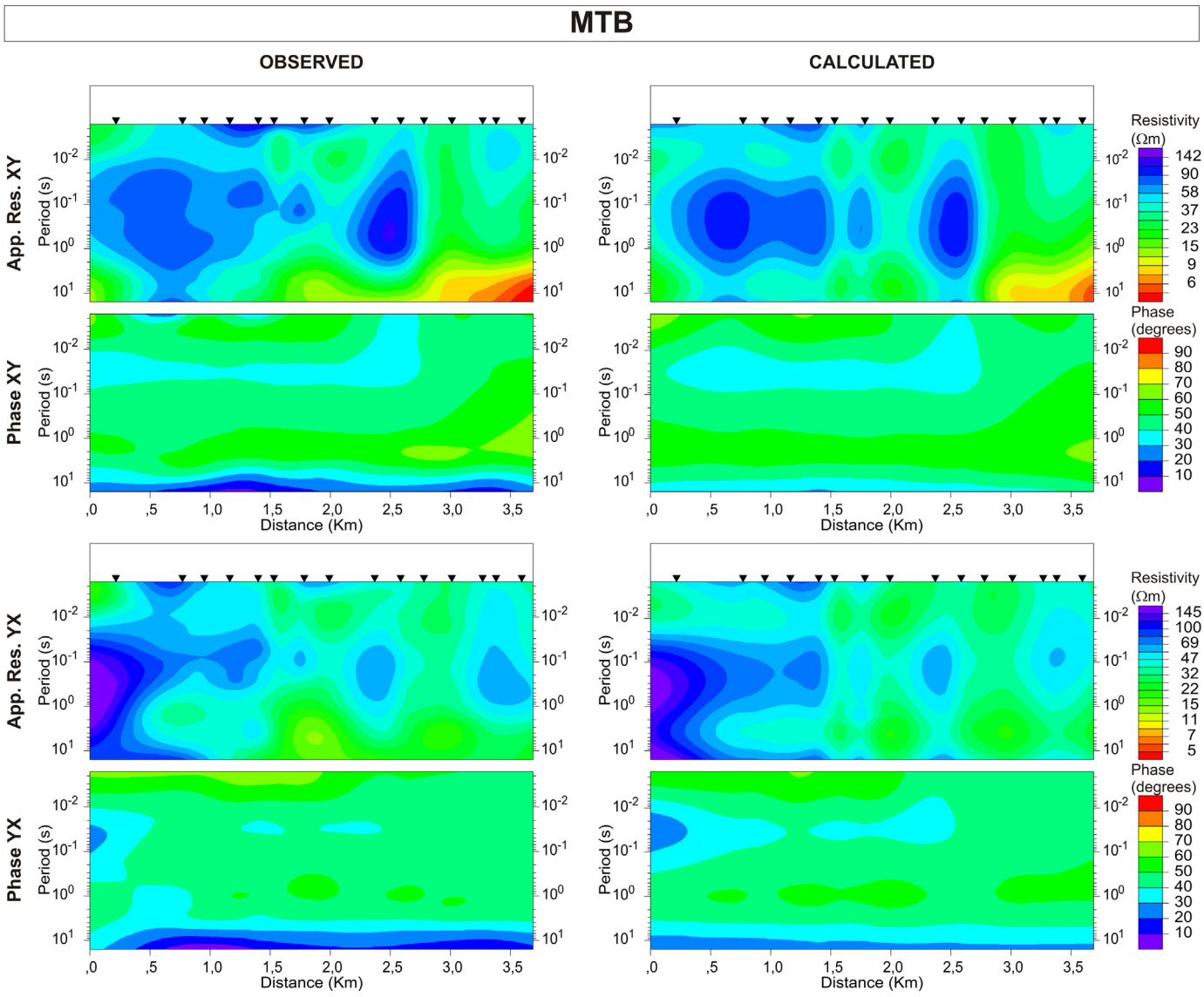

Fig. 11. Pseudosections of MTB profile: apparent resistivity and phase for observed data and model responses. The positions of the BBMT sites are marked by black triangles.

To address this issue, several inversions using the ModEM code were carried out for different period bands: the shortest periods were fitted first and then, the longest periods were inverted fixing the upper part of the model. The fit of the shortest periods was improved but improvement did not occur in the same manner with the longest ones. Through 3D synthetic studies it was corroborated that the primary system (primary reservoir and seal) MT responses were principally in the range of 0.1 to 1 s, as was previously affirmed by Ogaya et al. (2013). In this way, the data collected at the Hontomín site were imaging the deepest resistive layer R1 but a non-constrained 3D inversion was unable to recover the layer. The inversion needed to be better constrained at depth in order to resolve the bottom of the main reservoir and recover the R1 layer.

5.3. Final 3D resistivity model

For the final model, a more constrained inversion was carried out incorporating new information for the initial model. As has been discussed in other publications (e.g., Piña-Varas et al., 2013), an appropriate selection of the initial model is sometimes necessary to produce a meaningful model from a geological point of view. Thus, according to the existing resistivity-log data and the geoelectrical structure imaged in Ogaya et al. (2013), included in the initial model was a 25 Ωm conductive layer at approximately −220 m.a.s.l. and a resistive layer of 200 Ωm between −600 and −2000 m.a.s.l. Data from the single LMT site were incorporated to the inversion (period range of 10–340 s; see supplementary Fig. S12).

The final 3D model fits the data with an RMS misfit of 1.71 (Fig. 9). Fig. 10 plots the responses of model Ø and the final model at site MTD7 showing the improvement of the fit at the longest periods and also for the diagonal components. The data and model responses at all sites are plotted in supplementary Figs. S1–S17. Comparisons between data and final model responses for the off-diagonal components are shown in Fig. 11 for the MTB profile and in Fig. 12 for the MTD profile (approximate limits of the URL). The misfits of the other profiles are shown in supplementary Figs. S18–S22. As is illustrated, the fit is satisfactory and the residuals are random and small; no significant feature in the data is unexplained.

Supplementary material related to this article can be found, in the online version, at doi:10.1016/j.ijggc.2014.04.030.

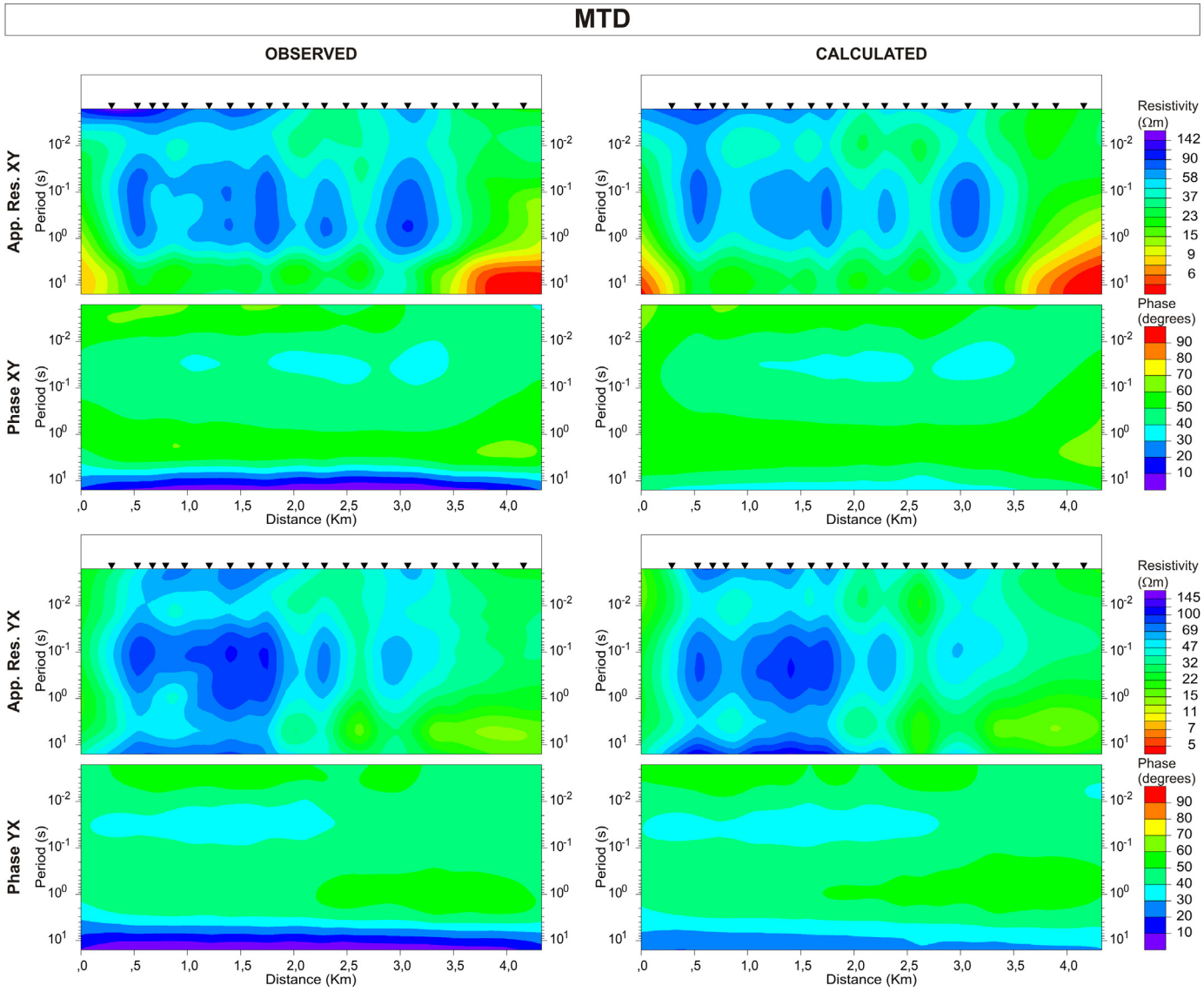

Fig. 12. Pseudosections of MTD profile: apparent resistivity and phase for observed data and model responses. Differences with pseudosections shown in Ogaya et al. (2013) are because the MT data were not rotated in this work. In Ogaya et al. (2013) the data were rotated 4° W; the transverse magnetic (TM) mode was identified with *XY* polarisation and the transverse electric (TE) mode, with *YX* polarisation. The positions of the BBMT sites are marked by black triangles.

The geoelectrical structure from near surface to −900 m.a.s.l. is an alternation of conductive and resistive layers (from bottom to top; Figs. 13–16): R1, C1, R2 and C2. The location of the tops and bottoms of the layers, as well as their thicknesses, vary along each profile and between profiles. The southern part of the model (F region) is mostly conductive, being much more conductive in the eastern part than in the western part. Through non-linear-sensitivity tests (e.g., Ledo and Jones, 2005) the most conductive eastern part of the F fault region (region 1 in Fig. 13b) and the continuity of the R2 layer in the southern part of the model (region 2 in Fig. 13b) were both evaluated. The tests consisted of replacing the resistivity values of these regions by their surrounding resistivity value: 30 Ωm for region 1 and 200 Ωm for region 2. In both cases, the difference between the responses of the final model and the modified one was greater than the error floor imposed in the MT data for the inversion (results for region 1 in Fig. 17 and results for region 2 in Fig. 18). In this way, that conductive region 1 is required by sites located in the southern part of the model, mainly the ones in the MTD and MTE profiles, was corroborated. This conductive feature was also imaged in the 2D model (Fig. 13a). Results from region 2 indicate that there is no continuity of the R1 layer in the southern region of the model (Fig. 18).

6. Comparison with other EM studies

6.1. MTD profile

Fig. 13 shows (a) the 2D model and (b) its equivalent section from the final 3D model. The topography of the two models is slightly different because of the smoothing of the 3D topography. The models are consistent and only relatively minor differences are apparent. In the 3D model: (i) R1 layer is more resistive under sites MTD14-MTD15 and does not extend under sites MTD21-MTD24; (ii) the most conductive portion of C1 layer is located in the north and there is not a clear discontinuity of the layer because of a more resistive area under sites MTD14-MTD15; (iii) in general terms, R2 range of resistivity values is narrower, and (iv) C2 layer contains less scattered bodies. Regarding the F region, its structure is less

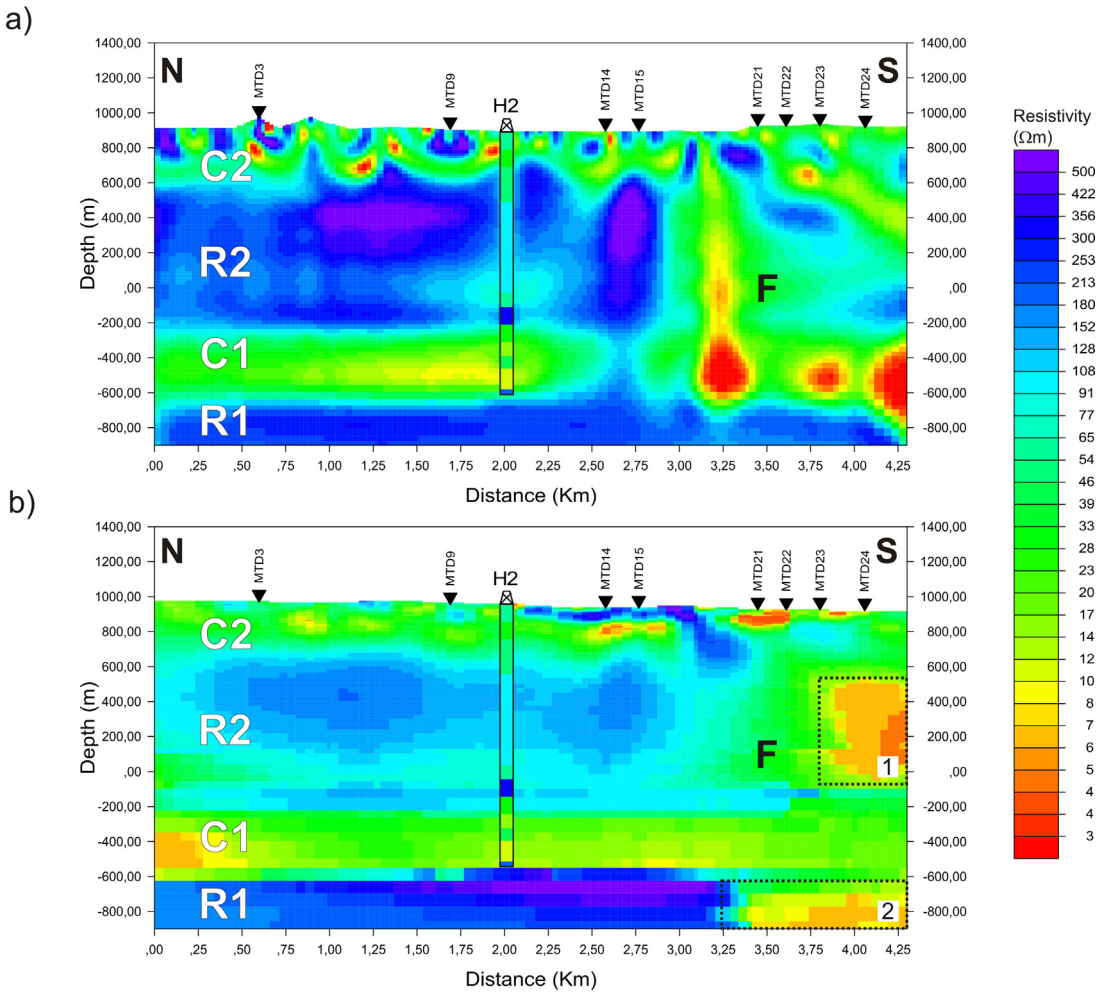

Fig. 13. (a) 2D model of the MTD profile (Ogaya et al., 2013) and (b) its equivalent section of the final 3D model. The same resistivity colour scale is used for both models. The main resistivity layers (R1, C1, R2 and C2) and the F region are indicated. The 1D model provided by the resistivity-log data of the H2 well is superimposed and BBMT sites are marked by black triangles. The differences in topography are apparent because it was defined on a smoother surface for the 3D model. Black dotted lines indicate the two more conductive regions studied through non-linear-sensitivity tests: region 1 (Fig. 17) and region 2 (Fig. 18). Depths are given in terms of m.a.s.l.

well defined. In none of the models (neither the 2D nor the 3D) does the F fault seem to outcrop.

The major discrepancies are observed in the deepest structures (R1 and C1 layers). These structures are located in the period range of 0.1–10 s (Ogaya et al., 2013) which is the band where the data are not purely 2D and some 3D effects are observed (Figs. 5 and 6). The observed differences are therefore concluded to be mainly because of two reasons: the greater smoothness of the 3D models, primarily due to larger cell sizes, and the possible influence of 3D structures in the previous 2D inversion.

6.2. Correlation with resistivity log data

Fig. 14 shows three sections (profiles I, II and III) that cut the resulting 3D model by the existing H1–H4 wells. The simplified resistivity-log data of each well correlate well with the 3D model. The main differences are noticed for the H4 well which is reasonable since its 1D resistivity model was derived from the H2 well log data and the H2 well is located 707 m away. Likewise, the structure of the upper part of the model agrees with the 1D model derived from the GW wells.

Correlation of the final 3D model with the resistivity log data show that discrepancies are not significant, neither for the H wells nor for the GW wells. Thus, it was seen that for this case study, the correction of the static shift prior to the inversion provided accurate results.

7. Interpretation: 3D geoelectrical baseline model

Resistive layer R1

R1 is the deepest layer imaged in the 3D model. Synthetic studies showed it was mainly sensed at periods around 1 s. The top of this layer is shallowest (−552 m.a.s.l.) in the centre-eastern part of the model under profiles MTC, MTD and MTE (Fig. 15 h). The layer is also more resistive in that region (up to 1000 Ωm; Fig. 14). There is not a continuity of this layer in the southern region of the model (Fig. 13).

The R1 layer is interpreted as the Upper Triassic unit (Keuper facies). This unit is constituted by a succession of dolomites, anhydrites, and salt, which could explain its high resistivity. It is an impermeable layer that may constitute a suitable bottom seal for the main reservoir.

Conductive layer C1

The C1 layer is sensed in the period range of 0.1–1 s. The top of the layer is approximately at −216 m.a.s.l. (Fig. 15f). It has a

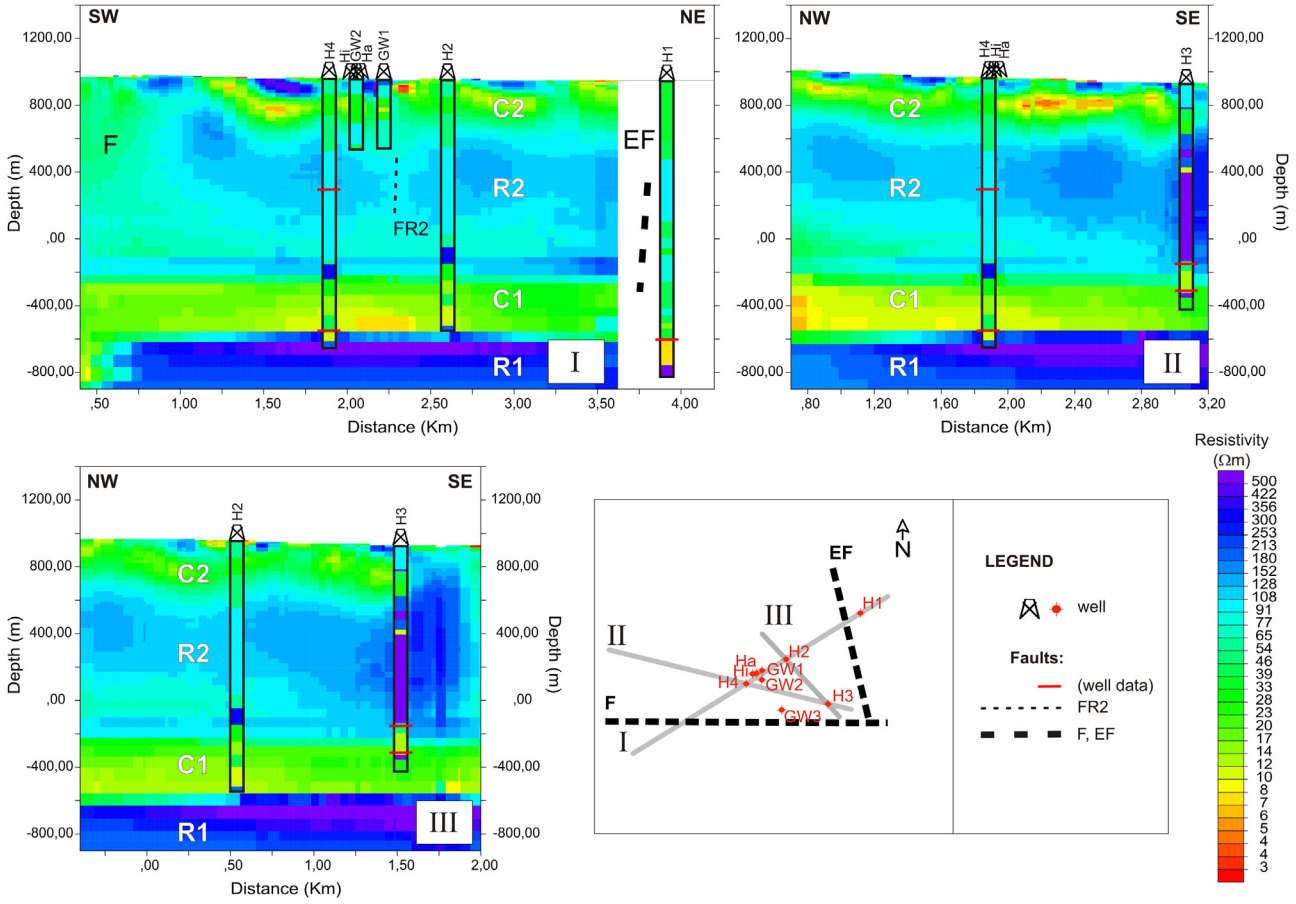

Fig. 14. Three sections (I, II and III) cutting the final 3D model by the existing wells. The main resistivity layers (R1, C1, R2 and C2) and the F and EF fault regions are indicated. Possible FR2 fracture regions and faults that cross the H wells according to well data, are also specified. The 1D resistivity models derived for each well (simplified resistivity-log data) are superimposed. Depths are given in terms of m.a.s.l.

dome-like structure with its axis situated in the injection area. The slope of the north flank is less steep and the dome seems to be elongated to the NW (Fig. 15f and g). The extension of the dome crest in this layer is about $1 \times 1\ km^2$.

The C1 layer contains Jurassic rocks according to the well log data. The main reservoir and seal units are interpreted to be located within it. The saline aquifer (main reservoir), is linked to the most conductive region inside C1, a 7–14 Ωm region labelled as C1a in Fig. 15g. The top of this most conductive layer is located around −400 m.a.s.l. The overlying primary seal also features a conductive behaviour, probably because of its marly composition (marlstones and black shales).

Resistive layer R2

R2 is the thickest layer within the model. The top of this layer is shallower in the NW part of the model, where is located at approximately 700 m.a.s.l. (Fig. 15b). R2 is interpreted as the upper part of Jurassic (upper part of the Dogger) and Early Cretaceous (Weald and Purbeck facies and Escucha Fm.) units. The secondary reservoir-seal system would be contained within the R2 layer.

Analysing the layer from bottom to top, one can deduce the possible evolution of the dome structure.

(i) The bottom of the R2 layer is defined by a more resistive sublayer of up to 130 Ωm and approximately 100 m thickness (Figs. 14 and 15e). According to the lithological information provided by the different wells, this increase in resistivity may be explained by a slightly increase on limestone content. In Fig. 15e is observed a less resistive region (below 100 Ωm) in the centre of R2, around the locations of the wells, which agrees with the dome-shape observed for the C1 layer.

(ii) Upwards, there exists a displacement of the dome crest to the east. At 177 m.a.s.l. (Fig. 15d), the crest of the dome seems to be located in the surroundings of the H2 well.

(iii) In the overlying layers (Fig. 15c) the resistive dome (resistivity values up to 220 Ωm) moves to the NW of the model. Consequently, at around 700 m.a.s.l. (Fig. 15b), the crest of the dome appears to be imaged in the NW region.

The R2 layer seems to be more conductive in the NW part of the model but this aspect may not be due to a geological explanation. As the quality of the data was lower in that region (wind turbine region; see Fig. 7), the error bars were larger. Thus resolution is poorer and naturally the smoothness constraint drives resistive regions to the lowest possible values they can take.

Conductive layer C2

The C2 layer is the surficial part of the model, i.e., the topmost layer. According to the well log data, it contains the Upper Cretaceous and Cenozoic materials that dominate the surface of the study area. The clear limit between the R2 and C2 layers (Figs. 13 and 14) is marked by the top of the Utrillas Fm. The R2 layer emerges in C2 (EW resistive body in Fig. 15a) due to the presence of the F region.

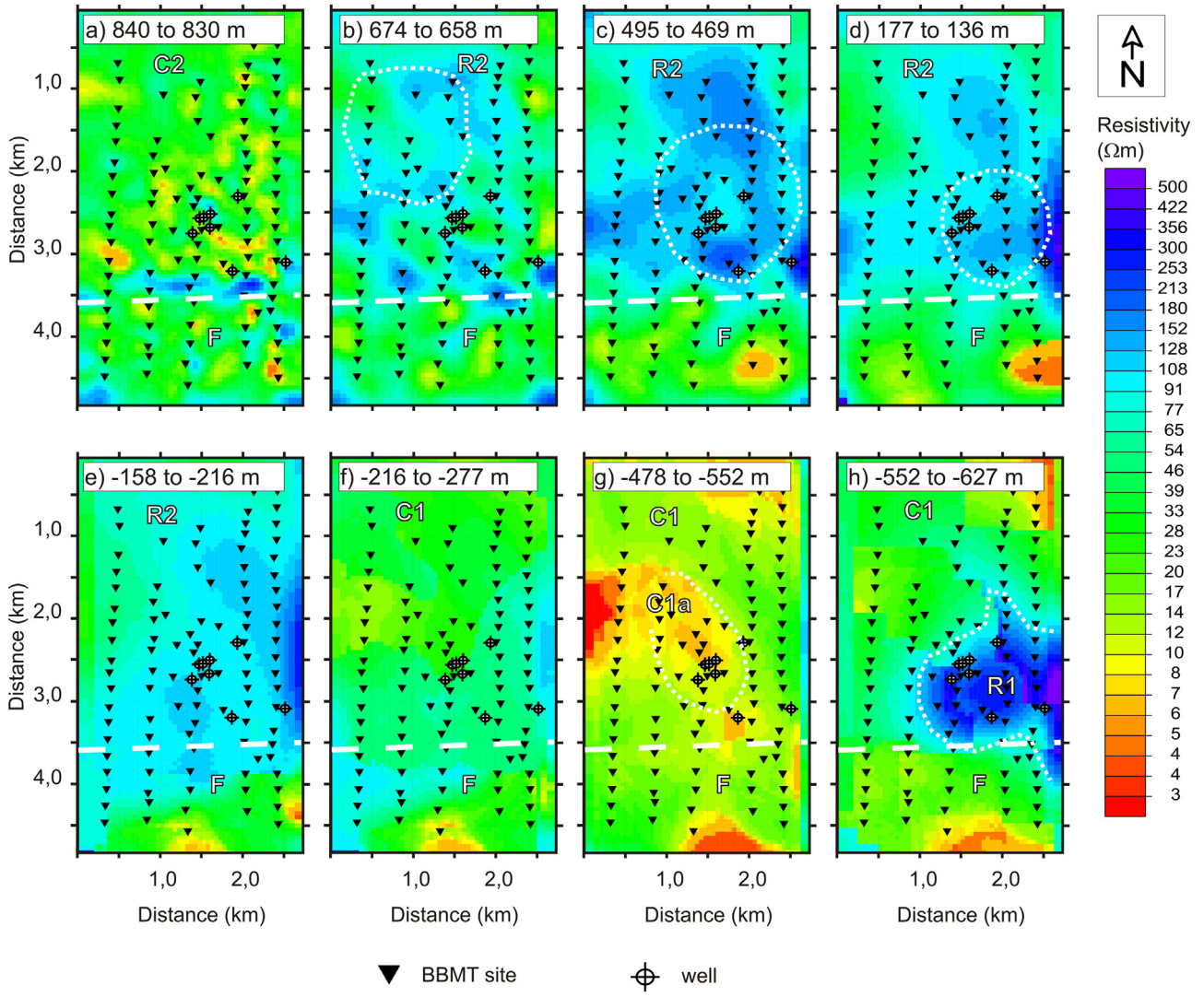

Fig. 15. Z-slices of the model from top (a) to bottom (h), with depths indicated in each sub-plot. The main resistivity layers (R1, C1, R2 and C2) and the F region are indicated. EW white dashed line indicates the approximate north-border of the F region. From bottom to top (depths given in terms of m.a.s.l.): (h) top of the R1 layer; (g) main reservoir C1a (saline aquifer); (f) top of the C1 layer; (e) bottom of the R2 layer; (d), (c) and (b) evolution of the R2 layer's dome structure and (a) C2 layer and bend of the R2 layer due to the presence of the F region. See text for more information about the white dotted lines.

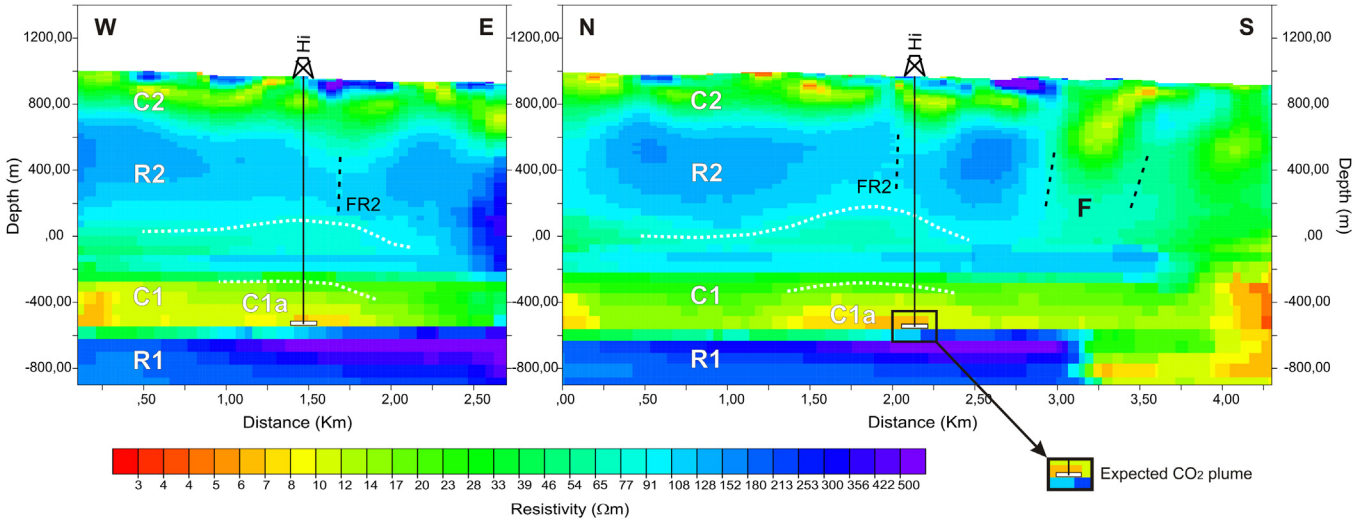

Fig. 16. NS and EW sections cutting the model by the injection well (Hi). The image shows the main resistivity layers (R1, C1, R2 and C2) and the F and FR2 fault regions. White dotted line traces the approximate soft dome-like structure of C1 and R2 layers. The expected CO_2 injection plume is indicated by a white square. Depths are given in terms of m.a.s.l.

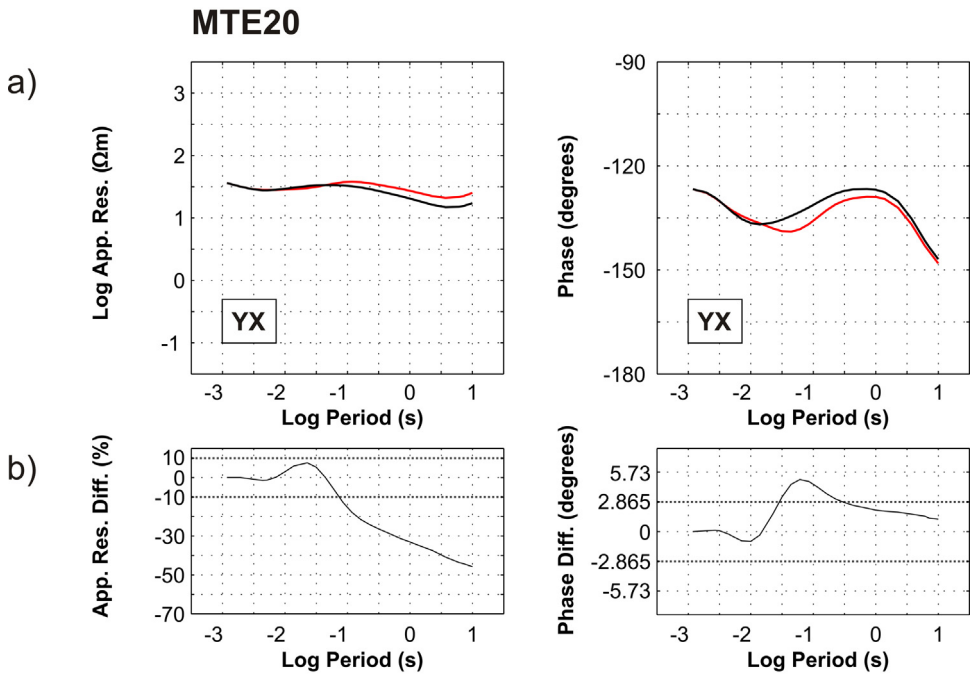

Fig. 17. Non-linear sensitivity test to study the conductive region 1 (indicated by black dotted lines in Fig. 13). (a) *YX* responses at site MTE20 of the final model (black) and the modified one (red) derived by replacing the resistivity values of the region 1 by 30 Ωm. (b) Difference between the *YX* apparent resistivity and phase responses. The differences are greater than the error floor imposed in the MT data for the inversion (10% for the *YX* apparent resistivity and 2.865 degrees for the *YX* phases). Thus the more conductive region 1 is required by sites located in the southern region of the model, mainly the ones in the MTD and MTE profiles. (For interpretation of the references to colour in this figure legend, the reader is referred to the web version of this article.)

Sets of faults

The 3D model shows the EW prolongation of the main fault F imaged in the previous 2D model (Fig. 6 in Ogaya et al., 2013). The F fault region is associated to the strike-slip movement of the Ubierna fault (Tavani et al., 2011; Quintà, 2013). The EW white dashed line in Fig. 15 indicates the approximate north-border of that region. The F fault affects all layers of the model, although it does not outcrop at surface and its top is observed at C2 layer's depth (Fig. 15a). It is characterised by a conductive behaviour, and the resistivity distribution suggests conductive fluid circulation along the fracture region. It is more conductive in the eastern part of the study

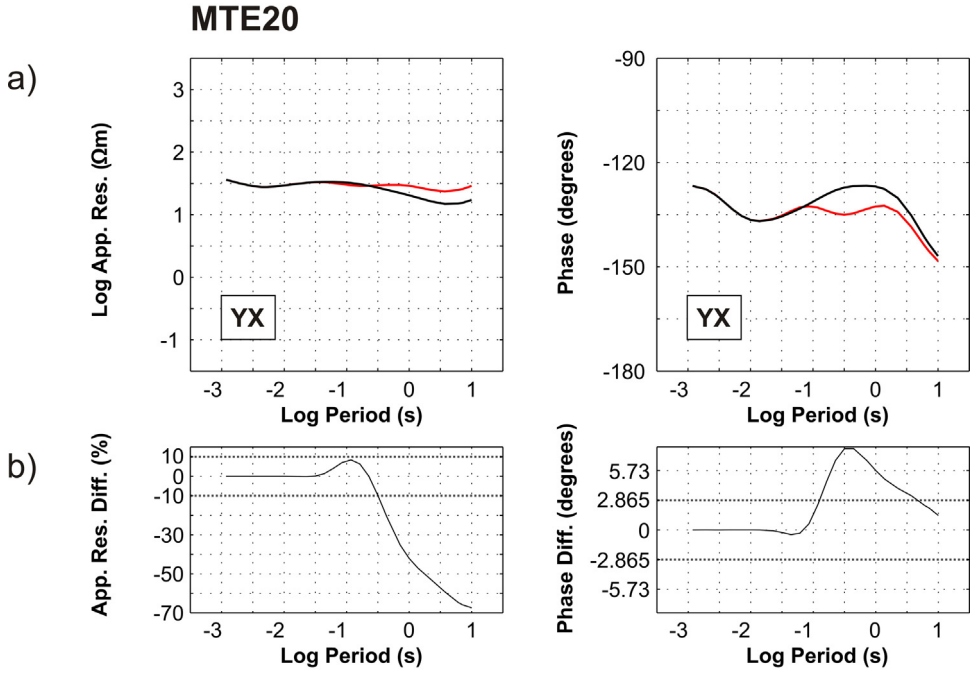

Fig. 18. Non-linear sensitivity test to study the conductive region 2 (indicated by black dotted lines in Fig. 13). (a) *YX* responses at site MTE20 of the final model (black) and the modified one (red) derived by replacing the resistivity values of the region 2 by 200 Ωm. (b) Difference between the *YX* apparent resistivity and phase responses. The differences are greater than the error floor imposed in the MT data for the inversion (10% for the *YX* apparent resistivity and 2.865 degrees for the *YX* phases). Thereby, the results indicate that there is not a continuity of the R1 layer in the southern region of the model. (For interpretation of the references to colour in this figure legend, the reader is referred to the web version of this article.)

area (Fig. 13) whereas in the western part it is less conductive and seems to be imaged as different faults (Fig. 16). These branches of the F fault are also observable in some sections of the seismic cube (Alcalde et al., 2013b). Consequently, the western part seems to be more sealed than the eastern part. Hydrogeochemical studies of surface and spring waters in the surroundings of the Hontomín URL (Buil et al., 2012; Nisi et al., 2013) found that water samples acquired in the eastern part of the F fault region could be indicative of mixing processes between deep and shallow aquifers. However, Elío et al. (2013) investigated the CO_2 flux baseline in the soil-atmosphere interface at the Hontomín site, and those authors did not find any anomaly in the F region, neither in the western nor in the eastern part.

In the eastern part of the model (under sites on the MTE profile) a more resistive behaviour of the R2 layer is observed (resistivity values up to 300 Ωm; see II and III profiles in Fig. 14). It could be due to a set of NS faults located in the east (Quintà, 2013; called EF hereafter and indicated in Fig. 14). The EF faults are located outside the modelled region, but their presence could explain the increase of the R2 layer thickness and resistivity in the eastern part of the model. The 1D resistivity model of the H3 well may differ from the others because is affected by F and EF sets of faults.

Small resistivity variations (more conductive areas) observed within the R2 layer could be associated with a set of minor faults in the Dogger and Purbeck units (Quintà, 2013). Some of these faults are indicated by FR2 in Figs. 14 and 16. In Fig. 14 are also shown the faults that cross the H wells according to well data (Quintà, 2013).

Injection area

Fig. 16 shows a NS and an EW section that cuts the 3D model by the injection well (Hi). Observed is the smooth dome-like structure of the C1 and R2 layers with Hi located close to the axis. The expected volume of CO_2 (20 kilotons, see above) is shown by a white square in Fig. 16. Since that the amount of CO_2 injection is small, none of the geoelectrical structures would appear to constitute a likely leakage pathway. However, according to the model, special attention should be paid to the possible FR2 faults neighbouring the Hi well and to the F fault (especially in the eastern part) during the monitoring of the URL.

8. Conclusions

The 3D resistivity model presented in this paper constitutes the geoelectrical baseline model of the Hontomín URL. It defines the subsurface structure in the pre-injection state and allows the detection of changes due to the CO_2 injection. It will be the reference model for the future EM monitoring experiments planned for the end of 2013.

The 3D inversion of the MT data combining different codes greatly enriched the inversion process. The 3D inversion made possible modelling the different 3D effects and improving the previous 2D model (Ogaya et al., 2013). The resistive layer located at approximately 1600 m TVD (under the conductive main reservoir-seal system) was only imaged when it was introduced into the initial model. Otherwise, the smoothness regularisation excluded exploration of that part of model space.

The final model contributes to a better understanding of the subsurface at the Hontomín site. In general, the electrical responses of each formation coincide with the ones imaged in the previous 2D model. However, the 3D model provides an important 3D spatial characterisation of the different units as well as images the prolongation of the main fault F. In this way, it is possible to determine the possible leakage pathway and design the monitoring setup according to the site requirements. Special attention needs to be paid to the possible FR2 faults neighbouring the Hi well, and to the eastern part of the F fault since the resistivity distribution there suggests conductive fluid circulation along this part of the fault.

The detailed geoelectrical characterisation presented here is an important contribution to CO_2 geological storage projects mainly for two reasons: (i) it demonstrates the valuable information that a 3D geoelectrical baseline model can provide and (ii) it shows the importance of a high-resolution reference model to define the monitoring requirements. Three-dimensional magnetotelluric surveys are complementary to other 3D reflection seismic and gravimetric characterisation studies, and, due to electrical conductivity's sensitivity to fluid flow, makes for a method with superior resolution of particular aspects of interest and importance for CO_2 storage and long-term monitoring.

Acknowledgements

This project has been partly financed by funds coming from the Spanish Ministry of Industry, Tourism and Trade, through the CIUDEN-UB Geomodels agreement related to the Development and Adaptation of Electromagnetic techniques: Characterisation of Storage Sites. This project is co-financed by the European Union through the Technological Development Plant of Compostilla OXYCFB300 Project (European Energy Programme for Recovery). This work was also developed in the framework of the Spanish MCI project PIER-CO_2 (CGL2009-07604). It is a contribution of the Research Group of Geodynamics and Basin Analysis (2009SGR1198) of the Generalitat de Catalunya and the Research Institute GEOMODELS. Xènia Ogaya was supported by the Fundación Ciudad de la Energía (CIUDEN) research training programme and by the Universitat de Barcelona (UB) through the Ajut per a Personal Investigador en Formació (APIF). EXES-UB group is thanked for their help in the MT data acquisition. The authors also want to thank Gary Egbert and Anna Kelbert for providing the ModEM code; Weerachai Siripunvaraporn for providing WSINV3DMT code; the Irish Centre for High-End Computing (ICHEC) for availing the Stokes cluster to carry out the numerical computations and Jan Vozar for his advice on the 3D inversion process. The authors sincerely thank the Associate Editor Charles Jenkins and the anonymous reviewers for their useful comments on the manuscript. Last, but not least, Modesto Montoto and Andrés Pérez-Estaún are thanked for their continuous support.

References

Alcalde, J., Martí, D., Calahorrano, A., Marzán, I., Ayarza, P., Carbonell, R., Juhlin, C., Pérez-Estaún, A., 2013a. Active seismic characterization experiments of the Hontomín research facility for geological storage of CO_2, Spain. Int. J. Greenhouse Gas Control 19, 785–795, http://dx.doi.org/10.1016/j.ijggc.2013.01.039.

Alcalde, J., Martí, D., Juhlin, C., Malehmir, A., Sopher, D., Saura, E., Marzán, I., Ayarza, P., Calahorrano, A., Pérez-Estaún, A., Carbonell, R., 2013b. 3-D reflection seismic imaging of the Hontomín structure in the Basque-Cantabrian basin (Spain). Solid Earth 4, 481–496, http://dx.doi.org/10.5194/se-4-481-2013.

Alemu, B.L., Aker, E., Soldal, M., Johnsen, Ø., Aagaard, P., 2011. Influence of CO_2 on rock physics properties in typical reservoir rock: a CO_2 flooding experiment of brine saturated sandstone in a CT-scanner. Energy Proc. 4, 4379–4386, http://dx.doi.org/10.1016/j.egypro.2011.02.390.

Archie, G.E., 1942. The electrical resistivity log as an aid in determining some reservoir characteristics. Trans. AIME 146, 54–67.

Avdeev, D.B., 2005. Three-dimensional electromagnetic modelling and inversion from theory to application. Surveys Geophys. 26 (6), 767–799, http://dx.doi.org/10.1007/s10712-005-1836-2.

Bedrosian, P.A., 2007. MT+, integrating magnetotellurics to determine earth structure, physical state, and processes. Surveys Geophys. 28, 121–167, http://dx.doi.org/10.1007/s10712-007-9019-6.

Benjumea, B., Macau, A., Figueres, S., Gabàs, S., Sendra, R., Marzán, I., 2012. Testificación geofísica de los sondeos de investigación hidrogeológica de Hontomín (Burgos). IGC – Institut Geològic de Catalunya Technical Report, GA-002/12. Generalitat de Catalunya, pp. 36.

Bergmann, P., Schmidt-Hattenberger, C., Kiessling, D., Rücker, C., Labitzke, T., Henninges, J., Baumann, G., Schütt, H., 2012. Surface-downhole electrical resistivity

tomography applied to monitoring of CO_2 storage at Ketzin, Germany. Geophysics 77, B253–B267, http://dx.doi.org/10.1190/geo2011-0515.1.
Börner, R.U., 2010. Numerical modelling in geo-electromagnetics: advances and challenges. Surv. Geophys. 31 (2), 225–245, http://dx.doi.org/10.1007/s10712-009-9087-x.
Börner, J.H., Herdengen, V., Repke, J.U., Spitzer, K., 2013. The impact of CO_2 on the electrical properties of water bearing porous madia-laboratory experiments with respect to carbon capture and storage. Geophys. Prospect. 61 (Suppl. 1), 446–460, http://dx.doi.org/10.1111/j.1365-2478.2012.01129.x.
Bourgeois, B., Girard, J.F., 2010. First modelling results of the EM response of a CO_2 storage in the Paris basin. Oil Gas Sci. Technol. Rev. – IFP 65 (4), 597–614, http://dx.doi.org/10.2516/ogst/2009076.
Buil, B., Gómez, P., Peña, J., Garralón, A., Galarza, C., Durán, J.M., Domínguez, R., Escribano, A., Turrero, M.J., Robredo, L.M., Sánchez, L., 2012. Caracterización y monitorización hidrogeoquímica de los acuíferos superiores a la formación almacenamiento de CO2 (Hontomín, Burgos) y actualización de la caracterización de aguas superficiales. Technical report CIEMAT/DMA/2G010/1/2012.
Caldwell, T.G., Bibby, H.M., Brown, C., 2004. The magnetotelluric phase tensor. Geophys. J. Int. 158, 457–469, http://dx.doi.org/10.1111/j.1365-246X.2004.02281.x.
Canal, J., Delgado, J., Falcón, I., Yang, Q., Juncosa, R., Barrientos, V., 2013. Injection of CO_2-saturated water through a siliceous sandstone plug from the Hontomin Test Site (Spain): experiments and modeling. Environ. Sci. Technol. 47 (1), 159–167, http://dx.doi.org/10.1021/es3012222.
Chave, A.D., Jones, A.G., 2012. The Magnetotelluric Method: Theory and Practice. Cambridge University Press, Cambridge (UK), ISBN 978-0-521-81927-5.
Chave, A.D., Thomson, D.J., 2004. Bounded influence magnetotelluric response function estimation. Geophys. J. Int. 157, 988–1006, http://dx.doi.org/10.1111/j.1365-246X. 2004.02203.x.
Egbert, G.D., Booker, J.R., 1986. Robust estimation of Geomagnetic transfer functions. Geophys. J. R. Astronom. Soc. 87, 173–194.
Egbert, G.D., Kelbert, A., 2012. Computational recipes for EM inverse problems. Geophys. J. Int. 189 (1), 251–267, http://dx.doi.org/10.1111/j.1365-246X.2011.05347.x.
Elío, J., Nisi, B., Ortega, M.F., Mazadiego, L.F., Vaselli, O., Grandia, F., 2013. CO_2 soil flux baseline at the technological development plant for CO_2 injection at Hontomin (Burgos, Spain). Int. J. Greenhouse Gas Control 18, 224–236, http://dx.doi.org/10.1016/j.ijggc.2013.07.013.
Escalas, M., Queralt, P., Ledo, J., Marcuello, A., 2013. Polarisation analysis of magnetotelluric time series using a wavelet-based scheme: a method for detection and characterisation of cultural noise sources. Phys. Earth Planet. Inter. 218, 31–50, http://dx.doi.org/10.1016/j.pepi.2013.02.006.
Farquharson, C.G., Craven, J.A., 2009. Three-dimensional inversion of magnetotelluric data for mineral exploration: an example from the McArthur River uranium deposit, Saskatchewan, Canada. J. Appl. Geophys. 68 (4), 450–458, http://dx.doi.org/10.1016/j.jappgeo.2008.02.002.
Gamble, T.D., Goubau, W.M., Clarke, J., 1979. Magnetotellurics with a remote magnetic reference. Geophysics 44, 53–68.
Giese, R., Henninges, J., Lüth, S., Morozova, D., Schmidt-Hattenberger, C., Würdemann, H., Zimmer, M., Cosma, C., Juhlin, C., CO2SINK Group, 2009. Monitoring at the CO_2SINK site: a concept integrating geophysics. Geochem. Microbiol. Energy Proc. 1, 2251–2259, http://dx.doi.org/10.1016/j.egypro.2009.01.293.
Ghaedrahmati, R., Moradzadeh, A., Fathianpour, N., Lee, S.K., Porkhial, S., 2013. 3-D inversion of MT data from the Sabalan geothermal field, Ardabil, Iran. J. Appl. Geophys. 93, 12–24, http://dx.doi.org/10.1016/j.jappgeo.2013.03.006.
Girard, J.F., Coppo, N., Rohmer, J., Bourgeois, B., Naudet, V., Schmidt-Hattenberger, C., 2011. Time-lapse CSEM monitoring at Ketzin (Germany) CO_2 injection using 2xMAM configuration. Energy Proc. 4, 3322–3329.
Groom, R.W., Bailey, R.C., 1989. Decomposition of magnetotelluric impedance tensor in the presence of local three-dimensional galvanic distortion. J. Geophys. Res. 94, 1913–1925.
He, Z., Hu, Z., Luo, W., Wang, C., 2010. Mapping reservoirs based on resistivity and induced polarization derived from continuous 3D magnetotelluric profiling: case study from Qaidim basin, China. Geophysics 75 (1), B25–B33, http://dx.doi.org/10.1190/1.3279125.
Heise, W., Caldwell, T.G., Bibby, H.M., Bannister, S.C., 2008. Three-dimensional modeling of the magnetotelluric data from the Rotakawa geothermal field, Taupo Volcanic Zone, New Zeland. Geophys. J. Int. 173, 740–750, http://dx.doi.org/10.1111/j.1365-246X.2008.03737.x.
Hoversten, G.M., Gasperikova, E., 2005. Non-seismic geophysical approaches to monitoring. In: Thomas, D.C., Benson, S.M. (Eds.), Carbon Dioxide Capture for Storage in Deep Geologic Formations, vol. 2. Elsevier Ltd., Oxford, UK, pp. 1071–1112.
Ingham, M.R., Bibby, H.M., Heise, W., Jones, K.A., Cairns, P., Dravitzki, S., Bennie, S.L., Caldwell, T.G., Ogawa, Y., 2009. A magnetotelluric study of Mount Ruapehu volcano, New Zealand. Geophys. J. Int. 179 (2), 887–904, http://dx.doi.org/10.1111/j.1365-246X.2009.04317.x.
IPCC – Intergovernmental Panel on Climate Change, 2005. In: Metz, B., Davidson, O., de Coninck, H.C., Loos, M., Meyer, L.A. (Eds.), IPCC Special Report on Carbon Dioxide Capture and Storage. Prepared by Wozzrking Group III of the Intergovernmental Panel on Climate Change. Cambridge University Press, Cambridge, United Kingdom and New York, NY, USA.
JafarGandomi, A., Curtis, A., 2011. Detectability of petrophysical properties of subsurface CO_2-saturated aquifer reservoirs using surface geophysical methods. Lead. Edge 30 (10), 1112–1121.
Jones, A.G., 2012. Distortion of magnetotelluric data: its identification and removal. In: Chave, A.D., Jones, A.G. (Eds.), The Magnetotelluric Method: Theory and Practice. Cambridge University Press, Cambridge (UK), ISBN 978-0-521-81927-5.
Kiessling, D., Schmidt-Hattenberger, C., Schuett, H., Schilling, F., Krueger, K., Schoebel, B., Danckwardt, E., Kummerow, J., CO2SINK Group, 2010. Geoelectrical methods for monitoring geological CO_2 storage: first results from cross-hole and surface-downhole measurements from the CO2SINK test site at Ketzin (Germany). Int. J. Greenhouse Gas Control 4 (5), 816–826, http://dx.doi.org/10.1016/j.ijggc.2010.05.001.
Kiyan, D., Jones, A.G., Vozar, J., 2014. The inability of magnetotelluric off-diagonal impedance tensor elements to sense oblique conductors in 3-D inversion. Geophys. J. Int. 196, 1351–1364, http://dx.doi.org/10.1093/gji/ggt470.
Ledo, J., Jones, A.G., 2005. Upper mantle temperature determined from combining mineral composition, electrical conductivity laboratory studies and magnetotelluric field observations: application to the intermontane belt, Northern Canadian Cordillera. Earth Sci. Lett. 236, 258–268, http://dx.doi.org/10.1016/j.epsl.2005.01.044.
Ledo, J., Queralt, P., Martí, A., Jones, A.G., 2002. Two-dimensional interpretation of three-dimensional magnetotelluric data: an example of limitations and resolution. Geophys. J. Int. 150 (1), 127–139, http://dx.doi.org/10.1046/j.1365-246X.2002.01705.x.
Lumley, D., 2010. 4D seismic monitoring of CO2 sequestrattion. Lead. Edge 29 (2), 150–155, http://dx.doi.org/10.1190/1.3304817.
MacGregor, L., 2012. Integrating seismic, CSEM, and well log data for reservoir characterization. Lead. Edge 31 (3), 268–277.
Mackie, R.L., Madden, T.R., 1993. Three dimensional magnetotelluric inversion using conjugate gradients. Geophys. J. Int. 115, 215–229, http://dx.doi.org/10.1111/j.1365-246X.1993.tb05600.x.
Márquez, M., Jurado, M.J., 2011. Petrophysical characterization of a CO_2 storage reservoir using well logs. Geophys. Res. Abstr. 13, EGU2011-6891-3. EGU General Assembly 2011.
Martí, A., Queralt, P., Ledo, J., 2009. WALDIM: A code for the dimensionality analysis of magnetotelluric data using rotational invariants of the magnetotelluric tensor. Comput. Geosci. 35 (12), 2295–2303, http://dx.doi.org/10.1016/j.cageo.2009.03.004.
Miensopust, M.P., Queralt, P., Jones, A.G., the 3D MT modellers, 2013. Magnetotelluric 3D inversion – a recapitulation of two successful workshops on forward and inversion code testing and comparison. Geophys. J. Int. 193 (3), 1216–1238, http://dx.doi.org/10.1093/gji/ggt066.
Muñoz, J.A., 2002. The Pyrenees. In: Gibbons, W., Moreno, T. (Eds.), The Geology of Spain. Geological Society, London, pp. 370–385.
Nakatsuka, Y., Xue, Z., Garcia, H., Matsuoka, T., 2010. Experimental study on CO_2 monitoring and quantification of stored CO_2 in saline formations using resistivity measurements. Int. J. Greenhouse Gas Control 4, 209–216, http://dx.doi.org/10.1016/j.ijggc.2010.01.001.
NETL-National Energy Technology Laboratory, U.S. Department of Energy, 2009. Monitoring, Verification, and Accounting of CO2 Stored in Deep Geologic Formations. DOE Document: DOE/NETL-311/081508, Accessed October, 2013. http://www.netl.doe.gov/technologies/carbon_seq/refshelf/MVA_Document.pdf
Newman, G.A., Gasperikova, E., Hoversten, G.M., Wannamaker, P.E., 2008. Three-dimensional magnetotelluric characterization of the Coso geothermal field. Geothermics 37, 369–399, http://dx.doi.org/10.1016/j.geothermics.2008.02.006.
Newman, G.A., Recher, S., Tezkan, B., Neubauer, M., 2003. 3D inversion of a scalar radio magnetotelluric field data set. Geophysics 68 (3), 791–802, http://dx.doi.org/10.1190/1.1581032.
Nisi, B., Vaselli, O., Tassi, F., Elío, J., Delgado Huertas, A., Mazadiego, L.P., Ortega, M.F., 2013. Hydrogeochemistry of surface and spring waters in the surroundings of the CO_2 injection site at Hontomín-Huermeces (Burgos Spain). Int. J. Greenhouse Gas Control 14, 151–168, http://dx.doi.org/10.1016/j.ijggc.2013.01.012.
Ogaya, X., Ledo, J., Queralt, P., Marcuello, A., Quintà, A., 2013. First geoelectrical image of the subsurface of the Hontomín site (Spain) for CO_2 geological storage: a magnetotelluric 2D characterization. Int. J. Greenhouse Gas Control 13, 168–179, http://dx.doi.org/10.1016/j.ijggc.2012.12.023.
Ogaya, X., Queralt, P., Ledo, J., Marcuello, A., Jones, A.G., 2012. Preliminary results of the 3-D magnetotelluric characterization of the subsurface of the Technology Demonstration Plant of Hontomín (Burgos, Spain) for geological storage of CO_2. In: Zurutuza, J. (Ed.), 7AHPGG: Proceedings. Portuguese-Spanish Assembly of Geodesy and Geophysics. , ISBN 978-84-941323-1-5, pp. 703–708.
Parker, R.L., 1980. The inverse problem of electromagnetic induction: existence and construction of solutions based on incomplete data. J. Geophys. Res. 85 (B8), 4421–4428, http://dx.doi.org/10.1029/JB085iB08p04421.
Parker, R.L., Whaler, K.A., 1981. Numerical methods for establishing solutions to the inverse problem of electromagnetic induction. J. Geophys. Res. 86 (B10), 9574–9584, http://dx.doi.org/10.1029/JB086iB10p09574.
Piña-Varas, P., Ledo, J., Queralt, P., Roca, E., García-Lobón, J.L., Ibarra, P., Biete, C., 2013. Two-dimensional magnetotelluric characterization of the El Hito Anticline (Loranca Basin, Spain). J. Appl. Geophys. 95, 121–134, http://dx.doi.org/10.1016/j.jappgeo.2013.06.002.
Quintà, A., (Ph.D. Thesis) 2013. El patrón de fracturación alpina en el sector suroccidental de los Pirineos Vascos. Universitat de Barcelona, Barcelona, Spain, pp. 153.
Rosell, O., Martí, A., Marcuello, A., Ledo, J., Queralt, P., Campanyà, J., 2011. Deep electrical resistivity structure of the northern Gibraltar Arc (western mediterranean): evidence of lithospheric slab break-off. Terra Nova 23 (3), 179–186, http://dx.doi.org/10.1111/j.1365-3121.2011.00996.x.

Rubio, F.M., Ayala, C., Gumiel, J.C., Rey, C., 2011. Caracterización mediante campo potencial y teledetección de la estructura geológica seleccionada para planta de desarrollo tecnológico de almacenamiento geológico de CO2 en Hontomín (Burgos). IGME-Instituto Geológico y Minero de España Technical Report, pp. 182.

Sato, K., Mito, S., Horie, T., Ohkuma, H., Saito, H., Watanabe, J., Yoshimura, T., 2011. Monitoring and simulation studies for assessing macro- and meso-scale migration of CO_2 sequestered in an onshore aquifer: experiences from the Nagaoka pilot site, Japan. Int. J. Greenhouse Gas Control 5, 125–137, http://dx.doi.org/10.1016/j.ijggc.2010.03.003.

Siripunvaraporn, W., 2012. Three-dimensional magnetotelluric inversion: an introductory guide for developers and users. Surv. Geophys. 33 (1), 5–27, http://dx.doi.org/10.1007/s10712-011-9122-6.

Siripunvaraporn, W., Egbert, G., Lenbury, Y., Uyeshima, M., 2005. Three-dimensional magnetotelluric inversion: data-space method. Phys. Earth Planet. Inter. 150, 3–14, http://dx.doi.org/10.1016/j.pepi.2004.08.023.

Streich, R., Becken, M., Ritter, O., 2010. Imaging of CO_2 storage sites, geothermal reservoirs, and gas shales using controlled-source magnetotellurics: modeling studies. Chem. Erde-Geochem. 70 (3), 63–75, http://dx.doi.org/10.1016/j.chemer.2010.05.004.

Tavani, S., Quintà, A., Granado, P., 2011. Cenozoic right-lateral wrench tectonics in the Western Pyrenees (Spain): the Ubierna Fault System. Tectonophysics 509, 238–253, http://dx.doi.org/10.1016/j.tecto.2011.06.013.

Tuncer, V., Unsworth, M.J., Siripunvaraporn, W., Craven, J.A., 2006. Exploration for unconformity-type uranium deposits with audiomagnetotellurics data: a case study from the McArthur River mine, Saskatchewan, Canada. Geophysics 71 (6), B201–B209, http://dx.doi.org/10.1190/1.2348780.

Ugalde, A., Villaseñor, A., Gaite, B., Casquero, S., Martí, D., Calahorrano, A., Marzán, I., Carbonell, R., Estaún, A.P., 2013. Passive seismic monitoring of an experimental CO_2 geological storage site in Hontomín (Northern Spain). Seismol. Res. Lett. 84 (1), 75–84, http://dx.doi.org/10.1785/0220110137.

Vilamajó, E., Queralt, P., Ledo, J., Marcuello, A., 2013. Feasibility of monitoring the Hontomín (Burgos Spain) CO_2 storage site using deep EM source. Surv. Geophys. 34, 441–461, http://dx.doi.org/10.1007/s10712-013-9238-y.

Weaver, J.T., Agarwal, A.K., Lilley, F.E.M., 2000. Characterisation of the magnetotelluric tensor in terms of its invariants. Geophys. J. Int. 141 (2), 321–336, http://dx.doi.org/10.1046/j.1365-246X.2000.00089.x.

Xiao, Q., Cai, X., Xu, X., Liang, G., Zhang, B., 2010. Application of the 3D magnetotelluric inversion code in a geologically complex area. Geophys. Prospect. 58 (6), 1177–1192, http://dx.doi.org/10.1111/j.1365-2478.2010.00896.x.

Zhdanov, M.S., Wan, L., Gribenko, A., Čuma, M., Key, K., Constable, S., 2011. Large-scale 3D inversion of marine magnetotelluric data: Case study from the Gemini prospect, Gulf of Mexico. Geophysics 76 (1), F77–F87, http://dx.doi.org/10.1190/1.3526299.